ROTOR BALANCING VIA AN ENHANCED AUTOMATIC DYNAMIC BALANCER WITH INDUCTIVELY COUPLED SHUNT CIRCUIT

A Dissertation Presented for the

Doctor of Philosophy

Degree

The University of Tennessee, Knoxville

Xiaowen Su

May 2019

Copyright © 2019 by Xiaowen Su

All rights reserved.

DEDICATION

To

My husband
Bin Wang

My parents
Minghua Deng & Hongquan Su

My grandparents
Shuzhen Feng & Xitang Deng

My little angel
Emily S. Wang

ACKNOWLEDGEMENTS

I would like to express my sincere gratitude to many people who have helped me through out my graduate study. Among them I am most indebted to my advisor Dr. Hans A. DeSmidt, whose extraordinary inspiration and great dedication gave me the opportunity to do this wonderful research on the rotor balancing via enhanced automatic dynamic balancer, and whose wide knowledge and continuously encouragement helped me in solving problems.

I am also very grateful for the supervising and assistance provided by my doctoral committee. Dr. Xiaopeng Zhao with his dynamics class, and Dr. Seddik M. Djouadi with his linear systems theory class. The knowledge I learnt from them has become an essential underpinning in my doctoral research. I also greatly learned from my doctoral committee, Dr. Kivanc Ekici his logical discussion on numerical algorithm.

There are many other professors who have guided me in my graduate educations. Dr. John Landes's advanced mechanics of materials course build a very concrete foundation for analysis of mechanics of materials. Dr. Toby Boulet's mechanical vibrations course encouraged me to build a profound foundation of vibration analysis. Dr. Andy Sarles's smart materials and structures course enlightened me on analysis of systems with mechanical energy, electrical energy and other different energies. Dr. Kai Sun's power system stability course inspired my curiosity in power system stability analysis. I also very appreciate the help and support from my friends and colleagues, Dr. Peng Guan and Dr. Wei Yao. Finally, I want to thank my husband Bin Wang, for his infinite patience and support during my graduate studies.

I gratefully acknowledge the funding received towards my PhD from my advisor Dr. Hans A. DeSmidt, from the department of Mechanical, Aerospace, Biomedical Engineering, and from the UTF Dr/Mrs Hui Pih Mem Eng fellowship. In the last year, I also grateful to the funding received through the VLRCOE.

The works in Chapter two and three have been published in Ref [52] and we are ready to submit our works in Chapter four and five for a publication.

ABSTRACT

To reduce manufacturing costs and maintenance frequency of rotordynamic systems resulting from rotational imbalance and associated vibration levels, this research has been focused on the automatic dynamic balancer (ADB) due to its achieving balancing without external power, sensors or a control system and due to its ability of automatically adjusting and compensating for uncertain and changing rotor imbalance levels in real-time. Conventional ADBs are essentially a set of moving balancer balls attached to a rotor, which, through nonlinear dynamic interactions between the rotor vibration and balancer mass motions, reach a stable limit-cycle solution that balances the combined system resulting low residual vibration. One of the drawbacks of ADBs is their inherently nonlinear dynamic nature which can lead to other co-existing non-balanced solutions depending on initial conditions and rotor speed. To resolve this, this research proposed and developed a novel Enhanced Automatic Dynamic Balancer (EADB) which replaces the conventional moving balancer masses with permanent magnet balancer masses. The magnetic balancer masses are then inductively coupled to a shunt circuit network to enable tailoring of the nonlinear dynamic system response via passive circuit parameters such as inductance and capacitance. This new EADB system shows significant improvement in stability and performance over the conventional ADB while still preserving the key benefits such as being passive and self-adapting. We provided a detailed design procedure and some possible implementation parameters. We derived the governing equations and obtained perfect-balancing solutions and whirling limit-cycle solutions for different rotordynamic systems with one EADB or two EADBs. We also explored some other practical concerns when applying the EADBs, such as the effect of gravity if applied on a vertical rotor, tilting vibration suppression if applied on a 3-dimension rotor and the eccentricity of the EADB and the assembling errors.

Keywords: Rotor balancing, Enhanced Automatic Dynamic Balancer, embedded shunt circuit, electromagnetic induction, whirling limit cycle, modified harmonic balance method, stability analysis, 3-dimensional rotor, eccentricity, assembling error, gravity.

TABLE OF CONTENTS

CHAPTER 1 INTRODUCTION 1

1.1 Background of the ADB (automatic dynamic balancer) and motivation for the EADB (enhanced automatic dynamic balancer) 1

1.2 Contributions 7

CHAPTER 2 DESIGN AND MODELING OF THE EADB AND ITS APPLICATION ON SYMMETRICALLY SUPPORTED PLANAR ROTOR SYSTEM 9

2.1 Introduction of Chapter Two 9

2.2 Design of the EADB 10

2.2.1 The magnetic ball and a closed-loop circuit 10

2.2.2 Coils and the self-inductance 13

2.2.3 Physical parameters and constraints 14

2.3 Symmetrically supported planar rotor/dual mass EADB system 16

2.3.1 Modeling of the symmetrically supported planar rotor/dual mass EADB system 16

2.3.2 Equilibrium points (EPs) 22

2.3.3 Conclusions 27

2.4 Stability analysis of EPs 28

2.4.1 Linearized model based on the EP 28

2.4.2 Shunt circuit parameter study 28

2.5 The effect of the EADB imperfect assembling on the perfect-balancing EP 32

2.5.1 Introduction of ADB imperfect assembling 32

2.5.2 Modeling including the eccentricity effect 32

2.5.2 The effect of eccentricity on half-balanced EP 34

CHAPTER 3 WHIRLING LIMIT-CYCLE OF THE EADB 37

3.1 Solve for the whirling limit-cycle 37

3.2 Stability analysis of the whirling limit-cycle 41

3.3 Shunt circuit parameter study 42

3.4 Examination of the whirling limit-cycle and the numerical study 49

3.5 The EADB implementation parameters 54

3.6 Conclusions of the symmetrically supported planar rotor/dual mass EADB system 56

CHAPTER 4 ASYMMETRICALLY SUPPORTED PLANAR ROTOR/DUAL MASS EADB SYSTEM 57

4.1 Asymmetrically supported planar rotor/dual mass EADB System 57

4.1.1 Background and motivation of chapter four 57

4.1.2 Modeling of the asymmetrically supported planar rotor/dual mass EADB system 57

4.1.3 Equilibrium points (EPs) 64

4.2 Stability of the perfect-balancing EP 66

4.2.1 Linearized model 66

4.2.2 Shunt circuit parameter Study 68

4.3 Examination of the perfect-balancing EP and the numerical study 71

CHAPTER 5 WHIRLING LIMIT-CYCLE BEHAVIORS OF THE ASYMMETRICALLY SUPPORTED ROTOR/EADB SYSTEM 76

5.1 Whirling limit-cycle 76

5.1.1 Multi-tone harmonic balance method 76

5.1.2 Matrix pencil method 79

5.1.3 Solve for the whirling limit -cycle 84

5.2 Stability analysis of the whirling limit-cycle 87

5.3 Shunt circuit parameter study 88

5.4 Numerical study and verification 90

CHAPTER 6 VERTICAL PLANAR ROTOR/DUAL MASS EADB SYSTEM 93

6.1 Background and motivation 93

6.1.1 Modeling of the vertically oriented planar rotor/dual mass EADB system 93

6.1.2 Equilibrium points (EPs) 97

6.2 Stability analysis of the “perfect-balancing EP” 98

6.2.1 Linearized model 98

6.2.2 Shunt circuit parameter study 100

CHAPTER 7 MULTI-PLANE BALANCING OF RIGID SHAFT ROTOR/ FOUR MASS DUAL EADB SYSTEM 104

7.1 Background and motivation 104

7.1.1 Modeling of the rigid shaft rotor/four mass dual EADB system 104

7.1.2 Equilibrium points (EPs) 113

7.2 Stability analysis of the perfect-balancing EP 116

7.2.1 Linearized model 116

7.2.2 Parameter study..... 118

..... 129

7.3 Conclusions for chapter 7 130

CHAPTER 8 CONLUSIONS AND FUTURE WORK..... 132

LIST OF REFERENCES..... 135

APPENDIX..... 140

A1..... 141

A2..... 143

A3..... 144

A4..... 147

A5..... 148

A6.1..... 149

A6.2..... 153

A6.3..... 156

A6.4..... 159

A7.1..... 164

A7.2..... 165

A7.3..... 166

A7.4..... 168

A7.5..... 169

VITA 170

LIST OF TABLES

Table 1. Physical parameters for the planar rotor/ADB system…… 17

Table 2. Dimensionless parameters for the symmetrically supported planar rotor/dual mass EADB system…… 29

Table 3. Design parameters for the EADB implementation……..55

Table 4. Physical parameters for the asymmetrically supported planar rotor /EADB system…… 59

Table 5. Dimensionless system parameters for the asymmetrically supported planar rotor/EADB…….. 67

Table 6. Dimensionless system parameters for the asymmetrically supported planar rotor/EADB used in chapter 5……77

Table 7. Dominant frequencies and multi-tone combinations for $x(\tau)$…….. 82

Table 8. Dominant frequencies and multi-tone combinations for $\phi_{b1\text{osc}}$ …… 82

Table 9. Dominant frequencies and multi-tone combinations for $q_1(\tau)$…….83

Table 10. Physical parameters for the vertically oriented planar rotor/EADB system…. 95

Table 11. Dimensionless parameters for the vertically-oriented planar rotor/EADB…... 99

Table 12. Physical parameters for the rigid shaft/ four mass duel EADB system…….. 107

Table 13. Dimensionless system parameters for the rigid shaft/four mass dual EADB system used in chapter 7……..117

LIST OF FIGURES

Figure 1. Configurations of balls' angular position for the planar rotor/ADB system in (a) perfect-balancing condition, and in (b) whirling limit-cycle 4

Figure 2. Basin of attraction for whirling limit-cycle and perfect-balancing condition of a planar rotor/ADB system based on rotor lateral-deflection directions in x and y[26] 5

Figure 3. Basin of attraction for whirling limit-cycle and perfect-balancing condition of a planar rotor/ADB system based on balancer balls' deviation from the perfect-balancing angular position 5

Figure 4. Magnetic ball and a closed-loop circuit..... 11

Figure 5. Transformation between *dl* element and $d\theta$ element..... 11

Figure 6. Transformation between the coil velocity *v* and the magnetic ball angular position ϕ_b 12

Figure 7. Air core toroid inductor 13

Figure 8. Symmetrically supported planar rotor/dual mass EADB system 15

Figure 9. Stability comparison of perfect-balancing EPs for the EADB and the ADB (1) Example (2) ς_e=0.001 (3) ς_e=0.01..... 31

Figure 10. Stability of two different in-phase EPs for the EADB 33

Figure 11. Stability of the half-balanced EP when R_{br} is 0, 9 $\times 10^{-4}$ and 1 $\times 10^{-2}$ in the (μ, Ω) plane, respectively (a) for the planar rotor/ADB or (b) for the planar rotor/EADB. 34

Figure 12. Stability of the half-balanced EP of when R_{br} is 0, 8 $\times 10^{-4}$ and 9 $\times 10^{-4}$ in the (ζ, Ω) plane, respectively (a) for the planar rotor/ADB or (b) for the planar rotor/EADB 35

Figure 13. Stability of the half-balanced EP for the planar rotor/ADB and for the planar rotor/EADB in the (R_{br}, Ω) plane. 36

Figure 14. Scheme of the Arc-length continuation method [39] 39

Figure 15. Comparison of the whirling limit-cycle for the ADB and the EADB/symmetrically supported planar rotor system (1) full picture (2) zoomed-in picture 43

Figure 16. The effect of the circuit parameters on the whirling limit-cycle for the EADB system (1) the effect of ς_e and (2) the effect of R_n 45

Figure 17. The root locus for eigenvalues of the Floquet Transition Matrices under different rotor speeds (a) $\overline{\Omega}$ from 1.1 to 0.1, (b) $\overline{\Omega}$ from 1.1 to 2.1 46

Figure 18. The discontinuity of the continuation curves (a) with one or two harmonic terms (b) with six or seven harmonic terms 47

Figure 19. The period-doubling bifurcation resulting from a narrow range of different rotor speeds (a) $\overline{\Omega}$ =1.11 (b) $\overline{\Omega}$ =1.13 (c) $\overline{\Omega}$ =1.16 (d) $\overline{\Omega}$ =1.17 48

Figure 20. Numerical verification of the solution curve for the ADB (1) stable points (2) unstable points 49

Figure 21. Numerical verification of the solution curve for the EADB (1) stable points (2) unstable points 50

Figure 22. Numerical simulation of rotor deflections for the rotor only, the ADB and the EADB under different rotor speeds and initial conditions 52

Figure 23. Transient response of the balancer balls' angular position and electric charges for the EADB system when (1) R_n=0.01, (2) R_n=100 53

Figure 24. Balancer balls' angular positions for the EADB when rotor speed is $\overline{\Omega}$ =0.97(1) deviate 0.1rad, (2) deviate 0.3rad..... 54

Figure 25. The asymmetrically supported planar rotor/dual mass EADB system..... 58

Figure 26. Stability of perfect-balancing EPs for the EADB and the ADB on the asymmetrically supported planar rotor system(1) Example (2) ς_e=0.001 (3) ς_e=0.01 70

Figure 27. Numerical simulations of the asymmetrically supported planar rotor/ADB or/EADB system initially from the perfect-balancing EP under system parameters ς_e=0.001, R_n=5, C_n=1, shown as point 'A' in Figure 26. 72

Figure 28. Numerical simulations of the asymmetrically supported planar rotor/ADB or/EADB system initially from the perfect-balancing EP under system parameters ς_e=0.001, R_n=6.5, C_n=1, shown as point 'B' in Figure 26. 72

Figure 29. Numerical simulations of the asymmetrically supported planar rotor/ADB or/EADB system initially from the perfect-balancing EP under system parameters ς_e=0.01, R_n=2, C_n=0.01, shown as point 'C' in Figure 26. 73

Figure 30. Numerical simulations of the asymmetrically supported planar rotor/ADB or/EADB system initially from the perfect-balancing EP under system parameters ς_e=0.01, R_n=15.5, C_n=0.04, shown as point 'D' in Figure 26. 73

Figure 31. Numerical simulations of the asymmetrically supported planar rotor/ADB or/EADB system initially from the perfect-balancing EP under system parameters ς_e=0.01, R_n=10.5, C_n=0.04, shown as point 'E' in Figure 26. 74

Figure 32. Numerical simulations of the asymmetrically supported planar rotor/ADB or/EADB system initially from the perfect-balancing EP under system parameters ς_e=0.01, R_n=5.5, C_n=1, shown as point 'F' in Figure 26. 74

Figure 33. Numerical simulations of the asymmetrically supported planar rotor/ADB or/EADB system initially from the perfect-balancing EP under system parameters ς_e=0.01, R_n=7.5, C_n=1, shown as point 'G' in Figure 26. 75

Figure 34. Numerical simulations of the dynamic system (4-11) under parameters shown in Table 5 when $\overline{\Omega}=1.03$, showing $x(\tau)$ and $\dot{x}(\tau)$. 77

Figure 35. Numerical simulations of the dynamic system (4-11) under parameters shown in Table 5 when $\overline{\Omega}=1.03$, showing $\phi_{b1}(\tau)$ and $\dot{\phi}_{b1}(\tau)$. 78

Figure 36. Numerical simulations of the whirling part $\omega\tau$ and the oscillatory part $\phi_{b1\text{osc}}$ of ϕ_{b1} as shown in Figure 35. 78

Figure 37. Comparison of the whirling limit-cycle of the ADB and the EADB/asymmetrically supported planar rotor system (1)full picture (2)zoomed-in picture 89

Figure 38. Numerical simulations of the stable points 'S1', 'S2', 'S3', 'S4' on the continuation curve for the ADB as shown in Figure 37 91

Figure 39. Numerical simulations of the unstable points 'U1', 'U2', 'U3', 'U4' on the continuation curve for the ADB as shown in Figure 37. 91

Figure 40. Numerical simulations of the stable points 's1', 's2', on the continuation curve for the EADB as shown in Figure 37. 92

Figure 41. Numerical simulations of the unstable points ‘u1’, ‘u2’, on the continuation curve for the EADB as shown in Figure 37. 92

Figure 42. Stability comparison of perfect-balancing EPs for the EADB and the ADB (1)Example with $R_w^2\mu$ (2)Example neglect $R_w^2\mu$ 101

Figure 43. Stability comparison of the perfect-balancing EP for the EADB and the ADB (1) Rn =0.01 (2) Rn = 1 102

Figure 44. Stability comparison of the perfect-balancing EP for the EADB and the ADB (1) ς_e=0.001 (2) ς_e=0.01 102

Figure 45. Numerical simulations of the EADB and the ADB showing (1) the balancer ball’s angular positions (2) the rotor deflections 103

Figure 46. The rigid shaft rotor/four mass dual EADB system 105

Figure 47. Two coordinate transformations to represent the rigid shaft motion 106

Figure 48. Ball angular position varying with rotor speed under different axial assembling error R_{bx} (a) R_{bx} = 0 (b) R_{bx} = 0.8 (c) R_{bx} = 1.6..... 119

Figure 49. Stability of perfect-balancing EP in ($\overline{\Omega}$, μ) plane showing the effect of different axial assembling error R_{bx} (a) R_{bx} = 0 (b) R_{bx} = 0.8 (c) R_{bx} = 2.1 120

Figure 50. Stability of perfect-balancing EP in ($\overline{\Omega}$, R_{ix}) plane showing the effect of axial assembling error R_{bx} (a) R_{bx} = 0 (b) R_{bx} = 0.8 (c) R_{bx} = 1.6 120

Figure 51. Stability of perfect-balancing EP in ($\overline{\Omega}$, R_{bL}) plane showing the effect of different axial assembling error R_{bx} (a) R_{bx} = 0 (b) R_{bx} = 0.8 (c) R_{bx} = 1.6 121

Figure 52. Stability of perfect-balancing EP in ($\overline{\Omega}$, ς) plane showing the effect of different axial assembling error R_{bx} (a) R_{bx} = 0 (b) R_{bx} = 0.8 (c) R_{bx} = 1.6 121

Figure 53. Stability of perfect-balancing EP in ($\overline{\Omega}$, ς_b) plane showing the effect of different axial assembling error R_{bx} (a) R_{bx} = 0 (b) R_{bx} = 0.8 (c) R_{bx} = 1.6 122

Figure 54. Numerical simulation of the rigid shaft/dual ADB system and the only shaft system in (R_{br}, Ω) plane showing the comparison of the shaft lateral deflections.. 123

Figure 55. Numerical simulation of the rigid shaft/dual ADB system and the only shaft system in (R_{br}, Ω) plane showing the comparison of the shaft tilting deflections .. 123

Figure 56. Stability of perfect-balancing EP in ($\overline{\Omega}$, μ) plane for the shaft/EADB system under different R_{bx} (a) R_{bx} = 0 (b) R_{bx} = 0.8 (c) R_{bx} = 1.6..... 125

Figure 57. Stability of perfect-balancing EP in ($\overline{\Omega}$, ς_e) plane for the shaft/EADB system under different R_{bx} (a) R_{bx} = 0 (b) R_{bx} = 0.8 (c) R_{bx} = 1.6..... 125

Figure 58. Numerical simulation of the shaft/EADB system under stable point 'P1' showing (a) x,y (b) x_p,y_p (c) ϕ_{bi} (d) Q_i..... 126

Figure 59. Numerical simulation of the shaft/EADB system under stable point 'P2' showing (a) x, y (b) x_p, y_p (c) ϕ_{bi} (d) Q_i..... 126

Figure 60. Two-dimensional optimization of the objective function (7-24a) to get coincident EPs and their stability when $\overline{\Omega}$ =0.8..... 128

Figure 61. Two-dimensional optimization of the objective function (7-24a) to get coincident EPs and their stability when $\overline{\Omega}$ =2.1..... 128

Figure 62. Stability analysis of the perfect-balancing EP for the EADB and the ADB on the rigid shaft system (1) ζ_e =0.001 (2) ζ_e = 0.01..... 129

Figure 63. Numerical simulation of the rigid shaft/ADB and /EADB system showing (1) $(x^2 + y^2)^{1/2}$(2) $(x_p^2 + y_p^2)^{1/2}$ (3) φ_{b1} and φ_{b2} (4) φ_{b3} and φ_{b4}..... 130

CHAPTER 1 INTRODUCTION

1.1 Background of the ADB (automatic dynamic balancer) and motivation for the EADB (enhanced automatic dynamic balancer)

Vibration is a common issue in rotating machinery. It is often caused by an imbalance, which is due to imperfect distributions of rotor mass. To compensate for the imbalance caused by the manufacturing process and assembly, off-line balancing procedures can be applied via attached balancer masses. However, due to effects of wear and damage, changing load imbalance, such as blade loss of turbine machinery, a load change in washing machines, a load imbalance in machine tools, many researchers have explored rotor vibration control methods based on Active Magnetic Bearing (AMB) and passive Automatic Dynamic Balancer (ADB) methods. The AMB has some implementation challenges due to complexity, fault tolerance and cost generated by external power, sensors, actuators, and a closed loop feedback system. Therefore, some researchers and engineers have investigated the ADB technique. Conventional ADBs are composed of several auto-balancer balls freely rolling within a circular track filled with viscous fluid mounted on a rotor. When the rotor operates at certain speeds, the auto-balancer balls move to some stable equilibrium positions so that they can compensate for the rotor imbalance. The ADB can passively reduce or even cancel the unknown imbalance without the requirement for a control system and is able to automatically adjust the balls' positions to eliminate changing imbalance conditions. Therefore, it is worthwhile to conduct research in rotor balancing via the ADB. It is known that the application of the ADB can be promising. In some prior work reported in the literature, the ADB was also called Self-Compensating Dynamic Balancer (SCDB) or Automatic Ball Balancer (ABB) or Automatic Ball-type Balancer Device (ABD).

As documented by the initial researchers on this subject, Thearle(1932), Sharp(1975), Kubo(1986) and Bövik(1986) demonstrated the effectiveness of ring-type and heavy-liquid chamber type passive dynamic balancer [1][6][7][8]. MacDuff(1958) and Tedeusz(1988) presented that the vibration suppression via a body of liquid does not

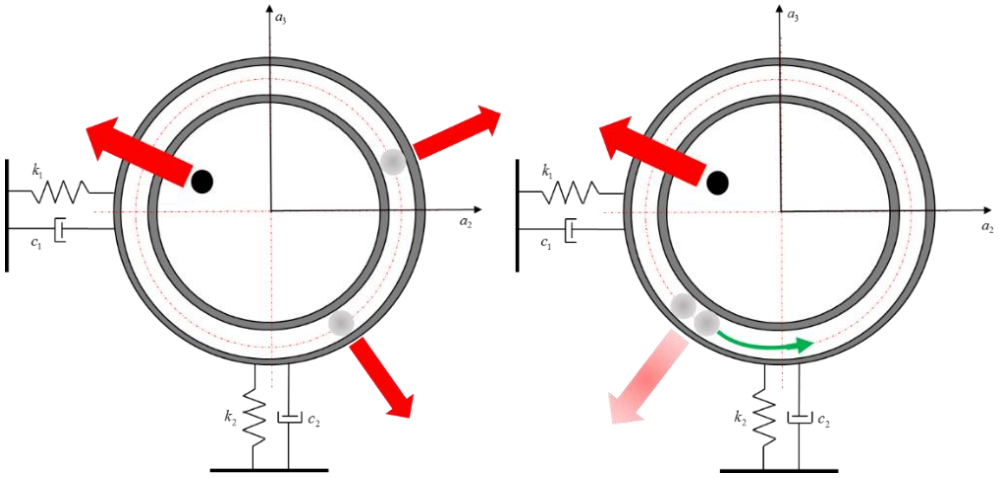
exceed half of the vibration generated by the initial imbalance of rotors, while solid moving bodies can theoretically balance the whole imbalance vibration [3][4]. Motivated by the solid-moving-body-type of balancer, Thearle(1932) invented a ball-type automatic balancer [1], and Clark invented(1940) a pendulum-type automatic balancer [2]. Later Thearle(1950) concluded that ball-type automatic balancers were superior among ring-type balancers and pendulum-type balancers [5]. Therefore, many patents have focused on the application of ball-type automatic balancers. These prototypes of the ADB essentially consists of several balancer balls that are free to move around a guided circular track, filled with a viscous fluid, and mounted on different rotating systems. Sharp(1975), Kubo(1986) and Bövik(1986) did some theoretical studies [6][7][8] and attempted to explain the auto-balancing phenomenon. Lee(1996), Chung(1999), Majewski(1988) and Lu(2009) carried out more recent fundamental studies [9][10][11][12] of ADB applied on a horizontally-oriented planar rotor. They derived the dynamic equations of the planar rotor/ADB system through the Lagrange-energy method and solved system equilibrium points and identified their stability. The planar rotor/ADB system has a symmetrical bearing support, and thus, can be modeled in rotating frame to simplify the system to autonomous system for ease analysis. They found that to fully reduce the vibration caused by the imbalance, total of the balancer masses need to be larger than the imbalance. Furthermore, to compensate the imbalance vibration, the planar rotor/ABD system must operate high above the critical speed of the rotor (zero rotor-speed natural frequency). The balancer mass and rotor speed are critical parameters to enable stable balancing equilibrium points for the planar rotor/ADB system. While other design parameters, such as the ball-rolling resistance, number of balls, bearing damping were studied by Tadeusz(1988), Kubo(1986) and Bövik(1986) in their paper [4][7][8].

The current application of the ADB can be found in computer hard-disk drives, CD-ROM drives, machine tools and energy storage flywheels in[13][14][15]. These are all rigid planar rotors running at super critical speeds with respect to their own rotordynamic systems. In order to develop the use of the ADB for some nonplanar and flexible rotors, Chao(2003), Kim(2005) and DeSmidt(2009) studied, respectively, the

non-planar optical disk drive/ADB system and the supercritical bladed-disk shaft/ADB system[15][16][17]. They found that the ADB can totally balance radial imbalance and can hardly balance the axial imbalance along a shaft. In order to enlarge the stable region for perfect balancing equilibrium points, and to eliminate transient vibration caused by the undesired movement of balls, Lu(2011), Rezaee(2015) and Kim(2013) [18][19][20]proposed three new mechanical structures for the ADB, and Chan(2011) investigated the effect of nonlinearity due to the bearing support[21]. Sung(2013), Bolton(2010) and Filimonikhin(2016) studied some general practical issues such as external force, gravity effect, coulomb friction, race eccentricity, and number of balls[22][23][24].

In above literature reviews, researchers continuously studied the elegant auto-balancing ability of the ADB by dynamic system modeling, solving equilibrium points and identifying their stability, numerical simulation, local bifurcation analysis, and experiments. This elegant ability only corresponds to the linear stability of perfect balancing equilibrium point of the rotor/ADB system. However, due to other potential movements of the ball masses in the circular track, the rotor/ADB system is highly nonlinear. To better understand the ADB, fully nonlinear dynamic system needs to be explored. Hence, Green(2006) presented the global bifurcation analysis of the dynamics of the planar rotor/ADB system via numerical continuation tools [25], and Lu(2011, 2012), Jung and DeSmidt(2017) studied the undesired, non-synchronous limit-cycle behaviors [26][27][28]. Their work revealed that some steady motions of the balls, such as non-trivial steady states, pure oscillatory limit-cycle, pure rotary limit-cycle (whirling limit-cycle), chaotic motions among oscillatory limit cycle, would aggravate associated vibration levels. Lu(2011) found that among these motions, most can be avoided by adjusting rotor speed to a high value since they only appear within a narrow range around the critical speed of the rotor [26]. However, one dominant motion of the balls known as whirling limit-cycle, which is described as all balancer masses merge together and keep whirling in the rotating frame shown in Figure 1(b), cannot be avoided simply by operating at higher speed because it appears in a wide range of rotor supercritical speeds. Furthermore, whirling limit-cycle coexists with perfect-balancing solution [26][27][28]

where ADB eccentric masses position themselves with appropriate phasing to compensate the rotor inherent imbalance shown in Figure 1(a). The coexistence of perfect-balancing solution and whirling limit-cycle for conventional ADBs shortens the rotor speed range for auto-balancing purpose. To take advantage of the auto-balancing ability of the ADB when rotor speed is a little above the rotor critical speed, exploration of the coexistence of a bi-stable region is necessary. Therefore, Refs [26][27]provided modified Incremental Harmonic Balance Method (IHBM) to solve the whirling limit-cycle, and ref [28] explored the whirling limit-cycle on asymmetric bearing support system. Initial conditions determine where the rotor/ADB system settles down, either in perfect-balancing condition or whirling limit-cycle. The settled motion of the balls depends on the system initial conditions as shown in Figure 2 and Figure 3.



(a) (b)

Figure 1. Configurations of balls' angular position for the planar rotor/ADB system in (a) perfect-balancing condition, and in (b) whirling limit-cycle

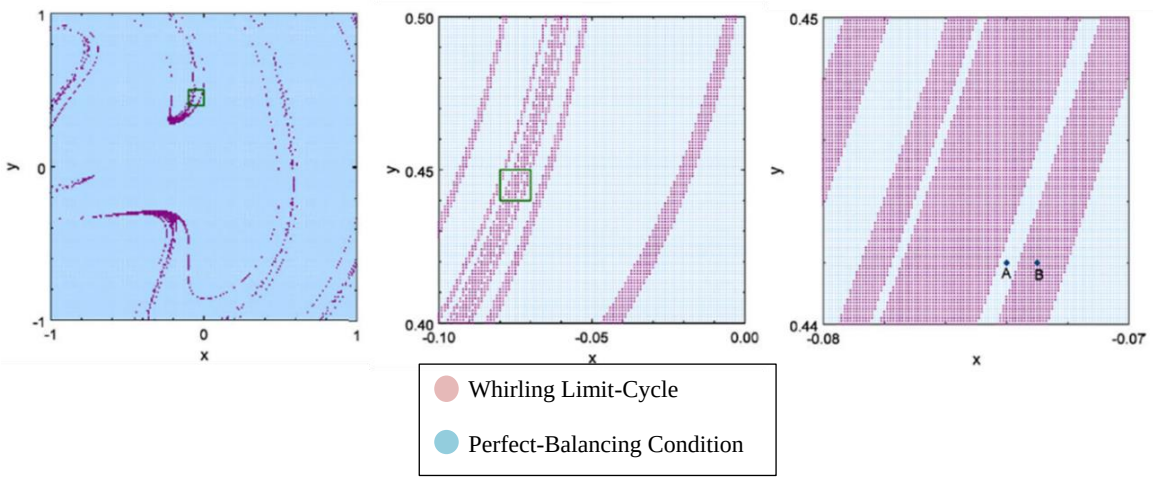


Figure 2. Basin of attraction for whirling limit-cycle and perfect-balancing condition of a planar rotor/ADB system based on rotor lateral-deflection directions in x and y[26]

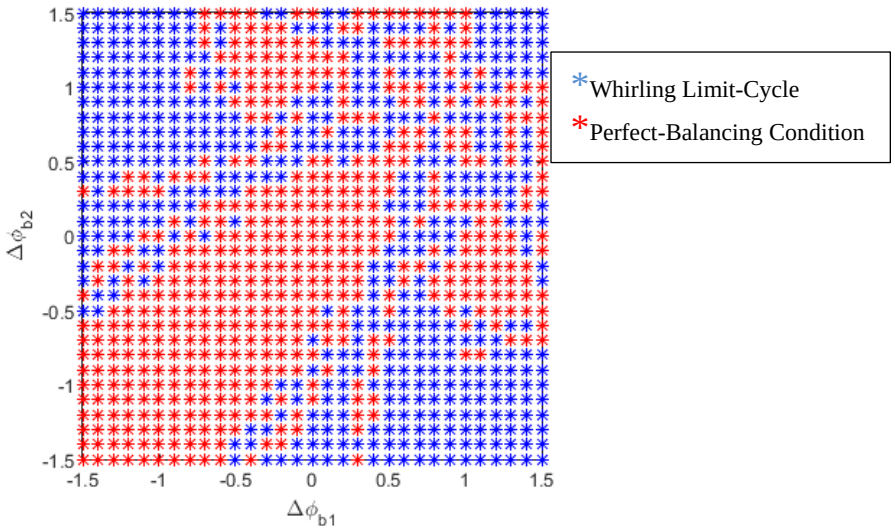


Figure 3. Basin of attraction for whirling limit-cycle and perfect-balancing condition of a planar rotor/ADB system based on balancer balls' deviation from the perfect-balancing angular position

This sensitivity motivates our objective to prevent the coexistence of the stable perfect-balancing condition and the stable whirling limit cycle condition. More specifically, increasing the stable perfect-balancing condition and eliminating the stable whirling limit cycle condition is the goal. If there is a drag force that can prevent the balls from whirling in the circular track, then it may be promising to eliminate stable whirling limit cycle. To future investigate this idea, we proposed and developed an Enhanced Automatic Dynamic Balancer (EADB). We incorporated the drag force in the form of electromagnetic force as we wrapped the circular track with wires to make a shunt circuit, and designed the balls as balancer magnets. Therefore, the drag force is induced by electro-magnetic induction when the balancer magnets move in a wired circular track regarded as a shunt circuit. Chapter Two includes a detailed design procedure where the dynamic equations for the planar rotor/EADB system are derived. The system equilibrium points are determined, and equilibrium points' stability are analyzed and compared with that of the planar rotor/ADB. In Chapter Two, manufacturing variation, such as the eccentricity between the EADB and the shaft are also considered. We found that the imbalance force can be compensated by the EADB, but the residual whirling motion of the rotor equals to the eccentricity. When the imbalance force is balanced, we call the system is in half-balanced equilibrium point. By comparing with the stability of the half-balanced equilibrium points between the planar rotor/EADB and the planar rotor/ADB system, we found that the circuit parameters have little effect on the half-balanced equilibrium points. Chapter Three solved the whirling limit-cycle for the planar rotor/EADB system and compared the solutions with that of the planar rotor/ADB system. By conducting research in Chapter Two and Three, we found that the new EADB system shows significant improvement in stability and performance over the conventional ADB. Therefore, we kept on studying of the novel EADB in general rotordynamic systems, such as a planar rotor with asymmetric bearing support, a vertical rotor with gravity and a 3-dimensional rotor with two EADBs. These studies are presented in Chapter Four and Five, Chapter Six and Chapter Seven. As for planar rotor/ADB or /EADB system, we found that the proposed EADB can greatly reduce the whirling limit-cycle while increasing the stable perfect-balancing condition by adjusting the circuit

parameters. As for the vertical rotor and the 3-dimensional rotor, firstly we need to explore the conventional ADB/rotor system to serve as the benchmark.

1.2 Contributions

In order to extend the auto-balancing condition of the ADB to a wide operating range, and to eliminate the co-existing whirling limit-cycle, we proposed and developed an Enhanced Automatic Dynamic Balancer (EADB), through which we incorporated a drag force in the form of an electromagnetic force as we wrapped the ADB circular track with wires to make a shunt circuit and replaced the balancer balls with magnets. Therefore, drag forces are induced by electro-magnetic induction when balancer magnets move in a wired circular track regarded as a shunt circuit.

Chapter Two includes a detailed design procedure. We derived dynamic equations for the planar rotor/EADB system and solved the system's equilibrium points. We analyzed the equilibrium points' stability and compared with that of the planar rotor/ADB system. In this chapter, we also took consideration of the rotating axis eccentricity between the EADB and the shaft.

Chapter Three solved whirling limit-cycle for the planar rotor/EADB system and compared the solution with that of the planar rotor/ADB system. We found that the proposed EADB can greatly improve the performance over the conventional ADB, so we conducted research on some general rotor/EADB systems, such as an asymmetrically supported planar rotor/EADB system, vertical rotor with gravity/EADB and shaft rotor with tilting/EADB system. We studied them, respectively, in Chapter Four and Five, Chapter Six, and Chapter Seven.

In Chapter Five, we proposed a modified harmonic balance method to solve the whirling limit-cycle of the asymmetrically supported planar rotor/EADB system. By assuming dominant multiple-frequency components in the solution, this approach is a good compromise between the efficiency and the accuracy. The dominant components were gotten from the numerical simulation via an advanced signal processing method known as Matrix Pencil Method (MPM).

In Chapter Six, we found that there are no perfect-balancing solutions rigorously as the balancer balls cannot compensate for both the imbalance and gravity of the system. But

in the normalized dynamic system of the vertical rotor/ADB, gravity resulting from the balancer balls can be neglected as their order of magnitudes are more than 300 times smaller than the vertical rotor gravity and more than 19000 times smaller than the imbalance. Therefore, we can neglect the effect of balancer balls' gravity and solve the system's perfect-balancing equilibrium points. The vertical rotor gravity caused a static vertical deflection of the rotor, and the ADB can compensate for the imbalance just as it can do in a horizontal rotor. Based on above results, we compared the stability of perfect-balancing solutions of the vertical rotor/ADB with that of the vertical rotor/EADB system. We also found that the EADB can enlarge the stable region of perfect-balancing solutions by adjusting circuit parameters.

In the Chapter Seven, we applied two EADBs to balance a shaft rotor (3-dimensional rotor) considering two practical issues. One is the rotating axis eccentricity between the EADB and the shaft, and other is the degree of symmetry when assembling two EADBs on the shaft, each of which contains two balancer masses. We solved the perfect-balancing solution, ball masses coincident in each race condition and the half-balanced solution, and we identified their stability. We proposed a numerical method to solve other equilibrium points at a given set of system parameters, but analytical solutions of other equilibrium points remain a problem as we need to focus on some practical issues at first. We applied an eccentricity on one EADB and found that the eccentricity has a big influence on the stability of half-balanced equilibrium point in the shaft/EADB system. When the eccentricity exceeds 0.1% of the EADB track radius, then the half-balanced equilibrium point may lose its stability. As for the influence of the degree of symmetry, balancer masses can compensate for the effect of asymmetry by adjusting balancer masses' perfect-balancing angular positions.

CHAPTER 2 DESIGN AND MODELING OF THE EADB AND ITS APPLICATION ON SYMMETRICALLY SUPPORTED PLANAR ROTOR SYSTEM

2.1 Introduction of Chapter Two

This chapter will show you how we designed an innovative EADB to reduce or even eliminate the coexistence of whirling limit-cycle and perfect-balancing condition, which appears in the conventional ADB/rotor system. We expect that the motion of balancer balls can stay at perfect-balancing position. If we can couple balancer balls' motion with the electrical circuit via electromagnetic induction, then we can passively tailor the balancer balls' motion within a desired operating range via adjusting the circuit parameters in advance.

The electromagnetic induction is applied widely in inductors, transformers, motors and generators. Some researchers explored this technique on energy harvesting devices, these devices harvest energy from unavoidable oscillations[29][30]. They made one end of the sustained oscillation to be a permanent magnet and let the other end be a close-coils circuit. Therefore, the oscillation energy transforms to the electrical energy through electromagnetic induction between the permanent magnet and the close-coils circuit. As is known in the Faraday's Law of induction that the electromagnetic induction would produce an electromotive force across an electrical conductor in a changing magnetic field. The electromotive force can move the charges in the electrical conductor, and the rate of flow of charges dissipated on the externally connected resistance.

In this work, we need to design auto-balancer balls to be permanent magnets. Their movements' tracks are winded with coils and connected to shunt circuits such that when balancer balls move in their tracks, the electromagnetic induction between balls and shunt circuits can induce current in closed circuits. At the same time the induced current generates a magnetic field that can prevent magnetic balls from whirling.

2.2 Design of the EADB

2.2.1 The magnetic ball and a closed-loop circuit

The design principle of the EADB is similar with that of a transducer. Faraday's law states that the voltage developed across a coil equals to the rate of change of the flux linkage. A conventional transducer is designed based on a stationary magnetic field and a changing flux linkage. In this work, we replace the balancer ball by a permanent cylindrical magnet, magnetized with **N** polar outer layer and **S** polar inner layer shown in Figure 4. Therefore, the magnetic ball can provide a uniform radial magnetic field ***B*** around its surface.

In fact, to make the magnetic ball moving in a torus track, and to produce a uniform radial magnetic field, it is designed as a sectional-torus, which can be made via appropriately bending the cylindrical magnet[31] as long as the bending curvature is small. We can treat the sectional-torus as the cylindrical in our analysis. In this study, the cylindrical magnets will be utilized as the moving balancer masses within the autobalancer device.

As shown in Figure 4, if the magnetic ball moves with a constant velocity *v'* in the magnetic field ***B***, then it is equal to the coil remains a constant velocity *v* in the same field. Faraday's law states that an increment in voltage, *de*, in the direction of the current flow *dl* is induced by the velocity *v*,

$$de = v \times \mathbf{B} \cdot dl \tag{2-1}$$

where *v* is the velocity of the conductor cutting through the magnetic field with the flux density **B**, *dl* is an element in the conductor along with the current flow. As shown in Figure 4, when the magnetic ball moves in the coil winded race, the electromotive force acts as a voltage source $e(t)$ propagating immediately on the circuit with internal resistance *R*. The direction of the voltage source is illustrated in Figure 4.

To treat a linear element *dl*, we consider one turn of coils. The relation between the linear element and its winding circumferential element $d\theta$ is $dl = rd\theta$ shown in Figure 5 where *r* is the coil winding radius.

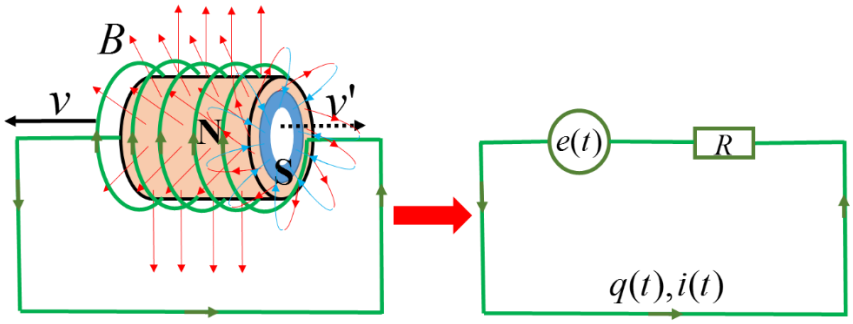


Figure 4. Magnetic ball and a closed-loop circuit

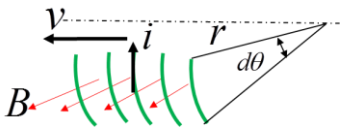


Figure 5. Transformation between *dl* element and $d\theta$ element

The magnetic field ***B*** is mutually perpendicular to the direction of the conductor, and to the direction of the velocity *v*. According to (2-1) and transformation in Figure 5, the incremental in the voltage in the direction of current flow is

$$de = vBrd\theta \tag{2-2}$$

Where *r* is a coil winding radius or magnetic ball radius when coils are winded closely around the magnetic ball. *v* is the velocity of the coil, ***B*** is the flux density, $d\theta$ is the winding circumferential variable.

The total voltage difference for *n* turns is obtained from integrating circumferential variable from 0 to $2\pi n$. Therefore, the terminal voltage $e(t)$ generated from the electromagnetic induction between effective coils (actually coupled coils) and the magnetic ball is

$$e = 2\pi nrBv \tag{2-3}$$

The constitutive relation (2-3) can be simplified by introducing the transducer constant θ_e, defined as

$$\theta_e = 2\pi nrB \tag{2-4}$$

Then, in place of (2-3), we have

$$e(t) = \theta_e v \tag{2-5}$$

To get the electromagnetic energy, we use the transducer co-energy defined in Ref [32],

$$W_t = \lambda i - W_{t0} \tag{2-6}$$

Where λ is the flux linkage, i is the current flow, W_{t0} is the datum value 0 (initial energy). Substituting the planar rotor/EADB parameters and integrating (2-5), we can obtain a useful representation of the flux linkage λ in (2-7),

$$\begin{aligned} \int e(t)dt &= -\int \theta_e R_b \dot{\phi}_b dt \\ \lambda &= -\theta_e R_b \phi_b \end{aligned} \tag{2-7}$$

Where the velocity of the coil v corresponds to the angular velocity of the magnetic ball shown in Figure 6. This transformation is $v = -R_b\dot{\phi}_b$. Where R_b equals to the magnetic ball moving radius, ϕ_b equals to the angular position of the magnetic ball.

Assuming the current flow on the coil is i, we obtain the transducer co-energy as

$$W_t = -\theta_e R_b \phi_b i \tag{2-8}$$

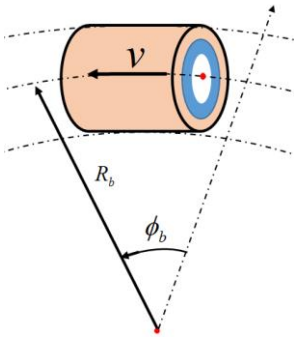


Figure 6. Transformation between the coil velocity v and the magnetic ball angular position ϕ_b

It is worth to note that the magnetic ball surface field strength is larger than the field strength it produced in the air since the field strength can gradually die away if far away from the magnetic ball surface. Therefore, we consider single-layer coil wrapping around the ball's moving track, which is the same surface of the magnetic ball.

2.2.2 Coils and the self-inductance

Different from designing most transducers, which neglects the influence of self-inductance since it is negligible if applying a current or an external force, we won't introduce the current or external forces to achieve a passive circuit. Therefore, we take considerations of the effect of coils self-inductance as well as the effect of its internal electrical resistance to design the dynamic electrical circuit system accurately.

As shown in Figure 7, we wind single-layer coils around a hollow torus track. Single-layer coils are to guarantee that the same flux linkage can be cut through each turn of coils when the magnetic ball moves inside the track. This design appears to be an air core toroid inductor with electrical resistance R_C.

Approximations of the inductance and the resistance are shown below[33],

$$L \approx 0.01257 N^2 (R_b - \sqrt{R_b^2 - r^2}) \times 10^{-4} \tag{2-9}$$

Where N is number of turns, R_b is the major radius, r is the minor radius.

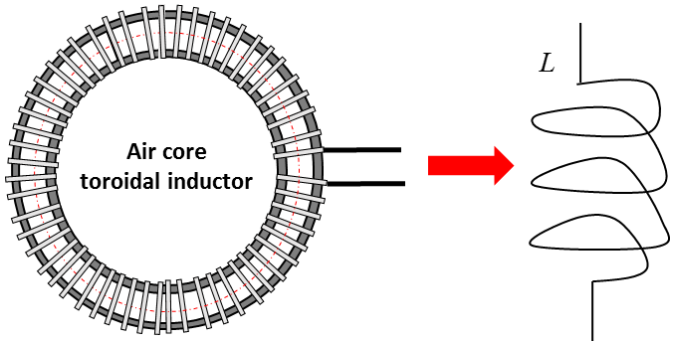


Figure 7. Air core toroid inductor

$$R_C = 8C_e rN / d_c^{\,2} \tag{2-10}$$

Where C_e is electrical resistivity with unit Ohm-m, where N is number of turns, r is the minor radius and d_c is wire diameter.

2.2.3 Physical parameters and constraints

For a given rotordynamic system with conventional ADB, parameters have been determined by the physical system. Therefore, designing the EADB is based on other physical parameters, such as the dimension of the ADB.

The air core toroid inductor is designed by winding copper coils around the ADB moving track. The torus minor radius r is determined by the radius of the balancer ball. To wind copper coils smoothly around the tube track, copper coils' wire diameter d_c need to be constrained,

$$d_c \ll r \tag{2-11}$$

Number of coils winded on tube track with major radius R_b is N with a constraint,

$$N < N_{\max}(2\pi R_b) \tag{2-12}$$

N_{max} is a maximum number of non-insulated coils with diameter d_c, which can be winded around length $2\pi R_b$. This maximum value is determined by a standardized wire gauge system known as American Wire Gauge (AWG).

It is known that one sufficient condition for the prefer-balancing solution is that the mass of balancer balls exceeds that of the rotor imbalance. For a given dimensional constraint, the heavier balancer balls the better. Therefore, we use Sm-Co permanent magnet material with the density 8.2-8.4 g/cm^3. This permanent magnet can provide a magnetic flux density $\boldsymbol{B}$ of about 0.9-1.15 tesla. The balancer ball is a sectional torus as well as a permanent magnet explained in section 2.2.1 and its mass can be calculated as,

$$m_b = V_b \rho_b \tag{2-13}$$

Where V_b is the volume of the sectional torus, ρ_b is the density of the permanent magnet material. The volume can be obtain as shown below,

$$V_b = \frac{\alpha}{2\pi}(\pi r^2)(2\pi R_b) \tag{2-14}$$

Where α is the angle of the sectional torus shown in Figure 8, R_b is torus major radius, r is torus minor radius.

The detailed configuration of the planar rotor/EADB system is shown in Figure 8. To make the EADB rotating along with the rotor, the tube track of the EADB should install tightly on the rotor. Number of turns of coils n, which is shown in (2-3), interacting with the magnetic ball can be obtained as,

$$n = \frac{\alpha}{2\pi} N \tag{2-15}$$

Where α is the angle of the sectional torus, N is the total number of coils winding on the track. Circuit parameters, such as electrical resistance R_C, inductance L, can be determined by (2-9) and (2-10) through 'N' the total number of turns of coils, 'R_b ' the torus major radius, 'r' the torus minor radius, 'C_e' the electrical resistivity, and 'd_c' the wire diameter. Other circuit parameters, such as the capacity of the capacitor C, the load resistance R_L can be designed later.

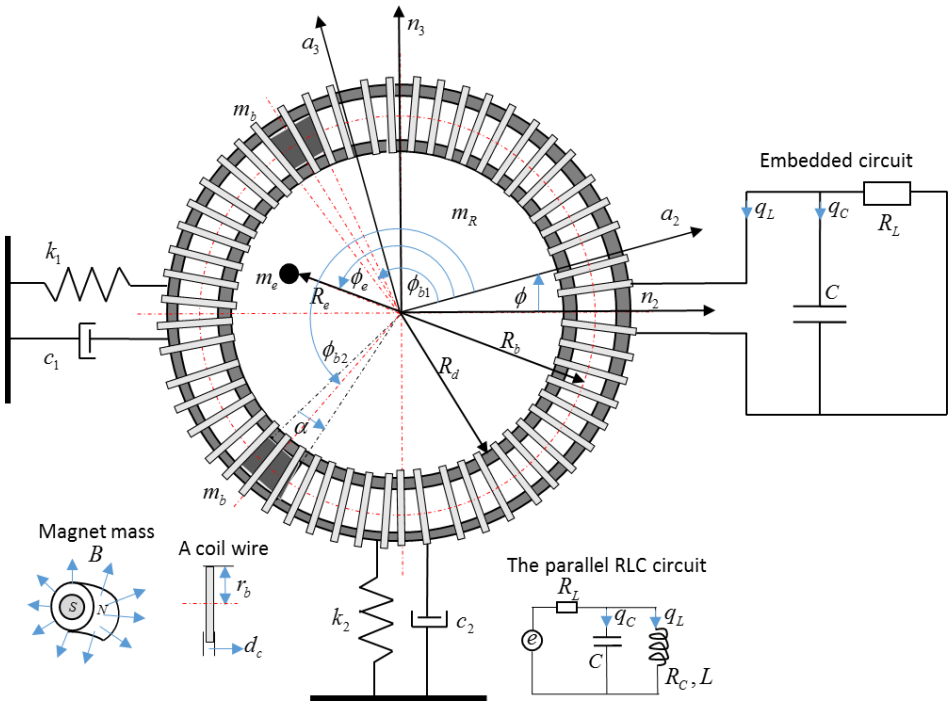


Figure 8. Symmetrically supported planar rotor/dual mass EADB system

2.3 Symmetrically supported planar rotor/dual mass EADB system

This design is shown in Figure 8. Balancer balls are sectional-torus magnets maintaining the uniform radial magnetic field $\boldsymbol{B}$ around their surfaces, and tracks fixed on the rotor is hollow torus tubes winded by copper coils. One track is also a toroid inductor with the inductance L. When the balancer ball moves in coils winded race, the electromotive force acts as a voltage source propagating immediately on a RLC circuit with the inductor and the capacitor connecting in parallel. Each balancer ball moves in an isolated race, so there is no interaction between balls and races. Each race can be placed parallel to or on top of each other. The imbalance added by the RLC circuit has been taken into consideration in the form of rotor imbalance m_e.

In this section, we provide a derivation of equations-of-motion for the symmetrically supported planar rotor/EADB system in the rotating frame enabling an autonomous form, and then we derive a dimensionless form.

As explained in section 2.2.3, the planar rotor/ADB system's parameters are fixed when applying the EADB to an existing physical model. One set of system parameters is shown in Table 1 as an example. The following numerical simulation and analysis are all based on parameters listed in Table 1unless stating otherwise.

2.3.1 Modeling of the symmetrically supported planar rotor/dual mass EADB system

1. Position vectors and total system kinetic energy

This object of our study is a symmetrically supported planar rotor/dual mass EADB system. To facilitate analysis, the equations-of-motion are derived in a set of rotating coordinate system, which follow the planar rotor rotation $\phi(t)$ about the $\mathbf{n}_1$ axis of the inertial coordinate system $\{\mathbf{n}\}$. The position vector locating the rotor spin center C relative to the rotor whirl center O is $\mathbf{r}_O$. $v_a(t)$ and $w_a(t)$ are the lateral deflections measured in the rotating coordinate system $\{\mathbf{a}\}$ in the direction of the $\mathbf{a}_2$ and the $\mathbf{a}_3$.

$$\mathbf{r}_O = v_a(t)\mathbf{a}_2 + w_a(t)\mathbf{a}_3 \tag{2-16}$$

Transformation from $\{\mathbf{n}\}$ to $\{\mathbf{a}\}$ is given as,

Table 1. Physical parameters for the planar rotor/ADB system

Parameter	Value	Units
Rotor radius R_d	0.045	m
Rotor mass m_R	1.3648	kg
Rotor polar inertia J_r	0.0014	kg-m^2
Imbalance quatity m_eR_e	5.215×10^{-4}	kg-m
Bearing support stiffness k	1×10^4	N-m
Bearing support damping c	23.4762	N-m-s
ADB track radius R_b	0.05	m
balancer ball m_b	0.0065	kg
balancer ball -fluid damping c_b	0.0565	N-m-s

$$\begin{bmatrix}\mathbf{a}_2\\ \mathbf{a}_3\end{bmatrix}=\begin{bmatrix}\cos(\phi) & \sin(\phi)\\ -\sin(\phi) & \cos(\phi)\end{bmatrix}\begin{bmatrix}\mathbf{n}_2\\ \mathbf{n}_3\end{bmatrix} \tag{2-17}$$

The planar rotor is assumed to be driven with a constant angular speed **Ω**, hence, the rotation angle is $\phi(t) = \Omega t$. Vectors $\mathbf{r}_{OB}$ and $\mathbf{r}_{OE}$ are the position vectors of the ith balancer mass and the imbalance respectively, and they can be written as,

$$(\mathbf{r}_{OB})_i = \mathbf{r}_O + (\mathbf{r}_B)_i \tag{2-18}$$

With

$$(\mathbf{r}_B)_i = R_b(\cos[\phi_{bi}(t)]\mathbf{a}_2 + \sin[\phi_{bi}(t)]\mathbf{a}_3) \text{ for } i=1, 2 \tag{2-18a}$$

$$\mathbf{r}_{OE} = \mathbf{r}_O + \mathbf{r}_E \tag{2-19}$$

With

$$\mathbf{r}_E = R_e(\cos(\phi_e)\mathbf{a}_2 + \sin(\phi_e)\mathbf{a}_3) \tag{2-19a}$$

Where R_b and R_e are the torus major radius and the imbalance radius; $\phi_{bi}(t)$ and ϕ_e are the ith balancer ball's angular position and the imbalance angular position measured from the $\mathbf{a}_2$ axis. The total system kinetic energy T consists of the planar rotor kinetic energy T_{rotor}, the balancer ball kinetic energy T_{ADB}, and the shunt circuit magnetic co-energy W_m^*.

$$T = T_{rotor} + T_{ADB} + W_m^* \tag{2-20}$$

$$T_{rotor} = \frac{1}{2} J_r \dot{\phi}^2 + \frac{1}{2} m_e \dot{\mathbf{r}}_{OE} \cdot \dot{\mathbf{r}}_{OE} + \frac{1}{2} m_R \dot{\mathbf{r}}_O \cdot \dot{\mathbf{r}}_O \tag{2-20a}$$

$$T_{ADB} = \frac{1}{2} m_b \sum_{i=1}^{2} (\dot{\mathbf{r}}_{OB})_i \cdot (\dot{\mathbf{r}}_{OB})_i \tag{2-20b}$$

$$W_m^* = \frac{1}{2} \sum_{i=1}^{2} L_i (\dot{q}_{Li})^2 \tag{2-20c}$$

Where $(\cdot) = \partial / \partial t$, m_R, m_e and m_b are respectively, the mass of the rotor, the imbalance and the magnetic ball. J_r is the rotor polar inertia, L_i is the inductance of the toroid inductor interacting with the ith magnetic ball, q_{Li} represents the electrical charge on the inductor of the ith shunt circuit.

2. Total system potential energy

The total system potential energy V contains the strain energy V_{rotor}, the electrical energy W_e of the capacitor and the transducer co-energy W_t as shown in Ref [29],

$$V = V_{rotor} + W_e + W_t \tag{2-21}$$

With

$$V_{rotor} = \frac{1}{2} k_1 v_a{}^2 + \frac{1}{2} k_2 w_a{}^2 \tag{2-21a}$$

$$W_e = \frac{1}{2} \sum_{i=1}^{2} \frac{1}{C_i} (q_{Ci})^2 \tag{2-21b}$$

$$W_t = \theta_e R_b \sum_{i=1}^{2} \phi_{bi} (\dot{q}_{Li} + \dot{q}_{Ci}) \tag{2-21c}$$

Where k_1 and k_2 are the bearing stiffness in two directions, C_i are the capacitance of the ith shunt circuit, q_{Ci} is the electrical charge on the capacitor of the ith shunt circuit. θ_e is the electromagnetic coupling coefficient defined as $\theta_e = \boldsymbol{B}\, l_{couple}$, where $\boldsymbol{B}$ is the magnetic

flux density. According to (2-3), we know that $l_{couple}=2\pi nr$ is the length of coils coupling with the magnetic ball.

3. Total system dissipation

To account for the effect of both mechanical and electrical dissipation in the system, we define a Rayleigh dissipation function of the system as,

$$D=\frac{1}{2}c_1\dot{v}_a{}^2+\frac{1}{2}c_2\dot{w}_a{}^2+\frac{1}{2}c_bR_b\sum_{i=1}^{2}(\dot{\phi}_{bi})^2+\frac{1}{2}\sum_{i=1}^{2}(R_{Ci}+R_{Li})(\dot{q}_{Li}+\dot{q}_{Ci})^2 \tag{2-22}$$

Where c_1 and c_2 are the bearing damping in two directions, c_b is the fluid viscous damping resulting from a relative motion between the balancer ball and its corresponding torus track. R_{Ci} and R_{Li} are the internal resistance of coils and the load resistance in the ith shunt circuit.

4. System equations-of-motion

The system equations-of-motion are obtained via Lagrange's method shown as,

$$\frac{\mathrm{d}}{\mathrm{d}t}\left(\frac{\partial(T-V)}{\partial\dot{\mathbf{q}}}\right)-\frac{\partial(T-V)}{\partial\mathbf{q}}+\frac{\partial D}{\partial\dot{\mathbf{q}}}=0 \tag{2-23}$$

With $\mathbf{q}(t)=\left[v_a(t),w_a(t),\phi_{b1}(t),\phi_{b2}(t),q_{C1}(t),q_{L1}(t),q_{C2}(t),q_{L2}(t)\right]$

Substituting (2-16) - (2-22) to (2-23), the system equations-of-motion are given as,

$$\mathbf{M_o}(\phi_{b1},\phi_{b2})\ddot{\mathbf{q}}+\mathbf{C_o}(\phi_{b1},\phi_{b2})\dot{\mathbf{q}}+\mathbf{K_o}(\phi_{b1},\phi_{b2})\mathbf{q}=\mathbf{F_o}(\phi_{b1},\phi_{b2},\dot{\phi}_{b1},\dot{\phi}_{b2}) \tag{2-24}$$

Where the system inertia matrix $\mathbf{M_o}$, stiffness $\mathbf{K_o}$ matrix, and the force vector $\mathbf{F_o}$ are given in A1. The damping matrix $\mathbf{C_o}$ is shown in A7.1.

The resulting equations-of-motion for the ith shunt circuit in (2-24) are not independent. For simplicity, we rearrange them and use q_{Ci} as the independent variable.

$$-L_i\ddot{q}_{Ci}-\frac{L_i}{(R_{Ci}+R_{Li})C_i}\dot{q}_{Ci}-\frac{1}{C_i}q_{Ci}+\frac{L_i\theta_eR_b}{R_{Ci}+R_{Li}}\ddot{\phi}_{bi}=0 \text{ for } i=1,\ 2 \tag{2-24a}$$

The resulting equations-of-motion for the ith balancer ball is given as,

$$\begin{aligned}&m_bR_b{}^2\ddot{\phi}_{bi}+c_bR_b{}^2\dot{\phi}_{bi}+m_bR_b(-\ddot{v}_a+2\Omega\dot{w}_a+v_a\Omega^2)\sin(\phi_{bi})+\\&m_bR_b(\ddot{w}_a+2\Omega\dot{v}_a-w_a\Omega^2)\cos(\phi_{bi})+\theta_eR_b(\dot{q}_{Ci}+\dot{q}_{Li})=0\end{aligned} \text{ for } i=1,\ 2 \tag{2-24b}$$

With

$$\dot{q}_{Li} = \frac{\theta_e R_b}{R_{Ci} + R_{Li}} \dot{\phi}_{bi} - \dot{q}_{Ci} - \frac{1}{(R_{Ci} + R_{Li}) C_i} q_{Ci} \tag{2-24c}$$

(2-24c) is obtained from the rearrangement of the equations-of-motion in (2-24).

After above rearrangement, the resulting nonlinear equations-of-motion for the symmetrically supported planar rotor/ dual mass EADB system are

$$\mathbf{M}(\phi_{b1}, \phi_{b2})\ddot{\mathbf{q}}_{new} + \mathbf{C}(\phi_{b1}, \phi_{b2})\dot{\mathbf{q}}_{new} + \mathbf{K}(\phi_{b1}, \phi_{b2})\mathbf{q}_{new} = \mathbf{F}(\phi_{b1}, \phi_{b2}, \dot{\phi}_{b1}, \dot{\phi}_{b2}) \tag{2-25}$$

With $\mathbf{q}_{new}(t) = \left[v_a(t), w_a(t), \phi_{b1}(t), \phi_{b2}(t), q_{C1}(t), q_{C2}(t)\right]$

Where the system inertia matrix **M**, stiffness matrix **K**, and the force vector **F** are given in A1. The damping matrix **C** is given in A7.1.

5. Dimensionless system equations-of-motion

To simplify the subsequent analysis, we assume the symmetrically supported condition by letting $k_1 = k_2 = k$, $c_1 = c_2 = c$, and we also assume a same set of parameters for different circuits, $R_{C1} = R_{C2} = R_C$, $R_{L1} = R_{L2} = R_L$, $C_1 = C_2 = C$, $L_1 = L_2 = L$. Furthermore, the following dimensionless variables are introduced,

$$\begin{aligned}
&x = \frac{v_a}{R_b}, y = \frac{w_a}{R_b}, \omega_n = \sqrt{\frac{k}{m_R + 2m_b}}, \tau = \omega_n t, \\
&\varsigma = \frac{c}{(m_R + 2m_b)\omega_n}, \varsigma_b = \frac{c_b}{(m_R + 2m_b)\omega_n}, \mu = \frac{m_b}{m_R + 2m_b}, \\
&\eta = \frac{m_e R_e}{(m_R + 2m_b)R_b}, \bar{\Omega} = \frac{\Omega}{\omega_n}, \varsigma_e = \frac{\theta_e^{\,2}}{(m_R + 2m_b)(R_C + R_L)\omega_n}, \\
&R_n = \frac{1}{C(R_C + R_L)\omega_n}, C_n = \frac{1}{CL\omega_n^{\,2}}
\end{aligned} \tag{2-26}$$

where x, y are dimensionless rotor lateral deflections, ς, ς_b, and ς_e are the damping ratio of the rotor, of the balancer ball, and the coupling coefficient between the circuit and the balancer ball. ω_n is the rotor system natural frequency, τ is the dimensionless time, μ is the balancer ball's mass ratio, η is the imbalance ratio, $\bar{\Omega}$ is the dimensionless rotor speed, R_n and C_n are the dimensionless resistance and capacitance. θ_e is the transducer constant.

Substituting (2-26) into (2-25) yields the dimensionless equations-of-motion as the following,

$$\mathbf{M_n}(\phi_{b1},\phi_{b2})\mathbf{q_n''}+\mathbf{C_n}(\phi_{b1},\phi_{b2})\mathbf{q_n'}+\mathbf{K_n}(\phi_{b1},\phi_{b2})\mathbf{q_n}=\mathbf{F_n}(\phi_{b1},\phi_{b2},\phi_{b1}',\phi_{b2}') \tag{2-27}$$

With a set of the general dimensionless coordinate $\mathbf{q_n}(\tau)=\left[x(\tau),y(\tau),\phi_{b1}(\tau),\phi_{b2}(\tau),q_1(\tau),q_2(\tau)\right]$

Where $(')=\partial/\partial\tau$, the dimensionless system mass matrix **M_n**, damping matrix **C_n**, stiffness matrix **K_n** and the force vector **F_n** are given as,

$$\mathbf{M_n}=\begin{bmatrix} 1 & 0 & -\mu\sin(\phi_{b1}) & -\mu\sin(\phi_{b2}) & 0 & 0 \\ 0 & 1 & \mu\cos(\phi_{b1}) & \mu\cos(\phi_{b2}) & 0 & 0 \\ -\mu\sin(\phi_{b1}) & \mu\cos(\phi_{b1}) & \mu & 0 & 0 & 0 \\ -\mu\sin(\phi_{b2}) & \mu\cos(\phi_{b2}) & 0 & \mu & 0 & 0 \\ 0 & 0 & \varsigma_e & 0 & -1 & 0 \\ 0 & 0 & 0 & \varsigma_e & 0 & -1 \end{bmatrix} \tag{2-27a}$$

$$\mathbf{C_n}=\begin{bmatrix} \varsigma & 2\bar{\Omega} & -2\mu\bar{\Omega}\cos(\phi_{b1}) & -2\mu\bar{\Omega}\cos(\phi_{b2}) & 0 & 0 \\ 2\bar{\Omega} & \varsigma & -2\mu\bar{\Omega}\sin(\phi_{b1}) & -2\mu\bar{\Omega}\sin(\phi_{b2}) & 0 & 0 \\ 2\mu\bar{\Omega}\cos(\phi_{b1}) & 2\mu\bar{\Omega}\sin(\phi_{b1}) & \varsigma_b+\varsigma_e & 0 & 0 & 0 \\ 2\mu\bar{\Omega}\cos(\phi_{b2}) & 2\mu\bar{\Omega}\sin(\phi_{b2}) & 0 & \varsigma_b+\varsigma_e & 0 & 0 \\ 0 & 0 & 0 & 0 & -R_n & 0 \\ 0 & 0 & 0 & 0 & 0 & -R_n \end{bmatrix} \tag{2-27b}$$

$$\mathbf{K_n}=\begin{bmatrix} 1-\bar{\Omega}^2 & -\varsigma\bar{\Omega} & 0 & 0 & 0 & 0 \\ \varsigma\bar{\Omega} & 1-\bar{\Omega}^2 & 0 & 0 & 0 & 0 \\ \mu\bar{\Omega}^2\sin(\phi_{b1}) & -\mu\bar{\Omega}^2\cos(\phi_{b1}) & 0 & 0 & -R_n & 0 \\ \mu\bar{\Omega}^2\sin(\phi_{b2}) & -\mu\bar{\Omega}^2\cos(\phi_{b2}) & 0 & 0 & 0 & -R_n \\ 0 & 0 & 0 & 0 & -C_n & 0 \\ 0 & 0 & 0 & 0 & 0 & -C_n \end{bmatrix} \tag{2-27c}$$

$$\mathbf{F_n}=\begin{bmatrix} \bar{\Omega}^2\eta\cos(\phi_e)+\sum_{i=1}^{2}\bar{\Omega}^2\mu\cos(\phi_{bi})+\mu\cos(\phi_{bi})\phi_{bi}'^{\,2} \\ \bar{\Omega}^2\eta\sin(\phi_e)+\sum_{i=1}^{2}\bar{\Omega}^2\mu\sin(\phi_{bi})+\mu\sin(\phi_{bi})\phi_{bi}'^{\,2} \\ 0 \\ 0 \\ 0 \\ 0 \end{bmatrix} \tag{2-27d}$$

It is worth to note that there are some couples between the electric part and the mechanical part. Taking the balancer ball one and its corresponding circuit one as an example, an extra damping coefficient ς_e is added to the balancer ball's damping

coefficient resulting from the effect of the electric circuit. Furthermore, an equivalent force $-R_n q_1$ is added on the eccentric circuit due to the effect of the balancer ball. The term $\varsigma_e \phi''_{b1}$ works as an external voltage source for the electric circuit. Therefore, the dynamics of the balancer ball is influenced by its corresponding circuit.

2.3.2 Equilibrium points (EPs)

To guarantee or even increase the perfect-balancing condition of the EADB, and to reduce or even eliminate the whirling limit-cycle of the EADB, we solved the perfect balancing equilibrium-point and the whirling limit-cycle for the EADB system. Other equilibrium points are also analyzed. When studying the equilibrium points (EPs) for the EADB system, the solutions can degenerate into the solutions of the conventional ADB system. When at EPs, balancer balls stay static in the rotating frame generating zero electric charges. The balancer balls' angles and the rotor deflections in the equilibrium points condition for the EADB system are the same with that of the conventional ADB system, but the stability of the EADB system determined by the perturbation of the state variables including newly introduced electric charges is different, and this stability can be determined with an associated linearized EADB system (2-27).

Assuming EPs for rotor deflections, two balancer balls' angular positions, and two electric charges as constants x_0, y_0, b_1, b_2, q_1, q_2, velocities and accelerations corresponding to these constant state variables are vanished. The steady state response of a second order linear system without the external force must be zero so q_1, q_2 are zeros since balancer balls' accelerations are zeros, which is the external force the electric circuit.

The derivation of the EPs can be found in[10]. To present clearly, we assume a set of the polar coordinates for the rotor deflections as shown below,

$$x_0 = r_o \cos(\theta), y_0 = r_o \sin(\theta) \tag{2-28}$$

Where r_o is the radial deflection of the rotor, θ is the circumferential angle corresponding to the radial deflection.

In order to solve the EPs, substituting the assumption (2-28), b_1, b_2, and q_1=0, q_2=0 into (2-27), we obtained four algebraic equations with r_o, θ, b_1, b_2 as unknowns shown in (2-29).

$$\begin{aligned} & r_o(1-\bar{\Omega}^2)\cos(\theta) - r_o\bar{\Omega}\zeta\sin(\theta) - \bar{\Omega}^2\eta\cos(\theta_e) \\ & -\bar{\Omega}^2\mu\cos(b_1) - \bar{\Omega}^2\mu\cos(b_2) = 0 \\ & r_o(1-\bar{\Omega}^2)\sin(\theta) + r_o\bar{\Omega}\zeta\cos(\theta) - \bar{\Omega}^2\eta\sin(\theta_e) \\ & -\bar{\Omega}^2\mu\sin(b_1) - \bar{\Omega}^2\mu\sin(b_2) = 0 \\ & r_o\bar{\Omega}^2\mu\sin(b_1-\theta) = 0 \\ & r_o\bar{\Omega}^2\mu\sin(b_2-\theta) = 0 \end{aligned} \tag{2-29}$$

If the rotor deflection r_0=0, then the latter two algebraic equations in (2-29) can vanish. The perfect-balancing EP can be obtained by solving (2-30).

$$\begin{aligned} & -\mu\cos(b_1) - \mu\cos(b_2) = \eta\cos(\theta_e) \\ & -\mu\sin(b_1) - \mu\sin(b_2) = \eta\sin(\theta_e) \\ & \frac{b_1+b_2}{2} - (\theta_e+\pi) = 0 \end{aligned} \tag{2-30}$$

If the rotor deflection r_0 is not zero, and balancer balls have a same value shown as $b_{1,2}$= θ or $b_{1,2}$= θ+π, the last two algebraic equations in (2-29) can also vanish. Therefore, the so-called in-phase EP can be obtained by solving (2-31), and '-' for $b_{1,2}$= θ, '+' for $b_{1,2}$= θ+π.

$$\begin{aligned} & (r_o(1-\bar{\Omega}^2) \pm 2\bar{\Omega}^2\mu)\cos(\theta) - r_o\bar{\Omega}\zeta\sin(\theta) = \bar{\Omega}^2\eta\cos(\theta_e) \\ & (r_o(1-\bar{\Omega}^2) \pm 2\bar{\Omega}^2\mu)\sin(\theta) + r_o\bar{\Omega}\zeta\cos(\theta) = \bar{\Omega}^2\eta\sin(\theta_e) \end{aligned} \tag{2-31}$$

If the rotor deflection r_0 is not zero, and balancer balls have an out of phase value with each other shown as b_1= θ, b_2= θ+π, the last two algebraic equations in (2-29) can vanish. Therefore, the Out-of-phase EP can be obtained by solving (2-32).

$$\begin{aligned} & r_o(1-\bar{\Omega}^2)\cos(\theta) - r_o\bar{\Omega}\zeta\sin(\theta) = \bar{\Omega}^2\eta\cos(\theta_e) \\ & r_o(1-\bar{\Omega}^2)\sin(\theta) + r_o\bar{\Omega}\zeta\cos(\theta) = \bar{\Omega}^2\eta\sin(\theta_e) \end{aligned} \tag{2-32}$$

To solve (2-30), (2-31), and (2-32), we use the same approach. Taking (2-30) as an example, we squared the left and the right side of the first and the second equation in (2-

30), and then we added the squared equations to simplify them. Using the third equation in (2-30) as a constraint, we can solve the resulting equation. After squared in (2-31) and (2-32), the resulting equations can become quadratic functions in r_0. Therefore, we need to solve the quadratic functions (2-33) (2-34) for r_0, and to get θ.

$$(1-2\bar{\Omega}^2+\zeta^2\bar{\Omega}^2+\bar{\Omega}^4){r_o}^2\pm(-4\bar{\Omega}^2\mu+4\bar{\Omega}^4\mu)r_o+(4\bar{\Omega}^4\mu^2-\bar{\Omega}^4\eta^2)=0 \qquad (2\text{-}33)$$

$$(1-2\bar{\Omega}^2+\zeta^2\bar{\Omega}^2+\bar{\Omega}^4){r_o}^2-\bar{\Omega}^4\eta^2=0 \qquad (2\text{-}34)$$

1. Perfect-balancing EP

As for the symmetrically supported planar rotor/ADB system, there is no deflections for the rotor, r_0=0, so x_s=0, y_s=0 when the system reaches perfect-balancing EP. The balancer balls position themselves to cancel out the imbalance in the rotating frame. As for the EADB system, perfect-balancing EP in the system (2-27) indicates no deflections for the rotor and for the electric charges while balancer balls occupy fixed positions to compensate for the imbalance in the rotating frame. Therefore, solutions are given as,

$$\begin{aligned} &b_{1,2}=(\phi_e+\pi)\pm\frac{1}{2}\arccos(\frac{\eta^2}{2\mu^2}-1),\\ &x_s=0, y_s=0,\\ &q_{1s}=0, q_{2s}=0 \end{aligned} \qquad (2\text{-}35)$$

Where b_1, b_2, x_s, y_s, q_{1s}, q_{2s} are the perfect-balancing EP for the balancer balls, the rotor deflections, and the electric charges. ϕ_e is the imbalance angular position measured from the $\mathbf{a}_2$ axis, μ is the balancer balls' mass ratio, η is the imbalance ratio. We use same expressions indicating steady-state solutions, such as in-phase EP, out-of-phase EP, in the following, and we will clarify otherwise.

2. In-phase EP

Assuming the balancer balls' steady-state b_1, b_2 locate at θ and θ, or at $\theta+\pi$ and $\theta+\pi$, we can get solution '-' and '+', in the (2-36), respectively.

$$r_{os}^{\pm} = \frac{-(-4\mu\bar{\Omega}^2 + 4\mu\bar{\Omega}^4)}{2\times(1-2\bar{\Omega}^2+\varsigma^2\bar{\Omega}^2+\bar{\Omega}^4)} \pm \frac{\sqrt{(-4\mu\bar{\Omega}^2+4\mu\bar{\Omega}^4)^2 - 4(1-2\bar{\Omega}^2+\varsigma^2\bar{\Omega}^2+\bar{\Omega}^4)(4\mu^2\bar{\Omega}^4-\eta^2\bar{\Omega}^4)}}{2\times(1-2\bar{\Omega}^2+\varsigma^2\bar{\Omega}^2+\bar{\Omega}^4)} \tag{2-36a}$$

$$b_{\pm} = \tan^{-1}\frac{r_{os}^{\pm}\varsigma\bar{\Omega}\cos(\phi_e) - r_{os}^{\pm}\sin(\phi_e) + (r_{os}^{\pm}+2\mu)\bar{\Omega}^2\sin(\phi_e)}{-r_{os}^{\pm}\varsigma\bar{\Omega}\sin(\phi_e) - r_{os}^{\pm}\cos(\phi_e) + (r_{os}^{\pm}+2\mu)\bar{\Omega}^2\cos(\phi_e)} \tag{2-36b}$$

$$x_{s,\pm} = r_{os}^{\pm}\cos(b_{\pm}),\ y_{s,\pm} = r_{os}^{\pm}\sin(b_{\pm}),\quad q_{1s}=0, q_{2s}=0 \tag{2-36c}$$

Where $\bar{\Omega}$ is the dimensionless rotor speed, ϕ_e is the imbalance angular position measured from the $\mathbf{a}_2$ axis, μ is the balancer balls' mass ratio, η is the imbalance ratio, ς is the damping ratio of the rotor. Picking '-' or '+' at a time would yield in-phase EP for $b_{1,2}=\theta$ or for $b_{1,2}=\theta+\pi$.

3. Out-of-phase EP

Assuming the balancer balls locate at θ and $\theta+\pi$, we can get solution given as,

$$r_{os} = \frac{\sqrt{-4(1-2\bar{\Omega}^2+\varsigma^2\bar{\Omega}^2+\bar{\Omega}^4)(-\eta^2\bar{\Omega}^4)}}{2\times(1-2\bar{\Omega}^2+\varsigma^2\bar{\Omega}^2+\bar{\Omega}^4)} \tag{2-37a}$$

$$b_1 = \tan^{-1}\frac{-\varsigma\bar{\Omega}\cos(\phi_e)+\sin(\phi_e)-\bar{\Omega}^2\sin(\phi_e)}{\varsigma\bar{\Omega}\sin(\phi_e)+\cos(\phi_e)-\bar{\Omega}^2\cos(\phi_e)},\ b_2 = b_1+\pi \tag{2-37b}$$

$$x_s = r_{os}\cos(b_1),\ y_s = r_{os}\sin(b_1),\quad q_{1s}=0, q_{2s}=0 \tag{2-37c}$$

Where $\bar{\Omega}$ is the dimensionless rotor speed, ϕ_e is the imbalance angular position measured from the $\mathbf{a}_2$ axis, μ is the balancer balls' mass ratio, η is the imbalance ratio, ς is the damping ratio of the rotor.

Now we obtained all the EPs, and we can discuss the existence of these EPs. It is known that the normalized parameters μ, ς, η, $\bar{\Omega}$ are all positive, with $\mu<<1$, $\varsigma<<1$.

4. Existence of all EPs when $2\mu\geq\eta$

Assuming $2\mu>\eta$, then according to (2-35) we know that the perfect-balancing EP exists when $\left|\eta^2/2\mu^2-1\right|$ is less than 1. To obtain the existence for in-phase EP, we analyze the quadratic function (2-33). To distinguish the expressions, we use bold letters

$\boldsymbol{a}$, $\boldsymbol{b}$, $\boldsymbol{c}$, $\boldsymbol{a_1}$, $\boldsymbol{b_1}$, $\boldsymbol{c_1}$, $\boldsymbol{a_2}$, $\boldsymbol{b_2}$, $\boldsymbol{c_2}$, $\boldsymbol{a_3}$, $\boldsymbol{b_3}$, $\boldsymbol{c_3}$, to generate discriminant functions Δ, Δ_1, Δ_2, Δ_3 one by one. In (2-33), the coefficient of the quadratic term is $\boldsymbol{a}$, the coefficient of the first order term is $\boldsymbol{b}$, the coefficient of the constant term is $\boldsymbol{c}$, shown in (2-38),

$$\begin{aligned} \boldsymbol{a} &= 1-2\bar{\Omega}^2+\zeta^2\bar{\Omega}^2+\bar{\Omega}^4 \\ \boldsymbol{b} &= \pm(-4\bar{\Omega}^2\mu+4\bar{\Omega}^4\mu) \\ \boldsymbol{c} &= 4\bar{\Omega}^4\mu^2-\bar{\Omega}^4\eta^2 \end{aligned} \tag{2-38}$$

$$\begin{aligned} \Delta &= \boldsymbol{b}^2-4\boldsymbol{a}\boldsymbol{c} \\ &= 4\bar{\Omega}^4(\eta^2\bar{\Omega}^4+(\eta^2\zeta^2-2\eta^2-4\zeta^2\mu^2)\bar{\Omega}^2+\eta^2) \end{aligned} \tag{2-38a}$$

Where $\boldsymbol{a}$ is another quadratic function in parameter $\bar{\Omega}^2$, and this function is open side up with no root when ς<2, so $\boldsymbol{a}$ **is always larger than 0**. To check the discriminant of the root, Δ function is examined, which is a quadratic function in parameter $\bar{\Omega}^2$. To examine Δ function, at first, we need to analyze the quadratic function (2-38a). The coefficient of the quadratic term is $\boldsymbol{a_1}$, the coefficient of the first order term is $\boldsymbol{b_1}$, the coefficient of the constant term is $\boldsymbol{c_1}$.

$$\begin{aligned} \boldsymbol{a}_1 &= \eta^2 \\ \boldsymbol{b}_1 &= \eta^2\zeta^2-2\eta^2-4\zeta^2\mu^2 \\ \boldsymbol{c}_1 &= \eta^2 \end{aligned} \tag{2-39}$$

$$\begin{aligned} \Delta_1 &= \boldsymbol{b}_1{}^2-4\boldsymbol{a}_1\boldsymbol{c}_1 \\ &= \zeta^2((\eta^4-8\eta^2\mu^2+16\mu^4)\zeta^2+(16\eta^2\mu^2-4\eta^4)) \end{aligned} \tag{2-39a}$$

Under assumption $2\mu\geq\eta>0$, $\boldsymbol{b_1}$ **is always smaller than 0**, $\boldsymbol{a_1}$ and $\boldsymbol{c_1}$ are larger than 0. To check the discriminant of the root, Δ_1 function is examined, which is a quadratic function in variable ζ. We need to analyze the quadratic function (2-39a). The coefficient of the quadratic term is $\boldsymbol{a_2}$, the coefficient of the first order term is $\boldsymbol{b_2}$, the coefficient of the constant term is $\boldsymbol{c_2}$.

$$\begin{aligned} a_2 &= \eta^4-8\eta^2\mu^2+16\mu^4 \\ b_2 &= 0 \\ c_2 &= 16\eta^2\mu^2-4\eta^4 \end{aligned} \tag{2-40}$$

$$\Delta_2 = b_2^{\,2} - 4a_2c_2 \tag{2-40a}$$

$$\begin{aligned} a_3 &= 1 \\ b_3 &= -8\mu^2 \\ c_3 &= 16\mu^4 \end{aligned} \tag{2-40b}$$

$$\begin{aligned} \Delta_3 &= b_3^{\,2} - 4a_3c_3 \\ &= 0 \end{aligned} \tag{2-40c}$$

Where $\boldsymbol{a_2}$ is another quadratic function in parameter η^2. The coefficient of the quadratic term is $\boldsymbol{a_3}$, the coefficient of the first order term is $\boldsymbol{b_3}$, the coefficient of the constant term is $\boldsymbol{c_3}$. Since the discriminant of the $\boldsymbol{a_2}$, $\boldsymbol{\Delta_3}$ **function always equals to 0, so** $\boldsymbol{a_2}$ =0, $\boldsymbol{c_2}$ =0 when $2\mu=\eta$ and $\boldsymbol{a_2}$ >0, $\boldsymbol{c_2}$ >0 when $2\mu>\eta$. $\boldsymbol{\Delta_2<0}$ **when** $2\mu>\eta$, $\boldsymbol{\Delta_2=0}$ **when** $2\mu=\eta$.

2.3.3 Conclusions

1.When $2\mu=\eta$, $\boldsymbol{a_2}$ =0, $\boldsymbol{c_2}$ =0, Δ_2=0, Δ_1=0, the rotor speed is

$$\bar{\Omega} = \sqrt{\frac{\eta^2\zeta^2 - 2\eta^2 - 4\zeta^2\mu^2}{-8\eta^2}} \tag{2-41}$$

Where two in-phase EPs collide, and other rotor speeds cause two different in-phase EPs. In-phase EPs exist when $2\mu=\eta$.

2.When $2\mu>\eta$, $\boldsymbol{a_2}$ >0, $\boldsymbol{c_2}$ >0, Δ_2<0, Δ_1>0, the rotor speed within (2-42), the in-phase EPs exist.

$$\begin{aligned} \bar{\Omega} \le \bar{\Omega}_{cr,1}, \bar{\Omega}_{cr,1} &= \sqrt{\frac{-(b_1) - \sqrt{\Delta_1(\zeta,\eta,\mu)}}{2a_1}}, \\ \bar{\Omega} \ge \bar{\Omega}_{cr,2}, \bar{\Omega}_{cr,2} &= \sqrt{\frac{-(b_1) + \sqrt{\Delta_1(\zeta,\eta,\mu)}}{2a_1}} \end{aligned} \tag{2-42}$$

As for the out-of-phase EPs shown in (2-34), the quadratic term coefficient and the constant term coefficient are all positive as shown in (2-43). Therefore, out-of-phase EPs always exist and their existence do not depend on parameter μ.

$$\begin{aligned} 1 - 2\bar{\Omega}^2 + \zeta^2\bar{\Omega}^2 + \bar{\Omega}^4 > 0 \\ \bar{\Omega}^4\eta^2 > 0 \end{aligned} \tag{2-43}$$

2.4 Stability analysis of EPs

2.4.1 Linearized model based on the EP

Based on parameters shown in Table 1, dimensionless system parameters are introduced via (2-26) and they are presented in Table 2.

In order to identify the stability of each EP, we linearized the system (2-27) around the steady-state EP [x_s, y_s, b_1, b_2, q_{1s}, q_{2s}], and we can obtain the linearized equations-of-motion,

$$\mathbf{M}_L(b_1,b_2)\mathbf{q}''_\Delta + \mathbf{C}_L(b_1,b_2)\mathbf{q}'_\Delta + \mathbf{K}_L(b_1,b_2,x_s,y_s)\mathbf{q}_\Delta = \mathbf{F}_L(b_1,b_2,x_s,y_s) \tag{2-44}$$

The perturbed general coordinate is $\mathbf{q}_\Delta(\tau) = \left[\Delta x_s(\tau), \Delta y(\tau),\ \Delta b_1(\tau),\ \Delta b_2(\tau),\ \Delta q_{1s}(\tau),\ \Delta q_{2s}(\tau)\right]$

Where $(') = \partial/\partial\tau$, the linearized mass matrix $\mathbf{M}_L$, damping matrix $\mathbf{C}_L$, and the force vector $\mathbf{F}_L$ are given in A1. The stiffness matrix $\mathbf{K}_L$ is given in A7.1.

In order to analyze the stability of the perturbed system (2-44), we need to calculate the eigenvalues of its state matrix $\mathbf{A}_\Delta$ shown in (2-45),

$$\mathbf{A}_\Delta = \begin{bmatrix} \mathbf{0} & \mathbf{I} \\ -\mathbf{M}_L^{-1}\mathbf{K}_L & -\mathbf{M}_L^{-1}\mathbf{C}_L \end{bmatrix} \tag{2-45}$$

Where **0** is a six by six zero matrix, **I** is a six by six identity matrix.

The perturbed system (2-44) is guaranteed to be asymptotic stable, if and Only if all the real parts of the eigenvalues $\lambda_{\mathbf{A}_\Delta}$ resulting from the state matrix $\mathbf{A}_\Delta$ are less than 0,

$$\mathrm{Re}(\lambda_{\mathbf{A}_\Delta}) < 0 \tag{2-46}$$

2.4.2 Shunt circuit parameter study

1. The effect on the perfect-balancing EP

Using the perturbed system derived in (2-44), and employing the methodology shown in section 2.4.1, this section will obtain the perfect-balancing EP and its stability. The effect of the coupling coefficient ς_e, the equivalent resistance R_n, and the equivalent capacitance C_n over a wide rotor speed range are identified. In order to enable perfect-balancing condition, $2\mu > \eta$ is required in the analysis. This condition means that balancer

Table 2. Dimensionless parameters for the symmetrically supported planar rotor/dual mass EADB system

Parameter	Value
balancer ball mass ratio μ	0.0047
Imbalance ratio η	0.0076
Suspension damping ratio ς	0.1
ADB fluid damping ratio ς_b	4.8×10^{-4}
Dimensionless rotor speed $\overline{\Omega}$	*
Coupling coefficient ς_e	*
Equivalent capacity C_n	*
Equivalent resistance R_n	*
Imbalance phase ϕ_e	$\pi/3$

*Various values used in the analysis

balls can compensate the imbalance totally. To explore the effect of the three new parameters ς_e, C_n, R_n on the perfect-balancing EP, we compare the EP stability region of the symmetrically supported planar rotor/ADB with that of the EADB shown as the example in Figure 9(1). 'st' is the stable region, 'un' is the unstable region, 'u2s' represents the unstable ADB but the stable EADB, and 's2u' represents the stable conventional ADB but the unstable EADB.

Figure 9 (1) (a) and (b) shows the stability region of the perfect-balancing EP for the conventional ADB and the EADB respectively. The stability for the conventional ADB does not change along the circuit parameters. Figure 9 (1)(a) can serve as a benchmark to compare with other results. For simplicity, we combine information in Figure 9 (1)(a) and Figure 9 (1)(b) to generate Figure 9(1) (c). The cyan area shows the enlarged stable perfect-balancing EP region. The magenta area shows the narrowed-down stable perfect-balancing EP region. To take advantages of the EADB, we need to use parameters that generate larger cyan area and smaller magenta area.

In Figure 9(2) and (3), every row shares a same value of ς_e. It is shown that some combinations of the electric circuit parameters ς_e, C_n, R_n would create larger cyan area. In Figure 9(2) and (3), rows indicate that increasing C_n would increase the total cyan area when varying R_n. In Figure 9(2) and (3), the second and the third columns indicate that the stability figures show similar patterns when C_n=0.04 with R_n varying in a smaller region, and when C_n=1 with R_n varying in a larger region. The left side boundaries of cyan areas, which are defined as base lines, are determined by the value of coupling coefficients ς_e. When ς_e=0.001, as shown in Figure 9(2), there is a weak coupling between the electric circuit and the balancer ball's movement. Therefore, there is little improvement in the stability region. When ς_e=0.01, as shown in Figure 9(3), there is a strong coupling. Therefore, it can generate larger cyan area with base lines down to $\overline{\Omega}$ <1. This phenomenon is verified by simulating point 'A' shown in Figure 9(b). However, Figure 9 does not imply that the larger coupling coefficient the better. One reason is that if ς_e gets even larger, the balancer balls may subject to so large damping that the balls' transient response can stay around their initial conditions for a long time. It means that a bad initial condition, which can enlarge the rotor vibration, can prolong its bad effect.

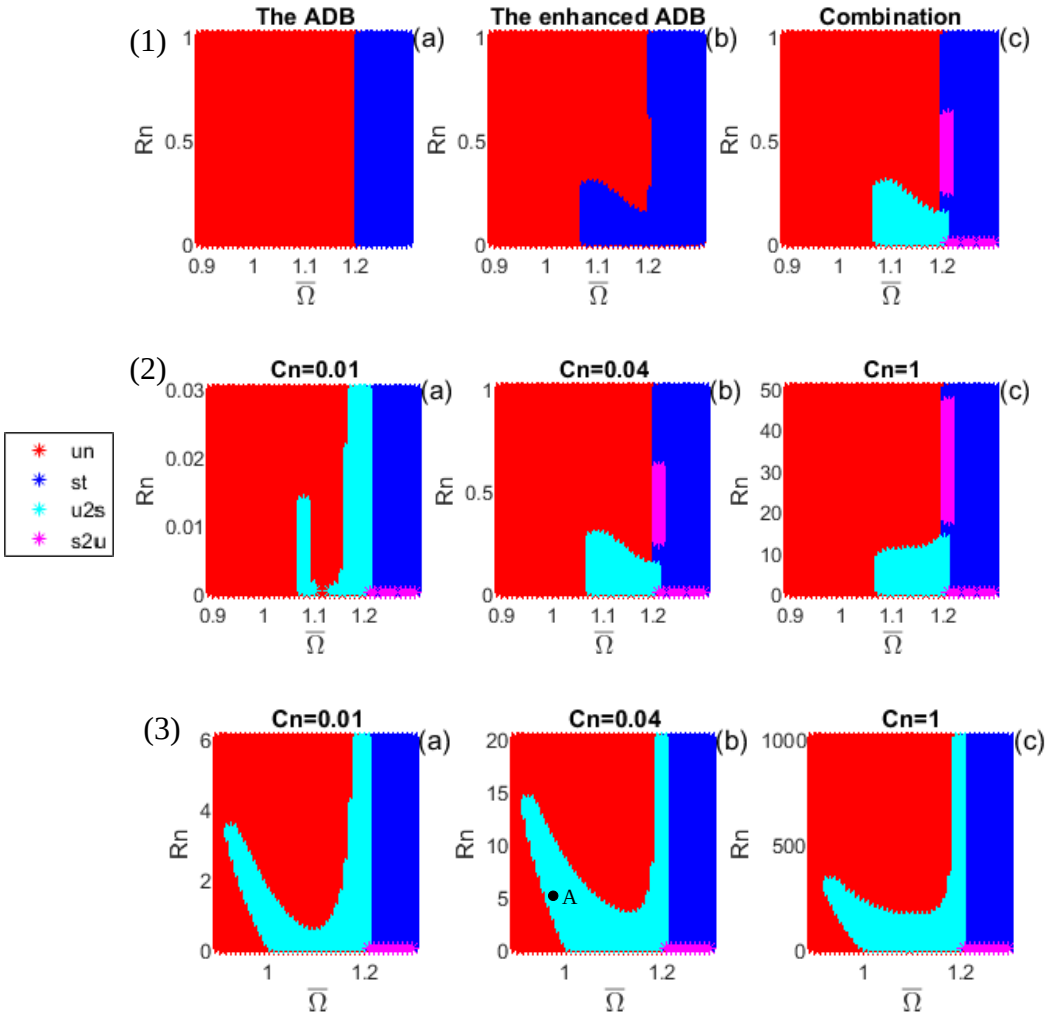


Figure 9. Stability comparison of perfect-balancing EPs for the EADB and the ADB (1) Example (2) ς_e=0.001 (3) ς_e=0.01

Another reason is that the base line could not go down further along the coupling coefficient.

2. The effect on the in-phase EP

As for the in-phase EPs, their existence are determined by (2-42). $\bar{\Omega}_{cr,1}$=0.98 is little smaller than 1, and $\bar{\Omega}_{cr,2}$=1.02 is little larger than 1. Their stability is examined as shown in Figure 10. i. $b_{1,2}=\theta$ is always stable when $\bar{\Omega}<\bar{\Omega}_{cr,1}$, its stability is similar to that of the conventional ADB system. ii. $b_{1,2}=\theta+\pi$ is always stable within a narrow range below $\bar{\Omega}_{cr,1}$, such as $\bar{\Omega}\in(0.97,0.98)$.

3. The effect on the out-of-phase EP

Examined by (2-43), the out-of-phase EP always exists, but the EP is always unstable. Its stability is similar to that of the conventional ADB system.

2.5 The effect of the EADB imperfect assembling on the perfect-balancing EP

2.5.1 Introduction of ADB imperfect assembling

The imperfect assembling is an essential issue when implementing the ADB on the rotating machineries. Therefore, the imperfect assembling especially the eccentricity of the ADB was studied by [34][35]. These studies were about the application of the ADB on hand grinders and treadmills. [36][37]studied the dynamics performance of the ADB with eccentricity and drew the conclusions on two EP solutions: 1. unbalanced EP; 2. half-balanced EP. In this section, we will explore the eccentricity of the symmetrically supported planar rotor/ADB or/EADB system.

2.5.2 Modeling including the eccentricity effect

The planar rotor with the imbalance and the assembling eccentricity cannot be balanced perfectly. However, the imbalance can be compensated by the balancer balls. The residual whirling motion of the rotor equals to the eccentricity [38]. This kind of EP is called the half-balanced EP, which is the only EP that will be considered in this section.

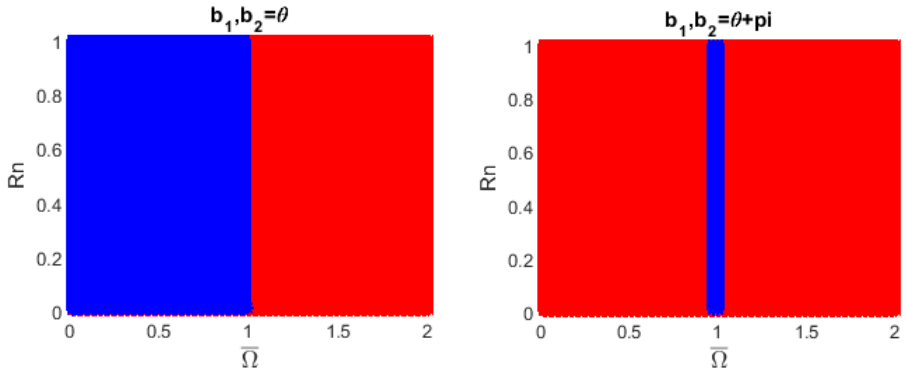


Figure 10. Stability of two different in-phase EPs for the EADB

To facilitate the study of the imperfect assembling issue on the planar rotor /ADB or/EADB system, we first modeled the system through modifying the position vectors shown in (2-16), (2-18) to (2-48) and (2-49) in a newly defined position vector shown as (2-47),

The position vector locating the EADB spinning center relative to whirling center is $\mathbf{r}_{ADB}$. $v_a(t)$ and $w_a(t)$ are the lateral deflections in $\mathbf{a_2}$ and $\mathbf{a_3}$ axis measured in the rotating coordinate system $\{\mathbf{a}\}$.

$$\mathbf{r}_{ADB} = v_a(t)\mathbf{a}_2 + w_a(t)\mathbf{a}_3 \tag{2-47}$$

$$\mathbf{r}_O = (\delta + v_a(t))\mathbf{a}_2 + (\delta + w_a(t))\mathbf{a}_3 \tag{2-48}$$

Where δ is the eccentricity of the spin center in one direction between the planar rotor and the EADB.

The position vector $\mathbf{r}_{OB}$ locating the ith balancer ball in the EADB can be written as,

$$(\mathbf{r}_{OB})_i = \mathbf{r}_{ADB} + (\mathbf{r}_B)_i \tag{2-49}$$

Other equations and derivations are similar to perfect-balancing EP derivations of the planar rotor/EADB system derived in section 2.3. Assuming zero deflections for the EADB, then the half-balanced EP is solved,

$$
\begin{aligned}
&b_{1,2} = (\phi_e + \pi) \pm \frac{1}{2}\arccos(\frac{A^2 + B^2}{2} - 1), \\
&x_s = 0, y_s = 0, \\
&q_{1s} = 0, q_{2s} = 0
\end{aligned}
\tag{2-50}
$$

$$
\begin{aligned}
A &= \frac{R_{br}(1-\varsigma\overline{\Omega})}{\overline{\Omega}^2} - \frac{R_{br}(1-2\mu+\mu_i)}{\mu} - \frac{\eta}{\mu}\cos(\phi_e) \\
B &= \frac{R_{br}(1-\varsigma\overline{\Omega})}{\overline{\Omega}^2} - \frac{R_{br}(1-2\mu+\mu_i)}{\mu} - \frac{\eta}{\mu}\sin(\phi_e)
\end{aligned}
\tag{2-50a}
$$

Where the newly introduced parameter R_{br} is defined by the eccentricity δ over the EADB track radius R_b. The stability analysis is similar to the perfect-balancing EP stability analysis of the planar rotor/EADB system.

2.5.2 The effect of eccentricity on half-balanced EP

The stability boundary for the half-balanced EP in the (μ, Ω) plane is shown in Figure 11. The stability boundary for the half-balanced EP is the black stars, yellow stars and green stars for R_{br} changes from 0 to 9 ×10^{-4} and to 1 ×10^{-2} in (μ, Ω) plane, respectively. Red represents unstable when R_{br} = 0. Magenta shows that, when R_{br} changes from 0 to 9 ×10^{-4}, the stable area transforms to the unstable area. Cyan shows that, when R_{br} changes from 9 ×10^{-4} to 1 ×10^{-2}, the stable area transforms to the unstable area. The blue area is always stable. Therefore, we know that the stable region shrinks when R_{br} gets larger.

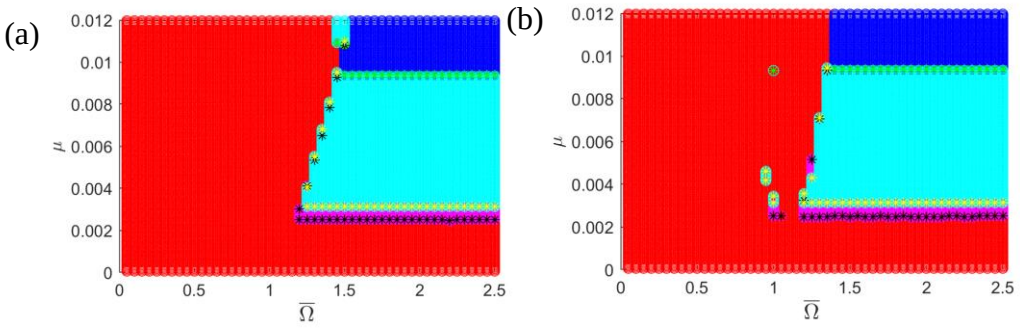


Figure 11. Stability of the half-balanced EP when R_{br} is 0, 9 ×10^{-4} and 1 ×10^{-2} in the (μ, Ω) plane, respectively (a) for the planar rotor/ADB or (b) for the planar rotor/EADB.

When balancer balls' mass ratio μ is large enough, then the half-balanced EP is always stable. However, overly increasing the value of μ will generate larger rotor deflections when speed up the rotor from the subcritical to the supercritical [38]. There is always a tradeoff to decide the value of balls' mass ration.

The stability boundary for the half-balanced EP in the (ζ, Ω) plane is shown in Figure 12. Red represents unstable when R_{br} = 0, green shows that, when R_{br} changes from 0 to 8 $\times 10^{-4}$, the stable area transforms to the unstable area, cyan shows that, when R_{br} changes from 8×10^{-4} to 9 $\times 10^{-4}$, the stable area transforms to the unstable area. It indicates that the stability of the half-balanced EP is sensitive to R_{br} in the (ζ, Ω) plane.

Setting the damping ratio ζ at 0.1, μ at 0.0033, and circuit parameters ζ_e at 0.01, C_n at 0.01, R_n at 0.1, we explored the stability of the half-balanced EP for the planar rotor/ADB and /EADB system in the (R_{br}, Ω) plane. It is shown in Figure 13 that, when Ω is larger than 1 and R_{br} is smaller than 9 $\times 10^{-4}$, the half-balanced EP is stable. When using the EADB instead of the ADB, the green region changes from stable to unstable. In the conclusion, the EADB can increase the stable region near the rotor critical speed about 1 but it cannot compensate any unstable effect due to the radial assembling error R_{br}.

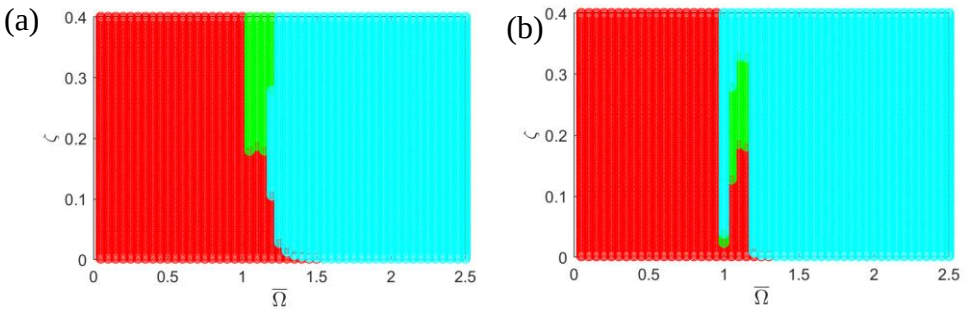


Figure 12. Stability of the half-balanced EP of when R_{br} is 0, 8 $\times 10^{-4}$ and 9 $\times 10^{-4}$ in the (ζ, Ω) plane, respectively (a) for the planar rotor/ADB or (b) for the planar rotor/EADB

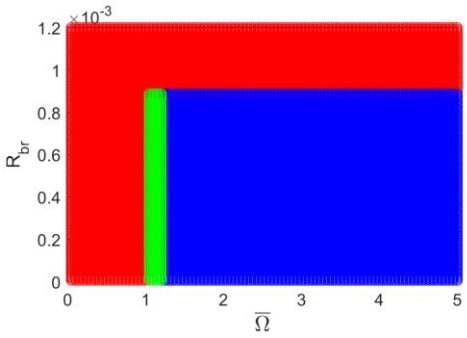


Figure 13. Stability of the half-balanced EP for the planar rotor/ADB and for the planar rotor/EADB in the (R_{br}, Ω) plane.

CHAPTER 3 WHIRLING LIMIT-CYCLE OF THE EADB

3.1 Solve for the whirling limit-cycle

Most severe rotor vibrations can happen when two balancer balls stick together and keep whirling in the rotating frame, thus their motions act as a harmonic force while the imbalance acts as a constant force in rotating frame. The balancer balls' angular acceleration is the external force played on the circuit. Therefore, when the balls have a whirling speed ω, then the whirling limit-cycle is assumed reasonably as shown in (3-1),

$$\mathbf{q}_{\mathrm{wlc}}(\tau) = \mathbf{q}_0 + \boldsymbol{\rho}\omega\tau + \sum_{n=1}^{\mathbf{N}}\left[\mathbf{q}_{Cn}\cos(n\omega\tau) + \mathbf{q}_{Sn}\sin(n\omega\tau)\right] \tag{3-1}$$

Where $\mathbf{q}_0 = [q_{01}, q_{02}, q_{03}, q_{04}, q_{05}, q_{06}]$ is the constant vector, $\boldsymbol{\rho} = [0,0,1,1,0,0]$ is the whirling speed coefficient vector; $\mathbf{q}_{Cn} = [q_{C1n}, q_{C2n}, q_{C3n}, q_{C4n}, q_{C5n}, q_{C6n}]$ is the cosine coefficient vector for the nth harmonic, $\mathbf{q}_{Sn} = [q_{S1n}, q_{S2n}, q_{S3n}, q_{S4n}, q_{S5n}, q_{S6n}]$ is the sine coefficient vector for the nth harmonic. $\mathbf{N} = [N_1, N_2, N_3, N_4, N_5, N_6]$ is the number vector. It is worth to note that the assumed solutions have been developed by other works[26][27][28].

There is a method to get sine terms out of sine term, which can be shown with the following example $\sin(\phi_{b1})$ with $\phi_{b1}(\tau) = q_{03} + \omega\tau + \sum_{n=1}^{N_3}\left[q_{C3n}\cos(n\omega\tau) + q_{S3n}\sin(n\omega\tau)\right]$. (3-2) is an identical transformation by step one, triangle identity transformation and step two, taylor expansion.

$$\begin{aligned}
&\sin\left(q_{03} + \omega\tau + \sum_{n=1}^{N}\left[q_{C3n}\cos(n\omega\tau) + q_{S3n}\sin(n\omega\tau)\right]\right)\\
&= \sin(\omega\tau)\cos(q_{03} + q_{03}^{osc}) + \cos(\omega\tau)\sin(q_{03} + q_{03}^{osc})\\
&= \sin(\omega\tau)\left(f_c(q_{03}) + f_c^{(1)}(q_{03})\cdot q_{03}^{osc} + \cdots\sum_{n=0}^{\infty}\frac{f_c^{(n)}}{n!}(q_{03}^{osc})^n\right) +\\
&\cos(\omega\tau)\left(f_s(q_{03}) + f_s^{(1)}(q_{03})\cdot q_{03}^{osc} + \cdots\sum_{n=0}^{\infty}\frac{f_s^{(n)}}{n!}(q_{03}^{osc})^n\right)
\end{aligned} \tag{3-2}$$

Where f_c is the cosine function, f_s is the sine function. Around constant whirling value q_{03}, there is some oscillations q_{03}^{osc}, which are $\sum_{n=1}^{N_3}\left[q_{C3n}\cos(n\omega\tau) + q_{S3n}\sin(n\omega\tau)\right]$. The

second step of (3-2) is rigorous if we include infinite summation terms. Although we cannot use infinite summation terms in the derivation, first several terms can work well since oscillation amplitude along the whirling is small.

Other terms, such as $\cos(\phi_{b1})$, $\sin(\phi_{b2})$, $\cos(\phi_{b2})$, can also be treated like (3-2). Substituting expansions (3-1) and (3-2) into equations-of-motion, (2-27), and equating like harmonic terms, we can get $6+2\times\sum_{i=1}^{6}N_i$ non-linear algebraic equations. Additional whirling speed ω can be solved by adding an extra coefficient equation of higher harmonics. The total non-linear algebraic equations for unknown coefficients and one whirling speed ω are obtained.

$$\mathbf{S}_0(\mathbf{X})=\mathbf{0} \tag{3-3}$$

Where $\mathbf{X}$ = [$\mathbf{q}_0$, $\mathbf{q}_C$, $\mathbf{q}_S$, ω] is the coefficient variable vector, $\mathbf{q}_C$ = [q_{C11}, q_{C12},… q_{C1N1}, q_{C21}, q_{C22},… q_{C2N2},… q_{C61}, q_{C62},… q_{C6N6}] is the total cosine coefficients, $\mathbf{q}_S$ = [q_{S11}, q_{S12},… q_{S1N1}, q_{S21}, q_{S22},… q_{S2N2},… q_{S61}, q_{S62},… q_{S6N6}] is the total sine coefficients. These nonlinear equations can be solved by Newton-Raphson iterations.

Based on the rotor speed, the approximate analytic whirling limit-cycle need to be analyzed. Therefore, the rotor speed can be treated as another control variable in (3-4) given as,

$$\mathbf{S}_0(\mathbf{Y})=\mathbf{0} \tag{3-4}$$

With a $8+2\times\sum_{i=1}^{6}N_i$ by 1 solution vector $\mathbf{Y}=[\mathbf{q}_0,\mathbf{q}_C,\mathbf{q}_S,\omega,\bar{\Omega}]$ including a $6+2\times\sum_{i=1}^{6}N_i$ by 1 harmonic coefficient vector and two extra variables $\omega,\bar{\Omega}$. The unknowns $\mathbf{Y}$ can be solved via arc-length continuation method [39]. Once whirling limit-cycle amplitudes, $\mathbf{Y}$, are calculated, the stability of the whirling limit-cycle can be determined via floquet theory by assuming small perturbations about $\mathbf{Y}$**.** The principle of arc-length continuation method is shown briefly in Figure 14 with a detailed explanation.

The solutions of the nonlinear algebraic equations (3-4) with different values of the rotor speed $\bar{\Omega}$, are obtained via numerical arc-length continuation. Essentially, the arc-

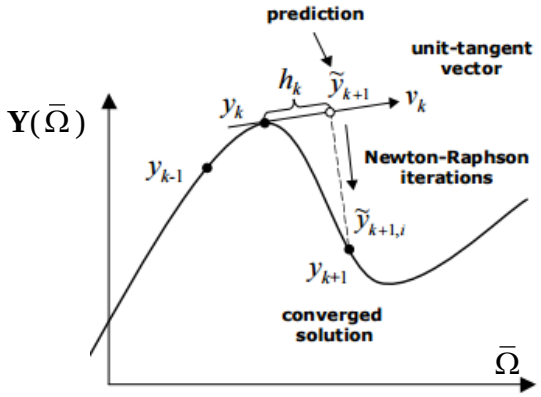


Figure 14. Scheme of the Arc-length continuation method [39]

length continuation approach treats parameter $\bar{\Omega}$ as another variable besides $\boldsymbol{X}$, and then add another constraint to conventional equations so that it can solve $8+2\times\sum_{i=1}^{6}N_i$ equations with $8+2\times\sum_{i=1}^{6}N_i$ variables by prediction and correction fashion. In order to explain in detail, we introduce a new solution vector $\mathbf{Y}\in R^{8+2\times\sum_{i=1}^{6}N_i}$,

$$\mathbf{Y}\left(\bar{\Omega}\right)=\left[\mathbf{X}\left(\bar{\Omega}\right)^{\mathbf{T}},\bar{\Omega}\right]^{\mathbf{T}} \tag{3-5}$$

Therefore, the original system (3-3) can be expressed as functions of the new solution vector $\mathbf{Y}$ as shown in (3-6),

$$\mathbf{S}_0=\left[S_0^1\left(\mathbf{Y}\left(\bar{\Omega}\right)\right),S_0^2\left(\mathbf{Y}\left(\bar{\Omega}\right)\right),\cdots S_0^{n+1}\left(\mathbf{Y}\left(\bar{\Omega}\right)\right)\right]^{\mathbf{T}} \tag{3-6}$$

Starting from a known solution $\mathbf{Y}_k$, short for $\mathbf{Y}_k(\bar{\Omega}_k)$, a prediction of the neighboring solution, $\tilde{\mathbf{Y}}_{k+1}$ (3-7) is made along the local unit tangent vector, $\mathbf{v}_k$, of the solution curve.

$$\tilde{\mathbf{Y}}_{k+1}=\mathbf{Y}_k+h_k\mathbf{v}_k \tag{3-7}$$

Where h_k is a predefined step-size and the local unit tangent vector, $\mathbf{v}_k$, is defind as $\mathbf{v}_k = \left.\frac{d\mathbf{Y}}{d\bar{\Omega}}\right|_{\substack{\bar{\Omega}=\bar{\Omega}_k \\ \mathbf{Y}=\mathbf{Y}_k}}$, is $8+2\times\sum_{i=1}^{6}N_i$ by 1 vector and is computed from a $7+2\times\sum_{i=1}^{6}N_i$ by $8+2\times\sum_{i=1}^{6}N_i$ system Jacobian matrix $J_0\left(\mathbf{Y}_{k-1}\right)=\left.\frac{d\mathbf{S}_0}{d\mathbf{Y}}\right|_{\substack{\bar{\Omega}=\bar{\Omega}_{k-1} \\ \mathbf{Y}=\mathbf{Y}_{k-1}}}$, and the previous tangent vector $\mathbf{v}_{k-1}$ as

$$\mathbf{v}_k = \begin{bmatrix} J_0\left(\mathbf{Y}_{k-1}\right) \\ \mathbf{v}_{k-1}{}^{\mathbf{T}} \end{bmatrix}^{-1} \begin{bmatrix} \mathbf{0} \\ 1 \end{bmatrix} \tag{3-8}$$

The equation (3-8) is based on two approximations (3-8a) and (3-8b),

$$J_0\left(\mathbf{Y}_{k-1}\right)\cdot\mathbf{v}_k = \mathbf{0} \tag{3-8a}$$

$$\mathbf{v}_{k-1}{}^{\mathbf{T}}\cdot\mathbf{v}_k = 1 \tag{3-8b}$$

These approximations are valid if and only if $\mathbf{Y}_k$ and $\mathbf{Y}_{k-1}$, as well as $\mathbf{v}_k$ and $\mathbf{v}_{k-1}$ are close enough. From the prediction procedures, we can know that given a starting-point solution $\mathbf{Y}_k$ and a local unit vector $\mathbf{v}_k$, a predicted solution $\tilde{\mathbf{Y}}_{k+1}$ can always be found by a small step size h_k. Nonetheless, this step only provides a predicted solution that is close to the solution curve. Corrections need to get from Newton-Raphson iterations indicated by the subscript *i*, iteration formula is shown in (3-9)

$$\tilde{\mathbf{Y}}_{k+1,i+1} = \tilde{\mathbf{Y}}_{k+1,i} - J^{-1}\mathbf{S} \tag{3-9}$$

Where the augmented system and the Jacobian, $\mathbf{S}$ and J are (3-9a) and (3-9b)

$$\mathbf{S} = \begin{bmatrix} \mathbf{S}_0(\mathbf{Y}_k) \\ (\tilde{\mathbf{Y}}_{k+1,i+1} - \tilde{\mathbf{Y}}_{k+1,i})^{\mathbf{T}}\mathbf{v}_k \end{bmatrix} \tag{3-9a}$$

$$J = \begin{bmatrix} J_0(\mathbf{Y}_k) \\ \mathbf{v}_k{}^{\mathbf{T}} \end{bmatrix} \tag{3-9b}$$

This approach enforces $\mathbf{S}(\mathbf{Y}_{k+1}) = \mathbf{0}$, and corrections are constrained along a path normal to $\mathbf{v}_k$ by enforcing $(\tilde{\mathbf{Y}}_{k+1,i+1} - \tilde{\mathbf{Y}}_{k+1,i})^{\mathbf{T}}\mathbf{v}_k = 0$. If $\mathbf{S}_0(\tilde{\mathbf{Y}}_{k+1}) \approx \mathbf{0}$ or $\tilde{\mathbf{Y}}_{k+1,i+1} - \tilde{\mathbf{Y}}_{k+1,i} \approx \mathbf{0}$ within

several correction iterations, then correction is converged in true solution, so the one can get (3-10).

$$\mathbf{Y}_{k+1} \approx \tilde{\mathbf{Y}}_{k+1,i} \tag{3-10}$$

3.2 Stability analysis of the whirling limit-cycle

In order to identify the stability of each whirling limit-cycle, we linearized the system (2-27) around whirling limit-cycle $[x_{\text{wlc}}, y_{\text{wlc}}, b_{\text{wlc},1}, b_{\text{wlc},2}, q_{\text{wlc},1}, q_{\text{wlc},2}]$ in (3-1), and got the linearized equations-of-motion as shown in (3-11),

$$\begin{aligned}&\mathbf{M}_{\text{wlc}}(b_{\text{wlc},1}, b_{\text{wlc},2})\mathbf{q}''_{\text{wlc}} + \mathbf{C}_{\text{wlc}}(b_{\text{wlc},1}, b_{\text{wlc},2})\mathbf{q}'_{\text{wlc}} + \\ &\mathbf{K}_{\text{wlc}}(b_{\text{wlc},1}, b_{\text{wlc},2}, x_{\text{wlc}}, y_{\text{wlc}})\mathbf{q}_{\text{wlc}} = \mathbf{F}_{\text{wlc}}(b_{\text{wlc},1}, b_{\text{wlc},2}, x_{\text{wlc}}, y_{\text{wlc}})\end{aligned} \tag{3-11}$$

Where $(') = \partial / \partial \tau$, $\mathbf{q}_{\text{wlc}}(\tau) = [x_{\text{wlc}}(\tau), y_{\text{wlc}}(\tau), b_{\text{wlc},1}(\tau), b_{\text{wlc},2}(\tau), q_{\text{wlc},1}(\tau), q_{\text{wlc},2}(\tau)]$ is the perturbed coordinate. The dimensionless system mass matrix $\mathbf{M}_{\text{wlc}}$ and the force vector $\mathbf{F}_{\text{wlc}}$ are given A2. The damping matrix $\mathbf{C}_{\text{wlc}}$ and stiffness matrix $\mathbf{K}_{\text{wlc}}$ are given in A7.2.

In order to analyze the stability of the perturbed system (3-11), we need to get its state matrix $\mathbf{A}_{\text{wlc}}$ as shown in (3-12),

$$\mathbf{A}_{\text{wlc}}(\tau) = \begin{bmatrix} \mathbf{0} & \mathbf{I} \\ -\mathbf{M}_{\text{wlc}}(\tau)^{-1}\mathbf{K}_{\text{wlc}}(\tau) & -\mathbf{M}_{\text{wlc}}(\tau)^{-1}\mathbf{C}_{\text{wlc}}(\tau) \end{bmatrix} \tag{3-12}$$

Where $\mathbf{0}$ is a six by six zero matrix, $\mathbf{I}$ is a six by six identity matrix.

Given identity initial condition x_0 and integrating $\mathbf{A}_{\text{wlc}}(\tau)$ from 0 to $T = 2\pi / \omega$, we can construct a fundamental matrix solution.

$$x(T) = \int_0^T \mathbf{A}_{\text{wlc}}(\tau) d\tau \cdot x_0 \tag{3-13}$$

Applying floquet theory, we identified the stability of this linear periodic time-variant differential equation from examining the eigenvalues of the fundamental matrix solution.

The perturbed system (3-11) is guaranteed to be asymptotic stable, if and Only if all the absolute values of the eigenvalues $\lambda_{x(T)}$ for the fundamental matrix solution $x(T)$ are less than 1,

$$\max \left| \lambda_{x(T)} \right| < 1 \tag{3-14}$$

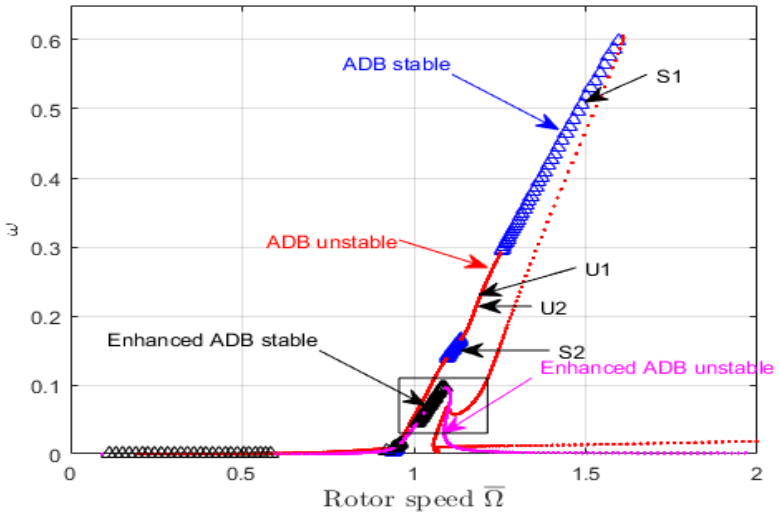
3.3 Shunt circuit parameter study

Before exploring the effect of circuit parameters on eliminating whirling limit-cycle, it is worth to note some concerns behind the exploration. As shown in Figure 9, we have explored the effect of circuit parameters within a large range on enlarging perfect-balancing EP. However, we haven't figured out a systematic approach to investigate the same large circuit parameter range on eliminating whirling limit-cycle. Therefore, we explored the effect of circuit parameters on perfect-balancing EP in Chapter two and on whilring limit-cycle in Chapter three, respectively. In this Chapter, we choose a group of circuit parameters in Figure 9(2)(a) since this group of parameters can increase the stability boundary of perfect-balancing EP and we are wondering if it can eliminate whirling limit-cycle as well.

To make results clear, it is also worth to note that we have dealt with steady-state solutions (both perfect-balancing EP and whirling limit-cycle) under different rotor speeds. Therefore, the results shown below are not transient dynamics along different rotor speeds.

Setting ς_e=0.001, C_n=0.01, R_n=0.01, we can explore the EADB circuit parameters' effect on the whirling limit-cycle. It is shown in Figure 15(1), comparing with the application of the ADB on the symmetrically supported planar rotor, the application fo the EADB would largely reduce the whirling limit-cycle. The conventional ADB has the whirling limit-cycle from $\overline{\Omega}$ =1 to 1.6, which is stable from $\overline{\Omega}$ =1.2 to 1.6, with the largest whirling speed exceeds 0.6. While the EADB has whirling stable limit-cycle from $\overline{\Omega}$ =1 to1.1 with the largest whirling speed only approach 0.1. Figure 15 shows that, when rotor speed is increased, the EADB can prevent the appearance of the whirling limit-cycle, and it can also reduce the whirling speed to 1/6 that generated by the conventional ADB. In order to check the accuracy of these results, we present a zoomed-in Figure 15(2). We pick up two stable points and two unstable points on the ADB solution curve and on the EADB solution curve, respectively, and called 'S1', 'S2', 'U1', 'U2', and 's1', 's2', 'u1', 'u2'.

(1)



(2)

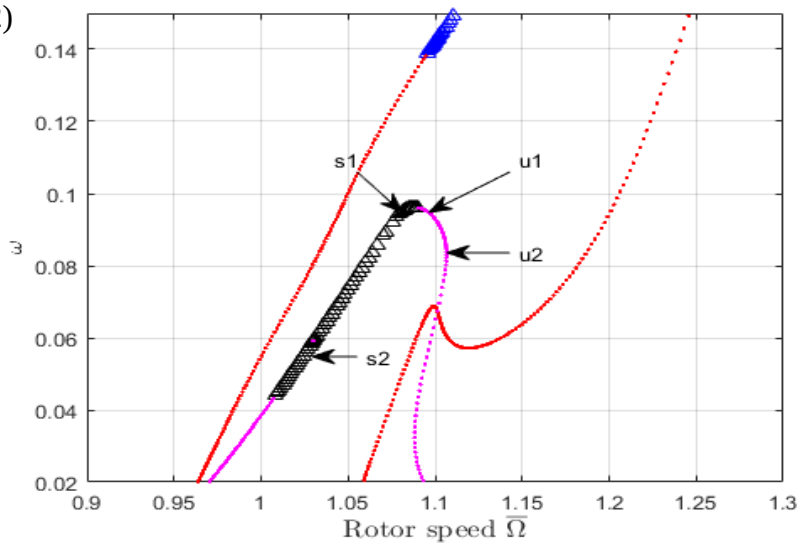


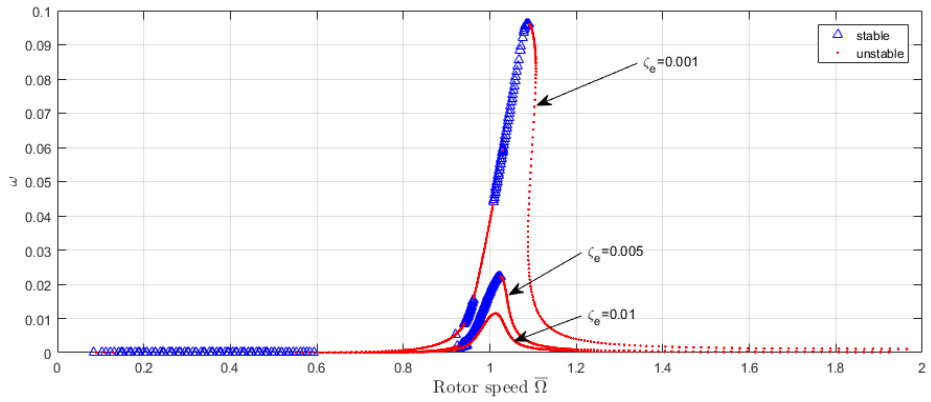
Figure 15. Comparison of the whirling limit-cycle for the ADB and the EADB/symmetrically supported planar rotor system (1) full picture (2) zoomed-in picture

Figure 16(1) and (2) show the effect of the coupling coefficient and the equivalent resistance on the whirling limit-cycle. Firstly, to explore the effect of ς_e on the whirling limit-cycle, C_n and R_n are fixed at 0.01, and ς_e is set to be 0.001, 0.005 and 0.01 respectively. It shows that when ς_e gets larger, the whirling limit-cycle is further eliminated. ς_e=0.001 has a whirling speed, which is 10 times larger than the speed associated with ς_e =0.01, and the whirling limit-cycle stable region is reduced remarkably. Secondly, to explore the effect of R_n on the whirling limit-cycle, we set ς_e =0.001, C_n=0.01, and R_n to be 0.001, 0.01 and 0.05 respectively. It shows that increasing R_n has an incremental contribution on reducing the whirling limit-cycle.

In the following, we will discuss the discontinuous property of the continuation curves shown in Figure 15 and Figure 16. Firstly, we assume **N**=1 or 2 in (3-1), and examine the floquet transition matrices in Figure 15 for the planar rotor/ADB system, and then we let $\overline{\Omega}$ change from 1.1 to 0.1, and later change from 1.1 to 2.1 to get root locus in Figure 17 where we plot eigenvalues in the real axis vs the imaginary axis with different rotor speeds. The color of the eigenvalues varies from dark green to light green gradually. It is shown in Figure 17(a) and (b) that, the real part of eigenvalues exists 1 so the unstable region appears in both $\overline{\Omega}$ = 1.1-0.1 and $\overline{\Omega}$ = 1.1-2.1. This analysis depends on the assumption that there is only one or two harmonic terms in the solution, which is acceptable to approximate our stability curves and maybe the cause of the artificial stability discontinuity.

Based on the discussion above, the conclusion of the cause for the discontinuity in Figure 15 is shown in Figure 18(a) and (b). Assuming **N**=1 or 2 or we have 1 or 2 harmonic terms in the format (3-1), we can get the unstable region I and the sectional unstable region II because of artificial problem generated with small **N**. Assuming **N**= 6 or 7 or we have 6 or 7 harmonic terms in (3-1), we can get rid of the unstable region I and the sectional unstable region II leaving a short piece of the unstable Region i.

(1)



(2)

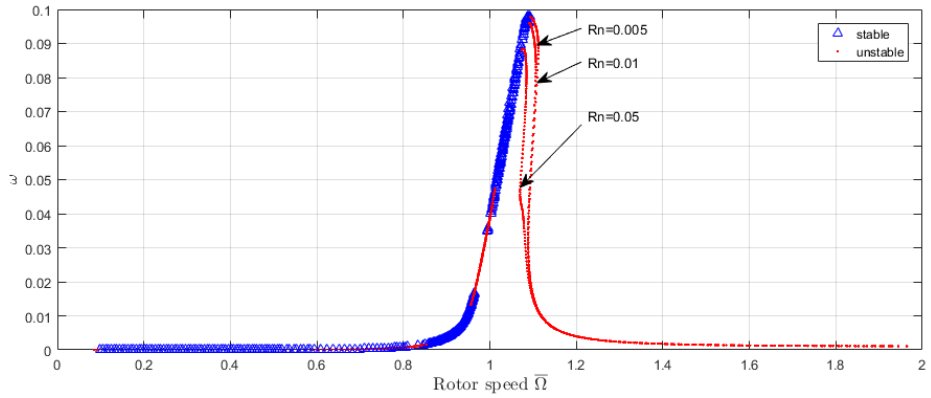


Figure 16. The effect of the circuit parameters on the whirling limit-cycle for the EADB system (1) the effect of ς_e and (2) the effect of R_n

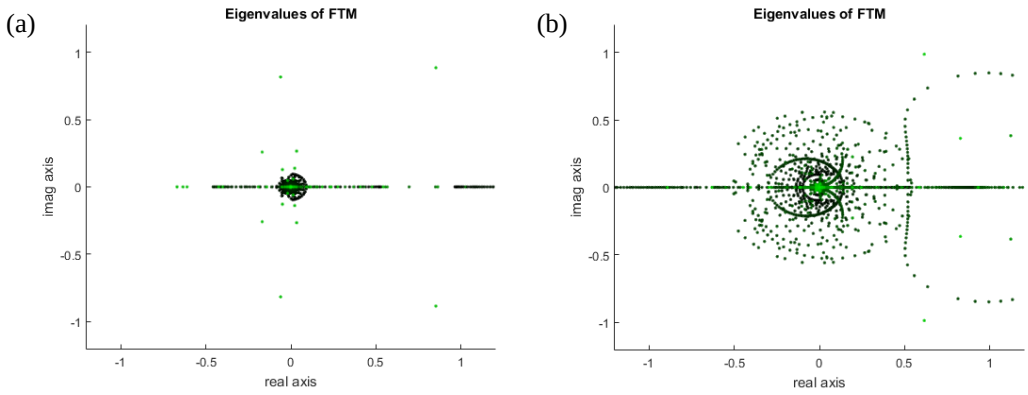


Figure 17. The root locus for eigenvalues of the Floquet Transition Matrices under different rotor speeds (a) $\overline{\Omega}$ from 1.1 to 0.1, (b) $\overline{\Omega}$ from 1.1 to 2.1

Then you may wonder why the sectional discontinuity still occurs around the unstable region i even if we improve the accuracy of the assumed solution. It is because a more complicated behavior besides the whirling limit-cycle is going on within a short range of the rotor speed from 1.11 to 1.17. The similar unstable phenomenon appears in [27] with a finer grid in the region of 1.08-1.24 in their paper.

To best of our knowledge, this thesis is the first one that discuss the unstable phenomenon. This embedded unstable region maybe a period-doubling bifurcation shown from our time-domain numerical simulation by using different parameters within the rotor speed value of 1.11-1.17. These results are presented in Figure 19. If only scanning the left figures in Figure 19 (a)(b)(c)(d), (a) is the period one limit-cycle, (b) is the period two limit-cycle, (c) is the period four limit-cycle, (d) is the chaotic. According to this evidence, we know that there may be a periodic-doubling decay in the narrow unstable region. But when the rotor speed gets larger, the solution curve becomes stable again. The right figures represent the balls' angular positions for the readers' reference.

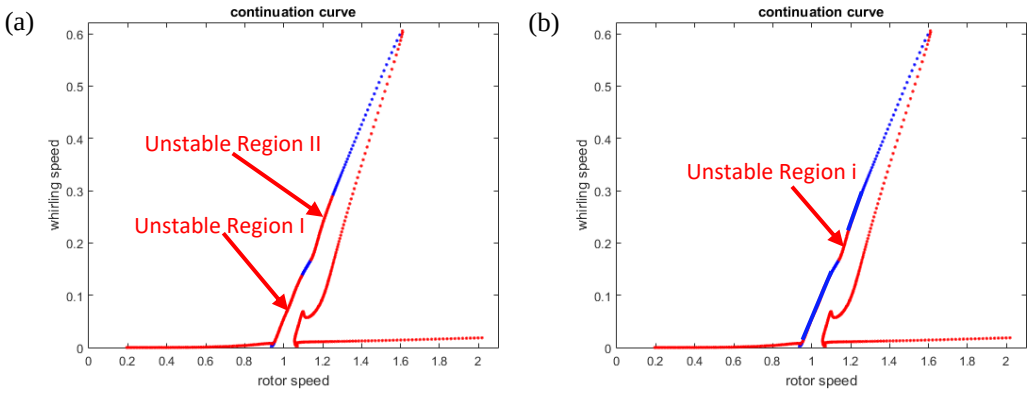


Figure 18. The discontinuity of the continuation curves (a) with one or two harmonic terms (b) with six or seven harmonic terms

It is worth to note that there may be some compound motions which contribute to the discontinuity in the unstable region II as shown in Figure 18, but they are not dominant compared with the whirling limit-cycle. These compound motions include (1) one ball whirls at one speed another ball whirls at a different speed (2) one ball whirls at one speed another ball oscillates around a mean value. These unique compound motions are also shown in [28], which indicates that these compound motions are very sensitive to system parameters. Their sensitivity can be a reason for our less concerns. This dissertation is also mainly focused on the whirling limit-cycle, which is the main concern. For example, balls' whirling together in one trace shows up most frequently in experiments and applications.

We assume **N**=2 in our circuit parameters' analysis because this assumption can capture the accuracy of the continuation curve with less computational burdens. In general, we can adopt the stability information as shown in Figure 15 to present the advantages of the EADB compared with the ADB.

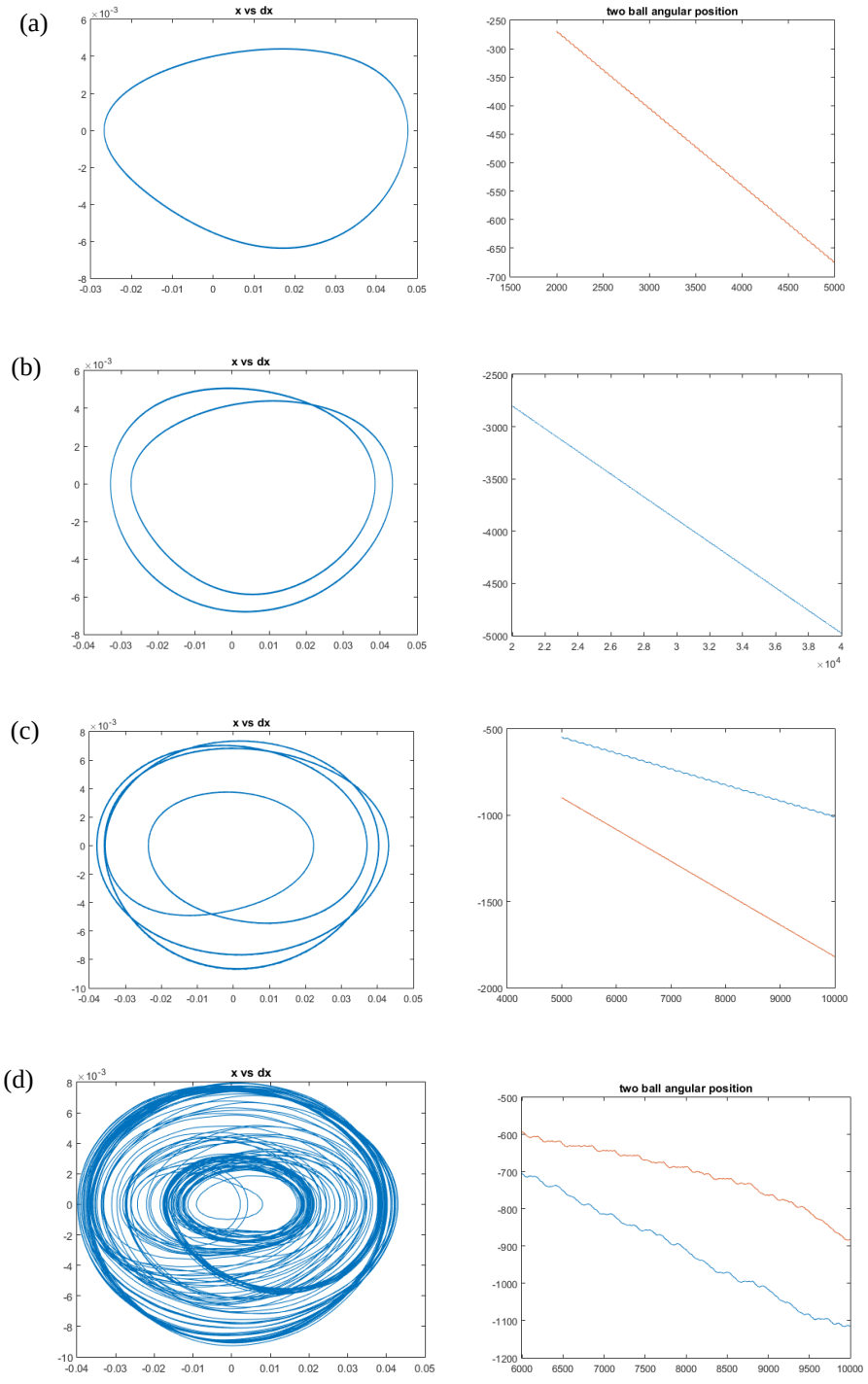


Figure 19. The period-doubling bifurcation resulting from a narrow range of different rotor speeds (a) $\overline{\Omega}$ =1.11 (b) $\overline{\Omega}$ =1.13 (c) $\overline{\Omega}$ =1.16 (d) $\overline{\Omega}$ =1.17

3.4 Examination of the whirling limit-cycle and the numerical study

To check the accuracy of the whirling limit-cycle continuation curves developed in section 3.3, a time-domain simulation via direct numerical integration of the full nonlinear equations-of-motion, (2-27), is performed. In this study, we conduct the numerical simulation for two stable points and two unstable points in Figure 15. 'HBM' represents the results getting from the harmonic balance method, 'NS' represents the results obtaining from the numerical integration. The accuracy of the solution is based on the assumed number of harmonic terms. For efficiency and accuracy, we assume the first two harmonic terms in whirling limit-cycle (3-1), therefore 5-10% error is allowed in our analysis.

It is shown in Figure 20(1) and Figure 21(1) that the approximate analytic solutions are consistent with the numerical simulations when the solutions are stable, while it is indicated from Figure 20(2) and Figure 21(2) that the unstable points would diverge from the analytic solutions.

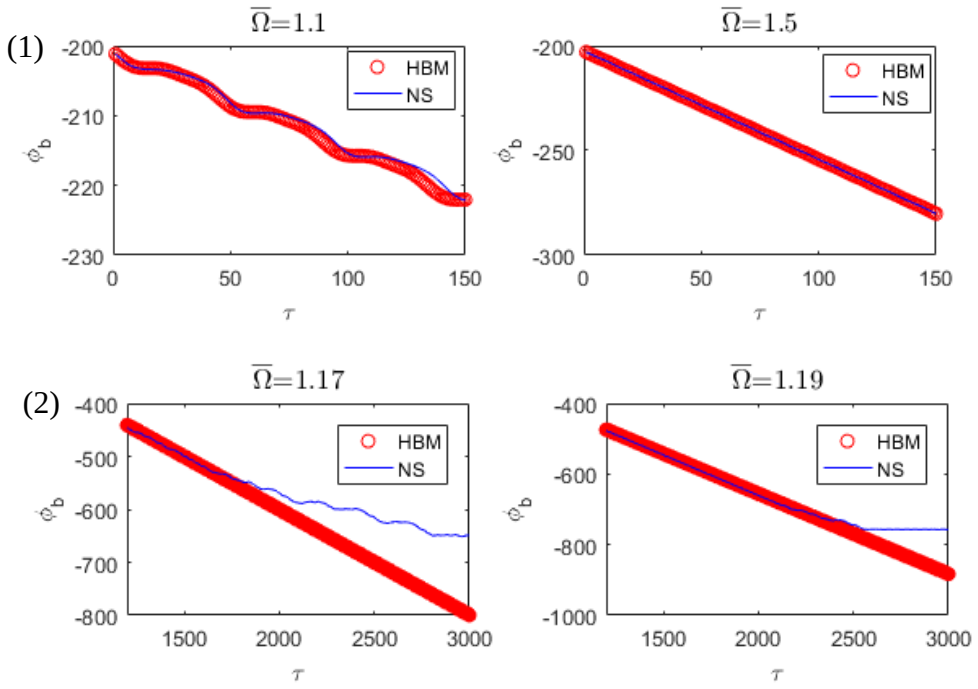


Figure 20. Numerical verification of the solution curve for the ADB (1) stable points (2) unstable points

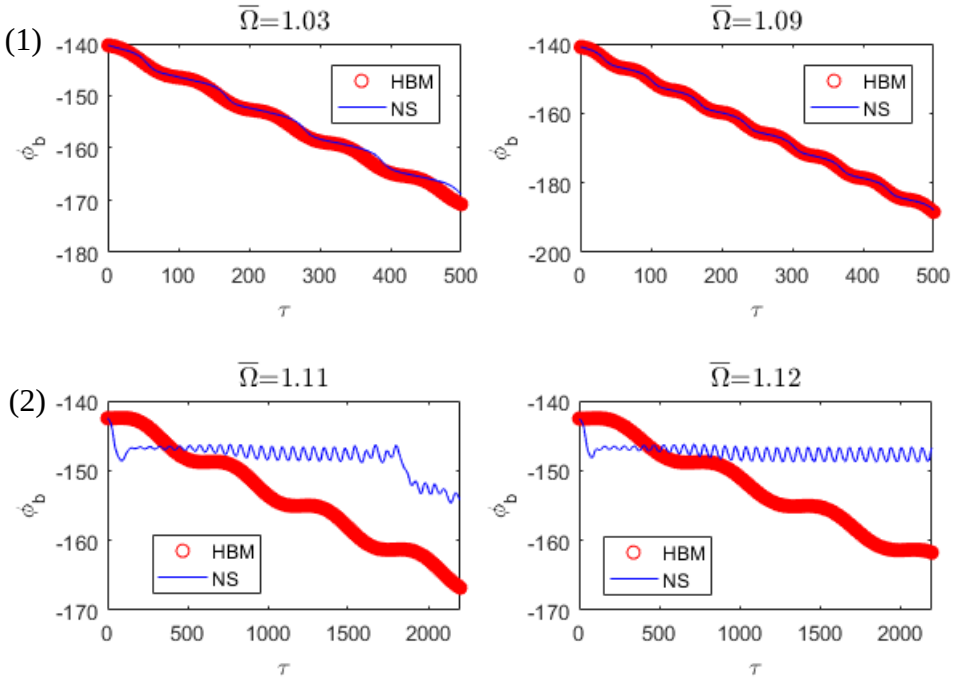


Figure 21. Numerical verification of the solution curve for the EADB (1) stable points (2) unstable points

To investigate the transient behavior of the EADB system compared with the conventional ADB system, we explore some conditions that can make the conventional ADB system settle into whirling limit-cycle.

In Figure 22, four simulation scenarios have the same electrical parameter, which are ς_e =0.01,C_n=1, R_n=0.01. As for Figure 22(1), we set the same initials [ϕ_e, ϕ_e] for the balancer balls and zeros for other variables' initials, and we also set different rotor speeds at 1.1 and 1.3, respectively; As for Figure 22(2), we set the same initials, which can generate whirling limit-cycle of the conventional ADB system, and we set zeros for electrical charges and currents, and then we set different rotor speeds at 1.3 and 1.5, respectively. These results indicate that, under different rotor speeds and initial conditions, the EADB can eliminate the vibration of the rotor when the conventional ADB can aggravate the vibration of the rotor. In Figure 22 (1)(a), the red line stays around 0.01 for

a while, and then drops to 0 after 1.5×10^4. This duration indicates a long transition. We explain this phenomenon via Figure 19.

Using the same parameters in Figure 22 (1)(a) case, it is shown in Figure 23(1)(b) that electric charges experience a long transition time, and gradually converge to zeros. Therefore, the balancer balls' angular position in Figure 23(1)(a) stay at -2.13rad for a long time. In fact, these angles oscillate around -2.13rad due to the effect of the electric charges transient response. If we set R_n from 0.01 as shown in Figure 23(1) to 100 as shown in Figure 23(2), then the transient response for the electric charges drops quickly. Therefore, the balancer balls' angular position split after 0.4×10^4, which is 4 times faster than the case when $R_n = 0.01$.

To check the accuracy of Figure 9(3) (b), we pick up point 'A' to show the stability for the perfect-balancing EP. We set initials right on the top of the perfect-balancing EP, the balancer balls can stay. In Figure 24(1) and (2), to show linear stability, we set the balancer balls' initials that deviate from the perfect-balancing EP about 0.1rad and 0.3rad respectively. The balancer balls' steady-state still converge to the perfect-balancing EP after the transient response. However, if we set the initial conditions deviating further from the perfect-balancing EP, the balancer balls can trap into the whirling limit-cycle since the coexisting stability region for perfect-balancing EP and the whirling limit-cycle appears around $\overline{\Omega}=1$. This problem belongs to the basin of attraction for the EADB system. We may explore it in the future.

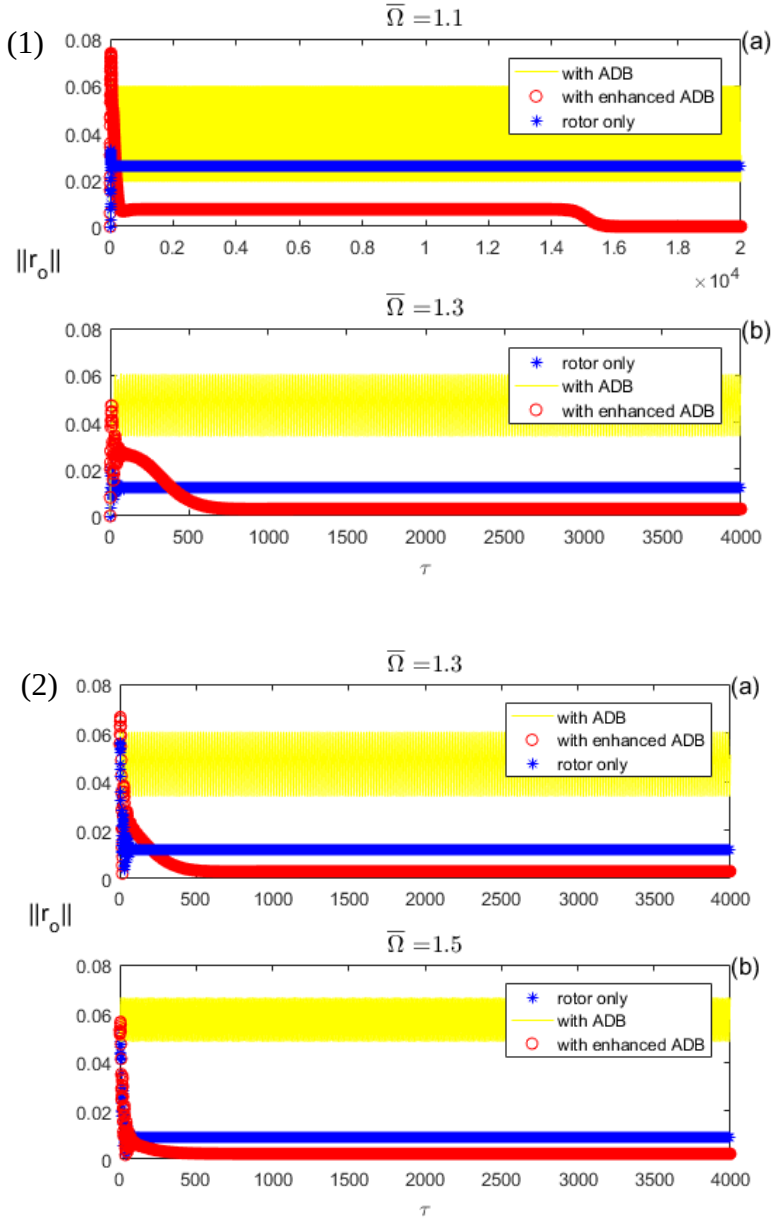


Figure 22. Numerical simulation of rotor deflections for the rotor only, the ADB and the EADB under different rotor speeds and initial conditions

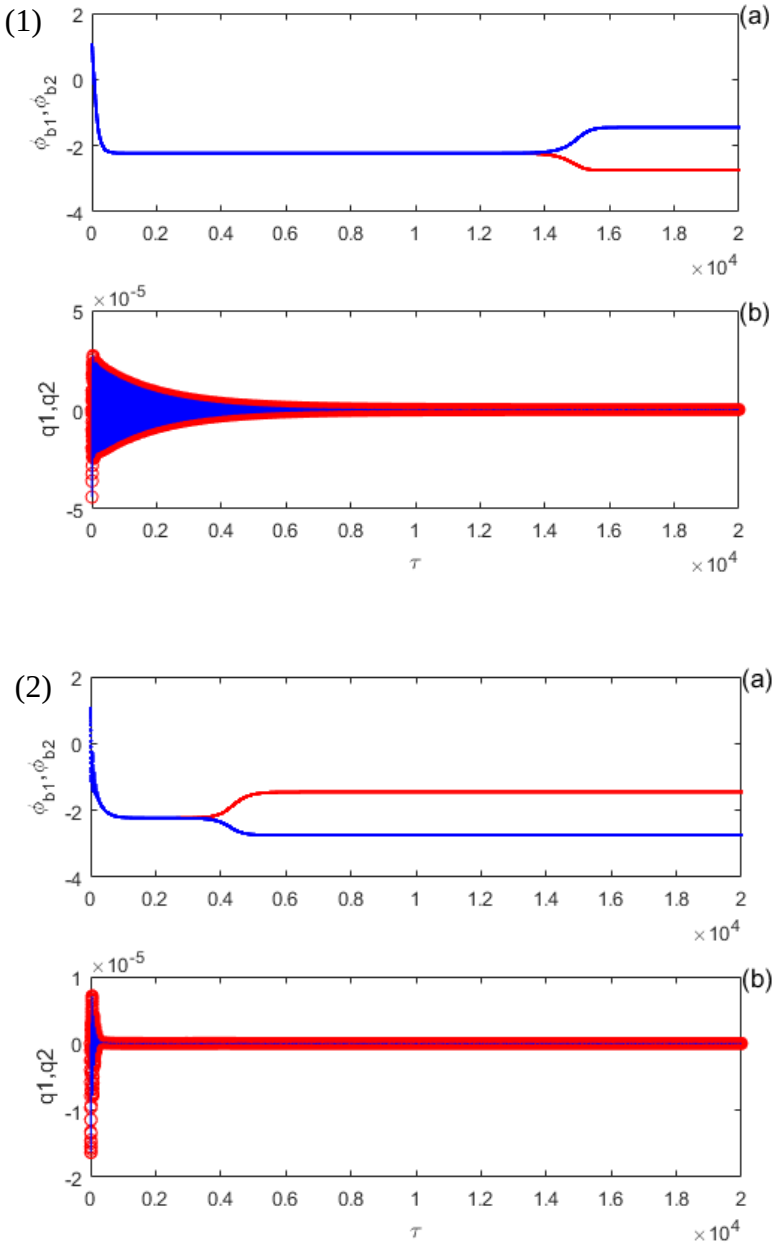


Figure 23. Transient response of the balancer balls' angular position and electric charges for the EADB system when (1) R_n=0.01, (2) R_n=100

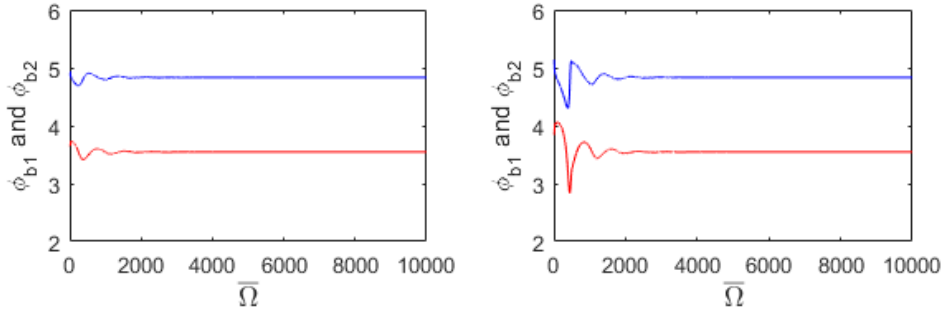


Figure 24. Balancer balls' angular positions for the EADB when rotor speed is $\overline{\Omega}$ =0.97(1) deviate 0.1rad, (2) deviate 0.3rad

3.5 The EADB implementation parameters

Although this study is based on dimensionless parameters, this EADB can be implemented with physical parameters. We pick one dimensionless scenario, which is ς_e =0.001, C_n=1, R_n=0.003; And then we convert them into physical design parameters.

Table 3 shows the physical parameters for the planar rotor/ EADB system. These parameters are determined once the physical model is picked up. Firstly, we choose magnet $SmCo_5$ as the permanent magnetic balancer ball, which has the flux density $\boldsymbol{B}$ value of 1.1, with the mass density 8.2 g/cm^3.

To realize dimensionless parameters, we need to design the copper coil diameter d_c, the number of coils N winding on the track, the torus minor radius r_b, the capacitance C, the load resistance R_L according to the physical parameters. Obeying two constraints on N and R_t, the self-inductance L of air core toroid inductor is approximately via Eq. (2-9) where N is number of turns of winded coil, R_t is torus radius, r_b is loop. Where d_c and its corresponding $N_{\max}$ can be determined through American wire gauge. Resistance of winded coils is given as (2-10), where C_e is electrical resistivity for aluminum with unit Ohm-m, where N is number of turns of winded coil, r_b is loop radius and d_c is wire diameter.

Table 3. Design parameters for the EADB implementation

Parameter	Value	Units
Eccentric magnet mass arc angle α	0.2	rad
Torus cross sectional radius r_b	0.005	m
Torus radius R_t	R_b	m
Number of coil winded on track N	$< N_{max}$	~
Copper coil diameter d_c	7.2295×10^{-4}	m
Magnetic flux density B	1.1	Teslas
toroid inductance L	1.2602×10^{-5}	H
Coil resistance R_C	0.4056	Ohm
Load resistance R_L	0	Ohm
Capacity of capacitor C	10	Farad
Transducer constant θ_e	0.22	T-m
Magnet and coil Coupled length L_c	0.2	m

3.6 Conclusions of the symmetrically supported planar rotor/dual mass EADB system

This section conducts a pioneering study of using the shunt circuit coupled to the ADB system via electromagnetic induction to improve the performance of the conventional ADB, which is known as EADB. It is shown that under different rotor speeds, this innovative EADB can enlarge the stable region of the perfect-balancing EP. It can also eliminate both the existence and the peak value of the whirling limit-cycle. This design would reduce dramatically the undesired coexisting stable region for perfect-balancing EP and the whirling limit-cycle.

1. Appropriately increasing coupling coefficient ς_e can further increase the stable region for the perfect-balancing EP and can reduce the peak value or even eliminate the existence of the whirling limit-cycle.
2. When ς_e and C_n are fixing at certain values, the stable region for perfect-balancing EP is enlarged when the value of R_n and the value of ς_e /0.0001×C_n has the same order of magnitude. While R_n has a negligible effect on the whirling limit-cycle but has some influence on the transient response of the EADB associated system.
3. When the rotor speed is above the rotor critical speed, the EADB can eliminate the vibration of the rotor when the conventional ADB appears to aggravate the vibration of the rotor.
4. Although this study is conducted via dimensionless parameters, the implementation of the physical design can be realized via properly designing parameters, such as, the copper coil diameter d_c, the number of coils N winding on the track, the torus minor radius r_b, the capacitance C, the load resistance R_L. As an example, a set of physical parameters are determined and presented in Table 3 following the procedure as shown in section 2.2.3.

CHAPTER 4 ASYMMETRICALLY SUPPORTED PLANAR ROTOR/DUAL MASS EADB SYSTEM

4.1 Asymmetrically supported planar rotor/dual mass EADB System

4.1.1 Background and motivation of chapter four

In previous chapters, a symmetrically supported planar rotor/dual mass EADB system was considered and studied because rolling/contacting type bearings, which have symmetric stiffness and damping properties, are wided used. However, the asymmetrically supported planar rotor is a more general type of rotors, such as a short journal bearing, a tilting pad bearing. Therefore, the application of the EADB on the asymmetrically supported planar rotor system need to be studied. It is known that an asymmetrically supported planar rotor/ dual mass ADB system was studied in [28][40][41].

In order to apply the knowledge obtained from existing works and to study the application of the EADB on the asymmetrically supported planar rotor system, we need to study the difference between the symmetrically supported rotor and the asymmetrically supported rotor. Different from the symmetrically supported planar rotor, the asymmetrically supported planar rotor has two natural frequencies due to the different bearing stiffness in $\boldsymbol{n}_2$ and $\boldsymbol{n}_3$ directions. The anisotropic support property makes the bearing forces applied on the rotor to be different in two directions. Therefore, the system is time variant dynamic system. We will study the asymmetrically supported rotor by considering the two difference.

4.1.2 Modeling of the asymmetrically supported planar rotor/dual mass EADB system

To investigate the properties of the EADB on the asymmetrically supported rotor system, we present a system as shown in Figure 25, which is same with the model in chapter 2. The balancer balls are sectional-torus magnets maintaining uniform radial magnetic field $\boldsymbol{B}$ around their surfaces. The race fixing on the rotor is a hollow torus winded by copper coils, which is known as the self-inductance L. When the magnetic balancer ball moves in the coils winded race, the electromotive force acts as a voltage source propagating

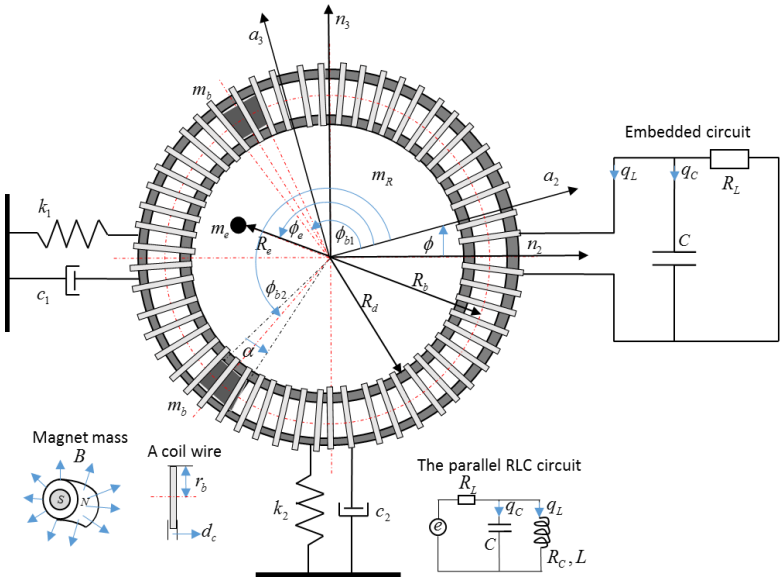


Figure 25. The asymmetrically supported planar rotor/dual mass EADB system

immediately on the associated shunt circuit with the self-inductance and capacitance connecting in parallel. Each balancer ball moves in an isolated race, so there is no interaction between balls and races, which can be placed parallel to or on top of others. The imbalance added by shunt circuits has been taken into consideration by assuming extra imbalance in m_e for the rotor.

In this section, we provide the derivation of the equations-of-motion for the asymmetrically supported planar rotor/dual mass EADB system, and then we derive a dimensionless form. This system is non-autonomous because of the dual excitations from balancer balls and the anisotropic bearing.

As an example, a set of system parameters is shown in Table 4. The following numerical simulations and the analysis are all based on parameters listed in Table 4. We will specify otherwise.

1. Position vectors and total system kinetic energy

In this chapter, our object of study is an asymmetrically supported planar rotor/EADB with dual balancer balls system. Unlike the symmetrically supported planar rotor/EADB system, the anisotropy characteristic of the bearing makes the derivation of

Table 4. Physical parameters for the asymmetrically supported planar rotor /EADB system

Parameter	Value	Units
Rotor radius R_d	0.06	m
Rotor mass m_R	1.3657	kg
Rotor polar inertia J_r	0.0025	kg-m^2
Imbalance quatity m_eR_e	3.36×10^{-4}	kg-m
Bearing support stiffness k_1	1×10^4	N-m
Bearing support stiffness k_2	2.25×10^4	N-m
Bearing support damping c_1, c_2	11.7221	N-m-s
ADB track radius R_b	0.05	m
balancer ball m_b	0.0042	kg
balancer ball -fluid damping c_b	0.0365	N-m-s

system equations to be non-autonomous either in the fixed frame or in the rotating frame. In this situation, we model the rotor deflections in the fixed frame in order to facilitate simple stiffness matrix and damping matrix. The equations-of-motion are derived in a set of inertial coordinate system. The position vector locating the planar rotor spin center *C* relative to the whirling center *O* is $\mathbf{r}_O$. $v(t)$ and $w(t)$ are the lateral deflections measured from the inertial coordinate system $\{\mathbf{n}\}$.

$$\mathbf{r}_O = v(t)\mathbf{n}_2 + w(t)\mathbf{n}_3 \tag{4-1}$$

The balancer balls' angular position and the imbalance angular position measured in the rotating coordinate system $\{\mathbf{a}\}$, which follow the planar rotor rotation ϕ(t) about the $\mathbf{n}_1$ axis of the inertial coordinate system $\{\mathbf{n}\}$. The transformation matrix from $\{\mathbf{n}\}$ to $\{\mathbf{a}\}$ is given as

$$\begin{bmatrix}\mathbf{a}_2\\ \mathbf{a}_3\end{bmatrix} = \begin{bmatrix}\cos(\phi) & \sin(\phi)\\ -\sin(\phi) & \cos(\phi)\end{bmatrix}\begin{bmatrix}\mathbf{n}_2\\ \mathbf{n}_3\end{bmatrix} \tag{4-2}$$

The planar rotor is assumed to be driven with constant rotor speed Ω so the rotation angle is $\phi(t) = \Omega t$. The position vectors $\mathbf{r}_{OB}$ and $\mathbf{r}_{OE}$ locating the *i*th balancer ball and the imbalance relative to the rotor whirling center *O* can be written as,

$$(\mathbf{r}_{OB})_i = \mathbf{r}_O + (\mathbf{r}_B)_i \tag{4-3}$$

With

$$(\mathbf{r}_B)_i = R_b(\cos[\phi_{bi}(t)]\mathbf{a}_2 + \sin[\phi_{bi}(t)]\mathbf{a}_3) \text{ for } i=1, 2 \tag{4-3a}$$

$$\mathbf{r}_{OE} = \mathbf{r}_O + \mathbf{r}_E \tag{4-4}$$

With

$$\mathbf{r}_E = R_e(\cos(\phi_e)\mathbf{a}_2 + \sin(\phi_e)\mathbf{a}_3) \tag{4-4a}$$

Where R_b and R_e are the torus major radius and the imbalance radius; $\phi_{bi}(t)$ and ϕ_e are the *i*th balancer ball's angular position and the imbalance angular position measured from the $\mathbf{a}_2$ axis. The total system kinetic energy *T* includes the planar rotor kinetic energy T_{rotor}, the ADB balancer balls' kinetic energy T_{ADB}, and the shunt circuit magnetic co-energy W_m^*,

$$T = T_{rotor} + T_{ADB} + W_m^* \tag{4-5}$$

$$T_{rotor} = \frac{1}{2}J_r\dot{\phi}^2 + \frac{1}{2}m_e\dot{\mathbf{r}}_{OE}\cdot\dot{\mathbf{r}}_{OE} + \frac{1}{2}m_R\dot{\mathbf{r}}_O\cdot\dot{\mathbf{r}}_O \tag{4-5a}$$

$$T_{ADB} = \frac{1}{2} m_b \sum_{i=1}^{2} (\dot{\mathbf{r}}_{OB})_i \cdot (\dot{\mathbf{r}}_{OB})_i \tag{4-5b}$$

$$W_m^* = \frac{1}{2} \sum_{i=1}^{2} L_i (\dot{q}_{Li})^2 \tag{4-5c}$$

Where $(\cdot) = \partial / \partial t$, m_R, m_e and m_b is the mass of the rotor, the imbalance and the balancer ball respectively. J_r is the rotor polar inertia, L_i is the self-inductance for the coils winded track, which is also a toroid inductor interacted with the ith balancer ball. q_{Li} is the electric charge on L_i.

2. Total system potential energy

The total system potential energy V consists of the rotor strain energy V_{rotor}, the capacitor electrical energy W_e and the transducer co-energy W_t as shown in [29],

$$V = V_{rotor} + W_e + W_t \tag{4-6}$$

With

$$V_{rotor} = \frac{1}{2} k_1 v^2 + \frac{1}{2} k_2 w^2 \tag{4-6a}$$

$$W_e = \frac{1}{2} \sum_{i=1}^{2} \frac{1}{C_i} (q_{Ci})^2 \tag{4-6b}$$

$$W_t = \theta_e R_b \sum_{i=1}^{2} \phi_{bi} (\dot{q}_{Li} + \dot{q}_{Ci}) \tag{4-6c}$$

Where k_1 and k_2 are the lateral bearing stiffness in two directions, C_i are the ith shunt circuit capacitance, q_{Ci} is the electrical charge variable on C_i. θ_e is the electromagnetic coupling coefficient. $\theta_e = \boldsymbol{B}\, l_{couple}$, where $\boldsymbol{B}$ is the magnetic flux density. According to (2-3), we know that $l_{couple} = 2\pi nr$ is the length of the coils coupled to the magnetic balancer ball.

3. Total system dissipation

To account for the effect of the mechanical and the electrical damping on the system, we define Rayleigh dissipation functions of the system as shown in (4-7),

$$D = \frac{1}{2} c_1 \dot{v}^2 + \frac{1}{2} c_2 \dot{w}^2 + \frac{1}{2} c_b R_b \sum_{i=1}^{2} (\dot{\phi}_{bi})^2 + \frac{1}{2} \sum_{i=1}^{2} (R_{Ci} + R_{Li})(\dot{q}_{Li} + \dot{q}_{Ci})^2 \tag{4-7}$$

Where c_1 and c_2 are the damping coefficients in two directions, c_b is the balancer ball fluid viscous damping coefficient arising from relative motion between the ball and its track. R_{Ci} and R_{Li} are the internal resistances of coils and the load resistance in the ith shunt circuit.

4. System equations-of-motion

The system equations-of-motion are then obtained via Lagrange's method as shown,

$$\frac{\mathrm{d}}{\mathrm{d}t}\left(\frac{\partial(T-V)}{\partial\dot{\mathbf{q}}}\right)-\frac{\partial(T-V)}{\partial\mathbf{q}}+\frac{\partial D}{\partial\dot{\mathbf{q}}}=0 \tag{4-8}$$

With $\mathbf{q}(t)=\left[v(t),w(t),\phi_{b1}(t),\phi_{b2}(t),q_{C1}(t),q_{L1}(t),q_{C2}(t),q_{L2}(t)\right]$

The system equations-of-motion are given as,

$$\mathbf{M_o}(\phi_{b1},\phi_{b2},t)\ddot{\mathbf{q}}+\mathbf{C_o}(\phi_{b1},\phi_{b2},t)\dot{\mathbf{q}}+\mathbf{K_o}\mathbf{q}=\mathbf{F_o}(\phi_{b1},\phi_{b2},\dot{\phi}_{b1},\dot{\phi}_{b2},t) \tag{4-9}$$

Where the overall system mass, damping matrices $\mathbf{M_o}$, $\mathbf{C_o}$ are given in A7.3. And stiffness matrix $\mathbf{K_o}$ and the force vector is $\mathbf{F_o}$ are given in A3.

The resulting equations-of-motion for the ith shunt circuit in (4-9) are not independent. For simplicity, we can rearrange them in terms of q_{Ci}, they are given as,

$$-L_i\ddot{q}_{Ci}-\frac{L_i}{(R_{Ci}+R_{Li})C_i}\dot{q}_{Ci}-\frac{1}{C_i}q_{Ci}+\frac{L_i\theta_e R_b}{R_{Ci}+R_{Li}}\ddot{\phi}_{bi}=0 \text{ for } i=1,\ 2 \tag{4-9a}$$

The resulting equations-of-motion for the ith balancer ball is given as,

$$\begin{aligned}&m_b{R_b}^2\ddot{\phi}_{bi}+c_b{R_b}^2\dot{\phi}_{bi}-m_bR_b\ddot{v}\sin(\phi_{bi}+\phi(t))+\\&m_bR_b\ddot{w}\cos(\phi_{bi}+\phi(t))+\theta_eR_b(\dot{q}_{Ci}+\dot{q}_{Li})=0\end{aligned} \text{ for } i=1,\ 2 \tag{4-9b}$$

With

$$\dot{q}_{Li}=\frac{\theta_eR_b}{R_{Ci}+R_{Li}}\dot{\phi}_{bi}-\dot{q}_{Ci}-\frac{1}{(R_{Ci}+R_{Li})C_i}q_{Ci} \tag{4-9c}$$

(4-9c) is obtained by the rearrangement of the equations-of-motion (4-9).

After the rearrangement, the resulting independent equations-of-motion for the asymmetrically supported planar rotor/dual mass EADB system are

$$\mathbf{M}(\phi_{b1},\phi_{b2},t)\ddot{\mathbf{q}}_{new}+\mathbf{C}(\phi_{b1},\phi_{b2},t)\dot{\mathbf{q}}_{new}+\mathbf{K}\mathbf{q}_{new}=\mathbf{F}(\phi_{b1},\phi_{b2},\dot{\phi}_{b1},\dot{\phi}_{b2},t) \tag{4-10}$$

With $\mathbf{q}_{new}(t)=\left[v(t),w(t),\phi_{b1}(t),\phi_{b2}(t),q_{C1}(t),q_{C2}(t)\right]$

Where the overall system inertia matrix $\mathbf{M}$ is given in A7.3. The damping, stiffness matrices $\mathbf{C}$, $\mathbf{K}$ and the force vector $\mathbf{F}$ are given in A3.

5. Dimensionless system equations-of-motion

In order to clarify the subsequent analysis, we assume a set of parameters in different circuits, which is shown as $R_{C1} = R_{C2} = R_C$, $R_{L1} = R_{L2} = R_L$, $C_1 = C_2 = C$, $L_1 = L_2 = L$. Then we substitute $\phi(t) = \Omega t$ into the equations-of-motion. Furthermore, the following dimensionless variables are introduced,

$$
\begin{aligned}
&x = \frac{v}{R_b}, y = \frac{w}{R_b}, \omega_{n1} = \sqrt{\frac{k_1}{m_R + 2m_b}}, \tau = \omega_{n1} t, \omega_{n2} = \sqrt{\frac{k_2}{m_R + 2m_b}}, \frac{\omega_{n2}}{\omega_{n1}} = R_r, \\
&\varsigma_1 = \frac{c_1}{(m_R + 2m_b)\omega_{n1}}, \varsigma_2 = \frac{c_2}{(m_R + 2m_b)\omega_{n1}}, \varsigma_b = \frac{c_b}{(m_R + 2m_b)\omega_{n1}}, \mu = \frac{m_b}{m_R + 2m_b}, \\
&\eta = \frac{m_e R_e}{(m_R + 2m_b)R_b}, \bar{\Omega} = \frac{\Omega}{\omega_{n1}}, \varsigma_e = \frac{\theta_e^{\,2}}{(m_R + 2m_b)(R_C + R_L)\omega_{n1}}, \\
&R_n = \frac{1}{C(R_C + R_L)\omega_{n1}}, C_n = \frac{1}{CL\omega_{n1}^{\,2}}
\end{aligned}
\tag{4-10}
$$

where x, y are dimensionless rotor deflections, ς_1, ς_2, ς_b, and ς_e are the damping ratio of the bearing in two directions and the balancer ball viscous fluid, and the coupling coefficient between the circuit and the balancer ball. ω_n is the rotor system natural frequency, τ is the dimensionless time, μ is the balancer ball's mass ratio, η is the imbalance ratio, $\bar{\Omega}$ is the dimensionless rotor speed, R_n and C_n are the dimensionless resistance and capacitance. θ_e is the transducer constant.

Substituting (4-10) into (4-9) yields the dimensionless equations-of-motion as follows,

$$\mathbf{M_n}(\phi_{b1}, \phi_{b2}, \tau)\mathbf{q_n''} + \mathbf{C_n}(\phi_{b1}, \phi_{b2}, \tau)\mathbf{q_n'} + \mathbf{K_n}\mathbf{q_n} = \mathbf{F_n}(\phi_{b1}, \phi_{b2}, \phi_{b1}', \phi_{b2}', \tau) \tag{4-11}$$

With the dimensionless general coordinate $\mathbf{q_n}(\tau) = [x(\tau), y(\tau), \phi_{b1}(\tau), \phi_{b2}(\tau), q_1(\tau), q_2(\tau)]$

Where $(') = \partial / \partial \tau$ and the overall dimensionless system matrices are $\mathbf{M_n}$, $\mathbf{C_n}$ and $\mathbf{K_n}$, respectively. The force vector is $\mathbf{F_n}$. All matrices are given as,

$$
\mathbf{M_n} = \begin{bmatrix}
1 & 0 & -\mu\sin(\phi_{b1} + \tau\bar{\Omega}) & -\mu\sin(\phi_{b2} + \tau\bar{\Omega}) & 0 & 0 \\
0 & 1 & \mu\cos(\phi_{b1} + \tau\bar{\Omega}) & \mu\cos(\phi_{b2} + \tau\bar{\Omega}) & 0 & 0 \\
-\mu\sin(\phi_{b1} + \tau\bar{\Omega}) & \mu\cos(\phi_{b1} + \tau\bar{\Omega}) & \mu & 0 & 0 & 0 \\
-\mu\sin(\phi_{b2} + \tau\bar{\Omega}) & \mu\cos(\phi_{b2} + \tau\bar{\Omega}) & 0 & \mu & 0 & 0 \\
0 & 0 & \varsigma_e & 0 & -1 & 0 \\
0 & 0 & 0 & \varsigma_e & 0 & -1
\end{bmatrix}
\tag{4-11a}
$$

$$\mathbf{C_n} = \begin{bmatrix} \varsigma_1 & 0 & -2\mu\bar{\Omega}\cos(\phi_{b1}+\tau\bar{\Omega}) & -2\mu\bar{\Omega}\cos(\phi_{b2}+\tau\bar{\Omega}) & 0 & 0 \\ 0 & \varsigma_2 & -2\mu\bar{\Omega}\sin(\phi_{b1}+\tau\bar{\Omega}) & -2\mu\bar{\Omega}\sin(\phi_{b2}+\tau\bar{\Omega}) & 0 & 0 \\ 0 & 0 & \varsigma_b+\varsigma_e & 0 & 0 & 0 \\ 0 & 0 & 0 & \varsigma_b+\varsigma_e & 0 & 0 \\ 0 & 0 & 0 & 0 & -R_n & 0 \\ 0 & 0 & 0 & 0 & 0 & -R_n \end{bmatrix} \tag{4-11b}$$

$$\mathbf{K_n} = \begin{bmatrix} 1 & 0 & 0 & 0 & 0 & 0 \\ 0 & R_r^{\,2} & 0 & 0 & 0 & 0 \\ 0 & 0 & 0 & 0 & -R_n & 0 \\ 0 & 0 & 0 & 0 & 0 & -R_n \\ 0 & 0 & 0 & 0 & -C_n & 0 \\ 0 & 0 & 0 & 0 & 0 & -C_n \end{bmatrix} \tag{4-11c}$$

$$\mathbf{F_n} = \begin{bmatrix} \bar{\Omega}^2\eta\cos(\phi_e+\tau\bar{\Omega}) + \sum_{i=1}^{2}\bar{\Omega}^2\mu\cos(\phi_{bi}+\tau\bar{\Omega}) + \mu\cos(\phi_{bi}+\tau\bar{\Omega})\phi_{bi}'^{\,2} \\ \bar{\Omega}^2\eta\sin(\phi_e+\tau\bar{\Omega}) + \sum_{i=1}^{2}\bar{\Omega}^2\mu\sin(\phi_{bi}+\tau\bar{\Omega}) + \mu\sin(\phi_{bi}+\tau\bar{\Omega})\phi_{bi}'^{\,2} \\ 0 \\ 0 \\ 0 \\ 0 \end{bmatrix} \tag{4-11d}$$

It is worth to note that there are some couplings between the electric part and the mechanical part. Let's take the interaction between one balancer ball and the corresponding electric circuit as an example. The electric circuit adds an extra damping ς_e to the balancer ball's damping term. And the circuit applies an equivalent force $-R_n\, q_1$ to prevent the motion of the balancer ball. At the same time, $\varsigma_e \phi_{b1}''$ works as an external voltage source for the electric circuit. Therefore, the dynamics of the balancer ball is influenced by its corresponding shunt circuit.

4.1.3 Equilibrium points (EPs)

In order to guarantee or even strengthen the perfect-balancing EP of the ADB, and to reduce or even cancel the whirling limit-cycle, we study the perfect-balancing EP and the whirling limit-cycle, respectively, for the asymmetrically supported planar rotor/ EADB system. For the asymmetrically supported planar rotor, other EPs, such as in-phase

EPs, out-ot-phase EP, are not exist. We will explain this no existence in the following. Solving the perfect-balancing EP for the asymmetrically supported planar rotor/EADB system can degenerate into solving that of the ssymmetrically supported/ ADB system. Because balancer balls do not move relative to the rotating frame thus making the electric charges to stay on zeros. Although the EPs for the EADB are the same in terms of balancer balls' angular position and the rotor deflections with that of the ADB, the stability of the EPs are different, which can be determined by the absolute eigenvalue values for the associated fundamental matrix solutions.

Assuming the value of the EP for the rotor deflections, the two balancer balls' angular position, and the electric charges are constants x_0, y_0, b_1, b_2, q_1, q_2, respectively. Therefore, velocities and accelerations corresponding to these constants state are vanished. The steady-state responses of a second order linear system without external force must be zeros, hence q_1, q_2 need to be zeros when balancer balls' angular acceleration are zeros.

The similar derivation for the EPs can be found in [10]. To present clearly, we assume a set of polar coordinates for the rotor deflections as follows,

$$x_0 = r_o \cos(\theta), y_0 = r_o \sin(\theta) \tag{4-12}$$

Where r_o is the radial deflection of the rotor, θ is the circumferential angle corresponding to the radial deflection.

In order to solve EPs, let's substitute (4-12), b_1, b_2, q_1=0, q_2=0 into (4-11). We can get two algebraic equations with r_o, θ, b_1, b_2 as unknowns.

$$\begin{aligned} &r_o \cos(\theta) - \bar{\Omega}^2(\eta\cos(\theta_e + \tau\bar{\Omega}) + \mu\cos(b_1 + \tau\bar{\Omega}) + \mu\cos(b_2 + \tau\bar{\Omega})) = 0 \\ &r_o \sin(\theta) R_r^{\,2} - \bar{\Omega}^2(\eta\sin(\theta_e + \tau\bar{\Omega}) + \mu\sin(b_1 + \tau\bar{\Omega}) + \mu\sin(b_2 + \tau\bar{\Omega})) = 0 \end{aligned} \tag{4-13}$$

If the rotor deflection r_0=0, then the first two algebraic equations in (4-13) can vanish. The perfect-balancing EP can be obtained by solving (4-14).

$$\begin{aligned} &-\mu\cos(b_1 + \tau\bar{\Omega}) - \mu\cos(b_2 + \tau\bar{\Omega}) = \eta\cos(\theta_e + \tau\bar{\Omega}) \\ &-\mu\sin(b_1 + \tau\bar{\Omega}) - \mu\sin(b_2 + \tau\bar{\Omega}) = \eta\sin(\theta_e + \tau\bar{\Omega}) \\ &\frac{b_1 + b_2}{2} - (\theta_e + \pi) = 0 \end{aligned} \tag{4-14}$$

If the rotor deflection $r_0 \neq 0$, then the first two algebraic equations in (4-13) always contain a time varying term $\tau\bar{\Omega}$, therefore unbalanced EPs exist.

As for the conventional ADB with asymmetrically supported rotor system, when it reaches perfect-balancing condition, there is no deflection for the rotor, $r_0=0$, so $x_s=0$, $y_s=0$. The balancer balls are positioning themselves to cancel out the imbalance. According to (4-11), as for the EADB with asymmetrically supported rotor system, the perfect-balancing condition indicates no deflection for the rotor where balancer balls compensate for the imbalance. Hence, balancer balls have zero accelerations, and then no electric charges in the shunt circuit when there is no power source. Solutions are given as,

$$\begin{aligned} &b_{1,2} = (\phi_e + \pi) \pm \frac{1}{2}\arccos(\frac{\eta^2}{2\mu^2} - 1), \\ &x_s = 0, y_s = 0, \\ &q_{1s} = 0, q_{2s} = 0 \end{aligned} \tag{4-15}$$

Where b_1, b_2, x_s, y_s, q_{1s}, q_{2s} are the constant value for the balancer balls, the rotor deflections, and the electric charges. ϕ_e is the imbalance angular position measured from the $\mathbf{a}_2$ axis, μ is balancer ball mass ratio, η is the imbalance ratio.

4.2 Stability of the perfect-balancing EP

4.2.1 Linearized model

Based on the parameters shown in Table 4, dimensionless system parameters are introduced via (4-10) and they are presented in Table 5.

In order to identify the stability of each EP, we linearized the system (4-11) around the EP [x_s, y_s, b_1, b_2, q_{1s}, q_{2s}], and we can obtain the linearized equations-of-motion,

$$\mathbf{M}_L(b_1,b_2,\tau)\mathbf{q}''_\Delta + \mathbf{C}_L(b_1,b_2,\tau)\mathbf{q}'_\Delta + \mathbf{K}_L(b_1,b_2,x_s,y_s,\tau)\mathbf{q}_\Delta = \mathbf{F}_L(b_1,b_2,x_s,y_s,\tau) \tag{4-16}$$

The perturbed general coordinate is $\mathbf{q}_\Delta(\tau) = \left[\Delta x_s(\tau), \Delta y(\tau), \Delta b_1(\tau), \Delta b_2(\tau), \Delta q_{1s}(\tau), \Delta q_{2s}(\tau)\right]$

Where $(') = \partial/\partial\tau$ and the overall dimensionless system matrices are $\mathbf{M}_L$, $\mathbf{C}_L$ and $\mathbf{K}_L$, respectively. The force vector is $\mathbf{F}_L$. All matrices are given in A3.

Table 5. Dimensionless system parameters for the asymmetrically supported planar rotor/EADB

Parameter	Value
balancer balls' mass ratio μ	0.0031
Imbalance ratio η	0.0049
Suspension damping ratio ς_1, ς_2	0.1
ADB fluid damping ratio ς_b	0.001
Natural frequency ratio R_r	1.5
Dimensionless rotor speed $\overline{\Omega}$	*
Coupling coefficient ς_e	*
Equivalent capacity C_n	*
Equivalent resistance R_n	*
Imbalance phase ϕ_e	$\pi/3$

*Various values used in the analysis

In order to analyze the stability of the perturbed system (4-16), we need to calculate the eigenvalues of its state matrix $\mathbf{A}_\Delta$ shown in (4-17),

$$\mathbf{A}_\Delta(\tau)=\begin{bmatrix}\mathbf{0} & \mathbf{I}\\ -\mathbf{M}_\Delta(\tau)^{-1}\mathbf{K}_\Delta(\tau) & -\mathbf{M}_\Delta(\tau)^{-1}\mathbf{C}_\Delta(\tau)\end{bmatrix} \tag{4-17}$$

Where **0** is a six by six zero matrix, **I** is a six by six identity matrix.

Given identity initial condition x_0 and integrating $\mathbf{A}_\Delta(\tau)$ from 0 to $T=2\pi/\bar{\Omega}$, we can construct a fundamental matrix solution.

$$x(T)=\int_0^T \mathbf{A}_\Delta(\tau)d\tau\cdot x_0 \tag{4-18}$$

Applying floquet theory, we identified the stability of the linear periodic time-variant differential equation from examining the eigenvalues of the fundamental matrix solution. The perturbed system (4-16) is guaranteed to be asymptotic stable, if and Only if all the absolute values of the eigenvalues $\lambda_{x(T)}$ of the fundamental matrix solution $x(T)$ are less than 1,

$$\max\left|\lambda_{x(T)}\right|<1 \tag{4-19}$$

4.2.2 Shunt circuit parameter Study

The perfect-balancing EP is the only EP for the asymmetrically supported planar rotor /EADB system. Using the planar rotor/EADB system model derived in (4-11) and the methodology developed in section 4.2.1, this section will solve for the perfect-balancing EP and identify the corresponding stability. Under different rotor speeds, the effect of the coupling coefficient ς_e, the resistance R_n, and the capacitance C_n are developed. In order to enable the perfect-balancing EP, $2\mu > \eta$ condition is met in the analysis. This condition means that balancer balls can totally compensate for the imbalance. To explore the effect of these three new parameters ς_e, C_n, R_n on the perfect-balancing EP, we compare the perfect-balancing EP stability region between the conventional ADB and the EADB for the asymmetrically supported planar rotor shown in the example plot in Figure 26(1). ‘st’ is the stable region, ‘un’ is the unstable region, ‘u2s’ is unstable for the ADB but stable for the EADB, and ‘s2u’ is stable for the ADB but unstable for the EADB.

Figure 26(1) (a) and (b) show the stability region of the perfect-balancing EP for the ADB and the EADB, respectively. The stability plot for the ADB does not change along with the circuit parameters. Therefore, Figure 26(1)(a) can be the benchmark for other figures. For the asymmetrically supported planar rotor/ADB system, there are two natural frequencies, which are 1 and 1.5 respectively. They are subjected to the rotor deflections in two directions. We observe two unstable regions around each of the two natural frequencies. We hope that the EADB can make each instability region smaller. For simplicity, we combine the information shown in Figure 26(1) (a) and (b) to Figure 26(1) (c). The cyan area shows the enlarged perfect-balancing EP stable region. The magenta area means the narrowed-down perfect-balancing EP stable region. Therefore, we want to design the system parameters, which can generate larger cyan area and smaller magenta area.

In Figure 26(2) and (3), every row shares the same ς_e, it is shown that some combinations of parameters ς_e, C_n, R_n would allow larger cyan area. In Figure 26(2) and (3), each row is an indication that increasing C_n can increase the total cyan area under different R_n. In Figure 26, scanning the second and third column, the stability figures show a similar pattern between C_n=0.04 with R_n varying in a smaller region and C_n=1 with R_n changing in a larger region. These results imply that base lines, which are left side boundaries of cyan areas, are determined by the value of coupling coefficients ς_e. Small ς_e, which is set to 0.001 in Figure 26(2), means weak coupling between the electrical circuit and balancer ball's movement, therefore there is little improvement in the stability region. Large ς_e, which is set to 0.01in Figure 26(3), means strong coupling, hence it can generate larger cyan area with base lines for each natural frequencies down to $\overline{\Omega}$ <1 and $\overline{\Omega}$ <1.5 respectively. This results are checking by simulating points 'A', 'B', 'C', 'D', 'E', 'F', 'G', shown in Figure 26(2),(3).

Figure 26 does not imply that the larger coupling coefficient the better. One reason is that if ς_e gets even larger, the balancer ball may have so large damping that the ball's transient response would stay around the initial condition for a long time. It means that a bad initial condition, which can enlarge the rotor vibration, can prolong its bad effect. Another reason is that the base lines could not go even smaller when ς_e gets even larger

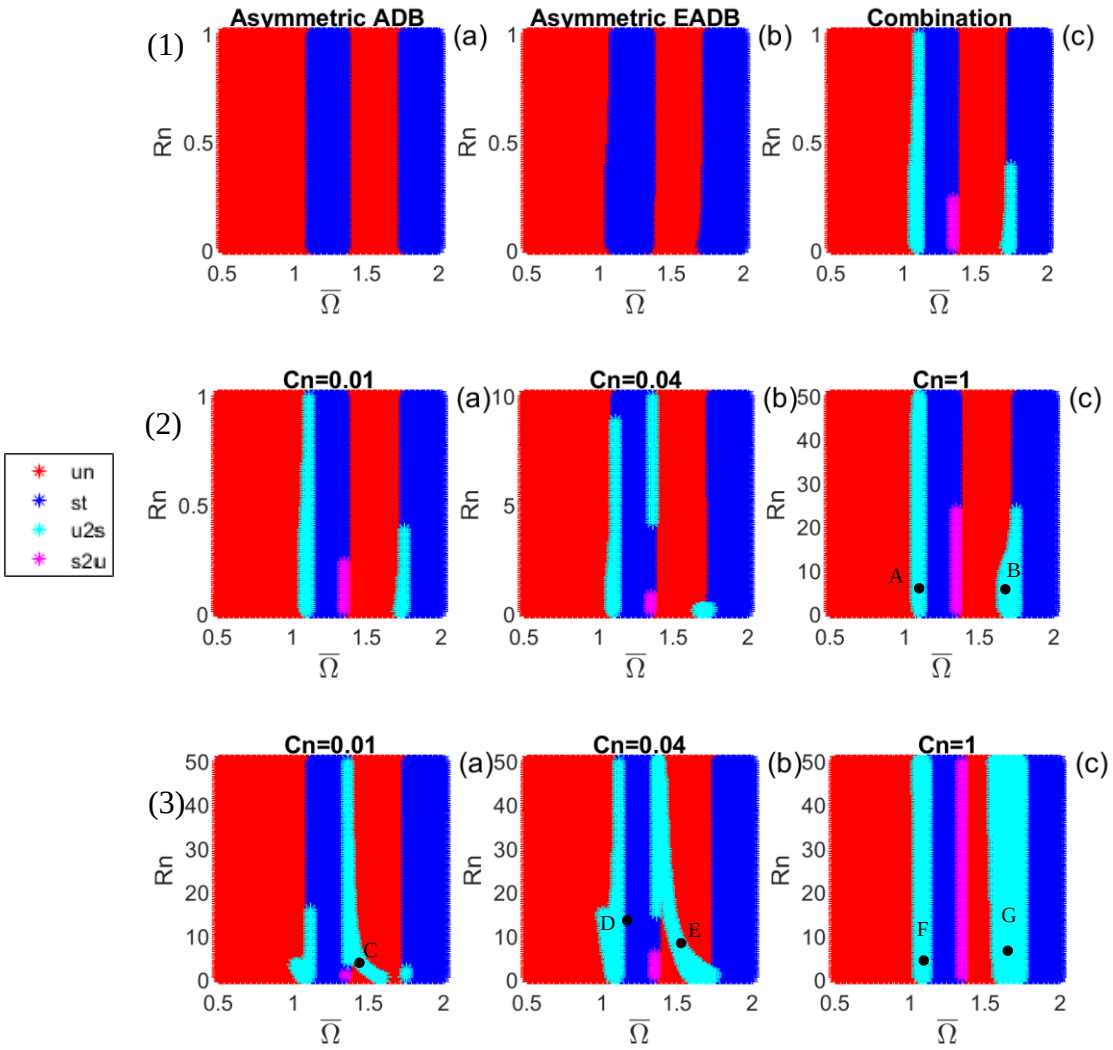


Figure 26. Stability of perfect-balancing EPs for the EADB and the ADB on the asymmetrically supported planar rotor system(1) Example (2) ς_e=0.001 (3) ς_e=0.01

4.3 Examination of the perfect-balancing EP and the numerical study

In this section, we will check the points shown in Figure 26 by conducting numerical simulations. We compared the simulation results for the applications of the ADB and the EADB, respectively, on the asymmetrically supported planar rotor system. We set initial conditions to be the perfect-balancing EP for all the numerical simulations.

Around the first rotor critical speed $\bar{\Omega}$ =1.09, as is shown in Figure 27(a) (b) (c), for the ADB/asymmetrically supported planar rotor, the balancer balls' angular positions ϕ_{b1} and ϕ_{b2} oscillate around the perfect-balancing EP thus it can enlarge the rotor deflection. For the EADB/asymmetrically supported planar rotor, the balancer balls angular positions ϕ_{b1} and ϕ_{b2} stay around the perfect-balancing EP thus it can make no rotor deflections.

Around the second rotor critical speed $\bar{\Omega}$ =1.68, as is shown in Figure 28(a) (b) (c), for the ADB/asymmetrically supported planar rotor, the balancer balls' angular positions ϕ_{b1} and ϕ_{b2} oscillate around the perfect-balancing EP thus it can enlarge the rotor deflection. For the EADB/asymmetrically supported planar rotor, the balancer balls' angular positions ϕ_{b1} and ϕ_{b2} stay around the perfect-balancing EP thus it can make no rotor deflection.

Around either the first or the second rotor critical speed, as is shown in the (a)(b)(c)of Figure 29, Figure 30, and Figure 31, the ADB balancer balls keep whirling while the EADB balancer balls stay around the perfect-balancing EP. Hence the ADB significantly aggravate the rotor deflections while the EADB eliminate the rotor deflections.

If the coupling coefficient and the capacitance ς_e=0.01 and C_n=1, around the first and the second rotor critical speed, as are shown in Figure 32(a) (b) (c) and in Figure 33(a) (b) (c), respectively, the ADB balancer balls can either oscillate around the perfect-balancing EP or keep whirling together thus making large rotor deflections, while, the EADB balancer balls stay at the perfect-balancing EP thus making no rotor deflections.

These numerical simulations show the accuracy of the stability plots shown in Figure 26. In the conclusion, we know that the EADB compared with the ADB can increase the stability region of the perfect-balancing EP in both critical speeds of the asymmetrically supported planar rotor

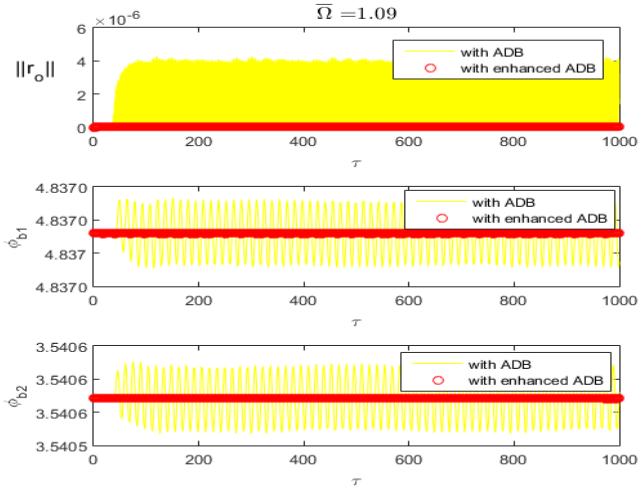


Figure 27. Numerical simulations of the asymmetrically supported planar rotor/ADB or/EADB system initially from the perfect-balancing EP under system parameters ς_e=0.001, R_n=5, C_n=1, shown as point 'A' in Figure 26.

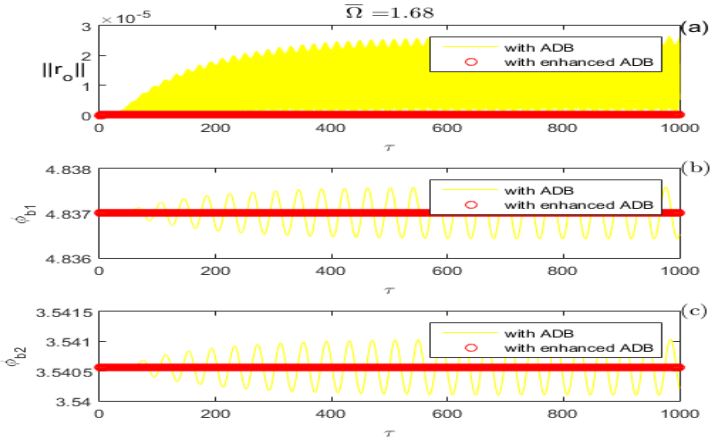


Figure 28. Numerical simulations of the asymmetrically supported planar rotor/ADB or/EADB system initially from the perfect-balancing EP under system parameters ς_e=0.001, R_n=6.5, C_n=1, shown as point 'B' in Figure 26.

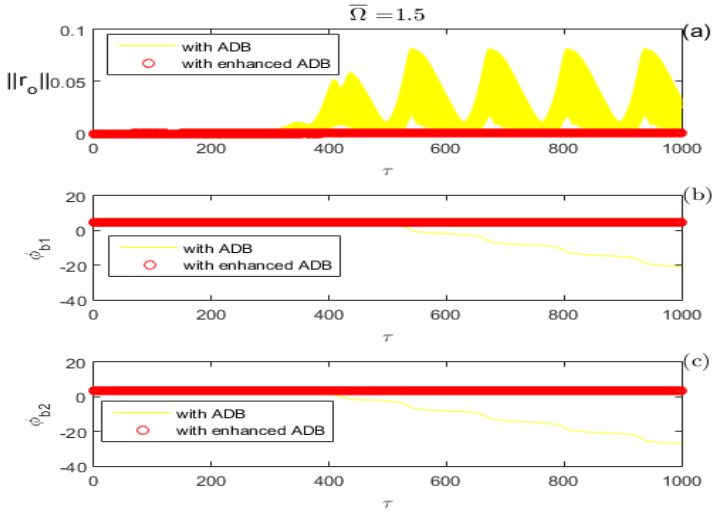


Figure 29. Numerical simulations of the asymmetrically supported planar rotor/ADB or/EADB system initially from the perfect-balancing EP under system parameters ς_e=0.01, R_n=2, C_n=0.01, shown as point 'C' in Figure 26.

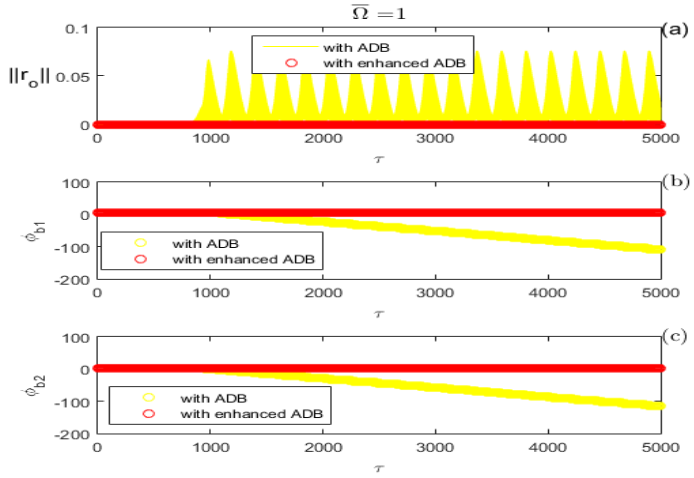


Figure 30. Numerical simulations of the asymmetrically supported planar rotor/ADB or/EADB system initially from the perfect-balancing EP under system parameters ς_e=0.01, R_n=15.5, C_n=0.04, shown as point 'D' in Figure 26.

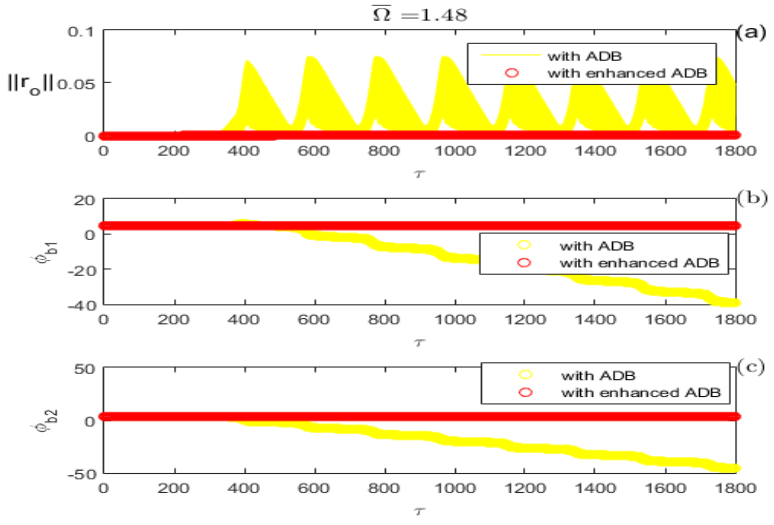


Figure 31. Numerical simulations of the asymmetrically supported planar rotor/ADB or/EADB system initially from the perfect-balancing EP under system parameters ς_e=0.01, R_n=10.5, C_n=0.04, shown as point 'E' in Figure 26.

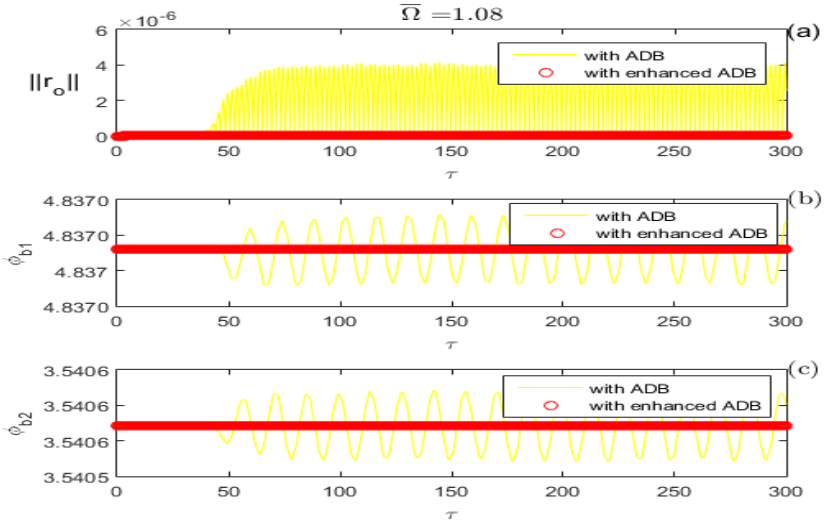


Figure 32. Numerical simulations of the asymmetrically supported planar rotor/ADB or/EADB system initially from the perfect-balancing EP under system parameters ς_e=0.01, R_n=5.5, C_n=1, shown as point 'F' in Figure 26.

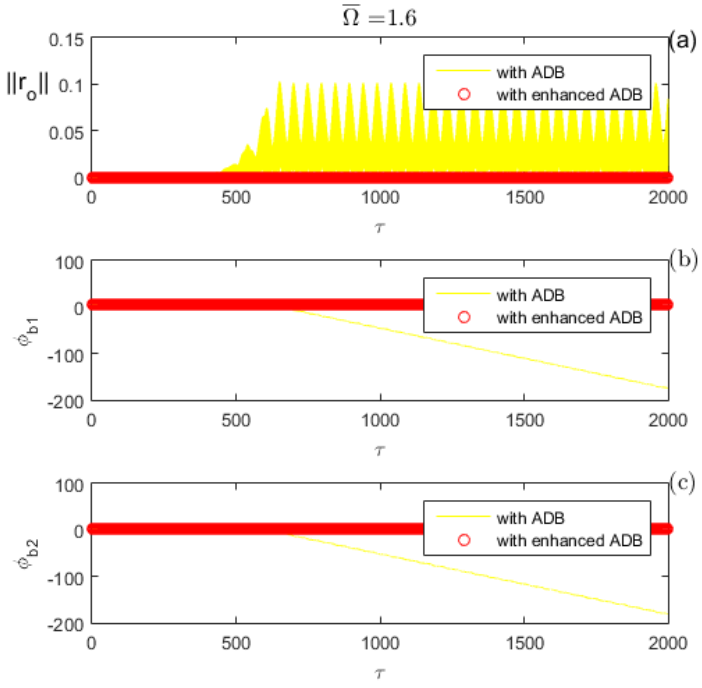


Figure 33. Numerical simulations of the asymmetrically supported planar rotor/ADB or/EADB system initially from the perfect-balancing EP under system parameters ς_e=0.01, R_n=7.5, C_n=1, shown as point 'G' in Figure 26.

CHAPTER 5 WHIRLING LIMIT-CYCLE BEHAVIORS OF THE ASYMMETRICALLY SUPPORTED ROTOR/EADB SYSTEM

5.1 Whirling limit-cycle

5.1.1 Multi-tone harmonic balance method

In order to explore the whirling limit-cycle for the asymmetrically supported planar rotor/EADB system, we introduced the assumptions and the methodology in this section. The system physical parameters are listed in Table 6.

Firstly, numerical integrations are conducted by the Runge-Kutta method, and the results are shown in Figure 34. We have two observations. Observation one: as is shown in Figure 34 (a) (b) that x is quasiperiodic so it is excited by at least two frequencies, which can be two similar frequencies since beat vibrations occur. Observation two: Figure 35(a) shows that $\phi_{b1}(\tau)$ is not synchronized with the term $\tau\overline{\Omega}$, which should be synchronized with by experience, but has a large oscillatory deviation from a declining line whose slope is defined as the average whirling frequency ω, which is also the mean value of $\dot{\phi}_{b1}(\tau)$ in Figure 35(b).

Large oscillatory deviation of ϕ_{b1} can be extracted by separating the whirling motion with oscillatory motion of ϕ_{b1} in Figure 35(a), then we can plot two motions in Figure 36(a) and (b). Therefore, it is easy to obtain the whirling frequency, which is $\omega \approx -0.0415$ rad/s, $f_\omega \approx -0.0066$ Hz. It is worth to note that oscillation is along a nonzero value in Figure 36(b). These observations lead to our ***first assumption*** that the whirling limit-cycle motion of the balancer ball consists of a large amplitude oscillation $\phi_{b1_{\text{osc}}}$ around a nonzero value $A_{0,0}$, and the whirling motion $\omega\tau$,

$$\phi_{b1}(\tau) = \omega\tau + A_{0,0} + \phi_{b1_{\text{osc}}} \tag{5-1}$$

According to Table 6 system parameters, we know that $\overline{\Omega} = 1.03$ rad/s, which is $f_{\overline{\Omega}} = 0.1639$ Hz. One observation is that rotor speed $\overline{\Omega}$ is incommensurable with the balancer ball's whirling speed ω and its ratio r_i is defined as follows,

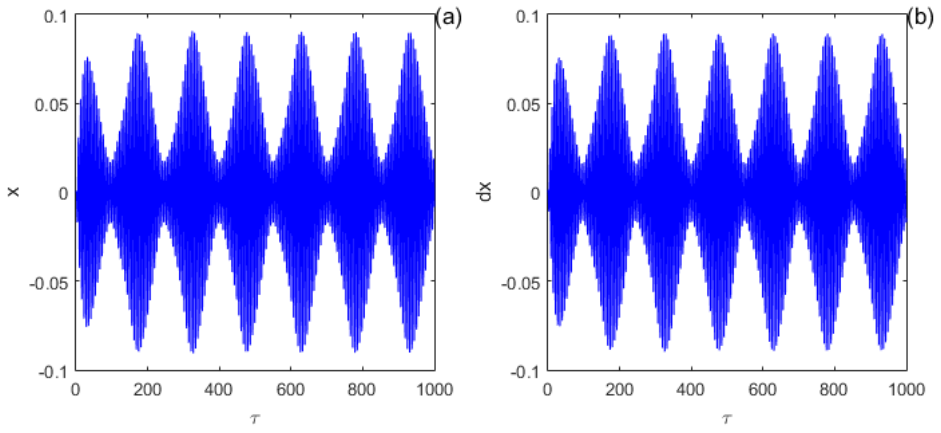


Figure 34. Numerical simulations of the dynamic system (4-11) under parameters shown in Table 5 when $\overline{\Omega}=1.03$, showing $x(\tau)$ and $\dot{x}(\tau)$.

Table 6. Dimensionless system parameters for the asymmetrically supported planar rotor/EADB used in chapter 5

Parameter	Value
balancer balls'mass ratio μ	0.0031
Imbalance ratio η	0.0049
Suspension damping ratio ς_1, ς_2	0.1
ADB fluid damping ratio ς_b	3.1155×10^{-4}
Natural frequency ratio R_r	1.5
Dimensionless rotor speed $\overline{\Omega}$	1.03
Coupling coefficient ς_e	0.001
Equivalent capacity C_n	0.01
Equivalent resistance R_n	0.01
Imbalance phase ϕ_e	$\pi/3$

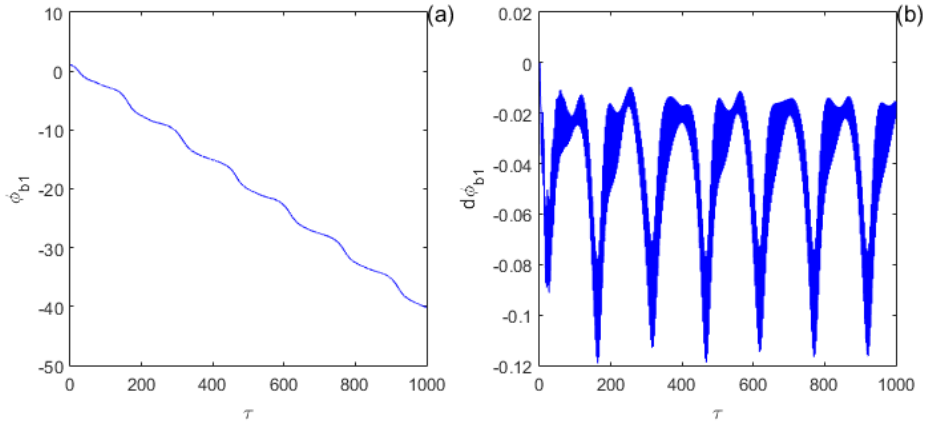


Figure 35. Numerical simulations of the dynamic system (4-11) under parameters shown in Table 5 when $\overline{\Omega} = 1.03$, showing $\phi_{b1}(\tau)$ and $\dot{\phi}_{b1}(\tau)$.

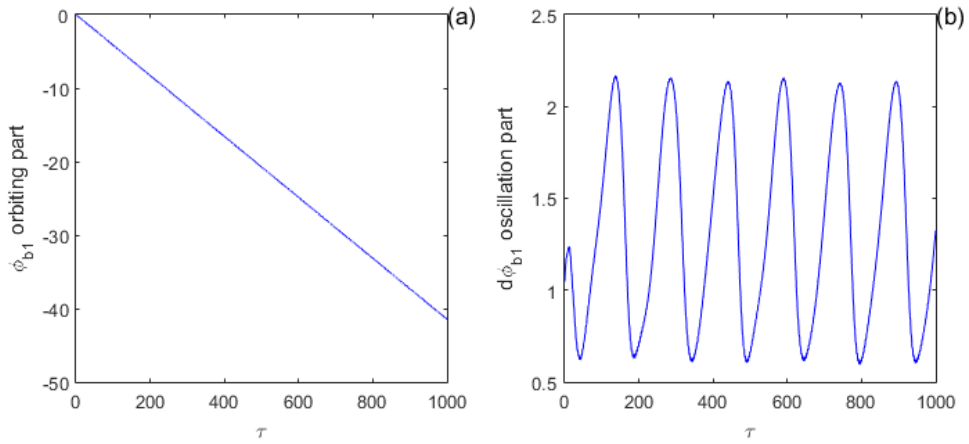


Figure 36. Numerical simulations of the whirling part $\omega\tau$ and the oscillatory part $\phi_{b1_{osc}}$ of ϕ_{b1} as shown in Figure 35.

$$r_i = \left| \frac{\overline{\Omega}}{\omega} \right| \approx 24.823 \tag{5-2}$$

From intensive numerical studies, we know that the speed ratio r_i is not an integral. Therefore, ***second assumption*** is made that the rotor speed frequency $\overline{\Omega}$ and the corresponding balancer ball's frequency ω can be considered as the multi-tone excitations, which are incommensurable with each other. These multi-tone excitations are difference from the multitone inputs described in [42]. In our definition, we consider both the external excitation, which is the rotor speed, and the internal excitation, which is the balancer ball whirling speed. In their definition, they only consider the external excitations, which are inputs of their system. This assumption tries to show that the system responses, such as balancer ball's oscillation part $\phi_{b1_{\mathrm{osc}}}$, the rotor deflection x, are composed of sinusoids, which have base frequencies of $\overline{\Omega}$ and ω.

5.1.2 Matrix pencil method

In order to clarify the two assumptions, an advanced signal processing method known as the Matrix Pencil Method (MPM) [43][44][45] is applied. This method is based on the signal model (5-3), which is the summation of the exponentially damped or undamped sinusoids. By using the signal model shown in (5-3), different from Fourier transformation analysis, the MPM could provide the accurate frequency, amplitude and the damping for each sinusoid.

$$z(t) = \sum_{i=1}^{M} R_i e^{(-\alpha_i t \pm j\beta_i t)} \tag{5-3}$$

Where M is the actual number of sinusoids in the signal, α_i is the damping, β_i is the frequency, and $2R_i$ is the peak amplitude.

Let's briefly introduce the idea of MPM. The method can use sample sequence $x(k)$ represented in (5-4) to construct Hankel matrix $[X_1]$ as shown in (5-5) and Hankel matrix $[X_2]$ as shown in (5-6). The two Hankel matrices can be decomposed into three special matrices as shown in (5-7) and (5-8), respectively. Therefore, according to (5-9), we know that eigenvalues z_i (i=1, 2, …, M) of the matrix $[X_1]^{-1}[X_2]$ contain the information of amplitudes α_i, the frequencies β_i for the signal sinusoids

$$x(k)=\sum_{i=1}^{M} R_i {z_i}^{k},\ x(k+1)=\sum_{i=1}^{M}(R_i z_i){z_i}^{k} \tag{5-4}$$

Where the *i*th exponential complex number $z_i = e^{((-\alpha_i \cdot \Delta t_s \pm j\beta_i \cdot \Delta t_s)}$, α_i is the damping, β_i is the frequency, Δt_s is the sampling period.

$$[X_1]=\begin{bmatrix} x(0) & x(1) & \cdots & x(L-1) \\ x(1) & x(2) & \cdots & x(L) \\ \vdots & \vdots & \ddots & \vdots \\ x(N-L-1) & x(N-L) & \cdots & x(N-2) \end{bmatrix} \tag{5-5}$$

$$[X_2]=\begin{bmatrix} x(1) & x(2) & \cdots & x(L) \\ x(2) & x(3) & \cdots & x(L+1) \\ \vdots & \vdots & \ddots & \vdots \\ x(N-L) & x(N-L+1) & \cdots & x(N-1) \end{bmatrix} \tag{5-6}$$

Where *N* is the assumed number of sinusoids in the signal, which can be identified by the MPM. *N* is the total number of sampling sequence points. *L* is a parameter, which needs to be set by the user and is required to be larger than *M*.

After substituting (5-4) into (5-5) and (5-6), a special decomposition can be illustrated in (5-7) and (5-8), thus $[X_1]^{-1}[X_2]$ is obtained in (5-9).

$$\begin{bmatrix} \sum_{i=1}^{M} R_i {z_i}^{0} & \sum_{i=1}^{M} R_i {z_i}^{1} & \cdots & \sum_{i=1}^{M} R_i {z_i}^{L-1} \\ \sum_{i=1}^{M} R_i {z_i}^{1} & \sum_{i=1}^{M} R_i {z_i}^{2} & \cdots & \sum_{i=1}^{M} R_i {z_i}^{L} \\ \vdots & \vdots & \ddots & \vdots \\ \sum_{i=1}^{M} R_i {z_i}^{N-L-1} & \sum_{i=1}^{M} R_i {z_i}^{N-L} & \cdots & \sum_{i=1}^{M} R_i {z_i}^{N-2} \end{bmatrix} \tag{5-7}$$

$$=\begin{bmatrix} 1 & 1 & \cdots & 1 \\ z_1 & z_2 & \cdots & z_M \\ \vdots & \vdots & \ddots & \vdots \\ {z_1}^{N-L-1} & {z_2}^{N-L-1} & \cdots & {z_M}^{N-L-1} \end{bmatrix} \begin{bmatrix} R_1 & & & \\ & R_2 & & \\ & & \ddots & \\ & & & R_M \end{bmatrix} \begin{bmatrix} 1 & z_1 & \cdots & {z_1}^{L-1} \\ 1 & z_2 & \cdots & {z_2}^{L-1} \\ \vdots & \vdots & \ddots & \vdots \\ 1 & z_M & \cdots & {z_M}^{L-1} \end{bmatrix}$$

$$\begin{bmatrix} \sum_{i=1}^{M} R_i z_i^{\,1} & \sum_{i=1}^{M} R_i z_i^{\,2} & \cdots & \sum_{i=1}^{M} R_i z_i^{\,L} \\ \sum_{i=1}^{M} R_i z_i^{\,2} & \sum_{i=1}^{M} R_i z_i^{\,3} & \cdots & \sum_{i=1}^{M} R_i z_i^{\,L+1} \\ \vdots & \vdots & \ddots & \vdots \\ \sum_{i=1}^{M} R_i z_i^{\,N-L} & \sum_{i=1}^{M} R_i z_i^{\,N-L+1} & \cdots & \sum_{i=1}^{M} R_i z_i^{\,N-1} \end{bmatrix} \tag{5-8}$$

$$= \begin{bmatrix} 1 & 1 & \cdots & 1 \\ z_1 & z_2 & \cdots & z_M \\ \vdots & \vdots & \ddots & \vdots \\ z_1^{\,N-L-1} & z_2^{\,N-L-1} & \cdots & z_M^{\,N-L-1} \end{bmatrix} \begin{bmatrix} R_1 z_1 & & & \\ & R_2 z_2 & & \\ & & \ddots & \\ & & & R_M z_M \end{bmatrix} \begin{bmatrix} 1 & z_1 & \cdots & z_1^{\,L-1} \\ 1 & z_2 & \cdots & z_2^{\,L-1} \\ \vdots & \vdots & \ddots & \vdots \\ 1 & z_M & \cdots & z_M^{\,L-1} \end{bmatrix}$$

$$[X_1]^{-1}[X_2] = \begin{bmatrix} 1 & z_1 & \cdots & z_1^{\,L-1} \\ 1 & z_2 & \cdots & z_2^{\,L-1} \\ \vdots & \vdots & \ddots & \vdots \\ 1 & z_M & \cdots & z_M^{\,L-1} \end{bmatrix} \begin{bmatrix} z_1 & & & \\ & z_2 & & \\ & & \ddots & \\ & & & z_M \end{bmatrix} \begin{bmatrix} 1 & z_1 & \cdots & z_1^{\,L-1} \\ 1 & z_2 & \cdots & z_2^{\,L-1} \\ \vdots & \vdots & \ddots & \vdots \\ 1 & z_M & \cdots & z_M^{\,L-1} \end{bmatrix}, \tag{5-9}$$

The ith complex number z_i including α_i the damping, β_i the frequency can be identified by computing the eigenvalues of the matrix $[X_1]^{-1}[X_2]$.

We can apply MPM to the signals of $x(\tau)$, $y(\tau)$, $\phi_{b1\text{osc}}, \phi_{b2\text{osc}}$, $q_1(\tau)$, $q_2(\tau)$ when they are in their steady-states. The rotor deflections $x(\tau)$ and $y(\tau)$ have the similar frequency components, the balancer balls' oscillation parts $\phi_{b1\text{osc}}$ and $\phi_{b2\text{osc}}$ have the same frequency components, the electric charges $q_1(\tau)$ and $q_2(\tau)$ have the same frequency components. Furthermore, we illustrate these frequency components by listing the results from MPM on the signals of $x(\tau)$, $\phi_{b1\text{osc}}$, $q_1(\tau)$. The first three rows of Table 7, Table 8 and Table 9.

can be obtained directly from MPM, respectively. The row 4 shows the percentage p_i of the amplitude R_i for the ith sinusoid contributing to the whole spectrum $\sum_{k=0}^{M} R_k$, p_i also indicates the importance of the ith sinusoid.

$$p_i = R_i \Big/ \sum_{k=0}^{M} R_k \tag{5-10}$$

Currently, we only know the dominant frequency components in each signal but we do not know how these frequencies are related to the rotor speed frequency and the balancer balls' whirling frequency. To understand the relation between the dominant frequency components in the response signal and the multi-tone excitations, based on

Table 7. Dominant frequencies and multi-tone combinations for $x(\tau)$

Name	Values				
Sinusoids i	1	2	3	4	5
Freq. $\beta_i/(2\pi)$	0.1573	0.1639	0.1507	0.1441	0.1705
Amp. $2R_i$	0.0509	0.0241	0.0123	0.0031	9.72×10^{-4}
Perc. p_i	54.83%	25.96%	13.21%	3.35%	1.05%
Comb.	$f_{\bar{\Omega}} + f_{\omega}$	$f_{\bar{\Omega}}$	$f_{\bar{\Omega}} + 2f_{\omega}$	$f_{\bar{\Omega}} + 3f_{\omega}$	$f_{\bar{\Omega}} - f_{\omega}$
From D	0.1573	0.1639	0.1507	0.1441	0.1705
|Freq.-D|	0	0	0	0	0

Table 8. Dominant frequencies and multi-tone combinations for $\phi_{b1_{\mathrm{osc}}}$

Name	Values				
Sinusoids i	1	2	3	4	5
Freq. $\beta_i/(2\pi)$	0.0066	0.0132	0.0198	0.0264	0.3147
Amp. $2R_i$	0.7345	0.1640	0.0477	0.0153	0.006
Perc. p_i	75.26%	16.81%	4.88%	1.56%	0.612%
Comb.	$\lvert f_{\omega}\rvert$	$2\lvert f_{\omega}\rvert$	$3\lvert f_{\omega}\rvert$	$4\lvert f_{\omega}\rvert$	$2f_{\bar{\Omega}} + 2f_{\omega}$
From D	0.0066	0.0132	0.0198	0.0264	0.3147
|Freq.-D|	0	0	0	0	0

Table 9. Dominant frequencies and multi-tone combinations for $q_1(\tau)$

Name	Values				
Sinusoids i	1	2	3	4	5
Freq. $\beta_i/(2\pi)$	0.0132	0.0066	0.0198	0.0264	0.0330
Amp. $2R_i$	3.51×10^{-4}	1.53×10^{-4}	1.31×10^{-4}	2.39×10^{-5}	6.63×10^{-6}
Perc. p_i	51.50%	22.38%	19.18%	3.51%	0.97%
Comb.	$\lvert f_\omega \rvert$	$2\lvert f_\omega \rvert$	$3\lvert f_\omega \rvert$	$4\lvert f_\omega \rvert$	$5\lvert f_\omega \rvert$
From D	0.0132	0.0066	0.0198	0.0264	0.0330
|Freq.-D|	0	0	0	0	0

Note for Table 7, Table 8 and Table 9

Freq. is short for Frequency, Comb. is short for combination, Amp. is short for amplitude, Perc. is short for percentage, D is short for Data Base.

second assumption, we consider that the dominant frequency consists of a summation of a integral multiplying by the whirling speed frequency $f_\omega \approx -0.0066$ and the rotor speed frequency $f_{\bar{\Omega}} = 0.1639$ as shown in (5-11). Therefore, we created a data base, which lists all the possible combinations and their corresponding values.

$$\sum_{n=0}^{N_1}\sum_{m=-N_1}^{N_1}\left(n\cdot f_{\bar{\Omega}} + m\cdot f_\omega\right) \tag{5-11}$$

Where N_1 needs to be sufficiently large to cover all dominant frequency combinations.

Then row 5 is obtained from the user created data base by comparing the value of each dominant frequency in row 2 with the whole data base, and obtained the value and the combination information in the data base with a smallest error=|Freq.-D|. Hence, row 5 shows the integral n and m for each sinusoid. Similar procedures can be applied to get Table 8 where we obtain frequency combinations for $\phi_{b1\text{osc}}$ in Figure 36(b). It is worth to note that we can always obtain one and only one smallest error bonded in 10^{-5}. Therefore,

we may conclude that $\phi_{b1\text{osc}}$, x and q_1 are composed of sinusoids based on the combinations of a summation of an integral multiplying by $\overline{\Omega}$ and ω.

5.1.3 Solve for the whirling limit -cycle

According to the two assumptions, ***first assumption*** $\phi_{b1}(\tau) = \omega\tau + A_{0,0} + \phi_{b1\text{osc}}$, $\phi_{b2}(\tau) = \omega\tau + A_{0,0} + \phi_{b2\text{osc}}$ and ***second assumption*** x, y, $\phi_{b1\text{osc}}, \phi_{b2\text{osc}}$, q_1, q_2 are composed of sinusoids based on the combinations of a summation of an integral multiplying by $\overline{\Omega}$ and ω, the system whirling limit-cycle solutions are assumed via the multi-tone exciations as follows,

$$b_{\text{wlc},i}(\tau) = \omega\tau + A^{i}{}_{0,0} + \sum_{n=-\infty}^{\infty}\sum_{m=-\infty}^{\infty}\left(A^{i}{}_{m,n}\cos\left(m\omega\tau + n\overline{\Omega}\tau\right) + B^{i}{}_{m,n}\sin\left(m\omega\tau + n\overline{\Omega}\tau\right)\right) \tag{5-12}$$

$$x_{\text{wlc}}(\tau) = \sum_{n=-\infty}^{\infty}\sum_{m=-\infty}^{\infty}\left(C_{m,n}\cos\left(m\omega\tau + n\overline{\Omega}\tau\right) + D_{m,n}\sin\left(m\omega\tau + n\overline{\Omega}\tau\right)\right) \tag{5-13}$$

$$y_{\text{wlc}}(\tau) = \sum_{n=-\infty}^{\infty}\sum_{m=-\infty}^{\infty}\left(E_{m,n}\cos\left(m\omega\tau + n\overline{\Omega}\tau\right) + F_{m,n}\sin\left(m\omega\tau + n\overline{\Omega}\tau\right)\right) \tag{5-14}$$

$$q_{\text{wlc},i}(\tau) = \sum_{n=-\infty}^{\infty}\sum_{m=-\infty}^{\infty}\left(G^{i}{}_{m,n}\cos\left(m\omega\tau + n\overline{\Omega}\tau\right) + H^{i}{}_{m,n}\sin\left(m\omega\tau + n\overline{\Omega}\tau\right)\right) \tag{5-15}$$

To explain the parameters in above solutions as shown in (5-12)-(5-15), m and n are dummy variables, which are integral multipliers for ω and $\overline{\Omega}$, respectively. $A^{i}{}_{m,n}, C_{m,n}, E_{m,n}, G^{i}{}_{m,n}$ are assumed coefficients for cosine terms, $B^{i}{}_{m,n}, D_{m,n}, F_{m,n}, H^{i}{}_{m,n}$ are assumed coefficients for sine terms. We consider the so called multi-tone harmonic balance method by using the assumed solutions in (5-12)-(5-15) to solve the asymmetrically supported planar rotor/EADB system. However, applying the multi-tone harmonic balance method directly would cause some problem, since $\phi_{b1}(\tau)$ in (5-12) includes $\phi_{b1\text{osc}}$ expressed by the summation of sinusoidal functions of τ. Furthermore, $\phi_{b1}(\tau)$ is also introduced in sinusoidal functions as follows, $\sin\left(\overline{\Omega}\tau + \phi_{b1}(\tau)\right)$ and $\cos\left(\overline{\Omega}\tau + \phi_{b1}(\tau)\right)$. Therefore, we cannot equating like terms by directly substituting (5-12)-(5-15) to (4-11). Approximating $\sin\left(\overline{\Omega}\tau + \phi_{b1}(\tau)\right)$,

we develop an approach. First of all, we can separate the whirling term with the oscillation terms in $\sin\left(\overline{\Omega}\tau+\phi_{b1}(\tau)\right)$ as follows,

$$\begin{aligned}&\sin\left(\overline{\Omega}\tau+\phi_{b1}(\tau)\right)\\&=\sin\left(\left(\overline{\Omega}\tau+\omega\tau\right)+\left({A^1}_{0,0}+\phi_{b1\text{osc}}\right)\right)\\&=\sin\left(\overline{\Omega}\tau+\omega\tau\right)\cos\left(A_{0,0}+\phi_{b1\text{osc}}\right)+\cos\left(\overline{\Omega}\tau+\omega\tau\right)\sin\left(A_{0,0}+\phi_{b1\text{osc}}\right)\end{aligned} \tag{5-16}$$

In fact, we want to approximate $\sin\left({A^1}_{0,0}+\phi_{b1\text{osc}}\right)$ and $\cos\left({A^1}_{0,0}+\phi_{b1\text{osc}}\right)$ around ${A^1}_{0,0}$ for one period through Taylor expansion.

In order to approximate those terms, Let's review Taylor expansion as follows,

$$f(x)=f\left(x_0\right)+\left.\frac{f'(x)}{1!}\right|_{x=x_0}\left(x-x_0\right)\cdots+\left.\frac{f'(x)}{n!}\right|_{x=x_0}\left(x-x_0\right)^n+o\left(\left(x-x_0\right)^{n+1}\right) \tag{5-17}$$

In this section, we can define $f(x):\sin\left(x\right)$, $x={A^1}_{0,0}+\phi_{b1\text{osc}}$, $x_0={A^1}_{0,0}$. It means that $\sin\left({A^1}_{0,0}+\phi_{b1\text{osc}}\right)$is expanded at ${A^1}_{0,0}$, thus (5-18) can be obtained.

$$\sin\left({A^1}_{0,0}+\phi_{b1\text{osc}}\right)\approx\sin\left({A^1}_{0,0}\right)+\cos\left({A^1}_{0,0}\right)\left(\phi_{b1\text{osc}}\right)\cdots+\frac{\sin^{(n)}({A^1}_{0,0})}{n!}\left(\phi_{b1\text{osc}}\right)^n \tag{5-18}$$

$$\cos\left({A^1}_{0,0}+\phi_{b1\text{osc}}\right)\approx\cos\left({A^1}_{0,0}\right)-\sin\left({A^1}_{0,0}\right)\left(\phi_{b1\text{osc}}\right)\cdots+\frac{\cos^{(n)}({A^1}_{0,0})}{n!}\left(\phi_{b1\text{osc}}\right)^n \tag{5-19}$$

Where $\phi_{b1\text{osc}}=\sum_{n=-\infty}^{\infty}\sum_{m=-\infty}^{\infty}\left({A^i}_{m,n}\cos\left(m\omega\tau+n\overline{\Omega}\tau\right)+{B^i}_{m,n}\sin\left(m\omega\tau+n\overline{\Omega}\tau\right)\right)$. And similarly (5-19) can be obtained by defining $f(x):\cos\left(x\right)$, $x={A^1}_{0,0}+\phi_{b1\text{osc}}$, $x_0={A^1}_{0,0}$ and then by using the same approach.

Observing the terms on the RHS of (5-18) and (5-19), there are no sinusoidal functions inside the sinusoidal function after the approximation. Hence, substituting (5-18), (5-19) in (5-16), we can obtain (5-20):

$$\begin{aligned}&\sin(\overline{\Omega}\tau+\omega\tau)\cos\left({A^1}_{0,0}+\phi_{b1\text{osc}}\right)+\cos\left(\overline{\Omega}\tau+\omega\tau\right)\sin\left({A^1}_{0,0}+\phi_{b1\text{osc}}\right)\\&\approx\sin(\overline{\Omega}\tau+\omega\tau)\left(\cos\left({A^1}_{0,0}\right)-\sin\left({A^1}_{0,0}\right)\left(\phi_{b1\text{osc}}\right)\cdots+\frac{\cos^{(n)}({A^1}_{0,0})}{n!}\left(\phi_{b1\text{osc}}\right)^n\right)\\&+\cos\left(\overline{\Omega}\tau+\omega\tau\right)\cdot\left(\sin\left({A^1}_{0,0}\right)+\cos\left({A^1}_{0,0}\right)\left(\phi_{b1\text{osc}}\right)\cdots+\frac{\sin^{(n)}({A^1}_{0,0})}{n!}\left(\phi_{b1\text{osc}}\right)^n\right)\end{aligned} \tag{5-20}$$

Equating like terms, reducing the order of sinusoids in (5-20) while treating $\cos\left({A^1}_{0,0}\right)$and

$\sin\left(A^1{}_{0,0}\right)$ as constants rather than sinusoids since they are independent of time when reaching state steady. Finally, (5-20) evolves to (5-21),

$$\begin{aligned}&\sin\left(\bar{\Omega}\tau+\phi_{b1}(\tau)\right)\\&\approx\sum_{n=0}^{\infty}\sum_{m=-\infty}^{\infty}\left(a_{n,m}\sin\left(n\bar{\Omega}\tau+m\omega\tau\right)+b_{n,m}\cos\left(n\bar{\Omega}\tau+m\omega\tau\right)\right)\end{aligned}\tag{5-21}$$

Where each coefficient $a_{n,m}$ is a function of assumed coefficients and the whirling frequency, and the same is for $b_{n,m}$,

$$a_{n,m}=f_a\left(\cos\left(A^1{}_{0,0}\right),\sin\left(A^1{}_{0,0}\right),\mathbf{A},\mathbf{B},\omega\right)\tag{5-22}$$

$$b_{n,m}=f_b\left(\cos\left(A^1{}_{0,0}\right),\sin\left(A^1{}_{0,0}\right),\mathbf{A},\mathbf{B},\omega\right)\tag{5-23}$$

Where $\mathbf{A}=\left\{A^1{}_{01},A^1{}_{02}\cdots\right\}$, $\mathbf{B}=\left\{B^1{}_{01},B^1{}_{02}\cdots\right\}$, these two are short notations for all assumed coefficients of $\phi_{b1\text{osc}}=\sum_{n=-\infty}^{\infty}\sum_{m=-\infty}^{\infty}\left(A^i{}_{m,n}\cos\left(m\omega\tau+n\bar{\Omega}\tau\right)+B^i{}_{m,n}\sin\left(m\omega\tau+n\bar{\Omega}\tau\right)\right)$.

To obtain the approximation for $\cos\left(\bar{\Omega}\tau+\phi_{b1}(\tau)\right)$, the same idea can be applied. We can equate multi-tone terms, which are sinusoidal functions of $\left(n\bar{\Omega}\tau+m\omega\tau\right)$. If using infinite multi-tone terms for implementation, we can obtain more accurate whirling limit-cycle solution. However, the order of Tylor expansion and the terms of the multi-tone harmonic method can great affect the time consumption of numerical simulations. Considering both efficiency and accuracy, we employ the second or the third order of the Tylor expansion, and then use the multi-tones, which contribute 90% to the signal, to assume the whirling limit-cycle solution. To best of the authors knowledge in this case, 2 or 3 multi-tones, which can contribute 90% of the oscillations, are accurate enough to solve the whirling limit-cycle. In this section, according to Table 7, Table 8 and Table 9.

we assume that both $x(\tau)$ and $y(\tau)$ contain $\left(\bar{\Omega}+\omega\right)\tau$ and $\bar{\Omega}\tau$, both $\phi_{b1}(\tau)$ and $\phi_{b2}(\tau)$ contain $\omega\tau$ and2 $\omega\tau$, both $q_1(\tau)$ and $q_2(\tau)$ contain $\omega\tau$, 2 $\omega\tau$ and 3 $\omega\tau$. Therefore, to implement the multi-tone harmonic balance method, there are 2, 2 and 3 multi-tone harmonic terms in the rotor deflections, balancer balls' motion and the electric charges, respectively.

The multi-tone harmonic balance method can be implemented by adopting the whirling limit-cycle solutions as shown in (5-12) -(5-15), equating the coefficients of like multi-tone terms and solving nonlinear algebraic equations by Newton Raphson iteration. To study the effect of other parameter, such as the rotor speed, on the whirling limit-cycle, we adopt the prediction-correction fashion arch- length continuation method described in chapter 3 section 3.1.

5.2 Stability analysis of the whirling limit-cycle

In order to identify the stability of the whirling limit-cycle solution, we linearized the system (4-11) around its whirling limit-cycle solution $[x_{\text{wlc}}, y_{\text{wlc}}, b_{\text{wlc},1}, b_{\text{wlc},2}, q_{\text{wlc},1}, q_{\text{wlc},2}]$ as shown in (5-12)-(5-15), and we obtained the linearized equations-of-motion,

$$\begin{aligned}&\mathbf{M}_{\text{wlc}}(b_{\text{wlc},1}, b_{\text{wlc},2}, \tau)\mathbf{q}''_{\text{wlc}} + \mathbf{C}_{\text{wlc}}(b_{\text{wlc},1}, b_{\text{wlc},2}, \tau)\mathbf{q}'_{\text{wlc}} + \\ &\mathbf{K}_{\text{wlc}}(b_{\text{wlc},1}, b_{\text{wlc},2}, x_{\text{wlc}}, y_{\text{wlc}}, q_{\text{wlc},1}, q_{\text{wlc},2}, \tau)\mathbf{q}_{\text{wlc}} \\ &= \mathbf{F}_{\text{wlc}}(b_{\text{wlc},1}, b_{\text{wlc},2}, x_{\text{wlc}}, y_{\text{wlc}}, q_{\text{wlc},1}, q_{\text{wlc},2}, \tau)\end{aligned} \tag{5-24}$$

Where $(') = \partial / \partial \tau$ and $\mathbf{q}_{\text{wlc}}(\tau) = [x_{\text{wlc}}(\tau), y_{\text{wlc}}(\tau), b_{\text{wlc},1}(\tau), b_{\text{wlc},2}(\tau), q_{\text{wlc},1}(\tau), q_{\text{wlc},2}(\tau)]$, the overall dimensionless system matrices $\mathbf{C}_{\text{wlc}}$ and $\mathbf{K}_{\text{wlc}}$ are shown in A4. And $\mathbf{M}_{\text{wlc}}$, the force vector $\mathbf{F}_{\text{wlc}}$ are shown in A7.4. Please do not be confused with the same notations as shown in (3-11).

In order to analyze the stability of the perturbed system (5-24), we need to get its state matrix $\mathbf{A}_{\text{wlc}}$ as shown in (5-25),

$$\mathbf{A}_{\text{wlc}}(\tau) = \begin{bmatrix} \mathbf{0} & \mathbf{I} \\ -\mathbf{M}_{\text{wlc}}(\tau)^{-1}\mathbf{K}_{\text{wlc}}(\tau) & -\mathbf{M}_{\text{wlc}}(\tau)^{-1}\mathbf{C}_{\text{wlc}}(\tau) \end{bmatrix} \tag{5-25}$$

Where $\mathbf{0}$ is a six by six zero matrix, $\mathbf{I}$ is a six by six identity matrix.

Given identity initial condition x_0 and integrating $\mathbf{A}_{\text{wlc}}(\tau)$ from 0 to $T = 2\pi / (\omega + \bar{\Omega})$, we can construct a fundamental matrix solution. This stability analysis may be not accurate enough near two rotor critical speed. Because the whirling limit-cycle is quasi-periodic motion for the asymmetrically supported planar rotor/EADB system, but Floquest theory can only be applied on periodic time-variant linear system.

$$x(T) = \int_0^T \mathbf{A}_{\text{wlc}}(\tau) d\tau \cdot x_0 \tag{5-26}$$

Applying Floquet theory, we identify the stability of the linear quasi-periodic time-variant differential equations by examining the eigenvalues of the fundamental matrix solutions. The perturbed system (5-24) is guaranteed to be asymptotic stable, if and Only if all the absolute values of the eigenvalues $\lambda_{x(T)}$ for the fundamental matrix solution $x(T)$ are less than 1,

$$\max\left|\lambda_{x(T)}\right| < 1 \tag{5-27}$$

5.3 Shunt circuit parameter study

To study the effect of the EADB compared with the ADB on the asymmetrically supported planar rotor system as shown in Figure 37, we employ a set of electric circuit parameters as follows ς_e=0.001, C_n=0.01, R_n=3. Figure 37(a) shows that the EADB can largely reduce the whirling limit-cycle for the asymmetrically supported planar rotor than the ADB by designing proper circuit parameters. The ADB has the whirling limit-cycle around the first and the second rotor critical speed, which are 1 and 1.5, respectively. The ranges of the whirling limit-cycle are from $\overline{\Omega}$ =0.9 to 1.4, and from 1.45 to 2.5, respectively. The stable branches are from $\overline{\Omega}$ =1 to 1.35 and from 1.5 to 2.3, respectively. The largest whirling speeds for each stable branch can exceed 0.3 and 1, respectively. As shown in a zoomed-in Figure 37(b), the EADB has the stable whirling limit-cycle from $\overline{\Omega}$ =0.8 to1.05 and from 1.4 to 1.55 around the first and the second rotor critical speed, respectively. The largest whirling speeds only approach 0.05 and 0.1, respectively. To sum up, Figure 37 shows that the EADB can both eliminate whirling limit-cycle under different rotor speed and reduce the peak value of the whirling speed to 1/6 and 1/10 that of the conventional ADB, respectively. In order to check the accuracy of these results, we pick up four stable points, four unstable points on the ADB continuation curve, and then pick up two stable points, two unstable points the EADB continuation curve. They are called ‘S1’, ‘S2’, ‘S3’, ‘S4’, ‘U1’, ‘U2’, ‘U3’, ‘U4’, and ‘s1’, ‘s2’, ‘u1’, ‘u2’ respectively.

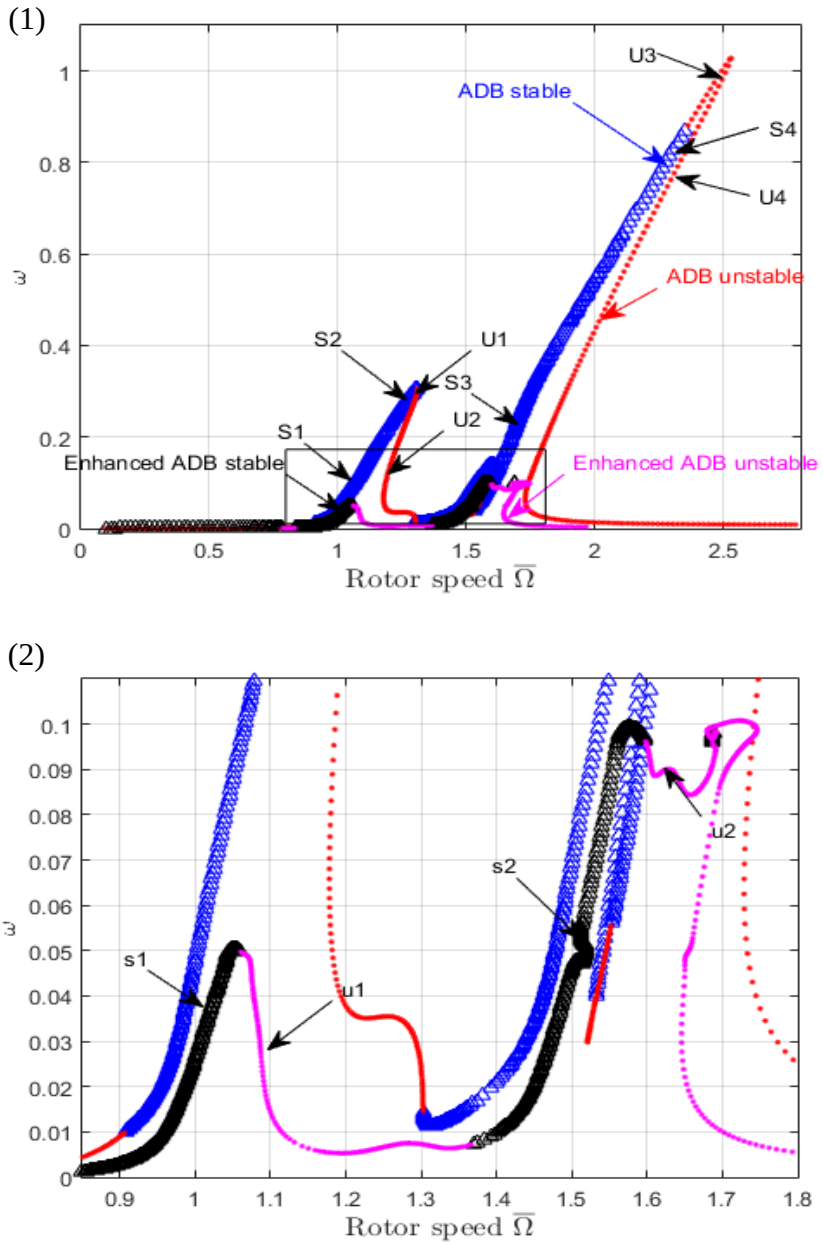


Figure 37. Comparison of the whirling limit-cycle of the ADB and the EADB/asymmetrically supported planar rotor system (1)full picture (2)zoomed-in picture

5.4 Numerical study and verification

We used the multi-tone harmonic balance method based on some assumptions and approximations thus we need to validate the accuracy of the continuation curves as shown in Figure 37. To check the stability of the curves explored in section 5.3, time-time-domain simulations via direct numerical integrations of the full nonlinear equations-of-motion (4-11) is performed. ‘HBM’ represents multi-tone harmonic balance method, ‘NS’ represents numerical simulation. The accuracy of the solution is based on the assumed terms of the harmonic balance method [42]. For efficiency and accuracy, we assume the first two harmonic terms in the whirling limit-cycle solutions as shown in (5-12) to (5-15). Therefore, 5-10% deviation is allowable in this analysis.

It is shown in Figure 38 and Figure 40 that the approximate analytic solutions in red circles getting from the multi-tone harmonic balance method are consistent with the numerical simulations in blue lines when the continuation curves are stable, while it is indicated from Figure 39 and Figure 41 that the unstable points numerical simulations can diverge from the analytic solutions. To sum up, numerical simulations have shown the acceptable accuracy of the continuation curves and their corresponding stability.

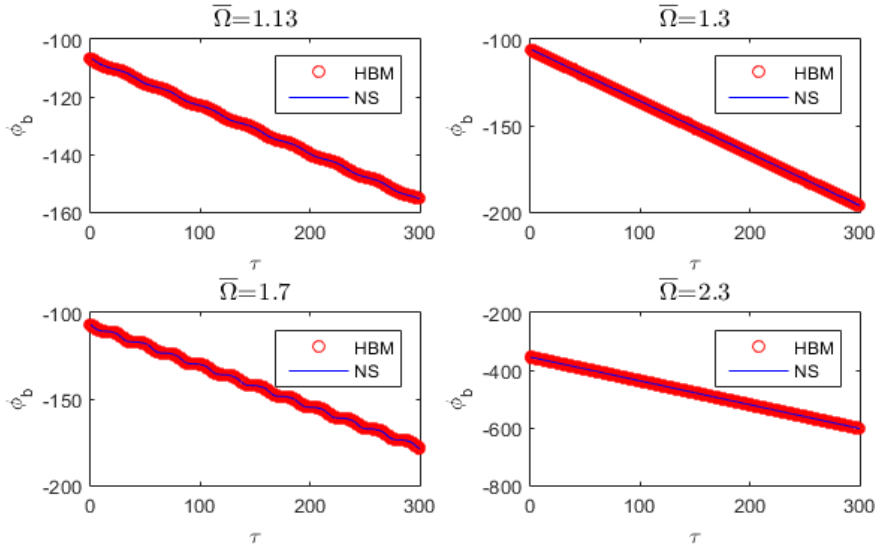


Figure 38. Numerical simulations of the stable points ‘S1’, ‘S2’, ‘S3’, ‘S4’ on the continuation curve for the ADB as shown in Figure 37

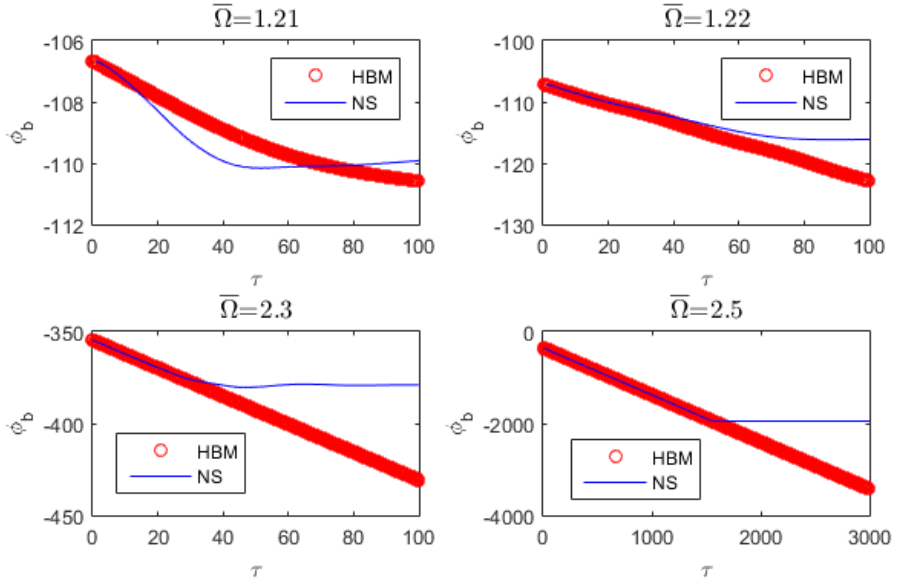


Figure 39. Numerical simulations of the unstable points ‘U1’, ‘U2’, ‘U3’, ‘U4’ on the continuation curve for the ADB as shown in Figure 37.

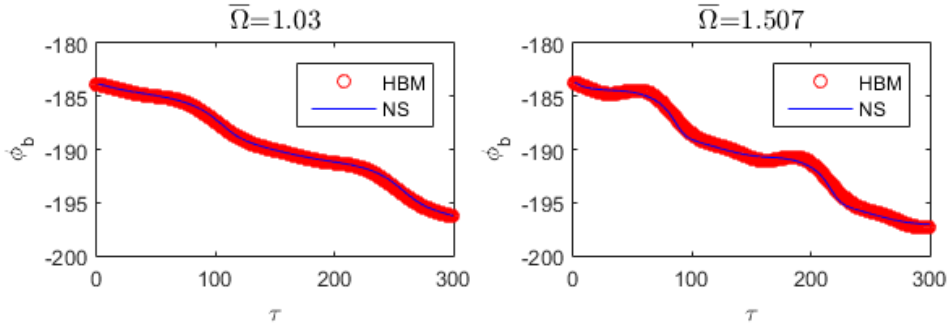


Figure 40. Numerical simulations of the stable points ‘s1’, ‘s2’, on the continuation curve for the EADB as shown in Figure 37.

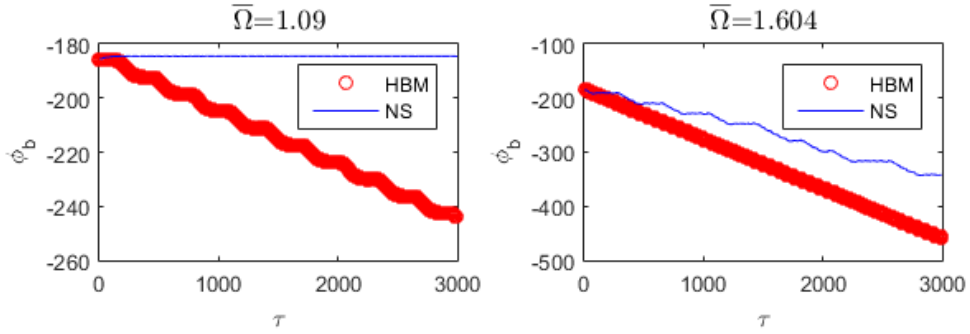


Figure 41. Numerical simulations of the unstable points ‘u1’, ‘u2’, on the continuation curve for the EADB as shown in Figure 37.

CHAPTER 6 VERTICAL PLANAR ROTOR/DUAL MASS EADB SYSTEM

6.1 Background and motivation

In the previous chapters, to show the goodness of our newly developed EADB, which can either increase the stable perfect-balancing EP or eliminate the whirling limit-cycle, we studied and presented planar rotor/EADB systems, which are horizontally oriented. Most literature about the ADB neglect the effect of gravity by introducing a horizontal rotor. However, vertically oriented rotors are commonly used in reality, such as the energy-storage flywheel, the washing machine with a vertical rotor, the tail rotor of a helicopter and etc. Therefore, it is necessary to study the application of the EADB on a vertically oriented rotor. The ADB on a vertically oriented rotor was studied in [46].

To study the vertically oriented planar rotor/EADB system, we need to know the difference between the horizontally and the vertically oriented rotors. Essentially different from the horizontally-oriented planar rotor, the vertically-oriented planar rotor suffers gravity, which apply to both the balancer balls and the rotor. As is known that the imbalance can act as a constant force in the rotating frame while gravity is a constant force in the fixed frame. Therefore, we cannot get the perfect-balancing EP either in a rotating frame or in a fixed frame since there always a constant force cannot be canceled by placing the balancer balls of the ADB in some fixed manner. Gravity and the imbalance make the dynamic system of the rotor/EADB to be time varying. This is very similar to the asymmetrically supported rotor/EADB system. As for the vertical rotor/EADB system, we will have rotor deflections due to gravity and deflections due to the imbalance. How the rotor deflections due to different sources are coupled together? We will explore chapter 6 by considering the coupled rotor deflections.

6.1.1 Modeling of the vertically oriented planar rotor/dual mass EADB system

In this section, we provide the derivation of equations-of-motion for the vertical rotor/EADB system and then derive its corresponding dimensionless form. This system is non-autonomous because of the excitations from both the balancer balls and from gravity.

A set of system parameters is shown in the Table 10 as an example. In this section, the numerical simulations and the analysis for the vertical rotor/EADB system are all based on parameters listing in the Table 10 unless noted otherwise. In this section, we only address the difference between the vertically-oriented rotor system and the horizontally-oriented rotor system. The position vector locating the planar rotor spin center C relative to whirling center O is $\mathbf{r}_o$, the lateral deflections are $v(t)$ and $w(t)$ measured from the fixed coordinate system $\{\mathbf{n}\}$ as follows,

$$\mathbf{r}_O = v(t)\mathbf{n}_2 + w(t)\mathbf{n}_3 \tag{6-1}$$

Then we can obtain the system kinetic energy through the same derivation in chapter 2 through (2-16) to (2-20). As for the system potential energy, vertically-oriented rotor includes the balancer balls' gravity and the rotor's gravity. The total gravitational energy is presented here

$$V_g = m_b g \sum_{i=1}^{2} (w_{OB})_i + m_R g w_O + m_e g w_e \tag{6-2}$$

Where $(w_{OB})_i$, w_O, w_e are vertical displacements of the balancer balls, rotor, and imbalance, respectively, in the fixed frame $\{\mathbf{n}\}$. These quantities are obtained by pulling out the coefficients in the $\mathbf{n}_3$ axis for each position vector $\mathbf{r}_O$, $\mathbf{r}_{OB}$, $\mathbf{r}_E$.

Other derivations are similar with that of chapter 2 section 2.3.1 or chapter 4 section 4.1.2. The resulting independent nonlinear equations-of-motion for the vertically-oriented planar rotor/dual mass EADB system are shown in (6-3),

$$\mathbf{M}(\varphi_{b1}, \varphi_{b2}, t)\ddot{\mathbf{q}} + \mathbf{C}(\varphi_{b1}, \varphi_{b2}, t)\dot{\mathbf{q}} + \mathbf{K}\mathbf{q} = \mathbf{F}(\varphi_{b1}, \varphi_{b2}, \dot{\varphi}_{b1}, \dot{\varphi}_{b2}, t) \tag{6-3}$$

With $\mathbf{q}(t) = \left[v_a(t), w_a(t),\ \varphi_{b1}(t),\ \varphi_{b2}(t),\ q_{C1}(t),\ q_{C2}(t)\right]$.

Where the overall system inertia, and stiffness matrices are **M**, and **K** showing in A5. The damping matrix **C** and the force vector **F** are given in A7.5.

In addition to the dimensionless parameters shown in Chapter 2 (2-26), the new dimensionless variables are introduced as follows,

$$\omega_g = \sqrt{\frac{g}{R_b}}, \frac{\omega_g}{\omega_n} = R_w \tag{6-4}$$

Table 10. Physical parameters for the vertically oriented planar rotor/EADB system

Parameter	Value	Units
Rotor radius R_d	0.06	m
Rotor mass m_R	1.3657	kg
Rotor transverse inertia J_r	0.0025	kg-m^2
Imbalance quatity m_eR_e	3.36×10^{-4}	kg-m
Bearing support stiffness k	1×10^4	N-m
Gravity acceleration constant g	9.8	m/s^2
Bearing support damping c_1, c_2	11.7221	N-m-s
ADB track radius R_b	0.05	m
balancer ball m_b	0.0042	kg
balancer ball -fluid damping c_b	0.0365	N-m-s

Where ω_g represents a special frequency due to the effect of gravity, R_w represents the frequency ratio.

The dimensionless equations-of-motion are obtained through Lagrange's method as follows,

$$\mathbf{M_n}(\phi_{b1},\phi_{b2},\tau)\mathbf{q_n''}+\mathbf{C_n}(\phi_{b1},\phi_{b2},\tau)\mathbf{q_n'}+\mathbf{K_n}\mathbf{q_n}=\mathbf{F_n}(\phi_{b1},\phi_{b2},\phi_{b1}',\phi_{b2}',\tau) \tag{6-5}$$

With the dimensionless general coordinate $\mathbf{q_n}(\tau)=\left[x(\tau),y(\tau),\phi_{b1}(\tau),\phi_{b2}(\tau),q_1(\tau),q_2(\tau)\right]$.

Where $(')=\partial/\partial\tau$ and the overall dimensionless system matrices are $\mathbf{M_n}$, $\mathbf{C_n}$ and $\mathbf{K_n}$, respectively. And the force vector is $\mathbf{F_n}$. All matrices are given as,

$$\mathbf{M_n}=\begin{bmatrix} 1 & 0 & -\mu\sin(\varphi_{b1}+\tau\bar{\Omega}) & -\mu\sin(\varphi_{b2}+\tau\bar{\Omega}) & 0 & 0 \\ 0 & 1 & \mu\cos(\varphi_{b1}+\tau\bar{\Omega}) & \mu\cos(\varphi_{b2}+\tau\bar{\Omega}) & 0 & 0 \\ -\mu\sin(\varphi_{b1}+\tau\bar{\Omega}) & \mu\cos(\varphi_{b1}+\tau\bar{\Omega}) & \mu & 0 & 0 & 0 \\ -\mu\sin(\varphi_{b2}+\tau\bar{\Omega}) & \mu\cos(\varphi_{b2}+\tau\bar{\Omega}) & 0 & \mu & 0 & 0 \\ 0 & 0 & \varsigma_e & 0 & -1 & 0 \\ 0 & 0 & 0 & \varsigma_e & 0 & -1 \end{bmatrix} \tag{6-5a}$$

$$\mathbf{C_n}=\begin{bmatrix} \varsigma_1 & 0 & -2\mu\bar{\Omega}\cos(\varphi_{b1}+\tau\bar{\Omega}) & -2\mu\bar{\Omega}\cos(\varphi_{b2}+\tau\bar{\Omega}) & 0 & 0 \\ 0 & \varsigma_2 & -2\mu\bar{\Omega}\sin(\varphi_{b1}+\tau\bar{\Omega}) & -2\mu\bar{\Omega}\sin(\varphi_{b2}+\tau\bar{\Omega}) & 0 & 0 \\ 0 & 0 & \varsigma_b+\varsigma_e & 0 & 0 & 0 \\ 0 & 0 & 0 & \varsigma_b+\varsigma_e & 0 & 0 \\ 0 & 0 & 0 & 0 & -R_n & 0 \\ 0 & 0 & 0 & 0 & 0 & -R_n \end{bmatrix} \tag{6-5b}$$

$$\mathbf{K_n}=\begin{bmatrix} 1 & 0 & 0 & 0 & 0 & 0 \\ 0 & 1 & 0 & 0 & 0 & 0 \\ 0 & 0 & 0 & 0 & -R_n & 0 \\ 0 & 0 & 0 & 0 & 0 & -R_n \\ 0 & 0 & 0 & 0 & -C_n & 0 \\ 0 & 0 & 0 & 0 & 0 & -C_n \end{bmatrix} \tag{6-5c}$$

$$\mathbf{F_n} = \begin{bmatrix} \bar{\Omega}^2\eta\cos(\varphi_e+\tau\bar{\Omega})+\sum_{i=1}^{2}\bar{\Omega}^2\mu\cos(\varphi_{bi}+\tau\bar{\Omega})+\mu\cos(\varphi_{bi}+\tau\bar{\Omega})\varphi_{bi}'^{\,2} \\ \bar{\Omega}^2\eta\sin(\varphi_e+\tau\bar{\Omega})+\sum_{i=1}^{2}\bar{\Omega}^2\mu\sin(\varphi_{bi}+\tau\bar{\Omega})+\mu\sin(\varphi_{bi}+\tau\bar{\Omega})\varphi_{bi}'^{\,2}-R_w{}^2(1+\mu_i) \\ -R_w{}^2\mu\cos(\varphi_{b1}+\tau\bar{\Omega}) \\ -R_w{}^2\mu\cos(\varphi_{b2}+\tau\bar{\Omega}) \\ 0 \\ 0 \end{bmatrix} \quad \text{(6-5d)}$$

Observing the force matrix $\mathbf{F_n}$ as shown in (6-5d) and (4-11d), we notice some major difference between them. There is an extra constant force in the vertical direction shown as $-R_w{}^2(1+\mu_i)$ due to gravity of the rotor, and there is an extra time varying force shown as $-R_w{}^2\mu\cos(\varphi_{b1}+\tau\bar{\Omega})$ due to gravity of the balancer ball one. The similar force also applies to the balancer ball two.

6.1.2 Equilibrium points (EPs)

According to the knowledge obtained from the system equations-of-motion as shown in (6-5), we know that a constant vertical deflection can be generated due to the rotor's gravity, while oscillations of the rotor can be generated due to both the imbalance and the balancer balls' gravity when observing in the fixed frame. We expect that the EADB can compensate for the imbalance but it cannot compensate for the rotor's gravity. Therefore, we can assume a constant vertical deflection for the rotor under perfect-balancing EP to compensate for the rotor's gravity. We derived the system equations-of-motion by using position vectors of the rotor deflections in the fixed frame. The balancer balls' angular positions is defined in terms of the rotating frame.

Assuming no horizontal rotor deflection, a constant vertical rotor deflection, the constant balls angular positions and zero electric charges in the shunt circuits, the perfect-balancing EP are presented as $[x_s, y_s, \phi_{b1s}, \phi_{b2s}, q_{1s}, q_{2s}]$ To sum up, we assumed the value of the perfect-balancing EP as $x_s = 0, y_s = y_0, \phi_{b1s} = \phi_1, \phi_{b2s} = \phi_2, q_{1s} = 0, q_{2s} = 0$. Substituting the assumption into (6-5) and making all the derivatives of the state variables to be zeros, we can obtain the following algebraic equations (6-6) as follows,

$$\begin{aligned}
&\cos(\phi_1+\tau\bar{\Omega})+\cos(\phi_2+\tau\bar{\Omega})=-\frac{\eta}{\mu}\cos(\theta_e+\tau\bar{\Omega})\\
&\sin(\phi_1+\tau\bar{\Omega})+\sin(\phi_2+\tau\bar{\Omega})=-\frac{\eta}{\mu}\sin(\theta_e+\tau\bar{\Omega})+y_0+R_w{}^2(1+\mu_i)\\
&R_w{}^2\mu\cos(\phi_1+\tau\bar{\Omega})=0\\
&R_w{}^2\mu\cos(\phi_2+\tau\bar{\Omega})=0
\end{aligned} \tag{6-6}$$

Observing the third and fourth equations in (6-6), $\cos(\phi_1+\tau\bar{\Omega})$ cannot be zero since its value varies with time τ. Therefore, it is indicated that there is no perfect-balancing EP for the vertically-oriented planar rotor/EADB system. Although there is no perfect-balancing EP rigorously, the value of $R_w{}^2\mu$ is much smaller than the value of $\frac{\eta}{\mu}$ and $R_w{}^2(1+\mu_i)$ so that we can consider that the third and fourth equations have been satisfied automatically due to a very small value of the term $R_w{}^2\mu$.

Then observing RHS of the second equation in (6-6), $y_0+R_w{}^2(1+\mu_i)$ is a constant term. If letting $y_0+R_w{}^2(1+\mu_i)$ to be zero, then ϕ_1 and ϕ_2 in equation (6-6) can be solved simultaneously by using the first and the second equations as follows,

$$\begin{aligned}
&\phi_{1,2}=(\phi_e+\pi)\pm\frac{1}{2}\arccos\left(\frac{\eta^2}{2\mu^2}-1\right),\\
&x_s=0, y_s=-R_w{}^2(1+\mu_i),\\
&q_{1s}=0, q_{2s}=0
\end{aligned} \tag{6-7}$$

6.2 Stability analysis of the "perfect-balancing EP"

6.2.1 Linearized model

Based on the parameters in Table 10, the dimensionless system parameters are introduced and presented in Table 11. In order to identify the stability of the "perfect-balancing EP", we linearized the system (6-5) around the perfect-balancing EP [x_s, y_s, φ_1, φ_2, q_{1s}, q_{2s}], and obtained the linearized equations-of-motion as follows,

Table 11. Dimensionless parameters for the vertically-oriented planar rotor/EADB

Parameter	Value
balancer ball mass ratio μ	0.0031
Imbalance ratio η	0.0049
Suspension damping ratio ς_1, ς_2	0.1
ADB fluid damping ratio ς_b	0.0003
Natural frequency ratio R_w	0.16
Dimensionless rotor speed $\overline{\Omega}$	0-3*
Coupling coefficient ς_e	0.001*
Equivalent capacity C_n	0.01*
Equivalent resistance R_n	0.01*
Imbalance phase ϕ_e	$\pi/3$

*Various values used in the analysis

$$\mathbf{M}_L(\phi_1,\phi_2,\tau)\mathbf{q}''_\Delta + \mathbf{C}_L(\phi_1,\phi_2,\tau)\mathbf{q}'_\Delta + \mathbf{K}_L(\phi_1,\phi_2,x_s,y_s,\tau)\mathbf{q}_\Delta = \mathbf{F}_L(\phi_1,\phi_2,x_s,y_s,\tau) \qquad (6\text{-}8)$$

The perturbed general coordinate is $\mathbf{q}_\Delta(\tau) = \left[\Delta x_s(\tau), \Delta y_s(\tau), \Delta\phi_1(\tau), \Delta\phi_2(\tau), \Delta q_{1s}(\tau), \Delta q_{2s}(\tau)\right]$

Where $(') = \partial/\partial\tau$ and the overall dimensionless system matrices are $\mathbf{M}_L$, $\mathbf{C}_L$ and $\mathbf{K}_L$, respectively. And the force vector is $\mathbf{F}_L$. All matrices are given in A5.

In order to analyze the stability of the perturbed system (6-8), we need to calculate the eigenvalues of its state matrix $\mathbf{A}_\Delta$ in (6-9),

$$\mathbf{A}_\Delta(\tau) = \begin{bmatrix} \mathbf{0} & \mathbf{I} \\ -\mathbf{M}_\Delta(\tau)^{-1}\mathbf{K}_\Delta(\tau) & -\mathbf{M}_\Delta(\tau)^{-1}\mathbf{C}_\Delta(\tau) \end{bmatrix} \qquad (6\text{-}9)$$

Where $\mathbf{0}$ is a six by six zero matrix, $\mathbf{I}$ is a six by six identity matrix.

Given identity initial condition x_0 and integrating $\mathbf{A}_\Delta(\tau)$ in τ from 0 to $T = 2\pi/\bar{\Omega}$, we can construct a fundamental matrix solution.

$$x(T) = \int_0^T \mathbf{A}_\Delta(\tau)d\tau \cdot x_0 \qquad (6\text{-}10)$$

Applying Floquet theory, we can identify the stability of the linear periodic time-variant differential equations from examining the eigenvalues of the fundamental matrix solution. The perturbed system (6-8) is guaranteed to be asymptotic stable, if and Only if all the absolute values of the eigenvalues $\lambda_{x(T)}$ of the fundamental matrix solution $x(T)$ are less than 1,

$$\max\left|\lambda_{x(T)}\right| < 1 \qquad (6\text{-}11)$$

6.2.2 Shunt circuit parameter study

Figure 42 (1) shows that one can obtain the wrong stability plots if analyzing the stability of the approximate perfect-balancing EP without neglecting the small term $R_w{}^2\mu$ in the stiffness matrix $\mathbf{K}_L$. According to the works conducted previously, the obvious faults appear in the subcritical region as shown in Figure 42 (1). The stable region should not appear below the rotor critical speed 1. After correcting the term $R_w{}^2\mu$ to 0 in the $\mathbf{K}_L$ in Figure 42 (2), we can get reasonable stability plots. The narrow stable region in Figure 42 (2) around zero rotor speed is due to the neglection of balancer balls' gravity effect. In general, we can accept the stability analysis results above zero rotor speed.

To study the effect of R_n, we explored the stability of the perfect-balancing EP under different ς_e and C_n. We know that the EADB can increase the stable region compared with the ADB by reducing R_n as shown in Figure 43. It is shown that R_n is not sensitive.

To explore the effect of ς_e, we explored the stability of the perfect-balancing EP under different R_n and C_n. Comparing the results in Figure 44(1) and (2), we know that the larger ς_e can increase more stable region around rotor critical speed but also decrease more stable region around stability boundaries. The enhanced stable regions in Figure 44(2) are cyan regions, which appear around rotor critical speed within narrow belts. The shrunken stable regions are magenta regions which appear around stability boundary as narrow belts. These figures show that the perfect-balancing EP stability can be enlarged when properly designing circuit parameters with the enlargement down to the resonance. Although we haven't explored the whirling limit-cycle for the vertical rotor/EADB system, the EADB is promising to reduce the whirling limit-cycle as shown in Figure 45(1) and (2). The EADB balancer balls stay around the perfect-balancing EP when the ADB balancer balls do the whirling limit-cycle. Therefore, the rotor deflections can be eliminated by the EADB. The similar observations are observed by simulating points as shown in Figure 43 and Figure 44, 'A', 'B', 'C', 'D', 'E', 'F', 'G', 'H', 'I'.

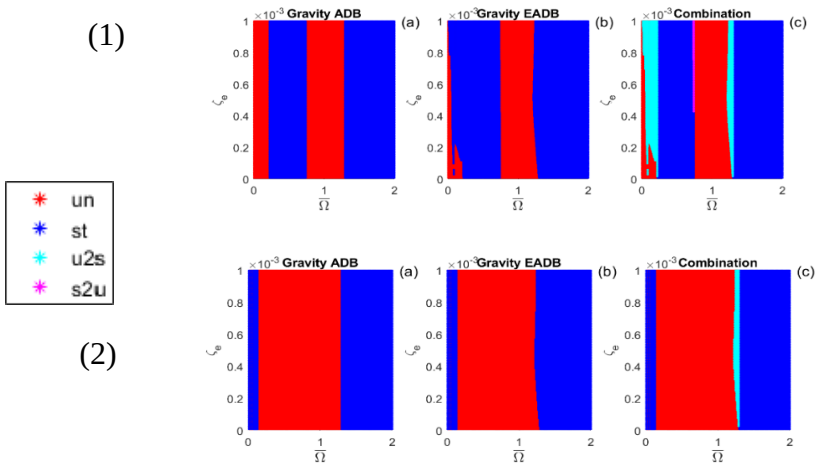


Figure 42. Stability comparison of perfect-balancing EPs for the EADB and the ADB (1)Example with $R_w^2\mu$ (2)Example neglect $R_w^2\mu$

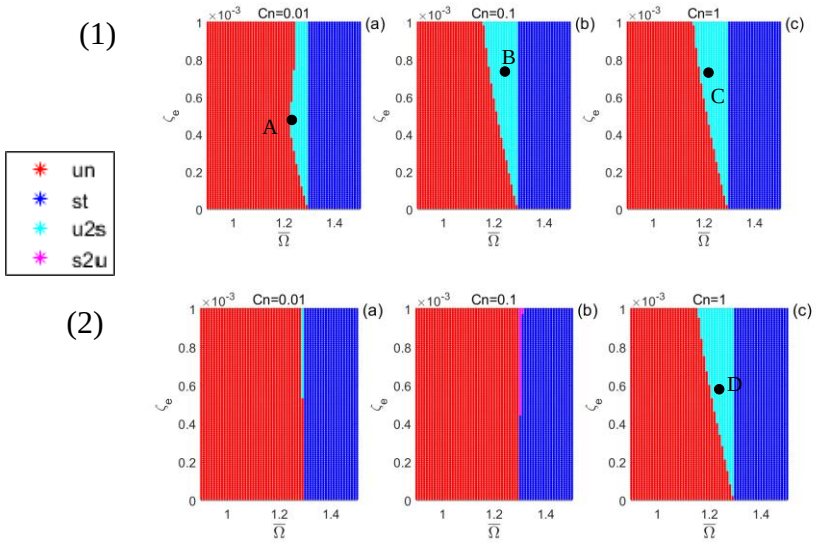


Figure 43. Stability comparison of the perfect-balancing EP for the EADB and the ADB (1) Rn =0.01 (2) Rn = 1

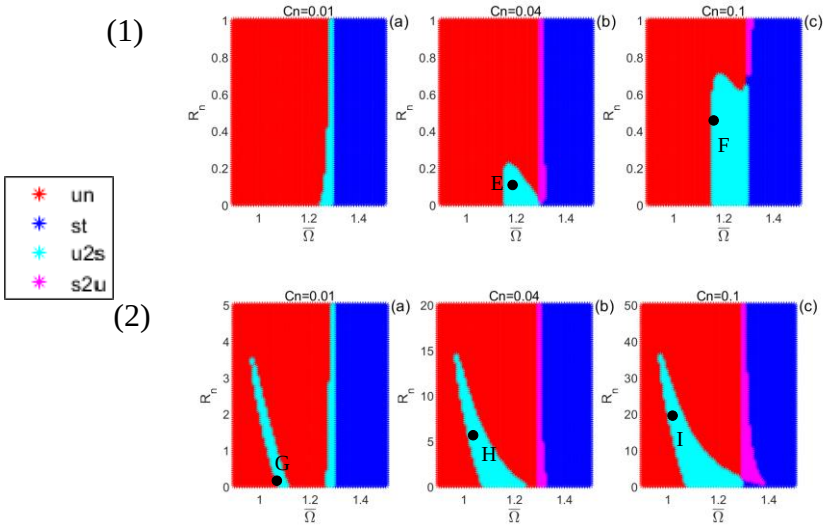


Figure 44. Stability comparison of the perfect-balancing EP for the EADB and the ADB (1) ς_e=0.001 (2) ς_e=0.01

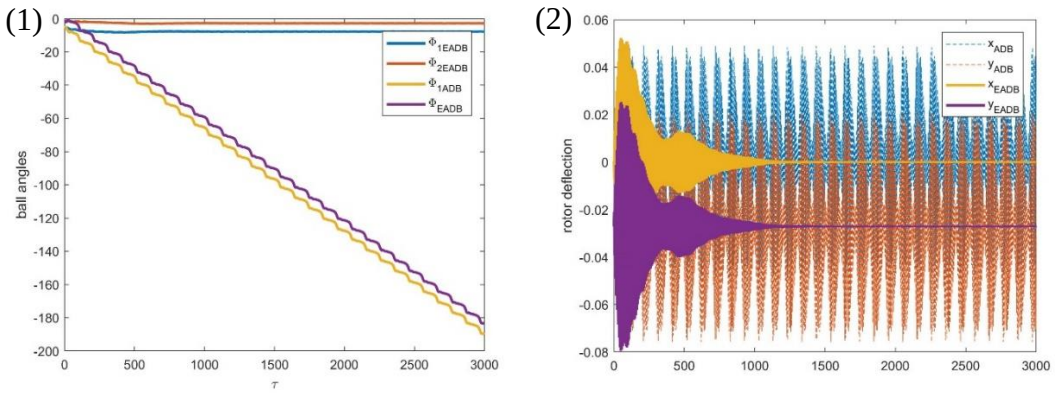


Figure 45. Numerical simulations of the EADB and the ADB showing (1) the balancer ball's angular positions (2) the rotor deflections

CHAPTER 7 MULTI-PLANE BALANCING OF RIGID SHAFT ROTOR/ FOUR MASS DUAL EADB SYSTEM

7.1 Background and motivation

Most literature only consider the planar rotor lateral deflections when exploring the application of the ADB. In this chapter, we will study the effect of the ADB and the EADB on a rigid shaft rotor with titling motion, because the rotors' tilting motion is very common in reality. Therefore, we use two ADBs to compensate for the tilting motions for the shaft rigid rotor. This is also known as multi-plane balancing.

In chapter 3, 4 and 5, we studied and presented planar rotor/EADB systems. In this chapter, we will introduce a rigid shaft rotor model, which is a 3-dimensional rotor with in-plane lateral deflections as well as out-of-plane tilting deflections. The performance of the ADB on flexible shafts with the out-of-plane motions was studied by [47][48]. In 1977, a two-plane balancing by dual ADB was firstly introduced in a rigid shaft rotor[49]. After then, some studies about rotor balancing via two-plane balancing with two ADBs were conducted [50]. We will explore the two-plane balancing by dual EADB system on a rigid shaft rotor, including solving EPs, analyzing the stability of perfect-balancing EP and some other EPs. The accuracy of these analysis will be tested via time domain simulations. We will exam if the EADB could enlarge the stable region of the perfect-balancing EP for a rigid shaft. We will also explore the effect of assembling errors as we have done for the symmetrically supported planar rotor/EADB system shown in section 2.5.

7.1.1 Modeling of the rigid shaft rotor/four mass dual EADB system

To investigate the properties of the rigid shaft rotor/four mass dual EADB system with tilting motions as shown in Figure 46. The configuration for each of EADB in Figure 46 is similar to that of EADB in Figure 8 or Figure 25. Therefore, we skip the description for the configuration of EADB and directly describe the structure of the rigid shaft model. As illustrated in Figure 46, the rigid shaft has a mass m_R, a polar moment of inertia J_p, a transverse moment of inertia J_t, and it is mounted on two compliant linear bearings, which are located at positions p_1 and p_2, respectively. These points locate at L_r and $-L_r$ from the

mid-span of the rigid shaft, respectively. The two-plane balancing system consists of a pair of EADBs that are mounted on the rigid shaft in two separate planes, which locate at L_b and $-L_b+\sigma$ from the mid-span of the shaft, respectively. The imbalance has a radial offset of R_i, and has an axial offset of x_i from the mid-span of the shaft. σ and x_i are all small quantities, which represent the small manufacturing and assembling errors. Each EADB contains two balancer balls of mass m_b, which can freely move through a viscous fluid. The balancer balls are at a fixed distance R_b from the shaft spin center. The position of the ith ball is specified by the corresponding EADB spin center displacement and the relative displacement of the ball in its body attached frame.

To model the rigid shaft/four mass dual EADB system, we need to present the position and the orientation of the rigid shaft. First of all, let distinguish two coordinate transformations illustrated in Figure 47. Transformation I depicts that the shaft axis rotates from fixed-frame $\{\mathbf{n}\} = \{\mathbf{n}_1, \mathbf{n}_2, \mathbf{n}_3\}$ to an intermediate frame $\{\mathbf{a}\} = \{\mathbf{a}_1, \mathbf{a}_2, \mathbf{a}_3\}$, and followed by the shaft rigid body rotation to a body-fixed frame $\{\mathbf{b}\} = \{\mathbf{b}_1, \mathbf{b}_2, \mathbf{b}_3\}$. Transformation II depicts that the shaft axis rotates from fixed-frame $\{\mathbf{n}\} = \{\mathbf{n}_1, \mathbf{n}_2, \mathbf{n}_3\}$ to a rotating frame $\{\mathbf{a}\} = \{\mathbf{a}_1, \mathbf{a}_2, \mathbf{a}_3\}$, and followed by the shaft arbitrary tilting rotation to a body-fixed frame $\{\mathbf{b}\} = \{\mathbf{b}_1, \mathbf{b}_2, \mathbf{b}_3\}$. It is worth to note that for symmetric rotor, using both

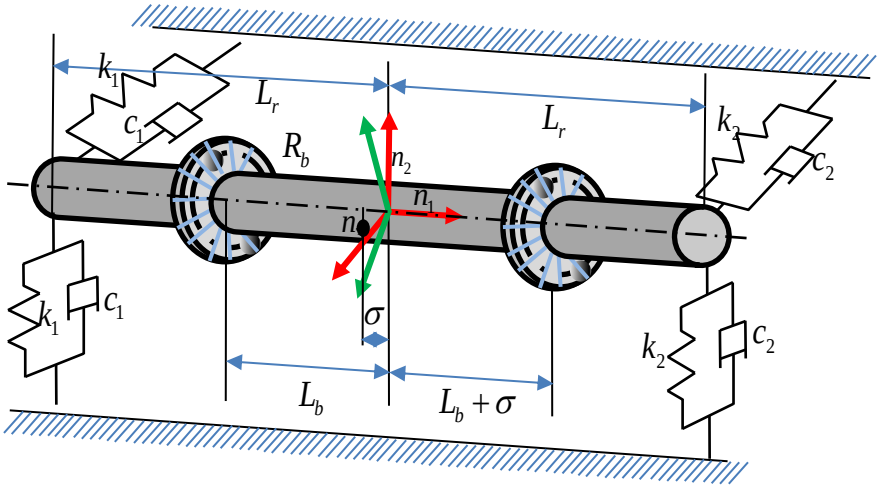
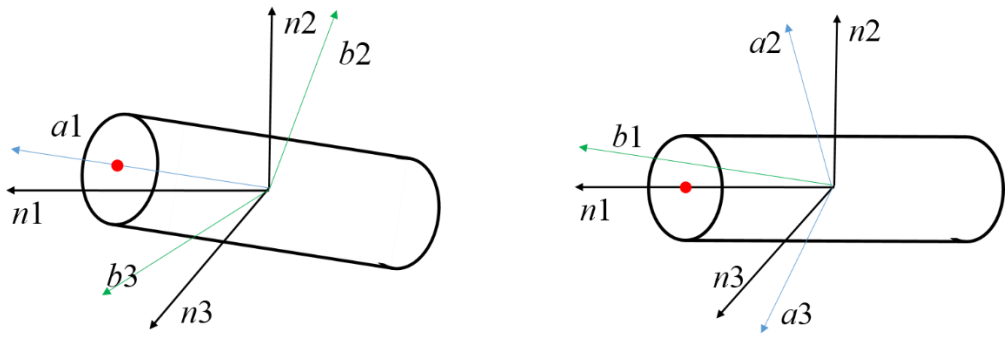


Figure 46. The rigid shaft rotor/four mass dual EADB system



(a) Transformation I (b)Transformation II

Figure 47. Two coordinate transformations to represent the rigid shaft motion

of the transformations can obtain the same equations-of-motion after derivation of the Lagrangian. However, we choose transformation II to generate the autonomous equations-of-motion since the rigid shaft /four mass dual EADB system has asymmetric properties due to the potential asymmetric movements of four masses.

A set of system parameters is shown in Table 12 as an example. The following numerical simulations and analysis are all based on parameters listed in Table 12 unless noted otherwise.

1. Rotation matrices

To facilitate analysis, the equations-of-motion for the rigid shaft/ EADB system are derived in a set of rotating coordinates, $\{\mathbf{a}\} = \{\mathbf{a_1}, \mathbf{a_2}, \mathbf{a_3}\}$, which rotates along $\mathbf{n_1}$ axis by an angle $\phi(t)$, from the fixed coordinates $\{\mathbf{n}\} = \{\mathbf{n_1}, \mathbf{n_2}, \mathbf{n_3}\}$. The shaft is assumed to be driven with a constant angular speed, Ω. Hence $\phi(t) = \Omega t$. The transformation matrix $\mathbf{T_{na}}$ transforms $[\mathbf{n}]$ to $[\mathbf{a}]$ as follows,

$$\begin{bmatrix} \mathbf{a}_1 \\ \mathbf{a}_2 \\ \mathbf{a}_3 \end{bmatrix} = \mathbf{T}_{\mathbf{na}} \begin{bmatrix} \mathbf{n}_1 \\ \mathbf{n}_2 \\ \mathbf{n}_3 \end{bmatrix} \tag{7-1}$$

Table 12. Physical parameters for the rigid shaft/ four mass duel EADB system

Parameter	Value	Units
Rotor radius R_d	0.1	m
Rotor mass m_R	252.8982	kg
Rotor polar inertia I_p	1.2645	kg-m^2
Rotor transverse inertia I_t	21.7071	kg-m^2
Imbalance quatity m_eR_e	0.0518	kg-m
Bearing support stiffness k	1×10^7	N-m
Bearing support damping c_1, c_2	3563.5	N-m-s
ADB track radius R_b	0.12	m
balancer ball m_b	0.2698	kg
balancer ball -fluid damping c_b	2.3373	N-m-s

Where $\mathbf{T_{na}} = \begin{bmatrix} 1 & 0 & 0 \\ 0 & \cos(\phi) & \sin(\phi) \\ 0 & -\sin(\phi) & \cos(\phi) \end{bmatrix}$. The transformation matrix$\mathbf{T_{ab}}$ transforms [**a**] to [**b**] as follows,

$$\begin{bmatrix} \mathbf{b}_1 \\ \mathbf{b}_2 \\ \mathbf{b}_3 \end{bmatrix} = \mathbf{T_{ab}} \begin{bmatrix} \mathbf{a}_1 \\ \mathbf{a}_2 \\ \mathbf{a}_3 \end{bmatrix} \tag{7-2}$$

Where $\mathbf{T_{ab}} = \dfrac{\mathrm{R}_2\mathrm{R}_3 + \mathrm{R}_3\mathrm{R}_2}{2}$, $\mathrm{R}_2 = \begin{bmatrix} \cos(\phi_2) & 0 & -\sin(\phi_2) \\ 0 & 1 & 0 \\ \sin(\phi_2) & 0 & \cos(\phi_2) \end{bmatrix}$, $\mathrm{R}_3 = \begin{bmatrix} \cos(\phi_3) & \sin(\phi_3) & 0 \\ -\sin(\phi_3) & \cos(\phi_3) & 0 \\ 0 & 0 & 1 \end{bmatrix}$.

Assuming $\phi_3 = v_p(t), \phi_2 = -w_p(t)$ and keeping up to second order terms in (7-2), we can obtain (7-3) as follows,

$$\mathbf{T_{ab}} = \begin{bmatrix} 1 - \dfrac{{v_p}^2(t)}{2} - \dfrac{{w_p}^2(t)}{2} & v_p(t) & w_p(t) \\ -v_p(t) & 1 - \dfrac{{v_p}^2(t)}{2} & -\dfrac{1}{2}v_p(t)w_p(t) \\ -w_p(t) & -\dfrac{1}{2}v_p(t)w_p(t) & 1 - \dfrac{{w_p}^2(t)}{2} \end{bmatrix} \tag{7-3}$$

By applying all assumptions and calculating $\mathbf{T_{nb}} = \mathbf{T_{ab}} \cdot \mathbf{T_{na}}$, we can obtain Transforamtion matrix $\mathbf{T_{nb}}$ (7-4),

$$\mathbf{T_{nb}} = \begin{bmatrix} 1 - \dfrac{{v_p}^2(t)}{2} - \dfrac{{w_p}^2(t)}{2} & \cos(\Omega t)v_p(t) - \sin(\Omega t)w_p(t) & \sin(\Omega t)v_p(t) + \cos(\Omega t)w_p(t) \\ -v_p(t) & \cos(\Omega t)(1 - \dfrac{{v_p}^2(t)}{2}) + \dfrac{1}{2}\sin(\Omega t)v_p(t)w_p(t) & \sin(\Omega t)(1 - \dfrac{{v_p}^2(t)}{2}) - \dfrac{1}{2}\cos(\Omega t)v_p(t)w_p(t) \\ -w_p(t) & -\sin(\Omega t)(1 - \dfrac{{w_p}^2(t)}{2}) - \dfrac{1}{2}\cos(\Omega t)v_p(t)w_p(t) & \cos(\Omega t)(1 - \dfrac{{w_p}^2(t)}{2}) - \dfrac{1}{2}\sin(\Omega t)v_p(t)w_p(t) \end{bmatrix} \tag{7-4}$$

2. Position vectors and total system kinetic energy

The position vector locating shaft spin center on the neutral axis at position *x* relative to whirling center of the neutral axis at *x* is

$$\mathbf{r}_o = v_r(x,t)\mathbf{a}_2 + w_r(x,t)\mathbf{a}_3\big|_{x=0} \tag{7-5}$$

Where $v_r(x,t) = v(t) + v_p(t)x$ and $w_r(x,t) = w(t) + w_p(t)x$. The position vectors of the bearings can be written as follows,

$$\mathbf{r}_{B1} = v_r(x,t)\mathbf{a}_2 + w_r(x,t)\mathbf{a}_3\big|_{x=-L_r}$$
$$\mathbf{r}_{B2} = v_r(x,t)\mathbf{a}_2 + w_r(x,t)\mathbf{a}_3\big|_{x=L_r} \quad (7\text{-}6)$$

Where L_r is the half length of the shaft rotor.

The position vector, $\mathbf{r}_{bi}$, (i=1, 2, 3, 4) of the ith balancer ball can be written as,

$$\mathbf{r}_{ob1} = v_r(L_b,t)\mathbf{a}_2 + w_r(L_b,t)\mathbf{a}_3 + R_b(\cos(\phi_{b1})\mathbf{b}_2 + \sin(\phi_{b1})\mathbf{b}_3) \quad (7\text{-}7)$$

$$\mathbf{r}_{ob2} = v_r(L_b,t)\mathbf{a}_2 + w_r(L_b,t)\mathbf{a}_3 + R_b(\cos(\phi_{b2})\mathbf{b}_2 + \sin(\phi_{b2})\mathbf{b}_3) \quad (7\text{-}8)$$

$$\mathbf{r}_{ob3} = v_r(-L_b+\sigma,t)\mathbf{a}_2 + w_r(-L_b+\sigma,t)\mathbf{a}_3 + R_b(\cos(\phi_{b3})\mathbf{b}_2 + \sin(\phi_{b3})\mathbf{b}_3) \quad (7\text{-}9)$$

$$\mathbf{r}_{ob4} = v_r(-L_b+\sigma,t)\mathbf{a}_2 + w_r(-L_b+\sigma,t)\mathbf{a}_3 + R_b(\cos(\phi_{b4})\mathbf{b}_2 + \sin(\phi_{b4})\mathbf{b}_3) \quad (7\text{-}10)$$

Where L_b is the axial position of the EADB away from the mid-span of the shaft. σ is the axial assembling error. R_b is the torus major radius and ϕ_{bi} is the ith balancer ball's angular positon measured about the $\mathbf{b}_1$ axis in the body attached frame. The position vector, $\mathbf{r}_{oi}$ for the imbalance on the shaft rotor is (7-11).

$$\mathbf{r}_{oi} = v_r(x_i,t)\mathbf{a}_2 + w_r(x_i,t)\mathbf{a}_3 + R_e(\cos(\phi_e)\mathbf{b}_2 + \sin(\phi_e)\mathbf{b}_3) \quad (7\text{-}11)$$

Where x_i is the radial position of the imbalance. ψ is angular position of the imbalance measured about the $\mathbf{b}_1$ axis in the body attached frame {**b**}.

The total system kinetic energy T consists of the shaft kinetic energy T_s, the balancer ball kinetic energy T_{ADB}, and the shunt circuit magnetic co-energy W_m^* .

$$T = T_s + T_{ADB} + W_m^* \quad (7\text{-}12)$$

$$T_s = \frac{m_R}{2}(\dot{\mathbf{r}}_o \cdot \dot{\mathbf{r}}_o) + \frac{m_e}{2}(\dot{\mathbf{r}}_{oi} \cdot \dot{\mathbf{r}}_{oi}) + \frac{1}{2}(J_p{\omega_{b1}}^2 + J_t{\omega_{b2}}^2 + J_t{\omega_{b3}}^2) \quad (7\text{-}12a)$$

$$T_{ADB} = \frac{m_b}{2}\sum_{i=1}^{4}(\dot{\mathbf{r}}_{obi}) \cdot (\dot{\mathbf{r}}_{obi}) \quad (7\text{-}12b)$$

$$W_m^* = \frac{1}{2}\sum_{i=1}^{4} L_i(\dot{q}_{Li})^2 \quad (7\text{-}12c)$$

Where $(\cdot) = \partial/\partial t$, m_R, m_e and m_b are the mass of the rotor, the imbalance and the balancer ball, respectively. J_p is the rotor polar inertia, J_t is the rotor transverse inertia, L_i is the self-inductance for the ith shunt circuit, which is a toroid inductor interacted with ith balancer

ball. q_{Li} is the electric charge variable on the L_i. ω_{b1}, $\omega_{b2,}$ ω_{b3} are angular velocity vectors of body attached frame as shown in (7-12d),

$$\begin{aligned} \omega_{b1} &= \Omega - \frac{1}{2}\Omega(v_p{}^2 + w_p{}^2) + \frac{1}{2}w_p\dot{v}_p - \frac{1}{2}v_p\dot{w}_p \\ \omega_{b2} &= -\dot{w}_p - v_p\Omega \\ \omega_{b3} &= \dot{v}_p - w_p\Omega \end{aligned} \tag{7-12d}$$

The angular velocity elecments of the body attached frame can be obtained by calculating $\boldsymbol{\omega}_{\mathbf{b}} = \mathbf{T}_{\mathbf{nb}} \cdot \dot{\mathbf{T}}_{\mathbf{bn}}$, and then the ω_{b1}, $\omega_{b2,}$ ω_{b3} can be obtained as shown in (7-12e).

$$\boldsymbol{\omega}_{\mathbf{b}} = \begin{bmatrix} 0 & -\omega_{b3} & \omega_{b2} \\ \omega_{b3} & 0 & -\omega_{b1} \\ -\omega_{b2} & \omega_{b1} & 0 \end{bmatrix} \tag{7-12e}$$

3. Total system potential energy

The total system potential energy V includes the shaft strain energy V_s, the electrical energy W_e and the transducer co-energy W_t as follows,

$$V = V_s + W_e + W_t \tag{7-13}$$

With

$$V_s = \frac{1}{2}k_1(\mathbf{r}_{B1} \cdot \mathbf{r}_{B1}) + \frac{1}{2}k_2(\mathbf{r}_{B2} \cdot \mathbf{r}_{B2}) \tag{7-13a}$$

$$W_e = \frac{1}{2}\sum_{i=1}^{4}\frac{1}{C_i}(q_{Ci})^2 \tag{7-13b}$$

$$W_t = \theta_e R_b \sum_{i=1}^{4}\phi_{bi}(\dot{q}_{Li} + \dot{q}_{Ci}) \tag{7-13c}$$

Where k_1 and k_2 are the bearing stiffness in two directions, C_i is the capacitance of the ith shunt circuit, q_{Ci} is the electric charge on C_i. θ_e is the electromagnetic coupling coefficient defined in Eq. (2-4) as $\theta_e = B\, l_{couple}$, where B is the magnetic flux density. According to Eq. (2-3) we know that $l_{couple} = 2\pi nr$ is the length of the coils coupled with the magnetic balancer ball.

3. Total system dissipation

To account for the effect of the mechanical and the electrical damping on the system, we define Rayleigh dissipation functions of the system as follows,

$$D=\frac{1}{2}c_1(\dot{\mathbf{r}}_{B1}\cdot\dot{\mathbf{r}}_{B1})+\frac{1}{2}c_2(\dot{\mathbf{r}}_{B2}\cdot\dot{\mathbf{r}}_{B2})+\frac{1}{2}c_bR_b\sum_{i=1}^{4}(\dot{\phi}_{bi})^2+\frac{1}{2}\sum_{i=1}^{4}(R_{Ci}+R_{Li})(\dot{q}_{Li}+\dot{q}_{Ci})^2 \qquad (7\text{-}14)$$

Where c_1 and c_2 are the damping coefficients for the two bearings. c_b is the viscous fluid damping coefficient. R_{Ci} and R_{Li} are the internal resistances of coils and of the load resistance in the ith shunt circuit, respectively.

4. System equations-of-motion

The system equations-of-motion are then obtained via Lagrange's method as,

$$\frac{\mathrm{d}}{\mathrm{d}t}\left(\frac{\partial(T-V)}{\partial\dot{\mathbf{q}}}\right)-\frac{\partial(T-V)}{\partial\mathbf{q}}+\frac{\partial D}{\partial\dot{\mathbf{q}}}=0 \qquad (7\text{-}15)$$

With $\mathbf{q}(t)=[v(t),w(t),v_p(t),w_p(t),\phi_{b1}(t),\phi_{b2}(t),\phi_{b3}(t),\phi_{b4}(t),\ldots$
$q_{C1}(t),q_{L1}(t),q_{C2}(t),q_{L2}(t),q_{C3}(t),q_{L3}(t),q_{C4}(t),q_{L4}(t)]$.

The system equations-of-motion are given as,

$$\mathbf{M_{RS}}(\phi_{bi},v_p,w_p)\ddot{\mathbf{q}}+\mathbf{C_{RS}}(\phi_{bi},\dot{\phi}_{bi},v_p,w_p)\dot{\mathbf{q}}+\mathbf{K_{RS}}(\phi_{bi})\mathbf{q}=\mathbf{F_{RS}}(\phi_{bi},\dot{\phi}_{bi}) \qquad (7\text{-}16)$$

Where the overall system inertia, damping, and stiffness matrices are $\mathbf{M_{RS}}$, $\mathbf{C_{RS}}$ and $\mathbf{K_{RS}}$, respectively. The force vector is $\mathbf{F_{RS}}$. All matrices are given in A6.1.

The resulting equations-of-motion for the $i$the shunt circuit in (7-16) are not independent. For simplicity, we can rearrange them in terms of q_{Ci} as follows,

$$-L_i\ddot{q}_{Ci}-\frac{L_i}{(R_{Ci}+R_{Li})C_i}\dot{q}_{Ci}-\frac{1}{C_i}q_{Ci}+\frac{L_i\theta_eR_b}{R_{Ci}+R_{Li}}\ddot{\phi}_{bi}=0 \text{ for } i=1,2,3,4 \qquad (7\text{-}16a)$$

The resulting equations-of-motion for the ith balancer ball is given as

$$\begin{aligned}&m_bR_b{}^2\ddot{\phi}_{bi}+c_bR_b{}^2\dot{\phi}_{bi}-m_bR_b\ddot{v}\sin(\phi_{bi}+\phi(t))+\\&m_bR_b\ddot{w}\cos(\phi_{bi}+\phi(t))+\theta_eR_b(\dot{q}_{Ci}+\dot{q}_{Li})=0\end{aligned} \text{ for } i=1,2,3,4 \qquad (7\text{-}16b)$$

With

$$\dot{q}_{Li}=\frac{\theta_eR_b}{R_{Ci}+R_{Li}}\dot{\phi}_{bi}-\dot{q}_{Ci}-\frac{1}{(R_{Ci}+R_{Li})C_i}q_{Ci} \qquad (7\text{-}16c)$$

(7-16c) can be obtained from the rearrangement of the equations-of-motion.

After above rearrangements, the resulting independent nonlinear equations-of-motion for the rigid shaft/four mass dual EADB system are,

$$\mathbf{M}(\phi_{bi},v_p,w_p)\ddot{\mathbf{q}}_{new}+\mathbf{C}(\phi_{bi},\dot{\phi}_{bi},v_p,w_p)\dot{\mathbf{q}}_{new}+\mathbf{K}(\phi_{bi})\mathbf{q}_{new}=\mathbf{F}(\phi_{bi},\dot{\phi}_{bi}) \qquad (7\text{-}17)$$

Where

$$\mathbf{q}_{new}(t) = [v(t), w(t), v_p(t), w_p(t), \phi_{b1}(t), \phi_{b2}(t), \phi_{b3}(t), \phi_{b4}(t), q_{C1}(t), q_{C2}(t), q_{C3}(t), q_{C4}(t)] .$$

Where the overall system inertia, damping, and stiffness matrices are **M**, **C** and **K**, respectively. The force vector is **F**. All matrices are given in A6.2.

5. Dimensionless system equations-of-motion

To facilitate the subsequent analysis, we substitute $\phi(t) = \Omega t$ into the equations-of-motion, and then we assume a same set of parameters in different circuits as follows, $R_{Ci} = R_C$, $R_{Li} = R_L$, $R = R_C + R_L$, $C_i = C$, $L_i = L$, $c_i = c$, $k_i = k$. Furthermore, the following dimensionless variables are introduced,

$$\begin{aligned}
&x = \frac{v}{R_b}, y = \frac{w}{R_b}, \omega_n = \sqrt{\frac{2k}{m_R + 4m_b}}, \tau = \omega_n t, \\
&\varsigma = \frac{c}{(m_R + 4m_b)\omega_n}, \varsigma_b = \frac{c_b}{(m_R + 4m_b)\omega_n}, \mu = \frac{m_b}{m_R + 4m_b}, \\
&\mu_i = \frac{m_e}{m_R + 4m_b}, J_t = \frac{I_t}{(m_R + 4m_b)R_b^2}, J_p = \frac{I_p}{(m_R + 4m_b)R_b^2}, \\
&R_{rL} = \frac{L_r}{R_b}, R_{ir} = \frac{R_e}{R_b}, R_{bL} = \frac{L_b}{R_b}, \bar{\Omega} = \frac{\Omega}{\omega_{n1}}, R_{ix} = \frac{x_e}{R_b}, \\
&\varsigma_e = \frac{\theta_e^2}{(m_R + 4m_b)R\omega_n}, R_n = \frac{1}{CR\omega_n}, C_n = \frac{1}{CL\omega_n^2}, R_{bx} = \frac{\sigma}{R_b}
\end{aligned} \tag{7-18}$$

where x, y are the rotor lateral deflections, ς, ς_b, and ς_e are the damping ratio of the shaft rotor and the balancer ball, and the coupling coefficient between the circuit and balancer ball. ω_n is the first critical speed of the shaft, τ is the dimensionless time, μ is the balancer ball mass ratio, μ_i, R_{ir}, R_{ix} are the imbalance mass ratio, the imbalance radial length ratio, the imbalance axial length ration, respectively. $\bar{\Omega}$ is the dimensionless rotor speed, R_n and C_n are the dimensionless resistance and capacitance. θ_e is the transducer constant, J_t is the shaft dimensionless transverse motion of inertia, J_p is the shaft dimensionless polar motion of inertia. R_{rL}, R_{bL}, R_{bx} are the shaft length ratio, the ADB or the EADB assembling length ratio, and the ADB or the EADB axial assembling error ratio.

To analyze the effect of the radial assembling error R_{br} of the ADB or the EADB by introducing $R_{br} = \delta / Rb$, we can replace the deflections of the ADB or the EADB in (7-

5) to be the deflections of the shaft as descriped in section 2.5.2, and can obtain the shaft neutral axis has a radial assembling error of δ in $\boldsymbol{a}_2$ and $\boldsymbol{a}_3$ axes in (7-6) as shown in Eq. (2-48). Substituting (7-18) into (7-17) yields the dimensionless equations-of-motion as follows,

$$\mathbf{M}_n(\phi_{bi}, x_p, y_p)\mathbf{q}''_{new} + \mathbf{C}_n(\phi_{bi}, \phi'_{bi}, x_p, y_p)\mathbf{q}'_{new} + \mathbf{K}_n(\phi_{bi})\mathbf{q}_{new} = \mathbf{F}_n(\phi_{bi}, \phi'_{bi}) \quad (7\text{-}19)$$

With dimensionless general coordinate as follows,

$$\mathbf{q}_{new}(\tau) = [x(\tau), y(\tau), x_p(\tau), y_p(\tau), \phi_{b1}(\tau), \phi_{b2}(\tau), \phi_{b3}(\tau), \phi_{b4}(\tau), q_1(\tau), q_2(\tau), q_3(\tau), q_4(\tau)]$$

Where $(') = \partial / \partial \tau$ and the overall dimensionless system matrices are $\mathbf{M_n}$, $\mathbf{C_n}$ and $\mathbf{K_n}$, respectively. The force vector is $\mathbf{F_n}$. All matrices are given in A6.3.

There are two major differences between the planar rotor modeling and the shaft rotor modeling. On one hand, position vectors for the shaft deflections in Eq. (7-5) includes the axial position vector x of the shaft, which should be distinguished from the dimensionless shaft lateral deflection used in Eq. (7-18). On the other hand, to represent the tilting deflections fo the shaft rotor, transformation matrix $\mathbf{T_{ab}}$ is introduced to transfer the rotating frame to the body attached frame. It is worth to mention that the modeling in this section also considered the effect of the radial assembling error R_{br} and the effect of the axial assembling error R_{bx}.

7.1.2 Equilibrium points (EPs)

When applying the EADB on the rigid shaft with tilting motion, the perfect-balancing EP is desirable in our rigid shaft/EADB system. Considering the axial assembling error R_{bx} of the EADB and the radial assembling error R_{br}, the perfect-balancing EP of the rigid shaft/EADB system can be solved analytically. The perfecting-balancing EP without the effect R_{bx} and R_{br} was study in Ref.[50]. Considering the effect of R_{bx} and R_{br}, we use a similar approach. Therefore, this section will analyze the solution by considering the difference.

1. Perfect-balancing EP

As for the rigid shaft/ADB system with its axial assembling error, when it reaches the perfect-balancing EP, there are neither lateral deflections nor tilting deflections for the

shaft rotor, where r_0=0, so x_s=0, y_s=0 [50]. And the balancer balls in two races position themselves in synchronized positions to compensate the effect of the imbalance. As for the rigid shaft/EADB system, perfect-balancing EP also indicates the same thing. The balancer balls have zero accelerations thus no electric charges in the shunt circuits when there is no power sources due to the value of the accelerations.

EPs can be obtained by setting all variables' time derivatives in the equations-of-motion (7-19) to zero. Moreover, if the deflections (x, y, x_p, y_p) = **0**, we can obtain the following algebraic equations for the perfect-balancing EP as follows,

$$\begin{aligned}
&\cos(\phi_{b1})+\cos(\phi_{b2})+\cos(\phi_{b3})+\cos(\phi_{b4}) = p_1\\
&\sin(\phi_{b1})+\sin(\phi_{b2})+\sin(\phi_{b3})+\sin(\phi_{b4}) = p_2\\
&a(\cos(\phi_{b1})+\cos(\phi_{b2}))-b(\cos(\phi_{b3})+\cos(\phi_{b4})) = p_3\\
&a(\sin(\phi_{b1})+\sin(\phi_{b2}))-b(\sin(\phi_{b3})+\sin(\phi_{b4})) = p_4
\end{aligned} \tag{7-20}$$

Where

$$\begin{aligned}
&p_1 = -\frac{Rir\,\mu_i}{\mu}\cos(\phi_e),\ p_2 = -\frac{Rir\,\mu_i}{\mu}\sin(\phi_e)\\
&p_3 = -Rir\ Rix\ \mu_i\cos(\phi_e),\ p_4 = -Rir\ Rix\ \mu_i\sin(\phi_e),\\
&a = (RbL)\mu, b = (RbL - Rbx)\mu
\end{aligned} \tag{7-20a}$$

These four algebraic equations (7-20) describe the force balance equations and momentum balance equations for the shaft rotor/EADB system, while the shunt circuit equations vanish. By rewriting (7-20) in terms of the average and the differential of balancer balls' angular displacements, the Eq. (7-20) is identically transformed to (7-21).

$$\begin{aligned}
\cos(\phi_{12}^{+})\cos(\phi_{12}^{-}) &= \frac{bp_1 + p_3}{2(a+b)}\\
\sin(\phi_{12}^{+})\cos(\phi_{12}^{-}) &= \frac{bp_2 + p_4}{2(a+b)}\\
\cos(\phi_{34}^{+})\cos(\phi_{34}^{-}) &= \frac{ap_1 - p_3}{2(a+b)}\\
\sin(\phi_{34}^{+})\cos(\phi_{12}^{-}) &= \frac{ap_2 - p_4}{2(a+b)}
\end{aligned} \tag{7-21}$$

Where

$$\phi_{12}^{+}=\frac{\phi_{b1}+\phi_{b2}}{2},\phi_{12}^{-}=\frac{\phi_{b1}-\phi_{b2}}{2},\phi_{34}^{+}=\frac{\phi_{b3}+\phi_{b4}}{2},\phi_{34}^{-}=\frac{\phi_{b3}-\phi_{b4}}{2}$$

As a physical constraint, the differential displacements of two balancer balls in one race need to be less than π. Therefore, $0\le\phi_{12}^{-},\phi_{34}^{-}\le\pi/2$. We can solve (7-21) as follows,

$$\begin{aligned}
\phi_{12}^{+}&=\arctan\left(\frac{bp_2+p_4}{bp_1+p_3}\right)+\begin{cases}0 \text{ if } bp_1+p_3\ge 0\\ \pi \text{ if } bp_1+p_3<0\end{cases}\\
\phi_{12}^{-}&=\arccos\left(\frac{1}{2(a+b)}\sqrt{(bp_1+p_3)^2+(bp_2+p_4)^2}\right)\\
\phi_{34}^{+}&=\arctan\left(\frac{ap_2-p_4}{ap_1-p_3}\right)+\begin{cases}0 \text{ if } ap_1-p_3\ge 0\\ \pi \text{ if } ap_1-p_3<0\end{cases}\\
\phi_{34}^{-}&=\arccos\left(\frac{1}{2(a+b)}\sqrt{(ap_1-p_3)^2+(ap_2-p_4)^2}\right)\\
\phi_{b1}&=\phi_{12}^{+}+\phi_{12}^{-},\phi_{b2}=\phi_{12}^{+}-\phi_{12}^{-},\phi_{b3}=\phi_{34}^{+}+\phi_{34}^{-},\phi_{b4}=\phi_{34}^{+}-\phi_{34}^{-}
\end{aligned}\tag{7-22}$$

This solution exists provided that the arguments for both the arccoses have modulus less than one, which ensures that the balls have enough mass to counteract the imbalance of the system. In the following, we refer to (7-22) as the perfect-balancing EP.

2. Balancer balls coincident in each race

Reducing the first and the second derivatives in (7-19), we can observe the four algebraic equations for the shaft rotor as shown in (7-23), and can also observe the four algebraic equations for the balancer balls as shown in (7-24).

$$\begin{bmatrix} A & B & C & 0\\ -B & A & 0 & C\\ C & 0 & F-\frac{1}{2}D\sum_{i=1}^{4}\cos(2\phi_{bi}) & G-\frac{1}{2}D\sum_{i=1}^{4}\sin(2\phi_{bi})\\ 0 & C & -G-\frac{1}{2}D\sum_{i=1}^{4}\sin(2\phi_{bi}) & F+\frac{1}{2}D\sum_{i=1}^{4}\cos(2\phi_{bi}) \end{bmatrix}\begin{bmatrix} x\\ y\\ x_p\\ y_p\end{bmatrix}=\begin{bmatrix} D\sum_{i=1}^{4}\cos(\phi_{bi})+E\cos(\phi_e)\\ D\sum_{i=1}^{4}\sin(\phi_{bi})+E\sin(\phi_e)\\ a\sum_{i=1}^{2}\cos(2\phi_{bi})+b\sum_{i=3}^{4}\cos(2\phi_{bi})+c\cdot\cos(\phi_e)\\ a\sum_{i=1}^{2}\sin(2\phi_{bi})+b\sum_{i=3}^{4}\sin(2\phi_{bi})+c\cdot\sin(\phi_e)\end{bmatrix}\tag{7-23}$$

Where

$$\begin{aligned}
&A=1-\bar{\Omega}^2,B=-2\varsigma\bar{\Omega},C=-2R_{bx}\mu\bar{\Omega}^2,D=-\mu\bar{\Omega}^2,\\
&E=-R_{ir}\mu_i\bar{\Omega}^2,F=R_{rL}{}^2+(J_p-J_t)\bar{\Omega}^2+(2-4R_{bL}{}^2+4R_{bL}R_{bx}-2R_{bx}{}^2)\mu\bar{\Omega}^2,\\
&G=-2R_{rL}{}^2\varsigma\bar{\Omega},a=-R_{bL}\mu\bar{\Omega}^2,b=(R_{bL}-R_{bx})\mu\bar{\Omega}^2,c=-R_{ir}R_{ix}\mu_i\bar{\Omega}^2
\end{aligned}$$

$$\begin{aligned}(Dy + ay_p)\cos(\phi_{bi}) &= (Dx + ax_p)\sin(\phi_{bi}), i = 1,2\\ (Dy + by_p)\cos(\phi_{bi}) &= (Dx + bx_p)\sin(\phi_{bi}), i = 3,4\end{aligned} \tag{7-24}$$

The steady-state of the shaft rotor lateral defletions and tilting deflections (x, y, x_p, y_p) can be represented by the steady-state balls' angular positions ϕ_{bi} (i=1, 2, 3, 4). By taking the inverse of the LHS matrix multiplied by the RHS column vector in (7-23), we can obtain (x, y, x_p, y_p) as functions of ϕ_{bi}. By assuming coincident condition as follows, $\phi_{b1} = \phi_{b2} = \phi_1$ and $\phi_{b3} = \phi_{b4} = \phi_2$, and then substituting $x(\phi_{bi})$, $y(\phi_{bi})$, $x_p(\phi_{bi})$, $y_p(\phi_{bi})$ into (7-24), we can get objective functions, which are the norms of the functions in (7-24a), and then we employ the two-dimensional searching approach or two-dimensional optimization to solve for the coincident steady-state solutions for ϕ_1 and ϕ_2.

$$\begin{aligned}f_i(\phi_1,\phi_2) &= (Dy(\phi_1,\phi_2) + ay_p(\phi_1,\phi_2))\cos(\phi_1) - (Dx(\phi_1,\phi_2) + ax_p(\phi_1,\phi_2))\sin(\phi_1), i = 1,2\\ f_i(\phi_1,\phi_2) &= (Dy(\phi_1,\phi_2) + by_p(\phi_1,\phi_2))\cos(\phi_2) - (Dx(\phi_1,\phi_2) + bx_p(\phi_1,\phi_2))\sin(\phi_2), i = 3,4\end{aligned} \tag{7-24a}$$

3. Other EPs

Other EPs include several senarios. One is that the four balancer balls ocuppy four different angular positions. Another one is that the four balancer balls ocuppy three different angular positions. These EPs can be solved numerically through solving the optimization problems. We will not discus other EPs since they are unstable via the most of our simulations.

7.2 Stability analysis of the perfect-balancing EP

7.2.1 Linearized model

Based on the parameters in Table 12, the dimensionless system parameters are introduced via (7-18) and are presented in Table 13.

In order to identify the stability of the steady-state solutions for the rigid shaft rotor/EADB system, specifically the perfect-balancing EP in this section, we can linear the system (7-19) around the EP [x_s, y_s, x_{ps}, y_{ps}, ϕ_{b1s}, ϕ_{b2s}, ϕ_{b3s}, ϕ_{b4s}, q_{1s}, q_{2s}, q_{3s}, q_{4s}], and can obtain the linearized equations-of-motion as follows.

$$\mathbf{M}_L(\phi_{bis})\mathbf{q}''_\Delta + \mathbf{C}_L(\phi_{bis})\mathbf{q}'_\Delta + \mathbf{K}_L(\phi_{bis}, x_s, y_s, x_{ps}, y_{ps})\mathbf{q}_\Delta = \mathbf{F}_L(\phi_{bis}, x_s, y_s, x_{ps}, y_{ps}) \tag{7-25}$$

Table 13. Dimensionless system parameters for the rigid shaft/four mass dual EADB system used in chapter 7

Parameter	Value
balancer ball mass ratio μ	0.0011
Imbalance ratio $\mu_i R_{ir}$	0.0017
Suspension damping ratio ς	*0.05
ADB fluid damping ratio ς_b	*3.28 $\times 10^{-5}$
Imbalance axial offset R_{ix}	*0.0833
EADB position ratio R_{bL}	*2.5
EADB axial assembling error R_{bx}	*0.0833
Rotor length ratio R_{rL}	4.1667
Rotor transverse motion of inertial J_t	5.9353
Rotor polar motion of inertial J_p	0.3457
Dimensionless rotor speed $\overline{\Omega}$	*0-10
Coupling coefficient ς_e	*2×10^{-6}-1×10^{-3}
Equivalent capacity C_n	*0.01
Equivalent resistance R_n	*0.5 or 0.005
Imbalance phase ϕ_e	$\pi/3$

*Various values used in the analysis

With the perturbed general coordinate as follows.

$$\mathbf{q}_{\Delta}(\tau)=\begin{bmatrix}\Delta x_s(\tau),\Delta y_s(\tau),\Delta x_{ps}(\tau),\Delta y_{ps}(\tau),\ \Delta\phi_{b1s}(\tau),\Delta\phi_{b2s}(\tau),\ldots\\ \Delta\phi_{b3s}(\tau),\ \Delta\phi_{b4s}(\tau),\Delta q_{1s}(\tau),\ \Delta q_{2s}(\tau),\Delta q_{3s}(\tau),\ \Delta q_{3s}(\tau)\end{bmatrix}$$

Where $(')=\partial/\partial\tau$ and the overall dimensionless system matrices are $\mathbf{M}_{\mathrm{L}}$, $\mathbf{C}_{\mathrm{L}}$ and $\mathbf{K}_{\mathrm{L}}$, respectively. The force vector is $\mathbf{F}_{\mathrm{L}}$. All matrices are given in A6.4. For simplicity, we will use [x, y, x_p, y_p, ϕ_{b1}, ϕ_{b2}, ϕ_{b3}, ϕ_{b4}, q_1, q_2, q_3, q_4] instead of [x_s, y_s, x_{ps}, y_{ps}, ϕ_{b1s}, ϕ_{b2s}, ϕ_{b3s}, ϕ_{b4s}, q_{1s}, q_{2s}, q_{3s}, q_{4s}] as steady-state notaions in the following analysis. They should be distinguished from a priory knowledge.

In order to analyze the stability of the perturbed system (7-25), we need to calculate the eigenvalues of its state matrix $\mathbf{A}_{\Delta}$ as shown in (7-26),

$$\mathbf{A}_{\Delta}=\begin{bmatrix}\mathbf{0} & \mathbf{I}\\ -\mathbf{M}_L^{-1}\mathbf{K}_L & -\mathbf{M}_L^{-1}\mathbf{C}_L\end{bmatrix} \tag{7-26}$$

Where $\mathbf{0}$ is a six by six zero matrix, $\mathbf{I}$ is a six by six identity matrix.

The perturbed system (7-25) is guaranteed to be asymptotic stable, if and Only if all the real parts of the eigenvalues $\lambda_{\mathbf{A}_{\Delta}}$ for the state matrix $\mathbf{A}_{\Delta}$ are less than 0,

$$\mathrm{Re}(\lambda_{\mathbf{A}_{\Delta}})<0 \tag{7-27}$$

7.2.2 Parameter study

1. The effect of axial assembling error R_{bx} on the rigid shaft/ADB system

To show the effect R_{bx} can be compensated, we present Figure 48 by analytical analysis, which shows that, when reaching the perfect-balancing EP, the balancer balls' angular positions can change along axial assembling error R_{bx}. When R_{bx} set to 0, 0.8, 1.6, respectively, the four balls' angular positions for the perfect-balancing EP can separate gradually to compensate the effect of R_{bx}.

At first, let's clarify some characteris for the rigid shaft ADB system. The shaft has two critical speeds around 1 and 1.8 respectively. These critical speeds are corresponding to the lateral deflection resonance and tilting deflection resonance. We also know that the perfect-

balancing EP can be stable when the balancer ball mass ratio μ is larger than ¼ of

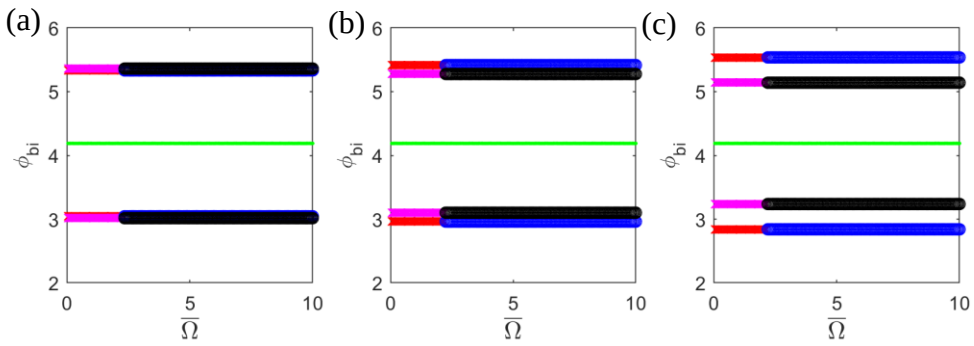


Figure 48. Ball angular position varying with rotor speed under different axial assembling error R_{bx} (a) R_{bx} = 0 (b) R_{bx} = 0.8 (c) R_{bx} = 1.6

the imbalance ratio μ_i. This prerequest needs the total balancer balls can compensate the imbalance. Then to explore the effect of R_{bx} on the stability of the perfect-balancing EP for the rigid shaft/ADB system, we generate five groups of comparisons of the stability plots in different parameter spaces, such as plane ($\overline{\Omega}$, μ), plane ($\overline{\Omega}$, R_{ix}), plane ($\overline{\Omega}$, R_{bL}), plane ($\overline{\Omega}$, ς) and plane ($\overline{\Omega}$, ς_b), showing in Figure 49, Figure 50, Figure 51, Figure 52 and Figure 53, respectively. In each group of comparison, we adopt three different values for R_{bx}. They are typically as follows, (a) R_{bx} = 0 (b) R_{bx} = 0.8 (c) R_{bx} = 1.6, which represent zero error, small error, big error, respectively. It is shown that axial assembling error R_{bx} has a very limited effect on the stability plots. We can observe some interesting phenomenons in Figure 49and Figure 51. Although we are not sure the cause for the narrow stable belt in Figure 49, we have checked the accuracy of the stability plots by simulating the points on (c), ‘A’, ‘B’, ‘C’. As for the unstable belt in Figure 51(c), we also simulated ‘D’ and ‘E’, respectively. The unstable belt shows that when the axial error R_{bx} is similar with shaft axial length R_{bx}, the system perfect-balancing EP is unstable. This is a good phenomenon that can show the analyzed model is reasonal.

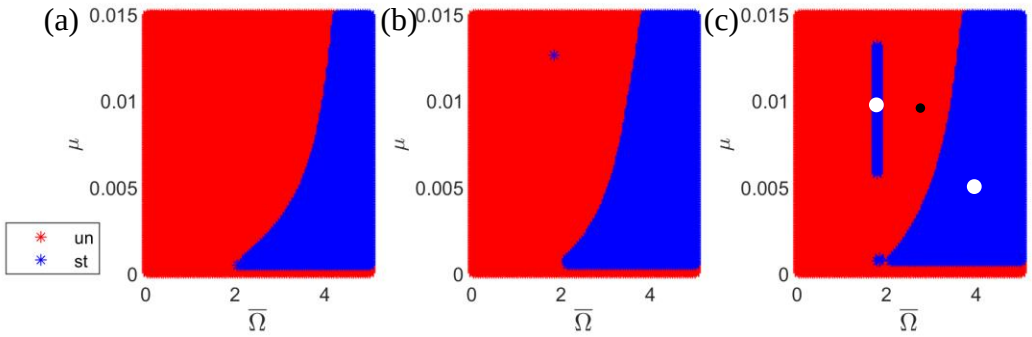


Figure 49. Stability of perfect-balancing EP in ($\bar{\Omega}$, μ) plane showing the effect of different axial assembling error R_{bx} (a) R_{bx} = 0 (b) R_{bx} = 0.8 (c) R_{bx} = 2.1

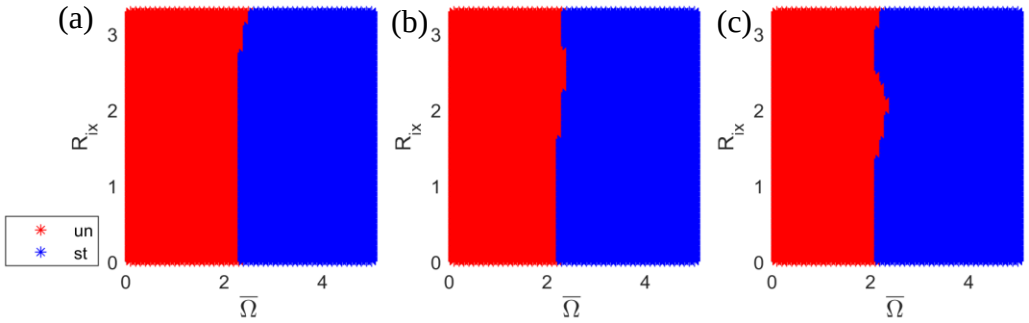


Figure 50. Stability of perfect-balancing EP in ($\bar{\Omega}$, R_{ix}) plane showing the effect of axial assembling error R_{bx} (a) R_{bx} = 0 (b) R_{bx} = 0.8 (c) R_{bx} = 1.6

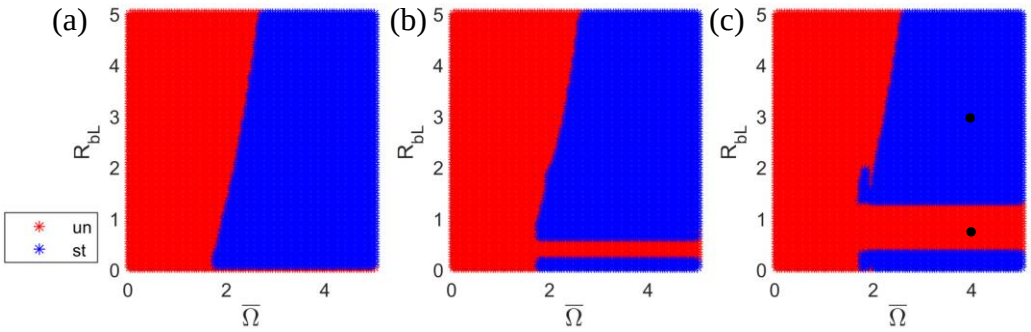


Figure 51. Stability of perfect-balancing EP in ($\overline{\Omega}$, R_{bL}) plane showing the effect of different axial assembling error R_{bx} (a) R_{bx} = 0 (b) R_{bx} = 0.8 (c) R_{bx} = 1.6

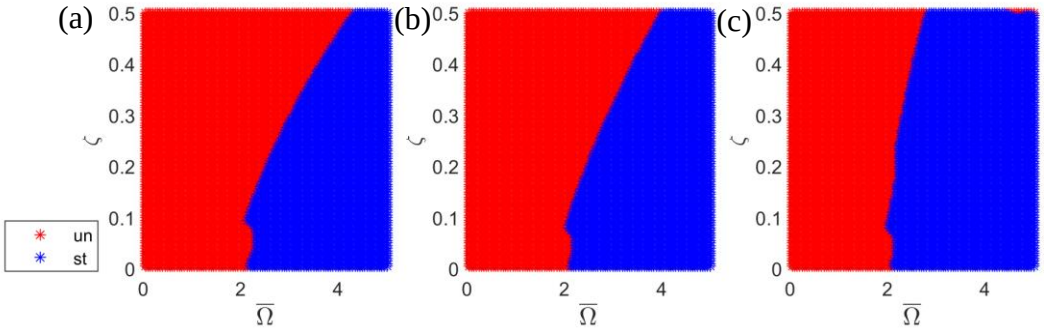


Figure 52. Stability of perfect-balancing EP in ($\overline{\Omega}$, ς) plane showing the effect of different axial assembling error R_{bx} (a) R_{bx} = 0 (b) R_{bx} = 0.8 (c) R_{bx} = 1.6

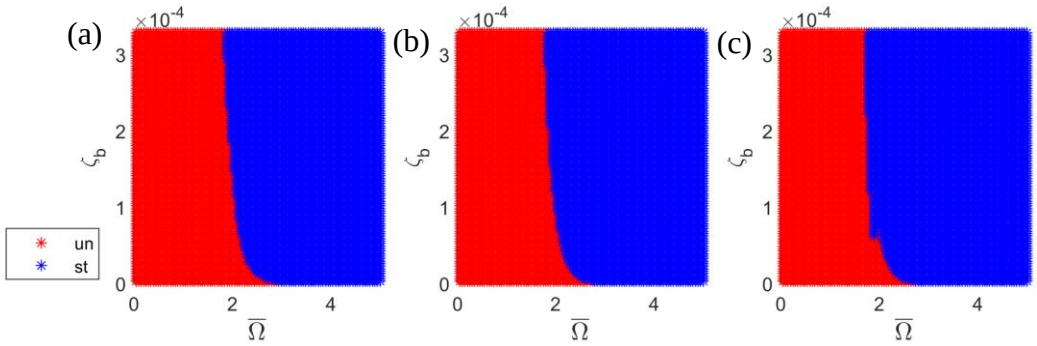


Figure 53. Stability of perfect-balancing EP in ($\bar{\Omega}$, ς_b) plane showing the effect of different axial assembling error R_{bx} (a) R_{bx} = 0 (b) R_{bx} = 0.8 (c) R_{bx} = 1.6

2. The effect of radial assembling error R_{br} on the rigid shaft/ADB system

R_{br} has a big negative effect on the performance of the ADB. As is known from section 2.5.2, a rotor/ADB system with effect of R_{br} only has the half-balanced EP. Different from solving the half-balanced EP for the planar rotor/ADB, the EP for the shaft rotor/ADB can not be solved analytically. Therefore, we use numerical simulations to study the effect of R_{br} on the shaft rotor/ADB system.

In general, radial assembling error R_{br} can occur in dual ADBs. However, we will first explore the effect of R_{br} in one ADB. Therefore, we put R_{br} on one ADB only and simulate the rigid shaft/dual ADB system. In order to better present the time-domain numerical integrations, the reduction coefficient of the lateral deflections α are the reduction coefficient of the tilting deflection β are defined as follows.

$$\alpha = \frac{x_a^{\,2} + y_a^{\,2}}{x_s^{\,2} + y_s^{\,2}}, \beta = \frac{\left(y_p^a\right)^2 + \left(x_p^a\right)^2}{\left(y_p^s\right)^2 + \left(x_p^s\right)^2}, \tag{7-28}$$

Where x_a, y_a and x_s, y_s are the lateral deflections in x and y directions for the shaft/ADBs and only the shaft, respectively. x_p^a, y_p^a and x_p^s, y_p^s are the tilting deflections about x and y directions for the shaft/ADBs and only the shaft, respectively.

Figure 54 and Figure 55 show the time-domain numerical integrations for the shaft/ADBs system and only the shaft system. These two figures have indicated the effect

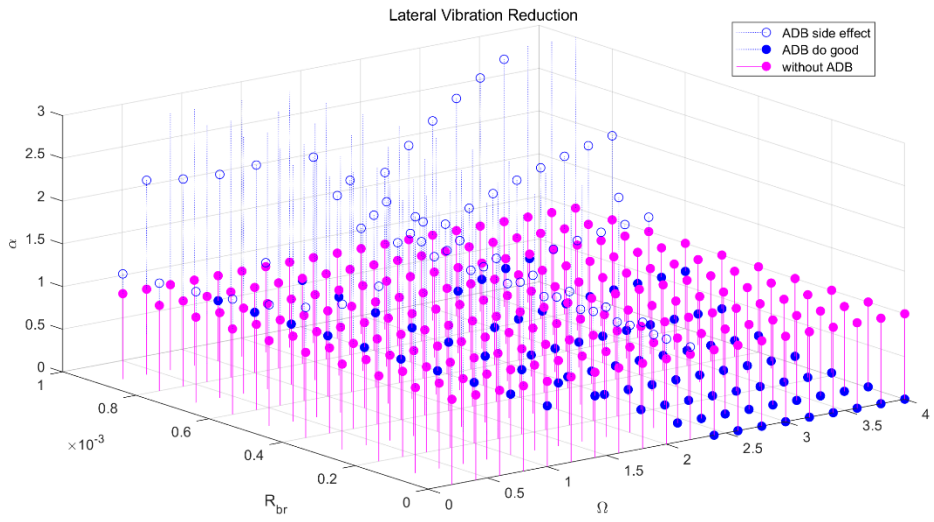


Figure 54. Numerical simulation of the rigid shaft/dual ADB system and the only shaft system in (R_{br}, Ω) plane showing the comparison of the shaft lateral deflections

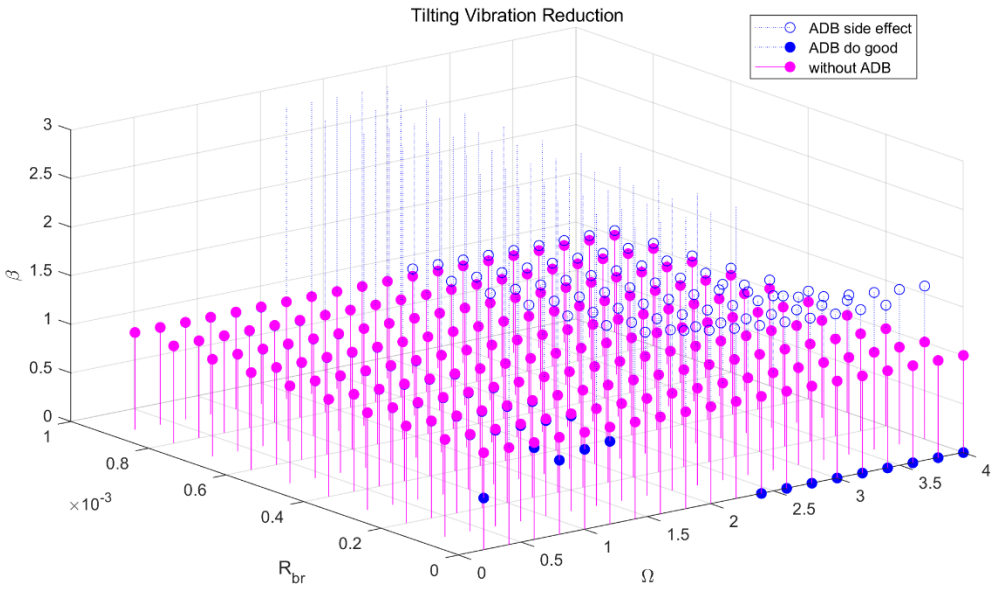


Figure 55. Numerical simulation of the rigid shaft/dual ADB system and the only shaft system in (R_{br}, Ω) plane showing the comparison of the shaft tilting deflections

of R_{br}. Comparing the results of the shaft/ADBs system with that of only the shaft, the hollow blue dots and the solid blue dots represent the aggravation and the reduction of the shaft deflections. The solid red dots are benchmarks which all located at ones showing the shaft deflections without ADB. These red dots can help to show how much the ADB can reduce the shaft deflecitons.

It is shown in Figure 54 that the ADBs can reduce shaft lateral deflections when the rotor speed Ω is larger than 2 and the radial assembling error R_{br} do not exceed 4×10^{-4}. We also notice that the ADBs can aggravate the shaft lateral deflections around the shaft critical speeds. Figure 55 indicates that the ADBs can reduce shaft tilting deflections when only when the radial assembling error R_{br} is small enough approaching zero.

3. The effect of axial assembling error R_{bx} on the rigid shaft/EADB system

In the above parameter analysis, we explored the effect of the axial assembling error and the radial assembling error on the rigid shaft/ADBs, these errors are essential to do the implementation. These factors are firstly examined by this research. We also initiate a study on the effect of the EADB on the rigid shaft, specifically the effect of R_{bx}.We solved the perfect-balancing EP and its corresponding stability for the rigid shaft/dual EADB system.

Then to explore the effect of R_{bx} on the stability of the perfect-balancing EP for the rigid shaft/dual EADB system, we set the electric circuit parameters at some fixed values, such as $R_n = 0.005$, $C_n = 0.01$ and coupling coefficient $\varsigma_e = 0.001$. we generate two groups of comparisons of the stability plots in different parameter spaces, such as plane ($\overline{\Omega}$, μ), and plane ($\overline{\Omega}$, ς_e) showing in Figure 56 and Figure 57, respectively. In each group of comparison, we adopt three different values for R_{bx}. They are typically as follows, (a) $R_{bx} = 0$ (b) $R_{bx} = 0.8$ (c) $R_{bx} = 1.6$, which represent zero error, small error, big error, respectively. It is shown that axial assembling error R_{bx} has a very limited effect on the stability plots.

We checked the stability results by simulation a stable point ‘P1’ and an unstable point ‘P2’ in Figure 56(a). The numerical simulation results are shown in Figure 58 and Figure 59. For a stable perfect-balancing EP, we expect to get no lateral deflections and tilting deflections for the rigid shaft. However, although the tilting deflections are about 1×10^{-6}, which can be neglected, they are still larger than the lateral deflections, which are

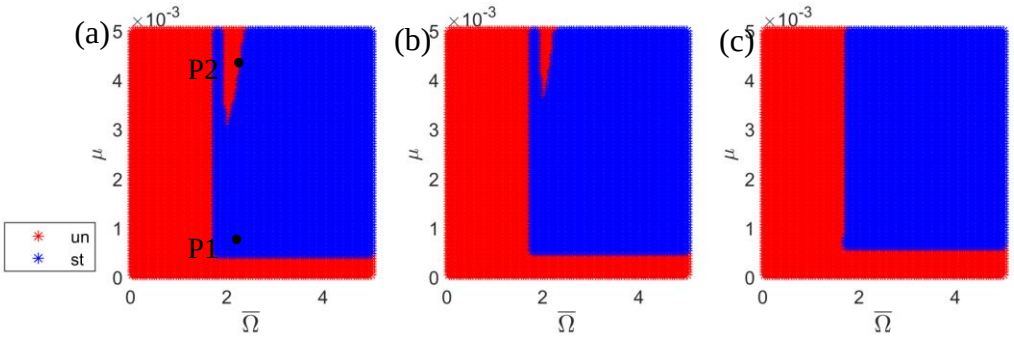


Figure 56. Stability of perfect-balancing EP in ($\bar{\Omega}$, μ) plane for the shaft/EADB system under different R_{bx} (a) R_{bx} = 0 (b) R_{bx} = 0.8 (c) R_{bx} = 1.6

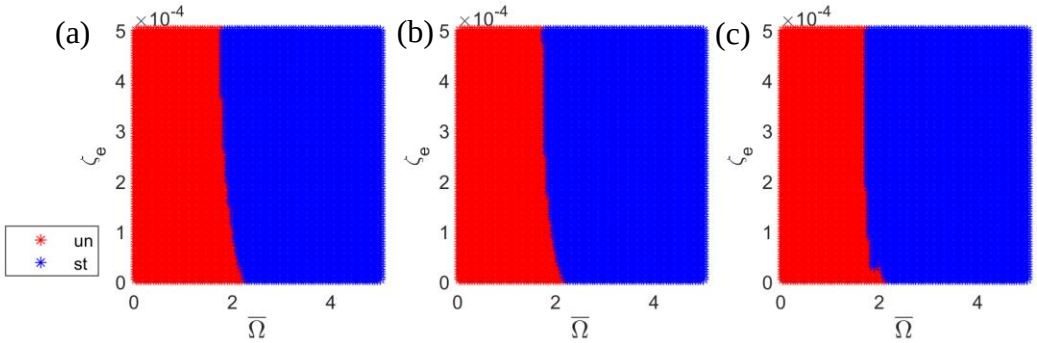


Figure 57. Stability of perfect-balancing EP in ($\bar{\Omega}$, ς_e) plane for the shaft/EADB system under different R_{bx} (a) R_{bx} = 0 (b) R_{bx} = 0.8 (c) R_{bx} = 1.6

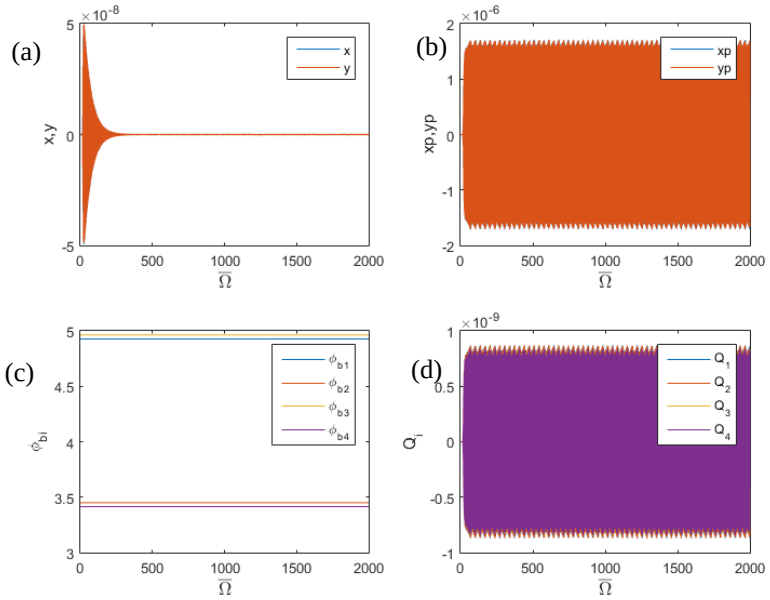


Figure 58. Numerical simulation of the shaft/EADB system under stable point 'P1' showing (a) x,y (b) x_p,y_p (c) ϕ_{bi} (d) Q_i

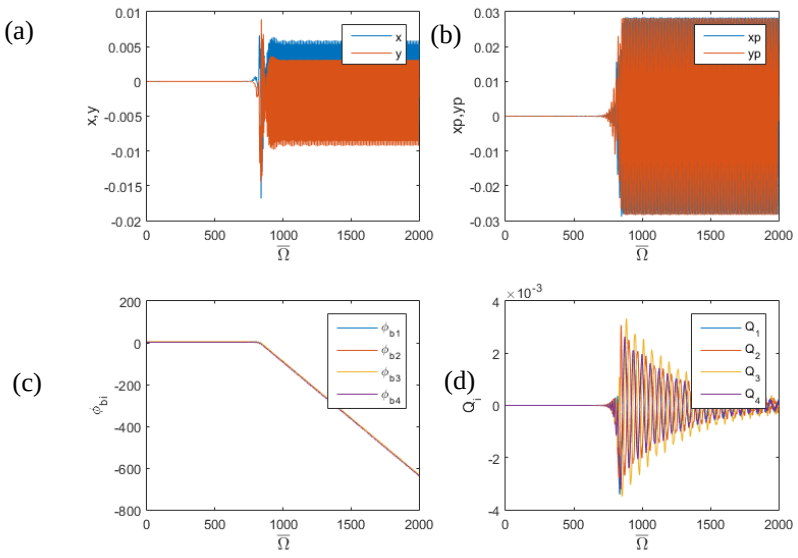


Figure 59. Numerical simulation of the shaft/EADB system under stable point 'P2' showing (a) x, y (b) x_p, y_p (c) ϕ_{bi} (d) Q_i

about 1×10^{-8}. The electric charges are also expected to be zeros. In fact, they ocuppy a very small order of magnitude as 1×10^{-9}. As for the two balanacer balls in the same race locating at a certain axial position on the shaft, their average angular position is approximately out of phase with that of the imbalance locating at another axial position on the shaft. This approximation is because of the tilting motions of the rigid shaft.

As for the unstable perfect-balancing EP "P2", it is shown that the lateral deflections have an order of magnitude about 1×10^{-3}, the tilting deflections have an order of magnitude about 1×10^{-2}. The electric charges have an order of magnitude about 1×10^{-3}. There magnitudes are much larger comparing with the stable point "P1". In the unstable condition, the balancer balls whirl together in the body-fixed frame. When balancer balls reach a steady-state whirling speed, the electric charges oscillate steadily.

4. Coincident EP for the rigid shaft/ADB system under different rotor speeds

To get coincident type of EPs and their corresponding stability as descripted in section 7.1.2, we assume that the two balancer balls in the first race occupy the angular position ϕ_1 and the two balancer balls in the second race occupy another angular position ϕ_2. There is no axial assembling error σ for the system when solving for the coincident EP.

To implement the searching approach to obtain the coincident EP, we set an objective function being a norm of equations (7-24a), and then we conduct the two-dimensional searching in the space of $[\phi_1, \phi_2] \epsilon [0, 2\pi]$. We obtain Figure 60 and Figure 61 depending upon the different rotor speeds. When $\overline{\Omega}$ =0.8, which is smaller than the first shaft critical speed 1, we get six minimal values and only one of them is a stable solution, which is a blue dot shown in Figure 60. This stable solution represents the soluaiton, which the four balancer balls are in-phase with the imbalance occurring below the shaft first critical speed. It is note that other minimal values are symmetric along $\phi_1 = \phi_2$. This symmetric property is reasonable by viewing physically since the two balancer balls in the same race have no difference in the mathematical model. These minimal points are unstable EPs. It shows that when the balancer balls in two race are out-of-phase with each other, and when the balancer balls are out-of-phase with the imbalance, the rigid shaft/ADB system can have unstable EPs, which are consistent with the unstable EPs for the planar rotor/ADB system.

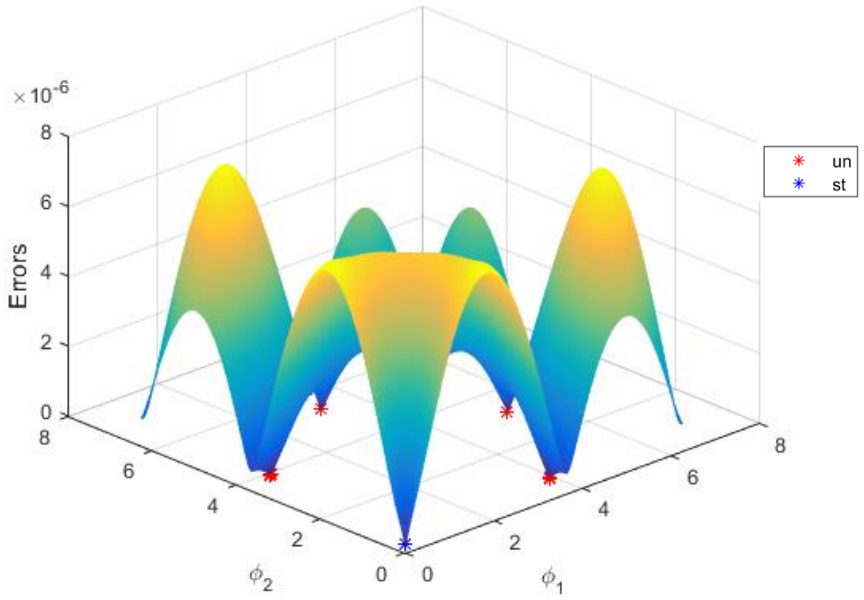


Figure 60. Two-dimensional optimization of the objective function (7-24a) to get coincident EPs and their stability when $\overline{\Omega}$ =0.8

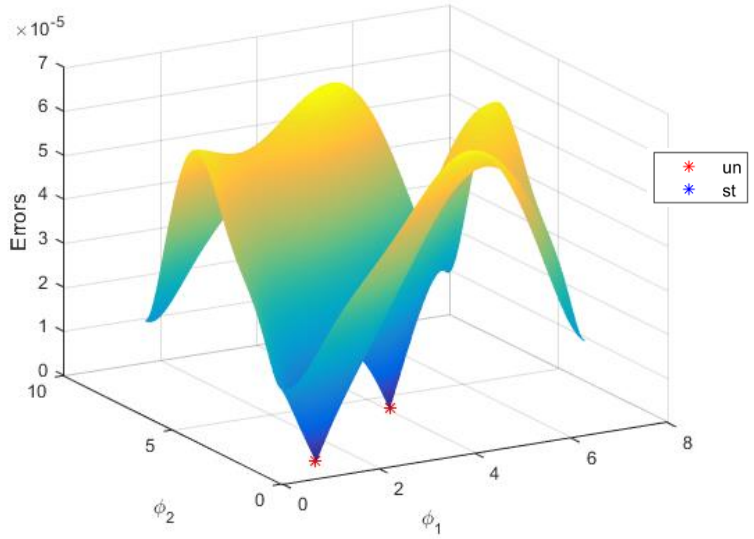


Figure 61. Two-dimensional optimization of the objective function (7-24a) to get coincident EPs and their stability when $\overline{\Omega}$ =2.1

When the rotor speed $\overline{\Omega}$ is 2.1 as illustrated in Figure 61, which is larger than the shaft second critical speed 1.8, we only get two minimal values and none of them is a stable solution. The balancer balls, which are out-of-phase with each other, do not exist. No mater they are in and out of phase with the imbalance, the EPs are always unstable.

5. Stability analysis of the perferect-balancing EP for the shaft rotor/EADB and the shaft rotor/ADB system

As shown in Figure 62, we did the stability analysis to show the effect of the EADB on the perfect-balancing EP compared with the effect of the ADB. The detailed explanation can be neglected since this figure has a similar patter with that in Figure 26. As shown in Figure 63, the EADB tends to reduce the deflections of the shaft when the ADB in a whirling limit-cycle, which can aggrave the shaft vibration. Similar results can be obtained by simulating points 'A', 'B', 'C', 'D' in Figure 62.

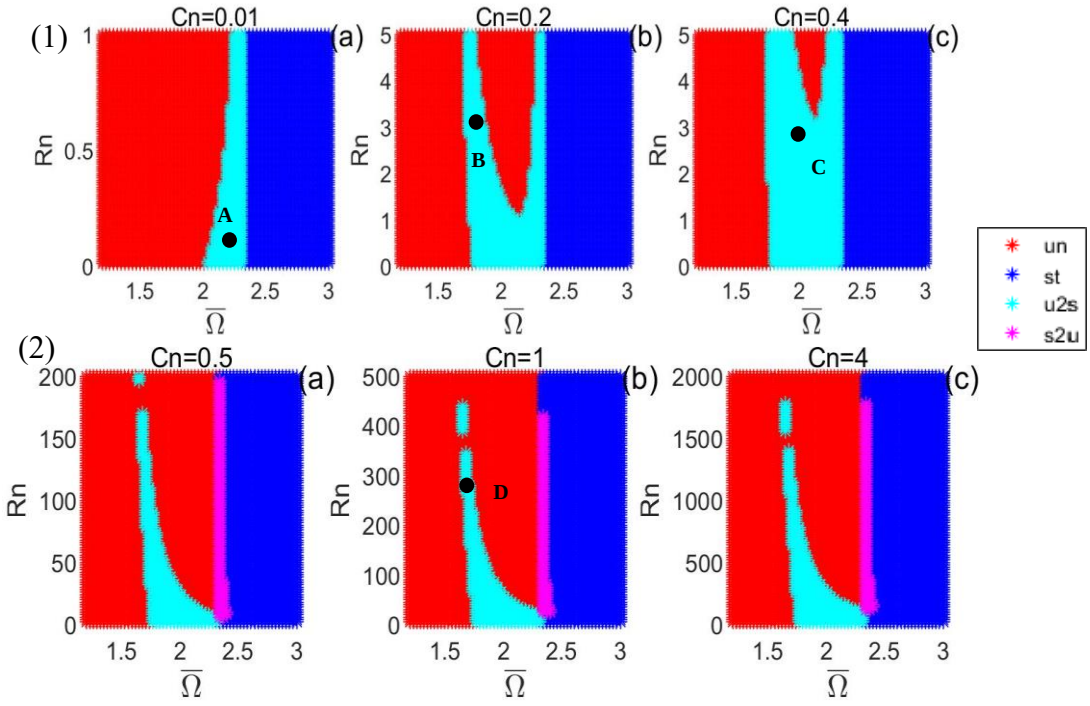


Figure 62. Stability analysis of the perfect-balancing EP for the EADB and the ADB on the rigid shaft system (1) ζ_e =0.001 (2) ζ_e = 0.01

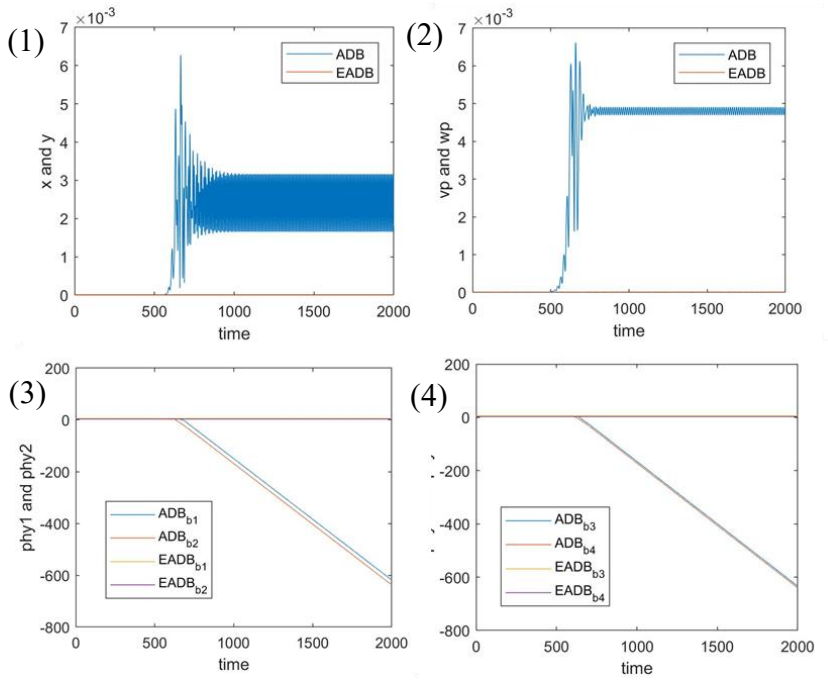


Figure 63. Numerical simulation of the rigid shaft/ADB and /EADB system showing (1) $(x^2 + y^2)^{1/2}$ (2) $(x_p^2 + y_p^2)^{1/2}$ (3) φ_{b1} and φ_{b2} (4) φ_{b3} and φ_{b4}

7.3 Conclusions for chapter 7

In this chapter, to show the effect of axial assembling error R_{bx} and radial assembling error R_{br}, we firstly explored the rigid shaft/ADBs system. We know that the axial assembling error R_{bx} has little influence on the stability of perfect-balancing EP in ($\bar{\Omega}$, μ) plane, ($\bar{\Omega}$, R_{ix}) plane, ($\bar{\Omega}$, R_{bL}) plane, ($\bar{\Omega}$, ς) plane, and ($\bar{\Omega}$, ς_b) plane. However, the radial assembling error R_{br} has a large influence on the stability of perfect-balancing EP in ($\bar{\Omega}$, μ) plane, ($\bar{\Omega}$, ς) plane. Usually when R_{br} is larger than 0.1% and 0.8%, the perfect-balancing EP becomes unstable in ($\bar{\Omega}$, μ) plane and ($\bar{\Omega}$, ς) plane.

As for the EADB applying on the rigid shaft rotor, we know that the EADB can compensate perfectly the lateral deflection and the tilting deflection for the rigid shaft system with axial assembling error. This compensation is the same when we apply the ADB on the rigid shaft system provided that the rotor speed is large enough and the balancer balls' mass is large enough. In addition to this, in general, we notice that the larger

the coupling coefficient, the larger the stable region for the perfect-balancing EP. Furthermore, by properly designing the electric parameters and comparing with the ADB, the EADB can improve the stability region for the perfect-balancing EP.

CHAPTER 8 CONLUSIONS AND FUTURE WORK

In order to extend the auto-balancing condition of the ADB to a wide operating range, and to eliminate the co-existing whirling limit-cycle, we proposed and developed an Enhanced Automatic Dynamic Balancer (EADB), through which we incorporated a drag force in the form of an electromagnetic force as we wrapped the ADB circular track with wires to make a shunt circuit and replaced the balancer balls with magnets. Therefore, drag forces are induced by electro-magnetic induction when balancer magnets move in a wired circular track regarded as a shunt circuit.

Chapter Two includes a detailed design procedure. We derived dynamic equations for the planar rotor/EADB system and solved the system's equilibrium points. We analyzed the equilibrium points' stability and compared with that of the planar rotor/ADB system. In this chapter, we also took consideration of the rotating axis eccentricity R_{br} between the EADB and the shaft.

Chapter Three solved whirling limit-cycle for the planar rotor/EADB system and compared the solution with that of the planar rotor/ADB system. We found that the proposed EADB can greatly improve the performance over the conventional ADB, so we conducted research on some general rotor/EADB systems, such as an asymmetrically supported planar rotor/EADB system, vertical rotor with gravity/EADB and shaft rotor with tilting/EADB system. We studied them, respectively, in Chapter Four and Five, Chapter Six, and Chapter Seven.

In Chapter Five, we proposed a multi-tone harmonic balance method to solve the whirling limit-cycle of the asymmetrically supported planar rotor/EADB system. We obervated that the whirling limit-cycle response of the system are composed of two harnomics, each of which has an incommensurable frequency with each other. These two frequencies are rotor speed and balancer ball whirling frequency. By assuming dominant multiple-frequency components in the solution, this approach is a good compromise between the efficiency and the accuracy. The dominant components were gotten from the numerical simulation via an advanced signal processing method known as Matrix Pencil Method (MPM).

In Chapter Six, we found that there are no perfect-balancing solutions rigorously as the balancer balls cannot compensate for both the imbalance and gravity of the system. But in the normalized dynamic system of the vertical rotor/ADB, gravity resulting from the balancer balls can be neglected as their order of magnitudes are more than 300 times smaller than the vertical rotor gravity and more than 19000 times smaller than the imbalance. Therefore, we can neglect the effect of balancer balls' gravity and solve the system's perfect-balancing equilibrium points. The vertical rotor gravity caused a static vertical deflection of the rotor, and the ADB can compensate for the imbalance just as it can do in a horizontal rotor. Based on above results, we compared the stability of perfect-balancing solutions of the vertical rotor/ADB with that of the vertical rotor/EADB system. We also found that the EADB can enlarge the stable region of perfect-balancing solutions by adjusting circuit parameters.

In the Chapter Seven, we applied two EADBs to balance a rigid shaft rotor (3-dimensional rotor) considering two practical issues. One is the rotating axis eccentricity R_{br} between the EADB and the shaft, and other is the degree of symmetry R_{bx} when assembling two EADBs on the shaft, each of which contains two balancer masses. We solved the perfect-balancing solution, ball masses coincident in each race condition and the half-balanced solution, and we identified their stability. We proposed a numerical method to solve other equilibrium points fixing system parameters, but analytical solutions of other equilibrium points remain a problem as we need to focus on some practical issues at first. We applied an eccentricity on one EADB and found that the eccentricity has a big influence on the stability of half-balanced equilibrium point in the shaft/EADB system. When the eccentricity exceeds 0.1% of the EADB track radius, then the half-balanced equilibrium point may lose its stability. As for the influence of the degree of symmetry, balancer masses can compensate for the effect of asymmetry by adjusting balancer masses' perfect-balancing angular positions.

As for the influence of the EADB for rotor balancing purpose, we know that the EADB can largely improves the performance of the ADB by eliminating the whirling limit-cycle and increasing the stable perfect-balancing EP via properly designing circuit parameters. It is shown that coupling coefficient ς_e has a big influence on the

enhancement. Comparing with a smaller ς_e, which is about 0.001, a bigger ς_e about 0.01 can further suppress whirling limit-cycle and can also increase stable region for perfect-balancing solutions. But too large ς_e , such as 0.1, can result in a long transient period, which means that the balancer masses can aggrave the rotor vibration if initially started from a bad initial condition. Capacitance C_n and resistance R_n are not sensitive on the stability of perfect-balancing EP unless they are designed in some particular regions, and they have a small influence on the whirling limit-cycle as well. The EADB cannot compensate for the radial assembling error.

In the future, to verify the effectiveness of the EADB comparing with the ADB for enhancing the stability of the perfect-balancing EP or for the eliminating of the whirling limit-cycle, experiments need to be conducted. Therefore, the test rig needs to be set up and the signals need to be analyzed. The automatic rotor balancing via controllable compensate masses can be achieved if balancer masses position can be controlled by energizing the newly-designed shunt circuit in EADB with appropriate circuit parameters. Furthermore, mass unbalance location and level should also be acquired by knowing where are compensate masses for health monitoring purpose. Another work in Ref [51] demonstrated that using a partitioned tracked in the ADB can prevent the whirling limit-cycle effectively in their experiment, which maybe interesting to look at as well.

LIST OF REFERENCES

[1] Thearle, E. L., 1932, "A New type of dynamic-balancing machine". *Transactions of ASME (Applied Mechanics)*, APM-54-12, pp. 131-141.
[2] Clark, K.,1940, "Domestic Appliance". United States Patent No. 2405404, Oct. 29.
[3] MacDuff, J. N. and Curreri, J. R.,1958, Vibration Control. McGraw-Hill, New York.
[4] Tadeusz, M.,1988, "Position error occurrence in self balancers used on rigid rotors of rotating machinery". *Mechanism and machine theory*, Dec. 31;23(1) pp.71-8.
[5] Thearle, E. L.,1950, "Automatic Dynamic Balancers (Part 2- Ring, pendulum, ball balancers)". *Machine Design*, 22, pp. 103-106.
[6] Sharp, R. S., 1975, "Analysis of a Self-Balancing System for Rigid Rotors". *Journal of Mechanical Engineering Science*, 17(4) pp. 186-189.
[7] Kubo, S., Jinouchi, Y., Araki, Y., Inoue, J., 1986, "Automatic Balancer (Pendulum Balancer)". *Bulletin of the JSME*, 29(249) pp. 924-928.
[8] Bövik, P., Högfors, C., 1986, "Autobalancing of Rotors". Journal of Sound and Vibration, December 22, 111(3) pp. 429-440.
[9] Lee, J., Van Moorhem WK., 1996, "Analytical and experimental analysis of a self-compensating dynamic balancer in a rotating mechanism". *Transactions of ASME (Journal of dynamic systems measurement an control)*, Sep. 1, 118 pp:468-75.
[10] Chung, J., Ro, D.S.,1999, "Dynamic analysis of an automatic dynamic balancer for rotating mechanisms". *J. Sound Vib*, 228(5):1035-56.
[11] Lu, C.J., Wang, M.C., Huang, S.H., 2009, "Analytical study of the stability of a two-ball automatic balancer". *Mechanical Systems and Signal Processing*, Apr 30, 23(3):884-96.
[12] Majewski, T., 1988, "Position Errors Occurrence in Self Balancers Used on Rigid Rotors of Rotating Machinery". *Mech. Mach. Theory*, 23(1) pp. 71–78.
[13] Lindell, H., 1996, "Vibration Reduction on Hand-Held Grinders by Automatic Balancers". *Cent Eur. J. Public Health*, 4 pp. 43–45.
[14] Rajalingham, C., and Rakheja, S., 1998, "Whirl Suppression in Hand-Held Power Tool Rotors Using Guided Rolling Balancers". *J. Sound Vib*. 217, pp.453–466.
[15] Chao, P. C. P., Huang, Y. D., and Sung, C. K., 2003, "Non-Planar Dynamic Modeling for the Optical Disk Drive Spindles Equipped With and Automatic Balancer". *Mech. Mach. Theory*, 38 pp. 1289–1305.
[16] Kim, W., Lee, D. J., and Chung, J., 2005, "Three-Dimensional Modelling and Dynamic Analysis of an Automatic Ball Balancer in an Optical Disk Drive," *J. Sound Vib.*, 285(3) pp. 547–569.
[17] DeSmidt, H.A.,2009, "Imbalance vibration suppression of a supercritical shaft via an automatic balancing device". *Journal of Vibration and Acoustics*, 131(4):041001.
[18] Lu, C.J., Wang, M.C., 2011, "Stability analysis of a ball–rod–spring automatic balancer". *International Journal of Mechanical Sciences*, 10(53) pp.846-54.
[19] Rezaee, M., Fathi, R., 2015, " Improving the working performance of automatic ball balancer by modifying its mechanism". *Journal of Sound and Vibration*. 358 pp.375-91.
[20] Kim, T., Na, S., 2013, "New automatic ball balancer design to reduce transient-response in rotor system". *Mechanical Systems and Signal Processing*, 37(1) pp.265-75.

[21] Chan, T.C., Sung, C.K., Chao, P.C., 2011, "Non-linear suspension of an automatic ball balancer". *International Journal of Non-Linear Mechanics*, 46(2) pp.415-24.

[22] Sung, C.K., Chan, T.C., Chao, C.P., Lu, C.H., 2013, "Influence of external excitations on ball positioning of an automatic balancer". *Mechanism and Machine Theory*, 69 pp.115-26.

[23] Bolton, J.N., 2010, "Single-and Dual-Plane Automatic Balancing of an Elastically-Mounted Cylindrical Rotor with Considerations of Coulomb Friction and Gravity". Doctoral dissertation, Virginia Tech.

[24] Filimonikhin, G., Filimonikhina, I., Dumenko, K., Lichuk, M., 2016, "Empirical criterion for the occurrence of auto-balancing and its application for axisymmetric rotor with a fixed point and isotropic elastic support". *Восточно-Европейский журнал передовых технологий*. 5 (7) pp.11-8.

[25] Green, K., Champneys, A.R., Lieven, N.J., 2006, "Bifurcation analysis of an automatic dynamic balancing mechanism for eccentric rotors". *Journal of Sound and Vibration*. 291(3) pp.861-81.

[26] Lu, C.J., Lin, Y.M.,2011, "A modified incremental harmonic balance method for rotary periodic motions". *Nonlinear Dynamics*, 66(4) pp.781-8.

[27] Lu, C.J., Tien, M.H., 2012, "Pure-rotary periodic motions of a planar two-ball auto-balancer system". *Mechanical Systems and Signal Processing*. 32 pp.251-68.

[28] Jung, D., DeSmidt, H., 2017, "Nonsynchronous Vibration of Planar Autobalancer/Rotor System With Asymmetric Bearing Support". *Journal of Vibration and Acoustics*, 139(3):031010.

[29] Wang, H., Tang. J., 2016, "Electromagnetic energy harvesting from a dual-mass pendulum oscillator". *In Active and Passive Smart Structures and Integrated Systems*, International Society for Optics and Photonics, 9799 pp. 979924.

[30] Kecik, K., Borowiec, M., 2013, "An autoparametric energy harvester". *The European Physical Journal Special Topics*, 222(7) pp.1597-605.

[31] Fuzhou AO Magnet Electronic Co., Ltd., "Radial Ring Magnets," Fuzhou AO Magnet Electronic, accessed Nov. 20, 2018, http://www.aomagnet.com/ 564 radial-ring-magnets-c-19/

[32] Crandall, S.H., 1968, *Dynamics of mechanical and electromechanical systems*. McGraw-Hill.

[33] Ness Engineering, Inc., "Toroid Inductor Formulas and Calculator," NessEngineering, accessed Nov. 20, 2018, http://www.nessengr.com/technical-557data/toroid-inductor-formulas-and-calculator/

[34] Agafonov, Y.V., 1976, "Automatic balancing device for hand grinders". *Russian engineering journal*. Jan 1, 56(9) pp.31-3.

[35] Agafonov, Y.V., Bazykin, Y.V., 1986, "Investigation of the influence of the ball auto-balancer's eccentricity of a treadmill to balance quality". *Vestn. Mashinostr*. (8) pp.23-5.

[36] Bykov, V.G., Kovachev, A.S., 2014, "Dynamics of a rotor with an eccentric ball auto-balancing device". *Vestnik St. Petersburg University: Mathematics*. Oct 1, 47(4) pp.173-80

[37] Bykov, V.G., Kovachev, A.S., 2015, "On stability of unbalanced steady-state motions of a rotor with eccentric ball autobalancing device". *In Mechanics-Seventh Polyakhov's Reading*, IEEE International Conference on 2015 Feb 2 pp.1-4.

[38] Horvath, R., Flowers, G.T., Fausz, J., 2005, "Influence of Nonideaities on the Performance of a Self-Balancing Rotor System". *In ASME 2005 International Mechanical Engineering Congress and Exposition* 2005 Jan 1, pp. 233-242.

[39] DeSmidt, H.A., 2010, "Analysis of a dual gearbox/shaft system with nonlinear dynamic mesh phase interactions". *In Proceedings of the 51st AIAA/ASME/ASCE/AHS/ASC structures, structural dynamics and materials conference*. 2010 Apr 12.

[40] Ryzhik, B., Sperling, L., Duckstein, H., 2004, "Auto-balancing of anisotropically supported rigid rotors". *Technische Mechanik*. 24(1) pp.37-50.

[41] Rodrigues, D.J., Champneys, A.R., Friswell, M.I., Wilson, R.E., 2008, "A consideration of support asymmetry in an automatic ball balancing system". *In Sixth EUROMECH Nonlinear Dynamics Conference*, ENOC-2008.

[42] Akgün, D., Çankaya, I., Jones, J.P., 2009, "A symbolic algorithm for the automatic computation of multitone-input harmonic balance equations for nonlinear systems". *Nonlinear Dynamics*. Apr 1, 56(1-2) pp.179-91.

[43] Hua, Y., Sarkar, T.K., 1990, "Matrix pencil method for estimating parameters of exponentially damped/undamped sinusoids in noise". *IEEE Transactions on Acoustics, Speech, and Signal Processing*. May, 38(5) pp.814-24.

[44] Sarkar, T.K., Pereira, O., 1995, "Using the matrix pencil method to estimate the parameters of a sum of complex exponentials". *IEEE Antennas and Propagation Magazine*, Feb, 37(1) pp.48-54.

[45] Suonan, J., Wang, B., Wang, L., Sun, J., Xiao, M., 2013, "A fast phasor calculation algorithm for power systems". *In Zhongguo Dianji Gongcheng Xuebao, Chinese Society for Electrical Engineering*. Jan 5, 33(1) pp.123-129.

[46] Chung, J., 2005, "Effect of gravity and angular velocity on an automatic ball balancer". Proceedings of the Institution of Mechanical Engineers, Part C: *Journal of Mechanical Engineering Science*. Jan 1, 219(1) pp.43-51.

[47] Chung, J., Jang, I., 2003, "Dynamic response and stability analysis of an automatic ball balancer for a flexible rotor". *Journal of Sound and Vibration*. Jan 2, 259(1) pp.31-43.

[48] Bykov, B.G., 2013, "Auto-balancing of a rotor with an orthotropic elastic shaft". *Journal of Applied Mathematics and Mechanics*. Dec 31, 77(4) pp.369-79.

[49] Hedaya, M.T., Sharp, R.S., 1977, "An analysis of a new type of automatic balancer". *Journal of Mechanical Engineering Science*. Oct, 19(5) pp.221-6.

[50] Rodrigues, D.J., Champneys, A.R., Friswell, M.I., Wilson, R.E., 2008, "Automatic two-plane balancing for rigid rotors". *International Journal of Non-Linear Mechanics*. Jul 31, 43(6) pp.527-41.

[51] Haidar, Ahmad M., and Jose L. Palacios., 2018, "Effect of Number of Tracks and Balancing Masses on Passive Balancing Performance". *2018 AIAA/ASCE/AHS/ASC Structures, Structural Dynamics, and Materials Conference*.

[52] Su, X. and DeSmidt, H.A., 2019. “Rotor balancing via an enhanced automatic dynamic balancer with inductively coupled shunt circuit”. Journal of Vibration and Acoustics, 141(3), p.031003

APPENDIX

A1

The inertia matrix $\mathbf{M_o}$, stiffness $\mathbf{K_o}$ matrix, and the force vector $\mathbf{F_o}$ are given below for Eq. (2-24).

$$\mathbf{M_o} = \begin{bmatrix} m_R + 2m_b & 0 & -m_b R_b \sin(\phi_{b1}) & -m_b R_b \sin(\phi_{b2}) & 0 & 0 & 0 & 0 \\ 0 & m_R + 2m_b & m_b R_b \cos(\phi_{b1}) & m_b R_b \cos(\phi_{b2}) & 0 & 0 & 0 & 0 \\ -m_b R_b \sin(\phi_{b1}) & m_b R_b \cos(\phi_{b1}) & m_b {R_b}^2 & 0 & 0 & 0 & 0 & 0 \\ -m_b R_b \sin(\phi_{b2}) & m_b R_b \cos(\phi_{b2}) & 0 & m_b {R_b}^2 & 0 & 0 & 0 & 0 \\ 0 & 0 & 0 & 0 & 0 & 0 & 0 & 0 \\ 0 & 0 & 0 & 0 & 0 & L_1 & 0 & 0 \\ 0 & 0 & 0 & 0 & 0 & 0 & 0 & 0 \\ 0 & 0 & 0 & 0 & 0 & 0 & 0 & L_2 \end{bmatrix}$$

$$\mathbf{K_o} = \begin{bmatrix} k - (m_R + 2m_b)\Omega^2 & -c\Omega & 0 & 0 & 0 & 0 & 0 & 0 \\ c\Omega & k - (m_R + 2m_b)\Omega^2 & 0 & 0 & 0 & 0 & 0 & 0 \\ m_b R_b \Omega^2 \sin(\phi_{b1}) & -m_b R_b \Omega^2 \cos(\phi_{b1}) & 0 & 0 & 0 & 0 & 0 & 0 \\ m_b R_b \Omega^2 \sin(\phi_{b2}) & -m_b R_b \Omega^2 \cos(\phi_{b2}) & 0 & 0 & 0 & 0 & 0 & 0 \\ 0 & 0 & 0 & 0 & \frac{1}{C_1} & 0 & 0 & 0 \\ 0 & 0 & 0 & 0 & 0 & 0 & 0 & 0 \\ 0 & 0 & 0 & 0 & 0 & 0 & \frac{1}{C_2} & 0 \\ 0 & 0 & 0 & 0 & 0 & 0 & 0 & 0 \end{bmatrix}$$

$$\mathbf{F_o} = \begin{bmatrix} \Omega^2 m_e R_e \cos(\phi_e) + \sum_{i=1}^{2} \Omega^2 m_b R_b \cos(\phi_{bi}) + m_b R_b \cos(\phi_{bi}) \dot{\phi}_{bi}^{\,2} \\ \Omega^2 m_e R_e \sin(\phi_e) + \sum_{i=1}^{2} \Omega^2 m_b R_b \sin(\phi_{bi}) + m_b R_b \sin(\phi_{bi}) \dot{\phi}_{bi}^{\,2} \\ 0 \\ 0 \\ 0 \\ 0 \\ 0 \\ 0 \end{bmatrix}$$

The inertia matrix **M**, stiffness **K** matrix, and the force vector **F** are given below for Eq. (2-25).

$$\mathbf{M}=\begin{bmatrix} m_R+2m_b & 0 & -m_bR_b\sin(\phi_{b1}) & -m_bR_b\sin(\phi_{b2}) & 0 & 0 \\ 0 & m_R+2m_b & m_bR_b\cos(\phi_{b1}) & m_bR_b\cos(\phi_{b2}) & 0 & 0 \\ -m_bR_b\sin(\phi_{b1}) & m_bR_b\cos(\phi_{b1}) & m_bR_b{}^2 & 0 & 0 & 0 \\ -m_bR_b\sin(\phi_{b2}) & m_bR_b\cos(\phi_{b2}) & 0 & m_bR_b{}^2 & 0 & 0 \\ 0 & 0 & \dfrac{L_1\theta_eR_b}{R_{C1}+R_{L1}} & 0 & -L_1 & 0 \\ 0 & 0 & 0 & \dfrac{L_2\theta_eR_b}{R_{C2}+R_{L2}} & 0 & -L_1 \end{bmatrix}$$

$$\mathbf{K}=\begin{bmatrix} k-(m_R+2m_b)\Omega^2 & -c\Omega & 0 & 0 & 0 & 0 \\ c\Omega & k-(m_R+2m_b)\Omega^2 & 0 & 0 & 0 & 0 \\ m_bR_b\Omega^2\sin(\phi_{b1}) & -m_bR_b\Omega^2\cos(\phi_{b1}) & 0 & 0 & -\dfrac{R_b\theta_e}{C_1(R_{C1}+R_{L1})} & 0 \\ m_bR_b\Omega^2\sin(\phi_{b2}) & -m_bR_b\Omega^2\cos(\phi_{b2}) & 0 & 0 & 0 & -\dfrac{R_b\theta_e}{C_2(R_{C2}+R_{L2})} \\ 0 & 0 & 0 & 0 & -\dfrac{1}{C_1} & 0 \\ 0 & 0 & 0 & 0 & 0 & -\dfrac{1}{C_2} \end{bmatrix}$$

$$\mathbf{F}=\begin{bmatrix} \Omega^2m_eR_e\cos(\phi_e)+\sum_{i=1}^{2}\Omega^2m_bR_b\cos(\phi_{bi})+m_bR_b\cos(\phi_{bi})\dot{\phi}_{bi}{}^2 \\ \Omega^2m_eR_e\sin(\phi_e)+\sum_{i=1}^{2}\Omega^2m_bR_b\sin(\phi_{bi})+m_bR_b\sin(\phi_{bi})\dot{\phi}_{bi}{}^2 \\ 0 \\ 0 \\ 0 \\ 0 \end{bmatrix}$$

The linearized mass matrix $\mathbf{M}_L$, stiffness matrix $\mathbf{K}_L$ and the force vector $\mathbf{F}_L$ are given for Eq. (2-44).

$$\mathbf{M}_L = \begin{bmatrix} 1 & 0 & -\mu\sin(b_1) & -\mu\sin(b_2) & 0 & 0 \\ 0 & 1 & \mu\cos(b_1) & \mu\cos(b_2) & 0 & 0 \\ -\mu\sin(b_1) & \mu\cos(b_1) & \mu & 0 & 0 & 0 \\ -\mu\sin(b_2) & \mu\cos(b_2) & 0 & \mu & 0 & 0 \\ 0 & 0 & \varsigma_e & 0 & -1 & 0 \\ 0 & 0 & 0 & \varsigma_e & 0 & -1 \end{bmatrix}$$

$$\mathbf{C}_L = \begin{bmatrix} \varsigma & -2\bar{\Omega} & -2\mu\bar{\Omega}\cos(b_1) & -2\mu\bar{\Omega}\cos(b_2) & 0 & 0 \\ 2\bar{\Omega} & \varsigma & -2\mu\bar{\Omega}\sin(b_1) & -2\mu\bar{\Omega}\sin(b_2) & 0 & 0 \\ 2\mu\bar{\Omega}\cos(b_1) & 2\mu\bar{\Omega}\sin(b_1) & \varsigma_b+\varsigma_e & 0 & 0 & 0 \\ 2\mu\bar{\Omega}\cos(b_2) & 2\mu\bar{\Omega}\sin(b_2) & 0 & \varsigma_b+\varsigma_e & 0 & 0 \\ 0 & 0 & 0 & 0 & -R_n & 0 \\ 0 & 0 & 0 & 0 & 0 & -R_n \end{bmatrix}$$

$$\mathbf{F}_L = \begin{bmatrix} -x_s + y_s\varsigma\bar{\Omega} + \bar{\Omega}^2(\eta\cos(\varphi_e) + x_s + \mu\cos(b_1) + \mu\cos(b_2)) \\ -y_s - x_s\varsigma\bar{\Omega} + \bar{\Omega}^2(\eta\sin(\varphi_e) + y_s + \mu\sin(b_1) + \mu\sin(b_2)) \\ \bar{\Omega}^2\mu(y_s\cos(b_1) - x_s\sin(b_1)) \\ \bar{\Omega}^2\mu(y_s\cos(b_2) - x_s\sin(b_2)) \\ 0 \\ 0 \end{bmatrix}$$

A2

The dimensionless system mass matrix $\mathbf{M}_{wlc}$ and the force vector $\mathbf{F}_{wlc}$ are given below for Eq. (3-11)

$$\mathbf{M}_{\text{wlc}} = \begin{bmatrix} 1 & 0 & -\mu\sin(b_{\text{wlc},1}) & -\mu\sin(b_{\text{wlc},2}) & 0 & 0 \\ 0 & 1 & \mu\cos(b_{\text{wlc},1}) & \mu\cos(b_{\text{wlc},2}) & 0 & 0 \\ -\mu\sin(b_{\text{wlc},1}) & \mu\cos(b_{\text{wlc},1}) & \mu & 0 & 0 & 0 \\ -\mu\sin(b_{\text{wlc},2}) & \mu\cos(b_{\text{wlc},2}) & 0 & \mu & 0 & 0 \\ 0 & 0 & \varsigma_e & 0 & -1 & 0 \\ 0 & 0 & 0 & \varsigma_e & 0 & -1 \end{bmatrix}$$

$$\mathbf{F}_{\text{wlc}} = \begin{bmatrix} -x''_{\text{wlc}} - x_{\text{wlc}} - \varsigma x'_{\text{wlc}} + 2y'_{\text{wlc}}\bar{\Omega} + y_{\text{wlc}}\varsigma\bar{\Omega} + x_{\text{wlc}}\bar{\Omega}^2 + \bar{\Omega}^2\eta\cos(\varphi_e) + \sum_{i=1}^{2}\mu b''_{\text{wlc},i}\sin(b_{\text{wlc},i}) + \sum_{i=1}^{2}\mu(b'_{\text{wlc},i} + \bar{\Omega})^2\cos(b_{\text{wlc},i}) \\ -y''_{\text{wlc}} - y_{\text{wlc}} - \varsigma y'_{\text{wlc}} - 2\bar{\Omega}x'_{\text{wlc}} - x_{\text{wlc}}\varsigma\bar{\Omega} + y_{\text{wlc}}\bar{\Omega}^2 + \bar{\Omega}^2\eta\cos(\varphi_e) - \sum_{i=1}^{2}\mu b''_{\text{wlc},i}\cos(b_{\text{wlc},i}) + \sum_{i=1}^{2}\mu(b'_{\text{wlc},i} + \bar{\Omega})^2\sin(b_{\text{wlc},i}) \\ q_{\text{wlc},1}R_n - \mu b''_{\text{wlc},1} - (\mu y''_{\text{wlc}} + 2\mu\bar{\Omega}x'_{\text{wlc}} - \mu\bar{\Omega}^2 y_{\text{wlc}})\cos(b_{\text{wlc},1}) + (\mu x''_{\text{wlc}} - 2\mu\bar{\Omega}y'_{\text{wlc}} - \mu\bar{\Omega}^2 x_{\text{wlc}})\sin(b_{\text{wlc},1}) - b'_{\text{wlc},1}(\varsigma_b + \varsigma_e) \\ q_{\text{wlc},2}R_n - \mu b''_{\text{wlc},2} - (\mu y''_{\text{wlc}} + 2\mu\bar{\Omega}x'_{\text{wlc}} - \mu\bar{\Omega}^2 y_{\text{wlc}})\cos(b_{\text{wlc},2}) + (\mu x''_{\text{wlc}} - 2\mu\bar{\Omega}y'_{\text{wlc}} - \mu\bar{\Omega}^2 x_{\text{wlc}})\sin(b_{\text{wlc},2}) - b'_{\text{wlc},2}(\varsigma_b + \varsigma_e) \\ q''_{\text{wlc},1} + C_n q_{\text{wlc},1} + R_n q'_{\text{wlc},1} - \varsigma_e b''_{\text{wlc},1} \\ q''_{\text{wlc},2} + C_n q_{\text{wlc},2} + R_n q'_{\text{wlc},2} - \varsigma_e b''_{\text{wlc},2} \end{bmatrix}$$

A3

The overall system stiffness matrices $\mathbf{K_o}$ and the force vector is $\mathbf{F_o}$ for Eq. (4-9) are given as follows.

$$\mathbf{K_o} = \begin{bmatrix} k_1 & 0 & 0 & 0 & 0 & 0 & 0 & 0 \\ 0 & k_2 & 0 & 0 & 0 & 0 & 0 & 0 \\ 0 & 0 & 0 & 0 & 0 & 0 & 0 & 0 \\ 0 & 0 & 0 & 0 & 0 & 0 & 0 & 0 \\ 0 & 0 & 0 & 0 & \dfrac{1}{C_1} & 0 & 0 & 0 \\ 0 & 0 & 0 & 0 & 0 & 0 & 0 & 0 \\ 0 & 0 & 0 & 0 & 0 & 0 & \dfrac{1}{C_2} & 0 \\ 0 & 0 & 0 & 0 & 0 & 0 & 0 & 0 \end{bmatrix}$$

$$\mathbf{F_o} = \begin{bmatrix} \Omega^2 m_e R_e \cos(\phi_e + \phi(t)) + \sum_{i=1}^{2} \Omega^2 m_b R_b \cos(\phi_{bi} + \phi(t)) + m_b R_b \cos(\phi_{bi} + \phi(t)) \dot{\phi}_{bi}^{\,2} \\ \Omega^2 m_e R_e \sin(\phi_e + \phi(t)) + \sum_{i=1}^{2} \Omega^2 m_b R_b \sin(\phi_{bi} + \phi(t)) + m_b R_b \sin(\phi_{bi} + \phi(t)) \dot{\phi}_{bi}^{\,2} \\ 0 \\ 0 \\ 0 \\ 0 \\ 0 \\ 0 \end{bmatrix}$$

Where the damping, and stiffness matrices are **C** and **K**, the force vector is **F**, which are given for Eq. (4-10).

$$\mathbf{C} = \begin{bmatrix} c_1 & 0 & -2m_b R_b \Omega \cos(\phi_{b1} + \phi(t)) & -2m_b R_b \Omega \cos(\phi_{b2} + \phi(t)) & 0 & 0 \\ 0 & c_2 & -2m_b R_b \Omega \sin(\phi_{b1} + \phi(t)) & -2m_b R_b \Omega \sin(\phi_{b2} + \phi(t)) & 0 & 0 \\ 0 & 0 & \dfrac{R_b^{\,2}(c_b(R_{C1} + R_{L1}) + \theta_e^{\,2})}{R_{C1} + R_{L1}} & 0 & 0 & 0 \\ 0 & 0 & 0 & \dfrac{R_b^{\,2}(c_b(R_{C2} + R_{L2}) + \theta_e^{\,2})}{R_{C2} + R_{L2}} & 0 & 0 \\ 0 & 0 & 0 & 0 & -\dfrac{L_1}{C_1(R_{C1} + R_{L1})} & 0 \\ 0 & 0 & 0 & 0 & 0 & -\dfrac{L_2}{C_2(R_{C2} + R_{L2})} \end{bmatrix}$$

$$\mathbf{K} = \begin{bmatrix} k_1 & 0 & 0 & 0 & 0 & 0 \\ 0 & k_2 & 0 & 0 & 0 & 0 \\ 0 & 0 & 0 & 0 & -\dfrac{R_b \theta_e}{C_1(R_{C1} + R_{L1})} & 0 \\ 0 & 0 & 0 & 0 & 0 & -\dfrac{R_b \theta_e}{C_2(R_{C2} + R_{L2})} \\ 0 & 0 & 0 & 0 & -\dfrac{1}{C_1} & 0 \\ 0 & 0 & 0 & 0 & 0 & -\dfrac{1}{C_2} \end{bmatrix}$$

$$\mathbf{F}=\begin{bmatrix} \Omega^2 m_e R_e \cos(\phi_e+\phi(t))+\sum_{i=1}^{2}\Omega^2 m_b R_b \cos(\phi_{bi}+\phi(t))+m_b R_b \cos(\phi_{bi}+\phi(t))\dot{\phi}_{bi}^{\,2} \\ \Omega^2 m_e R_e \sin(\phi_e+\phi(t))+\sum_{i=1}^{2}\Omega^2 m_b R_b \sin(\phi_{bi}+\phi(t))+m_b R_b \sin(\phi_{bi}+\phi(t))\dot{\phi}_{bi}^{\,2} \\ 0 \\ 0 \\ 0 \\ 0 \end{bmatrix}$$

The dimensionless system matrices are $\mathbf{M}_L$, $\mathbf{C}_L$, $\mathbf{K}_L$, $\mathbf{F}_L$ are given for Eq. (4-16) as follows,

$$\mathbf{M}_L=\begin{bmatrix} 1 & 0 & -\mu\sin(b_1+\tau\bar{\Omega}) & -\mu\sin(b_2+\tau\bar{\Omega}) & 0 & 0 \\ 0 & 1 & \mu\cos(b_1+\tau\bar{\Omega}) & \mu\cos(b_2+\tau\bar{\Omega}) & 0 & 0 \\ -\mu\sin(b_1+\tau\bar{\Omega}) & \mu\cos(b_1+\tau\bar{\Omega}) & \mu & 0 & 0 & 0 \\ -\mu\sin(b_2+\tau\bar{\Omega}) & \mu\cos(b_2+\tau\bar{\Omega}) & 0 & \mu & 0 & 0 \\ 0 & 0 & \varsigma_e & 0 & -1 & 0 \\ 0 & 0 & 0 & \varsigma_e & 0 & -1 \end{bmatrix}$$

$$\mathbf{C}_L=\begin{bmatrix} \varsigma_1 & 0 & -2\mu\bar{\Omega}\cos(b_1+\tau\bar{\Omega}) & -2\mu\bar{\Omega}\cos(b_2+\tau\bar{\Omega}) & 0 & 0 \\ 0 & \varsigma_2 & -2\mu\bar{\Omega}\sin(b_1+\tau\bar{\Omega}) & -2\mu\bar{\Omega}\sin(b_2+\tau\bar{\Omega}) & 0 & 0 \\ 0 & 0 & \varsigma_b+\varsigma_e & 0 & 0 & 0 \\ 0 & 0 & 0 & \varsigma_b+\varsigma_e & 0 & 0 \\ 0 & 0 & 0 & 0 & -R_n & 0 \\ 0 & 0 & 0 & 0 & 0 & -R_n \end{bmatrix}$$

$$\mathbf{K}_L=\begin{bmatrix} 1 & 0 & \mu\bar{\Omega}^2\sin(b_1+\tau\bar{\Omega}) & \mu\bar{\Omega}^2\sin(b_2+\tau\bar{\Omega}) & 0 & 0 \\ 0 & R_r^{\,2} & -\mu\bar{\Omega}^2\cos(b_1+\tau\bar{\Omega}) & -\mu\bar{\Omega}^2\cos(b_2+\tau\bar{\Omega}) & 0 & 0 \\ 0 & 0 & 0 & 0 & -R_n & 0 \\ 0 & 0 & 0 & 0 & 0 & -R_n \\ 0 & 0 & 0 & 0 & -C_n & 0 \\ 0 & 0 & 0 & 0 & 0 & -C_n \end{bmatrix}$$

$$\mathbf{F}_L = \begin{bmatrix} -x_s + \bar{\Omega}^2(\eta\cos(\varphi_e + \tau\bar{\Omega}) + x_s + \mu\cos(b_1 + \tau\bar{\Omega}) + \mu\cos(b_2 + \tau\bar{\Omega})) \\ -y_s R_r{}^2 + \bar{\Omega}^2(\eta\sin(\varphi_e + \tau\bar{\Omega}) + y_s + \mu\sin(b_1 + \tau\bar{\Omega}) + \mu\sin(b_2 + \tau\bar{\Omega})) \\ 0 \\ 0 \\ 0 \\ 0 \end{bmatrix}$$

A4

The overall dimensionless system matrices $\mathbf{C}_{\text{wlc}}$ and $\mathbf{K}_{\text{wlc}}$ are given for Eq. (5-24).

$$\mathbf{C}_{\text{wlc}} = \begin{bmatrix} \varsigma_v & 0 & -2\mu(\bar{\Omega} + b'_{\text{wlc},1})\cos(b_{\text{wlc},1} + \bar{\Omega}\tau) & -2\mu(\bar{\Omega} + b'_{\text{wlc},2})\cos(b_{\text{wlc},2} + \bar{\Omega}\tau) & 0 & 0 \\ 0 & \varsigma_w & -2\mu(\bar{\Omega} + b'_{\text{wlc},1})\sin(b_{\text{wlc},1} + \bar{\Omega}\tau) & -2\mu(\bar{\Omega} + b'_{\text{wlc},2})\sin(b_{\text{wlc},2} + \bar{\Omega}\tau) & 0 & 0 \\ 0 & 0 & \varsigma_b + \varsigma_e & 0 & 0 & 0 \\ 0 & 0 & 0 & \varsigma_b + \varsigma_e & 0 & 0 \\ 0 & 0 & 0 & 0 & -R_n & 0 \\ 0 & 0 & 0 & 0 & 0 & -R_n \end{bmatrix}$$

$$\mathbf{K}_{\text{wlc}} = \begin{bmatrix} 1 & 0 & \mu(-b''_{\text{wlc},1}\cos(b_{\text{wlc},1} + \bar{\Omega}\tau) + (b'_{\text{wlc},1} + \bar{\Omega})^2\sin(b_{\text{wlc},1} + \bar{\Omega}\tau)) \\ 0 & R_r{}^2 & -\mu(b''_{\text{wlc},1}\sin(b_{\text{wlc},1} + \bar{\Omega}\tau) + (b'_{\text{wlc},1} + \bar{\Omega})^2\cos(b_{\text{wlc},1} + \bar{\Omega}\tau)) \\ 0 & 0 & -\mu(x''_{\text{wlc}}\cos(b_{\text{wlc},1} + \bar{\Omega}\tau) + y''_{\text{wlc}}\sin(b_{\text{wlc},1} + \bar{\Omega}\tau)) \\ 0 & 0 & 0 \\ 0 & 0 & 0 \\ 0 & 0 & 0 \end{bmatrix}$$

$$\begin{bmatrix} \mu(-b''_{\text{wlc},2}\cos(b_{\text{wlc},2} + \bar{\Omega}\tau) + (b'_{\text{wlc},2} + \bar{\Omega})^2\sin(b_{\text{wlc},2} + \bar{\Omega}\tau) & 0 & 0 \\ -\mu(b''_{\text{wlc},2}\sin(b_{\text{wlc},2} + \bar{\Omega}\tau) + (b'_{\text{wlc},2} + \bar{\Omega})^2\cos(b_{\text{wlc},2} + \bar{\Omega}\tau)) & 0 & 0 \\ 0 & -R_n & 0 \\ -\mu(x''_{\text{wlc}}\cos(b_{\text{wlc},2}) + y''_{\text{wlc}}\sin(b_{\text{wlc},2})) & 0 & -R_n \\ 0 & -C_n & 0 \\ 0 & 0 & -C_n \end{bmatrix}$$

A5

The system inertia and stiffness matrices **M** and **K** are given here for Eq. (6-3)

$$\mathbf{M}=\begin{bmatrix} m_R+2m_b & 0 & -m_bR_b\sin(\varphi_{b1}+\Omega t) & -m_bR_b\sin(\varphi_{b2}+\Omega t) & 0 & 0 \\ 0 & m_R+2m_b & m_bR_b\cos(\varphi_{b1}+\Omega t) & m_bR_b\cos(\varphi_{b2}+\Omega t) & 0 & 0 \\ -m_bR_b\sin(\varphi_{b1}+\Omega t) & m_bR_b\cos(\varphi_{b1}+\Omega t) & m_bR_b{}^2 & 0 & 0 & 0 \\ -m_bR_b\sin(\varphi_{b2}+\Omega t) & m_bR_b\cos(\varphi_{b2}+\Omega t) & 0 & m_bR_b{}^2 & 0 & 0 \\ 0 & 0 & \dfrac{L_1\theta_eR_b}{R_{C1}+R_{L1}} & 0 & -L_1 & 0 \\ 0 & 0 & 0 & \dfrac{L_2\theta_eR_b}{R_{C2}+R_{L2}} & 0 & -L_1 \end{bmatrix}$$

$$\mathbf{K}=\begin{bmatrix} k & 0 & 0 & 0 & 0 & 0 \\ 0 & k & 0 & 0 & 0 & 0 \\ 0 & 0 & 0 & 0 & -\dfrac{R_b\theta_e}{C_1(R_{C1}+R_{L1})} & 0 \\ 0 & 0 & 0 & 0 & 0 & -\dfrac{R_b\theta_e}{C_2(R_{C2}+R_{L2})} \\ 0 & 0 & 0 & 0 & -\dfrac{1}{C_1} & 0 \\ 0 & 0 & 0 & 0 & 0 & -\dfrac{1}{C_2} \end{bmatrix}$$

the overall dimensionless system matrices $\mathbf{M}_L$, $\mathbf{C}_L$, $\mathbf{K}_L$, $\mathbf{F}_L$ are shown here for Eq. (6-8)

$$\mathbf{M}_L=\begin{bmatrix} 1 & 0 & -\mu\sin(\phi_1+\tau\bar{\Omega}) & -\mu\sin(\phi_2+\tau\bar{\Omega}) & 0 & 0 \\ 0 & 1 & \mu\cos(\phi_1+\tau\bar{\Omega}) & \mu\cos(\phi_2+\tau\bar{\Omega}) & 0 & 0 \\ -\mu\sin(\phi_1+\tau\bar{\Omega}) & \mu\cos(\phi_1+\tau\bar{\Omega}) & \mu & 0 & 0 & 0 \\ -\mu\sin(\phi_2+\tau\bar{\Omega}) & \mu\cos(\phi_2+\tau\bar{\Omega}) & 0 & \mu & 0 & 0 \\ 0 & 0 & \varsigma_e & 0 & -1 & 0 \\ 0 & 0 & 0 & \varsigma_e & 0 & -1 \end{bmatrix}$$

$$\mathbf{C}_L = \begin{bmatrix} \varsigma_1 & 0 & -2\mu\bar{\Omega}\cos(\phi_1+\tau\bar{\Omega}) & -2\mu\bar{\Omega}\cos(\phi_2+\tau\bar{\Omega}) & 0 & 0 \\ 0 & \varsigma_2 & -2\mu\bar{\Omega}\sin(\phi_1+\tau\bar{\Omega}) & -2\mu\bar{\Omega}\sin(\phi_2+\tau\bar{\Omega}) & 0 & 0 \\ 0 & 0 & \varsigma_b+\varsigma_e & 0 & 0 & 0 \\ 0 & 0 & 0 & \varsigma_b+\varsigma_e & 0 & 0 \\ 0 & 0 & 0 & 0 & -R_n & 0 \\ 0 & 0 & 0 & 0 & 0 & -R_n \end{bmatrix}$$

$$\mathbf{K}_L = \begin{bmatrix} 1 & 0 & \mu\bar{\Omega}^2\sin(\phi_1+\tau\bar{\Omega}) & \mu\bar{\Omega}^2\sin(\phi_2+\tau\bar{\Omega}) & 0 & 0 \\ 0 & R_r^{\,2} & -\mu\bar{\Omega}^2\cos(\phi_1+\tau\bar{\Omega}) & -\mu\bar{\Omega}^2\cos\phi b_2+\tau\bar{\Omega}) & 0 & 0 \\ 0 & 0 & -\mu R_{\mathrm{w}}^{\,2}\sin(\phi_1+\tau\bar{\Omega}) & 0 & -R_n & 0 \\ 0 & 0 & 0 & -\mu R_{\mathrm{w}}^{\,2}\sin(\phi_2+\tau\bar{\Omega}) & 0 & -R_n \\ 0 & 0 & 0 & 0 & -C_n & 0 \\ 0 & 0 & 0 & 0 & 0 & -C_n \end{bmatrix}$$

$$\mathbf{F}_L = \begin{bmatrix} -x_s+\bar{\Omega}^2(\eta\cos(\varphi_e+\tau\bar{\Omega})+x_s+\mu\cos(b_1+\tau\bar{\Omega})+\mu\cos(b_2+\tau\bar{\Omega})) \\ -y_s-R_{\mathrm{w}}^{\,2}(1+\mu_i)+\bar{\Omega}^2(\eta\sin(\varphi_e+\tau\bar{\Omega})+y_s+\mu\sin(b_1+\tau\bar{\Omega})+\mu\sin(b_2+\tau\bar{\Omega})) \\ -R_{\mathrm{w}}^{\,2}\mu\cos(b_1+\tau\bar{\Omega}) \\ -R_{\mathrm{w}}^{\,2}\mu\cos(b_2+\tau\bar{\Omega}) \\ 0 \\ 0 \end{bmatrix}$$

A6.1

The overall system inertia, damping, and stiffness matrices $\mathbf{M_{RS}}$, $\mathbf{C_{RS}}$ and $\mathbf{K_{RS}}$, $\mathbf{F_{RS}}$, are shown here for Eq. (7-16).

$$\mathbf{M_{RS}} = \begin{bmatrix} \mathbf{M_{11}} & \mathbf{M}_{21} & \mathbf{O}^{\mathrm{T}} \\ \mathbf{M_{21}} & \mathbf{M}_{22} & \mathbf{O}^{\mathrm{T}} \\ \mathbf{O} & \mathbf{O} & \mathbf{M}_{33} \end{bmatrix}$$

Where $\mathbf{M_{RS}}$ is a rigid shaft 16×16 mass matrix, $\mathbf{O}$ is a 8×4 zero matrix, $\mathbf{M}_{11}$ and $\mathbf{M}_{21}$ are 4×4 matrices, $\mathbf{M}_{33}$ is a 8×8 matrix;

$$\mathbf{M_{11}} = \begin{bmatrix} m_R + 4m_b & 0 & 2m_b\sigma & 0 \\ 0 & m_R + 4m_b & 0 & 2m_b\sigma \\ 2m_b\sigma & 0 & m_{33} & \frac{1}{2} m_b {R_b}^2 \sum_{i=1}^{4} \sin(2\phi_{bi}) \\ 0 & 2m_b\sigma & \frac{1}{2} m_b {R_b}^2 \sum_{i=1}^{4} \sin(2\phi_{bi}) & m_{44} \end{bmatrix}$$

$$m_{33} = (I_{mr} + m_b(4{L_b}^2 + 2{R_b}^2 - 4L_b\sigma + 2\sigma^2)) + \frac{1}{2} m_b {R_b}^2 \sum_{i=1}^{4} \cos(2\phi_{bi})$$

$$m_{44} = (I_{mr} + m_b(4{L_b}^2 + 2{R_b}^2 - 4L_b\sigma + 2\sigma^2)) - \frac{1}{2} m_b {R_b}^2 \sum_{i=1}^{4} \cos(2\phi_{bi})$$

$$\mathbf{M_{21}} = \begin{bmatrix} -m_b R_b \sin(\phi_{b1}) & L_b m_b R_b \cos(\phi_{b1}) & -L_b m_b R_b \sin(\phi_{b1}) & L_b m_b R_b \cos(\phi_{b1}) \\ -m_b R_b \sin(\phi_{b2}) & L_b m_b R_b \cos(\phi_{b2}) & -L_b m_b R_b \sin(\phi_{b2}) & L_b m_b R_b \cos(\phi_{b2}) \\ -m_b R_b \sin(\phi_{b3}) & L_b m_b R_b \cos(\phi_{b3}) & (L_b - \sigma) m_b R_b \sin(\phi_{b3}) & (-L_b + \sigma) m_b R_b \cos(\phi_{b3}) \\ -m_b R_b \sin(\phi_{b4}) & L_b m_b R_b \cos(\phi_{b4}) & (L_b - \sigma) m_b R_b \sin(\phi_{b4}) & (-L_b + \sigma) m_b R_b \cos(\phi_{b4}) \end{bmatrix}$$

$$\mathbf{M}_{22} = \begin{bmatrix} m_b {R_b}^2 & 0 & 0 & 0 \\ 0 & m_b {R_b}^2 & 0 & 0 \\ 0 & 0 & m_b {R_b}^2 & 0 \\ 0 & 0 & 0 & m_b {R_b}^2 \end{bmatrix}$$

$$\mathbf{M}_{33} = \begin{bmatrix} 0 & 0 & 0 & 0 & 0 & 0 & 0 & 0 \\ 0 & L_1 & 0 & 0 & 0 & 0 & 0 & 0 \\ 0 & 0 & 0 & 0 & 0 & 0 & 0 & 0 \\ 0 & 0 & 0 & L_2 & 0 & 0 & 0 & 0 \\ 0 & 0 & 0 & 0 & 0 & 0 & 0 & 0 \\ 0 & 0 & 0 & 0 & 0 & L_3 & 0 & 0 \\ 0 & 0 & 0 & 0 & 0 & 0 & 0 & 0 \\ 0 & 0 & 0 & 0 & 0 & 0 & 0 & L_4 \end{bmatrix}$$

$$\mathbf{C_{RS}} = \begin{bmatrix} \mathbf{C_{11}} & -\mathbf{C}_{21}^{\mathrm{T}} & \mathbf{O}_{4\times 8} \\ \mathbf{C_{21}} & \mathbf{C}_{22} & -\mathbf{C}_{32}^{\mathrm{T}} \\ \mathbf{O}_{8\times 4} & \mathbf{C}_{32} & \mathbf{C}_{33} \end{bmatrix}$$

Where $\mathbf{C_{RS}}$ is a rigid shaft 16×16 damping matrix, $\mathbf{C}_{32}$ is a 8×4 damping matrix respectively, $\mathbf{C}_{11}$ and $\mathbf{C}_{21}$ are 4×4 matrices, $\mathbf{C}_{33}$ is a 8×8 matrix;

$$\mathbf{C_{11}} = \begin{bmatrix} 2c & -2\Omega(m_R + 4m_b) & 0 & 4m_b\sigma\Omega \\ 2\Omega(m_R + 4m_b) & 2c & 4m_b\sigma\Omega & 0 \\ 0 & -4m_b\sigma\Omega & 2cL_r{}^2 - m_bR_b{}^2\sum_{i=1}^{4}\sin(2\phi_{bi})\dot{\phi}_{bi} & c_{34} \\ 4m_b\sigma\Omega & 0 & c_{43} & 2cL_r{}^2 + m_bR_b{}^2\sum_{i=1}^{4}\sin(2\phi_{bi})\dot{\phi}_{bi} \end{bmatrix}$$

$$c_{43} = 2I_{mr}\Omega - J_{mr}\Omega + m_b\Omega(8L_b{}^2 - 8L_b\sigma + 4\sigma^2) - 2m_bR_b{}^2\sum_{i=1}^{4}\sin^2(\phi_{bi})\dot{\phi}_{bi}$$

$$c_{34} = -2I_{mr}\Omega + J_{mr}\Omega - m_b\Omega(8L_b{}^2 - 8L_b\sigma + 4\sigma^2) + 2m_bR_b{}^2\sum_{i=1}^{4}\cos^2(\phi_{bi})\dot{\phi}_{bi}$$

$$\mathbf{C_{21}} = \begin{bmatrix} 2m_bR_b\Omega\cos(\phi_{b1}) & 2m_bR_b\Omega\sin(\phi_{b1}) & 2L_bm_bR_b\Omega\cos(\phi_{b1}) & 2L_bm_bR_b\Omega\sin(\phi_{b1}) \\ 2m_bR_b\Omega\cos(\phi_{b2}) & 2m_bR_b\Omega\sin(\phi_{b2}) & 2L_bm_bR_b\Omega\cos(\phi_{b2}) & 2L_bm_bR_b\Omega\sin(\phi_{b2}) \\ 2m_bR_b\Omega\cos(\phi_{b3}) & 2m_bR_b\Omega\sin(\phi_{b3}) & 2(-L_b+\sigma)m_bR_b\Omega\cos(\phi_{b3}) & 2(-L_b+\sigma)m_bR_b\Omega\sin(\phi_{b3}) \\ 2m_bR_b\Omega\cos(\phi_{b4}) & 2m_bR_b\Omega\sin(\phi_{b4}) & 2(-L_b+\sigma)m_bR_b\Omega\cos(\phi_{b4}) & 2(-L_b+\sigma)m_bR_b\Omega\sin(\phi_{b4}) \end{bmatrix}$$

$$\mathbf{C}_{22} = \begin{bmatrix} c_bR_b{}^2 & 0 & 0 & 0 \\ 0 & c_bR_b{}^2 & 0 & 0 \\ 0 & 0 & c_bR_b{}^2 & 0 \\ 0 & 0 & 0 & c_bR_b{}^2 \end{bmatrix}$$

$$\mathbf{C}_{33} = \begin{bmatrix} R_{C1}+R_{L1} & R_{C1}+R_{L1} & 0 & 0 & 0 & 0 & 0 & 0 \\ R_{C1}+R_{L1} & R_{C1}+R_{L1} & 0 & 0 & 0 & 0 & 0 & 0 \\ 0 & 0 & R_{C2}+R_{L2} & R_{C2}+R_{L2} & 0 & 0 & 0 & 0 \\ 0 & 0 & R_{C2}+R_{L2} & R_{C2}+R_{L2} & 0 & 0 & 0 & 0 \\ 0 & 0 & 0 & 0 & R_{C3}+R_{L3} & R_{C3}+R_{L3} & 0 & 0 \\ 0 & 0 & 0 & 0 & R_{C3}+R_{L3} & R_{C3}+R_{L3} & 0 & 0 \\ 0 & 0 & 0 & 0 & 0 & 0 & R_{C4}+R_{L4} & R_{C4}+R_{L4} \\ 0 & 0 & 0 & 0 & 0 & 0 & R_{C4}+R_{L4} & R_{C4}+R_{L4} \end{bmatrix}$$

$$\mathbf{C}_{32}=\begin{bmatrix} -\theta_e R_b & 0 & 0 & 0 \\ -\theta_e R_b & 0 & 0 & 0 \\ 0 & -\theta_e R_b & 0 & 0 \\ 0 & -\theta_e R_b & 0 & 0 \\ 0 & 0 & -\theta_e R_b & 0 \\ 0 & 0 & -\theta_e R_b & 0 \\ 0 & 0 & 0 & -\theta_e R_b \\ 0 & 0 & 0 & -\theta_e R_b \end{bmatrix}$$

$$\mathbf{K_{RS}}=\begin{bmatrix} \mathbf{K_{11}} & \mathbf{O}_{4\times4} & \mathbf{O}_{4\times8} \\ \mathbf{K}_{21} & \mathbf{O}_{4\times4} & \mathbf{O}_{4\times8} \\ \mathbf{O}_{8\times4} & \mathbf{O}_{8\times4} & \mathbf{K}_{33} \end{bmatrix}$$

Where $\mathbf{K_{RS}}$ is a rigid shaft 16×16 stiffness matrix, $\mathbf{K}_{11}$ and $\mathbf{K}_{21}$ are 4×4 matrices, $\mathbf{K}_{33}$ is a 8×8 matrix;

$$\mathbf{K_{11}}=\begin{bmatrix} 2k-\Omega^2(m_R+4m_b) & -2c\Omega & -2m_b\sigma\Omega^2 & 0 \\ 2c\Omega & 2k-\Omega^2(m_R+4m_b) & 0 & -2m_b\sigma\Omega^2 \\ -2m_b\sigma\Omega^2 & 0 & k_{33} & k_{34} \\ 0 & -2m_b\sigma\Omega^2 & k_{43} & k_{44} \end{bmatrix}$$

$$k_{33}=2kL_r{}^2-I_{mr}\Omega^2+J_{mr}\Omega^2-m_b\Omega^2(4L_b{}^2-2R_b{}^2-4L_b\sigma+2\sigma^2)+\frac{1}{2}m_bR_b{}^2\Omega^2\sum_{i=1}^{4}\cos(2\phi_{bi})+2m_bR_b{}^2\Omega\sum_{i=1}^{4}\cos^2(\phi_{bi})\dot{\phi}_{bi}$$

$$k_{43}=2cL_r{}^2\Omega+\frac{1}{2}m_bR_b{}^2\sum_{i=1}^{4}(\sin(2\phi_{bi})\Omega^2+2\Omega\sin(2\phi_{bi})\dot{\phi}_{bi}-\ddot{\phi}_{bi})$$

$$k_{34}=-2cL_r{}^2\Omega+\frac{1}{2}m_bR_b{}^2\sum_{i=1}^{4}(\sin(2\phi_{bi})\Omega^2+2\Omega\sin(2\phi_{bi})\dot{\phi}_{bi}+\ddot{\phi}_{bi})$$

$$k_{44}=2kL_r{}^2-I_{mr}\bar{\Omega}^2+J_{mr}\Omega^2-m_b\Omega^2(4L_b{}^2-2R_b{}^2-4L_b\sigma+2\sigma^2)-\frac{1}{2}m_bR_b{}^2\Omega^2\sum_{i=1}^{4}\cos(2\phi_{bi})+2m_bR_b{}^2\Omega\sum_{i=1}^{4}\sin^2(\phi_{bi})\dot{\phi}_{bi}$$

$$\mathbf{K}_{21}=\begin{bmatrix} m_bR_b\Omega^2\sin(\phi_{b1}) & -m_bR_b\Omega^2\cos(\phi_{b1}) & L_bm_bR_b\Omega^2\sin(\phi_{b1}) & -L_bm_bR_b\Omega^2\cos(\phi_{b1}) \\ m_bR_b\Omega^2\sin(\phi_{b2}) & -m_bR_b\Omega^2\cos(\phi_{b2}) & L_bm_bR_b\Omega^2\sin(\phi_{b2}) & -L_bm_bR_b\Omega^2\cos(\phi_{b2}) \\ m_bR_b\Omega^2\sin(\phi_{b3}) & -m_bR_b\Omega^2\cos(\phi_{b3}) & (-L_b+\sigma)m_bR_b\Omega^2\sin(\phi_{b3}) & (L_b-\sigma)m_bR_b\Omega^2\cos(\phi_{b3}) \\ m_bR_b\Omega^2\sin(\phi_{b4}) & -m_bR_b\Omega^2\cos(\phi_{b4}) & (-L_b+\sigma)m_bR_b\Omega^2\sin(\phi_{b4}) & (L_b-\sigma)m_bR_b\Omega^2\cos(\phi_{b4}) \end{bmatrix}$$

$$\mathbf{K}_{33}=\begin{bmatrix} 1/C_1 & 0 & 0 & 0 & 0 & 0 & 0 & 0 \\ 0 & 0 & 0 & 0 & 0 & 0 & 0 & 0 \\ 0 & 0 & 1/C_2 & 0 & 0 & 0 & 0 & 0 \\ 0 & 0 & 0 & 0 & 0 & 0 & 0 & 0 \\ 0 & 0 & 0 & 0 & 1/C_3 & 0 & 0 & 0 \\ 0 & 0 & 0 & 0 & 0 & 0 & 0 & 0 \\ 0 & 0 & 0 & 0 & 0 & 0 & 1/C_4 & 0 \\ 0 & 0 & 0 & 0 & 0 & 0 & 0 & 0 \end{bmatrix}$$

$$\mathbf{F}_{\mathrm{RS}}=\begin{bmatrix} m_e R_e \Omega^2 \cos(\phi_e)+m_b R_b \sum_{i=1}^{4}(\Omega^2\cos(\phi_{bi})+\cos(\phi_{bi})\dot{\phi}_{bi}^{\,2}) \\ m_e R_e \Omega^2 \sin(\phi_e)+m_b R_b \sum_{i=1}^{4}(\Omega^2\sin(\phi_{bi})+\sin(\phi_{bi})\dot{\phi}_{bi}^{\,2}) \\ m_e R_e x_e \Omega^2 \cos(\phi_e)+m_b R_b L_b \sum_{i=1}^{2}(\Omega^2\cos(\phi_{bi})+\cos(\phi_{bi})\dot{\phi}_{bi}^{\,2})+m_b R_b(-L_b+\sigma)\sum_{i=3}^{4}(\Omega^2\cos(\phi_{bi})+\cos(\phi_{bi})\dot{\phi}_{bi}^{\,2}) \\ m_e R_e x_e \Omega^2 \sin(\phi_e)+m_b R_b L_b \sum_{i=1}^{2}(\Omega^2\sin(\phi_{bi})+\sin(\phi_{bi})\dot{\phi}_{bi}^{\,2})+m_b R_b(-L_b+\sigma)\sum_{i=3}^{4}(\Omega^2\sin(\phi_{bi})+\sin(\phi_{bi})\dot{\phi}_{bi}^{\,2}) \\ 0 \\ 0 \\ 0 \\ 0 \\ 0 \\ 0 \\ 0 \\ 0 \\ 0 \\ 0 \\ 0 \\ 0 \end{bmatrix}$$

Where $\mathbf{F_{RS}}$ is a rigid shaft 16×1 force vector.

A6.2

The overall system inertia, damping, and stiffness matrices **M**, **C** and **K**, **F**, are shown here for Eq. (7-17).

$$\mathbf{M} = \begin{bmatrix} \mathbf{M_{11}} & \mathbf{M}_{21}{}^{\mathrm{T}} + \mathbf{M}_{12} & \mathbf{O}_{4\times4} \\ \mathbf{M_{21}} & \mathbf{M}_{22} & \mathbf{O}_{4\times4} \\ \mathbf{O}_{4\times4} & \mathbf{M}_{32}^{new} & \mathbf{M}_{33}^{new} \end{bmatrix}$$

Where **M** is a 12×12 mass matrix, **O** is a 4×4 zero matrix, $\mathbf{M}_{11}$, $\mathbf{M}_{21}$ and $\mathbf{M}_{22}$ are 4×4 matrices that are the same with previous definitions; $\mathbf{M}_{32}^{new}$ and $\mathbf{M}_{33}^{new}$ are newly defined as below:

$$\mathbf{M}_{32}^{new} = \begin{bmatrix} \frac{L_1\theta_e R_b}{R_{C1}+R_{L1}} & 0 & 0 & 0 \\ 0 & \frac{L_2\theta_e R_b}{R_{C2}+R_{L2}} & 0 & 0 \\ 0 & 0 & \frac{L_3\theta_e R_b}{R_{C3}+R_{L3}} & 0 \\ 0 & 0 & 0 & \frac{L_4\theta_e R_b}{R_{C4}+R_{L4}} \end{bmatrix}$$

$$\mathbf{M}_{12} = \frac{1}{2} m_b R_b{}^2 \begin{bmatrix} 0 & 0 & 0 & 0 \\ 0 & 0 & 0 & 0 \\ w_p & w_p & w_p & w_p \\ v_p & v_p & v_p & v_p \end{bmatrix}$$

$$\mathbf{M}_{33}^{new} = \begin{bmatrix} -L_1 & 0 & 0 & 0 \\ 0 & -L_2 & 0 & 0 \\ 0 & 0 & -L_3 & 0 \\ 0 & 0 & 0 & -L_4 \end{bmatrix}$$

$$\mathbf{C} = \begin{bmatrix} \mathbf{C_{11}} & -\mathbf{C}_{21}{}^{\mathrm{T}} + \mathbf{C}_{12} & \mathbf{O}_{4\times4} \\ \mathbf{C_{21}} & \mathbf{C}_{22}^{new} & \mathbf{O}_{4\times4} \\ \mathbf{O}_{4\times4} & \mathbf{O}_{4\times4} & \mathbf{C}_{33}^{new} \end{bmatrix}$$

Where **C** is a 12×12 damping matrix, $\mathbf{C}_{11}$ and $\mathbf{C}_{21}$ are 4×4 matrices that are the same with previous definitions; $\mathbf{C}_{22}^{new}$ and $\mathbf{C}_{33}^{new}$ are newly defined as below:

$$\mathbf{C}_{22}^{new}=\begin{bmatrix}\frac{R_b{}^2(c_b(R_{C1}+R_{L1})+\theta_e{}^2)}{R_{C1}+R_{L1}} & 0 & 0 & 0\\ 0 & \frac{R_b{}^2(c_b(R_{C2}+R_{L2})+\theta_e{}^2)}{R_{C2}+R_{L2}} & 0 & 0\\ 0 & 0 & \frac{R_b{}^2(c_b(R_{C3}+R_{L3})+\theta_e{}^2)}{R_{C3}+R_{L3}} & 0\\ 0 & 0 & 0 & \frac{R_b{}^2(c_b(R_{C4}+R_{L4})+\theta_e{}^2)}{R_{C4}+R_{L4}}\end{bmatrix}$$

$$\mathbf{C}_{33}^{new}=\begin{bmatrix}-\frac{L_1}{C_1(R_{C1}+R_{L1})} & 0 & 0 & 0\\ 0 & -\frac{L_2}{C_2(R_{C2}+R_{L2})} & 0 & 0\\ 0 & 0 & -\frac{L_3}{C_3(R_{C3}+R_{L3})} & 0\\ 0 & 0 & 0 & -\frac{L_4}{C_4(R_{C4}+R_{L4})}\end{bmatrix}$$

$$\mathbf{C}_{12}=2m_bR_b{}^2\begin{bmatrix}0 & 0 & 0 & 0\\ 0 & 0 & 0 & 0\\ \cos(\phi_{b1})^2v_p+\cos(\phi_{b1})\sin(\phi_{b1})w_p & \cos(\phi_{b2})^2v_p+\cos(\phi_{b2})\sin(\phi_{b2})w_p & \cos(\phi_{b3})^2v_p+\cos(\phi_{b3})\sin(\phi_{b3})w_p & \cos(\phi_{b4})^2v_p+\cos(\phi_{b4})\sin(\phi_{b4})w_p\\ \cos(\phi_{b1})\sin(\phi_{b1})v_p+\sin(\phi_{b1})^2w_p & \cos(\phi_{b2})\sin(\phi_{b2})v_p+\sin(\phi_{b2})^2w_p & \cos(\phi_{b3})\sin(\phi_{b3})v_p+\sin(\phi_{b3})^2w_p & \cos(\phi_{b4})\sin(\phi_{b4})v_p+\sin(\phi_{b4})^2w_p\end{bmatrix}$$

$$\mathbf{K}=\begin{bmatrix}\mathbf{K_{11}} & \mathbf{O}_{4\times4} & \mathbf{O}_{4\times4}\\ \mathbf{K}_{21} & \mathbf{O}_{4\times4} & \mathbf{K}_{23}^{new}\\ \mathbf{O}_{4\times4} & \mathbf{O}_{4\times4} & \mathbf{K}_{33}^{new}\end{bmatrix}$$

Where $\mathbf{K}$ is a 12×12 stiffness matrix, $\mathbf{K}_{11}$ and $\mathbf{K}_{21}$ are 4×4 matrices that are the same with previous definitions; $\mathbf{K}_{23}^{new}$ and $\mathbf{K}_{33}^{new}$ are newly defined as below:

$$\mathbf{K}_{23}^{new}=\begin{bmatrix}-\frac{R_b\theta_e}{C_1(R_{C1}+R_{L1})} & 0 & 0 & 0\\ 0 & -\frac{R_b\theta_e}{C_2(R_{C2}+R_{L2})} & 0 & 0\\ 0 & 0 & -\frac{R_b\theta_e}{C_3(R_{C3}+R_{L3})} & 0\\ 0 & 0 & 0 & -\frac{R_b\theta_e}{C_4(R_{C4}+R_{L4})}\end{bmatrix}$$

$$\mathbf{K}_{33}^{new}=\begin{bmatrix}-1/C_1 & 0 & 0 & 0\\ 0 & -1/C_2 & 0 & 0\\ 0 & 0 & -1/C_3 & 0\\ 0 & 0 & 0 & -1/C_4\end{bmatrix}$$

$$\mathbf{F}=\begin{bmatrix}
m_eR_e\Omega^2\cos(\phi_e)+m_bR_b\sum_{i=1}^{4}(\Omega^2\cos(\phi_{bi})+\cos(\phi_{bi})\dot{\phi}_{bi}{}^2)\\
m_eR_e\Omega^2\sin(\phi_e)+m_bR_b\sum_{i=1}^{4}(\Omega^2\sin(\phi_{bi})+\sin(\phi_{bi})\dot{\phi}_{bi}{}^2)\\
m_eR_ex_e\Omega^2\cos(\phi_e)+m_bR_bL_b\sum_{i=1}^{2}(\Omega^2\cos(\phi_{bi})+\cos(\phi_{bi})\dot{\phi}_{bi}{}^2)+m_bR_b(-L_b+\sigma)\sum_{i=3}^{4}(\Omega^2\cos(\phi_{bi})+\cos(\phi_{bi})\dot{\phi}_{bi}{}^2)\\
m_eR_ex_e\Omega^2\sin(\phi_e)+m_bR_bL_b\sum_{i=1}^{2}(\Omega^2\sin(\phi_{bi})+\sin(\phi_{bi})\dot{\phi}_{bi}{}^2)+m_bR_b(-L_b+\sigma)\sum_{i=3}^{4}(\Omega^2\sin(\phi_{bi})+\sin(\phi_{bi})\dot{\phi}_{bi}{}^2)\\
0\\0\\0\\0\\0\\0\\0\\0
\end{bmatrix}$$

A6.3

The overall system inertia, damping, and stiffness matrices $\mathbf{M_n}$, $\mathbf{C_n}$ and $\mathbf{K_n}$, $\mathbf{F_n}$, are shown here for Eq. (7-19).

$$\mathbf{M}_n=\begin{bmatrix}\mathbf{M}_{11}^n & \mathbf{M}_{21}^{n\,\mathrm{T}}+\mathbf{M}_{12}^n & \mathbf{O}_{4\times4}\\ \mathbf{M}_{21}^n & \mu\mathbf{I} & \mathbf{O}_{4\times4}\\ \mathbf{O}_{4\times4} & \varsigma_e\mathbf{I} & -\mathbf{I}\end{bmatrix}$$

Where $\mathbf{M}_n$ is a 12×12 nondimensional mass matrix, $\mathbf{O}$ and $\mathbf{I}$ are 4×4 zero matrix and identity matrix respectively, $\mathbf{M}_{11}^n$, $\mathbf{M}_{21}^n$ are 4×4 matrices;

$$\mathbf{M}_{11}^{n}=\begin{bmatrix} 1 & 0 & 2R_{bx}\mu & 0 \\ 0 & 1 & 0 & 2R_{bx}\mu \\ 2R_{bx}\mu & 0 & m_{33}^{n} & \frac{1}{2}\mu\sum_{i=1}^{4}\sin(2\phi_{bi}) \\ 0 & 2R_{bx}\mu & \frac{1}{2}\mu\sum_{i=1}^{4}\sin(2\phi_{bi}) & m_{44}^{n} \end{bmatrix}$$

$$m_{33}^{n}=J_{t}+2\mu+4\mu{R_{bL}}^{2}-4R_{bL}R_{bx}\mu+4\mu{R_{bx}}^{2}+\frac{1}{2}\mu\sum_{i=1}^{4}\cos(2\phi_{bi})$$

$$m_{44}^{n}=J_{t}+2\mu+4\mu{R_{bL}}^{2}-4R_{bL}R_{bx}\mu+4\mu{R_{bx}}^{2}-\frac{1}{2}\mu\sum_{i=1}^{4}\cos(2\phi_{bi})$$

$$\mathbf{M}_{21}^{n}=\begin{bmatrix} -\mu\sin(\phi_{b1}) & \mu\cos(\phi_{b1}) & -\mu R_{bL}\sin(\phi_{b1}) & \mu R_{bL}\cos(\phi_{b1}) \\ -\mu\sin(\phi_{b2}) & \mu\cos(\phi_{b2}) & -\mu R_{bL}\sin(\phi_{b2}) & \mu R_{bL}\cos(\phi_{b2}) \\ -\mu\sin(\phi_{b3}) & \mu\cos(\phi_{b3}) & \mu(R_{bL}-R_{bx})\sin(\phi_{b3}) & -\mu(R_{bL}-R_{bx})\cos(\phi_{b3}) \\ -\mu\sin(\phi_{b4}) & \mu\cos(\phi_{b4}) & \mu(R_{bL}-R_{bx})\sin(\phi_{b4}) & -\mu(R_{bL}-R_{bx})\cos(\phi_{b4}) \end{bmatrix}$$

$$\mathbf{M}_{12}^{n}=\frac{1}{2}\mu\begin{bmatrix} 0 & 0 & 0 & 0 \\ 0 & 0 & 0 & 0 \\ y_p & y_p & y_p & y_p \\ x_p & x_p & x_p & x_p \end{bmatrix}$$

$$\mathbf{C}_{n}=\begin{bmatrix} \mathbf{C}_{11}^{n} & -\mathbf{C}_{21}^{n\,\mathrm{T}}+\mathbf{C}_{12}^{n} & \mathbf{O}_{4\times4} \\ \mathbf{C}_{21}^{n} & (\varsigma_b+\varsigma_e)\mathbf{I} & \mathbf{O}_{4\times4} \\ \mathbf{O}_{4\times4} & \mathbf{O}_{4\times4} & -R_n\mathbf{I} \end{bmatrix}$$

Where $\mathbf{C}_n$ is a 12×12 nondimensional damping matrix, **O** and **I** are 4×4 zero matrix and identity matrix respectively, $\mathbf{C}_{11}^{n}$, $\mathbf{C}_{21}^{n}$ are 4×4 matrices;

$$\mathbf{C}_{11}^{n}=\begin{bmatrix} 2\varsigma & -2\bar{\Omega} & 0 & -4R_{bx}\mu\bar{\Omega} \\ 2\bar{\Omega} & 2\varsigma & 4R_{bx}\mu\bar{\Omega} & 0 \\ 0 & -4R_{bx}\mu\bar{\Omega} & 2{R_{rL}}^{2}\varsigma-\mu\sum_{i=1}^{4}\sin(2\phi_{bi})\phi'_{bi} & c_{34}^{n} \\ 4R_{bx}\mu\bar{\Omega} & 0 & c_{43}^{n} & 2{R_{rL}}^{2}\varsigma+\mu\sum_{i=1}^{4}\sin(2\phi_{bi})\phi'_{bi} \end{bmatrix}$$

$$c_{43}^{n} = (-J_p + 2J_t + 8\mu {R_{bL}}^2 - 8R_{bL}R_{bx}\mu + 4\mu {R_{bx}}^2)\bar{\Omega} - 2\mu\sum_{i=1}^{4}\sin^2(\phi_{bi})\phi'_{bi}$$

$$c_{34}^{n} = (J_p - 2J_t - 8\mu {R_{bL}}^2 + 8R_{bL}R_{bx}\mu - 4\mu {R_{bx}}^2)\bar{\Omega} + 2\mu\sum_{i=1}^{4}\cos^2(\phi_{bi})\phi'_{bi}$$

$$\mathbf{C}_{21}^{n} = \begin{bmatrix} 2\mu\bar{\Omega}\cos(\phi_{b1}) & 2\mu\bar{\Omega}\sin(\phi_{b1}) & 2\mu R_{bL}\bar{\Omega}\cos(\phi_{b1}) & 2\mu R_{bL}\bar{\Omega}\sin(\phi_{b1}) \\ 2\mu\bar{\Omega}\cos(\phi_{b2}) & 2\mu\bar{\Omega}\sin(\phi_{b2}) & 2\mu R_{bL}\bar{\Omega}\cos(\phi_{b2}) & 2\mu R_{bL}\bar{\Omega}\sin(\phi_{b2}) \\ 2\mu\bar{\Omega}\cos(\phi_{b3}) & 2\mu\bar{\Omega}\sin(\phi_{b3}) & -2\mu(R_{bL}-R_{bx})\bar{\Omega}\cos(\phi_{b3}) & -2\mu(R_{bL}-R_{bx})\bar{\Omega}\sin(\phi_{b3}) \\ 2\mu\bar{\Omega}\cos(\phi_{b4}) & 2\mu\bar{\Omega}\sin(\phi_{b4}) & -2\mu(R_{bL}-R_{bx})\bar{\Omega}\cos(\phi_{b4}) & -2\mu(R_{bL}-R_{bx})\bar{\Omega}\sin(\phi_{b4}) \end{bmatrix}$$

$$\mathbf{C}_{12}^{n} = 2\mu\bar{\Omega}\begin{bmatrix} 0 & 0 & 0 & 0 \\ 0 & 0 & 0 & 0 \\ \cos(\phi_{b1})^2 x_p + \cos(\phi_{b1})\sin(\phi_{b1}) y_p & \cos(\phi_{b2})^2 x_p + \cos(\phi_{b2})\sin(\phi_{b2}) y_p & \cos(\phi_{b3})^2 x_p + \cos(\phi_{b3})\sin(\phi_{b3}) y_p & \cos(\phi_{b4})^2 x_p + \cos(\phi_{b4})\sin(\phi_{b4}) y_p \\ \cos(\phi_{b1})\sin(\phi_{b1}) x_p + \sin(\phi_{b1})^2 y_p & \cos(\phi_{b2})\sin(\phi_{b2}) x_p + \sin(\phi_{b2})^2 y_p & \cos(\phi_{b3})\sin(\phi_{b3}) x_p + \sin(\phi_{b3})^2 y_p & \cos(\phi_{b4})\sin(\phi_{b4}) x_p + \sin(\phi_{b4})^2 y_p \end{bmatrix}$$

$$\mathbf{K}_n = \begin{bmatrix} \mathbf{K}_{11}^{n} & \mathbf{O}_{4\times4} & \mathbf{O}_{4\times4} \\ \mathbf{K}_{21}^{n} & \mathbf{O}_{4\times4} & -R_n\mathbf{I} \\ \mathbf{O}_{4\times4} & \mathbf{O}_{4\times4} & -C_n\mathbf{I} \end{bmatrix}$$

Where $\mathbf{K}_n$ is a 12×12 nondimensional stiffness matrix, **O** and **I** are 4×4 zero matrix and identity matrix respectively, $\mathbf{K}_{11}^{n}$, $\mathbf{K}_{21}^{n}$ are 4×4 matrices;

$$\mathbf{K}_{11}^{n} = \begin{bmatrix} 1-\bar{\Omega}^2 & 2\varsigma\bar{\Omega} & -2R_{bx}\mu\bar{\Omega}^2 & 0 \\ 2\varsigma\bar{\Omega} & 1-\bar{\Omega}^2 & 0 & -2R_{bx}\mu\bar{\Omega}^2 \\ -2R_{bx}\mu\bar{\Omega}^2 & 0 & k_{33}^{n} & k_{34}^{n} \\ 0 & -2R_{bx}\mu\bar{\Omega}^2 & k_{43}^{n} & k_{44}^{n} \end{bmatrix}$$

$$k_{33}^{n} = {R_{rL}}^2 + (J_p - J_t + 2\mu - 4{R_{bL}}^2\mu + 4R_{bL}R_{bx}\mu - 2{R_{bx}}^2\mu)\bar{\Omega}^2 + \frac{1}{2}\mu\sum_{i=1}^{4}(\bar{\Omega}^2\cos(2\phi_{bi}))$$

$$k_{43}^{n} = 2\bar{\Omega}{R_{rL}}^2\varsigma + \frac{1}{2}(\mu\sum_{i=1}^{4}(\sin(2\phi_{bi})\bar{\Omega}^2)\ \ k_{34}^{n} = -2\bar{\Omega}{R_{rL}}^2\varsigma + \frac{1}{2}(\mu\sum_{i=1}^{4}(\sin(2\phi_{bi})\bar{\Omega}^2)$$

$$k_{44}^{n} = {R_{rL}}^2 + (J_p - J_t + 2\mu - 4{R_{bL}}^2\mu + 4R_{bL}R_{bx}\mu - 2{R_{bx}}^2\mu)\bar{\Omega}^2 - \frac{1}{2}\mu\sum_{i=1}^{4}(\bar{\Omega}^2\cos(2\phi_{bi}))$$

$$\mathbf{K}_{21}^{n}=\begin{bmatrix} \mu\bar{\Omega}^2\sin(\phi_{b1}) & -\mu\bar{\Omega}^2\cos(\phi_{b1}) & \mu R_{bL}\bar{\Omega}^2\sin(\phi_{b1}) & -\mu R_{bL}\bar{\Omega}^2\cos(\phi_{b1}) \\ \mu\bar{\Omega}^2\sin(\phi_{b2}) & -\mu\bar{\Omega}^2\cos(\phi_{b2}) & \mu R_{bL}\bar{\Omega}^2\sin(\phi_{b2}) & -\mu R_{bL}\bar{\Omega}^2\cos(\phi_{b2}) \\ \mu\bar{\Omega}^2\sin(\phi_{b3}) & -\mu\bar{\Omega}^2\cos(\phi_{b3}) & -\mu(R_{bL}-R_{bx})\bar{\Omega}^2\sin(\phi_{b3}) & \mu(R_{bL}-R_{bx})\bar{\Omega}^2\cos(\phi_{b3}) \\ \mu\bar{\Omega}^2\sin(\phi_{b4}) & -\mu\bar{\Omega}^2\cos(\phi_{b4}) & -\mu(R_{bL}-R_{bx})\bar{\Omega}^2\sin(\phi_{b4}) & \mu(R_{bL}-R_{bx})\bar{\Omega}^2\cos(\phi_{b4}) \end{bmatrix}$$

$$\mathbf{F}_n=\begin{bmatrix} R_{ir}\mu_i\bar{\Omega}^2\cos(\phi_e)+\mu\sum_{i=1}^{4}(\bar{\Omega}^2\cos(\phi_{bi})+\cos(\phi_{bi})\phi_{bi}'^{\,2}) \\ R_{ir}\mu_i\bar{\Omega}^2\sin(\phi_e)+\mu\sum_{i=1}^{4}(\bar{\Omega}^2\sin(\phi_{bi})+\sin(\phi_{bi})\phi_{bi}'^{\,2}) \\ R_{ir}\mu_i R_{ix}\bar{\Omega}^2\cos(\phi_e)+\mu R_{bL}\sum_{i=1}^{2}(\bar{\Omega}^2\cos(\phi_{bi})+\cos(\phi_{bi})\phi_{bi}'^{\,2})-\mu(R_{bL}-R_{bx})\sum_{i=3}^{4}(\bar{\Omega}^2\cos(\phi_{bi})+\cos(\phi_{bi})\phi_{bi}'^{\,2}) \\ R_{ir}\mu_i R_{ix}\bar{\Omega}^2\sin(\phi_e)+\mu R_{bL}\sum_{i=1}^{2}(\bar{\Omega}^2\sin(\phi_{bi})+\sin(\phi_{bi})\phi_{bi}'^{\,2})-\mu(R_{bL}-R_{bx})\sum_{i=3}^{4}(\bar{\Omega}^2\sin(\phi_{bi})+\sin(\phi_{bi})\phi_{bi}'^{\,2}) \\ 0 \\ 0 \\ 0 \\ 0 \\ 0 \\ 0 \\ 0 \\ 0 \end{bmatrix}$$

A6.4

The dimensionless system matrices $\mathbf{M}_L$, $\mathbf{C}_L$, $\mathbf{K}_L$, $\mathbf{F}_L$ are shown here for Eq. (7-25).

$$\mathbf{M}_L=\begin{bmatrix} \mathbf{M}_{11}^{L} & \mathbf{M}_{12}^{L} & \mathbf{O}_{4\times4} \\ \mathbf{M}_{21}^{L} & \mu\mathbf{I} & \mathbf{O}_{4\times4} \\ \mathbf{O}_{4\times4} & \mathbf{O}_{4\times4} & -\mathbf{I} \end{bmatrix}$$

Where $\mathbf{M}_L$ is a 12×12 nondimensional mass matrix, $\mathbf{O}$ and $\mathbf{I}$ are 4×4 zero matrix and identity matrix respectively, $\mathbf{M}_{11}^{L}$, $\mathbf{M}_{21}^{L}$, $\mathbf{M}_{12}^{L}$ are 4×4 matrices;

$$\mathbf{M}_{11}^{L}=\begin{bmatrix} 1 & 0 & 2R_{bx}\mu & 0 \\ 0 & 1 & 0 & 2R_{bx}\mu \\ 2R_{bx}\mu & 0 & m_{33}^{L} & \frac{1}{2}\mu\sum_{i=1}^{4}\sin(2\phi_{bi}) \\ 0 & 2R_{bx}\mu & \frac{1}{2}\mu\sum_{i=1}^{4}\sin(2\phi_{bi}) & m_{44}^{L} \end{bmatrix}$$

$$m_{33}^{L}=J_{t}+4\mu {R_{bL}}^{2}-4R_{bL}R_{bx}\mu+2\mu {R_{bx}}^{2}+\mu\sum_{i=1}^{4}\cos^{2}(\phi_{bi})$$

$$m_{44}^{L}=J_{t}+4\mu+4\mu {R_{bL}}^{2}-4R_{bL}R_{bx}\mu+2\mu {R_{bx}}^{2}-\mu\sum_{i=1}^{4}\cos^{2}(\phi_{bi})$$

$$\mathbf{M}_{21}^{L}=\begin{bmatrix} -\mu\sin(\phi_{b1}) & \mu\cos(\phi_{b1}) & -\mu R_{bL}\sin(\phi_{b1}) & \mu R_{bL}\cos(\phi_{b1}) \\ -\mu\sin(\phi_{b2}) & \mu\cos(\phi_{b2}) & -\mu R_{bL}\sin(\phi_{b2}) & \mu R_{bL}\cos(\phi_{b2}) \\ -\mu\sin(\phi_{b3}) & \mu\cos(\phi_{b3}) & \mu(R_{bL}-R_{bx})\sin(\phi_{b3}) & -\mu(R_{bL}-R_{bx})\cos(\phi_{b3}) \\ -\mu\sin(\phi_{b4}) & \mu\cos(\phi_{b4}) & \mu(R_{bL}-R_{bx})\sin(\phi_{b4}) & -\mu(R_{bL}-R_{bx})\cos(\phi_{b4}) \end{bmatrix}$$

$$\mathbf{M}_{12}^{L}=\begin{bmatrix} -\mu\sin(\phi_{b1}) & -\mu\sin(\phi_{b2}) & -\mu\sin(\phi_{b3}) & -\mu\sin(\phi_{b4}) \\ \mu\cos(\phi_{b1}) & \mu\cos(\phi_{b2}) & \mu\cos(\phi_{b3}) & \mu\cos(\phi_{b4}) \\ \frac{1}{2}\mu(y_{p}-2R_{bL}\sin(\phi_{b1})) & \frac{1}{2}\mu(y_{p}-2R_{bL}\sin(\phi_{b2})) & \frac{1}{2}\mu(y_{p}+2(R_{bL}-R_{bx})\sin(\phi_{b3})) & \frac{1}{2}\mu(y_{p}+2(R_{bL}-R_{bx})\sin(\phi_{b4})) \\ -\frac{1}{2}\mu(x_{p}-2R_{bL}\cos(\phi_{b1})) & -\frac{1}{2}\mu(x_{p}-2R_{bL}\cos(\phi_{b2})) & -\frac{1}{2}\mu(x_{p}+2(R_{bL}-R_{bx})\cos(\phi_{b3})) & -\frac{1}{2}\mu(x_{p}+2(R_{bL}-R_{bx})\cos(\phi_{b4})) \end{bmatrix}$$

$$\mathbf{C}_{L}=\begin{bmatrix} \mathbf{C}_{11}^{L} & \mathbf{C}_{12}^{L} & \mathbf{O}_{4\times4} \\ \mathbf{C}_{21}^{L} & (\varsigma_{b}+\varsigma_{e})\mathbf{I} & \mathbf{O}_{4\times4} \\ \mathbf{O}_{4\times4} & \mathbf{O}_{4\times4} & -R_{n}\mathbf{I} \end{bmatrix}$$

Where $\mathbf{C}_{\mathrm{L}}$ is a 12×12 nondimensional damping matrix, **O** and **I** are 4×4 zero matrix and identity matrix respectively, $\mathbf{C}_{11}^{L}$, $\mathbf{C}_{21}^{L}$, $\mathbf{C}_{12}^{L}$ are 4×4 matrices;

$$\mathbf{C}_{11}^{L}=\begin{bmatrix} 2\varsigma & -2\bar{\Omega} & 0 & -4R_{bx}\mu\bar{\Omega} \\ 2\bar{\Omega} & 2\varsigma & 4R_{bx}\mu\bar{\Omega} & 0 \\ 0 & -4R_{bx}\mu\bar{\Omega} & 2{R_{rL}}^{2}\varsigma-\mu\sum_{i=1}^{4}\sin(2\phi_{bi})\phi'_{bi} & c_{34}^{L} \\ 4R_{bx}\mu\bar{\Omega} & 0 & c_{43}^{L} & 2{R_{rL}}^{2}\varsigma+\mu\sum_{i=1}^{4}\sin(2\phi_{bi})\phi'_{bi} \end{bmatrix}$$

$$c_{43}^{L}=(-J_p+2J_t+8\mu {R_{bL}}^2-8R_{bL}R_{bx}\mu+4\mu {R_{bx}}^2)\bar{\Omega}-2\mu\sum_{i=1}^{4}\sin^2(\phi_{bi})\phi'_{bi}$$

$$c_{34}^{L}=(J_p-2J_t-8\mu {R_{bL}}^2+8R_{bL}R_{bx}\mu-4\mu {R_{bx}}^2)\bar{\Omega}+2\mu\sum_{i=1}^{4}\cos^2(\phi_{bi})\phi'_{bi}$$

$$\mathbf{C}_{21}^{L}=\begin{bmatrix}2\mu\bar{\Omega}\cos(\phi_{b1}) & 2\mu\bar{\Omega}\sin(\phi_{b1}) & 2\mu R_{bL}\bar{\Omega}\cos(\phi_{b1}) & 2\mu R_{bL}\bar{\Omega}\sin(\phi_{b1})\\ 2\mu\bar{\Omega}\cos(\phi_{b2}) & 2\mu\bar{\Omega}\sin(\phi_{b2}) & 2\mu R_{bL}\bar{\Omega}\cos(\phi_{b2}) & 2\mu R_{bL}\bar{\Omega}\sin(\phi_{b2})\\ 2\mu\bar{\Omega}\cos(\phi_{b3}) & 2\mu\bar{\Omega}\sin(\phi_{b3}) & -2\mu(R_{bL}-R_{bx})\bar{\Omega}\cos(\phi_{b3}) & -2\mu(R_{bL}-R_{bx})\bar{\Omega}\sin(\phi_{b3})\\ 2\mu\bar{\Omega}\cos(\phi_{b4}) & 2\mu\bar{\Omega}\sin(\phi_{b4}) & -2\mu(R_{bL}-R_{bx})\bar{\Omega}\cos(\phi_{b4}) & -2\mu(R_{bL}-R_{bx})\bar{\Omega}\sin(\phi_{b4})\end{bmatrix}$$

$$\mathbf{C}_{12}^{L}=\begin{bmatrix}-2\mu(\bar{\Omega}+\phi'_{b1})\cos(\phi_{b1}) & -2\mu(\bar{\Omega}+\phi'_{b2})\cos(\phi_{b2}) & -2\mu(\bar{\Omega}+\phi'_{b3})\cos(\phi_{b3}) & -2\mu(\bar{\Omega}+\phi'_{b4})\cos(\phi_{b4})\\ -2\mu(\bar{\Omega}+\phi'_{b1})\sin(\phi_{b1}) & -2\mu(\bar{\Omega}+\phi'_{b2})\sin(\phi_{b2}) & -2\mu(\bar{\Omega}+\phi'_{b3})\sin(\phi_{b3}) & -2\mu(\bar{\Omega}+\phi'_{b4})\sin(\phi_{b4})\\ c_{31} & c_{32} & c_{33} & c_{34}\\ c_{41} & c_{42} & c_{43} & c_{44}\end{bmatrix}$$

$$c_{3i}=2\mu\cos(\phi_{bi})(-\phi'_{bi}R_{bL}+y_p\cos(\phi_{bi})-x_p\sin(\phi_{bi})+\bar{\Omega}(-R_{bL}+x_p\cos(\phi_{bi})+y_p\sin(\phi_{bi}))\ i=1,2$$

$$c_{4i}=2\mu\sin(\phi_{bi})(-\phi'_{bi}R_{bL}+y_p\cos(\phi_{bi})-x_p\sin(\phi_{bi})+\bar{\Omega}(-R_{bL}+x_p\cos(\phi_{bi})+y_p\sin(\phi_{bi}))\ i=1,2$$

$$c_{3i}=2\mu\cos(\phi_{bi})(\phi'_{bi}(R_{bL}-R_{bx})+y_p\cos(\phi_{bi})-x_p\sin(\phi_{bi})+\bar{\Omega}((R_{bL}-R_{bx})+x_p\cos(\phi_{bi})+y_p\sin(\phi_{bi}))\ i=3,4$$

$$c_{4i}=2\mu\sin(\phi_{bi})(\phi'_{bi}(R_{bL}-R_{bx})+y_p\cos(\phi_{bi})-x_p\sin(\phi_{bi})+\bar{\Omega}((R_{bL}-R_{bx})+x_p\cos(\phi_{bi})+y_p\sin(\phi_{bi}))\ i=3,4$$

$$\mathbf{K}_L=\begin{bmatrix}\mathbf{K}_{11}^{L} & \mathbf{K}_{12}^{L} & \mathbf{O}_{4\times4}\\ \mathbf{K}_{21}^{L} & \mathbf{K}_{22}^{L} & -R_n\mathbf{I}\\ \mathbf{O}_{4\times4} & \mathbf{O}_{4\times4} & -C_n\mathbf{I}\end{bmatrix}$$

Where $\mathbf{K}_n$ is a 12×12 nondimensional stiffness matrix, **O** and **I** are 4×4 zero matrix and identity matrix respectively, $\mathbf{K}_{11}^{n}$, $\mathbf{K}_{21}^{n}$ are 4×4 matrices;

$$\mathbf{K}_{11}^{L}=\begin{bmatrix}1-\bar{\Omega}^2 & 2\zeta\bar{\Omega} & -2R_{bx}\mu\bar{\Omega}^2 & 0\\ 2\zeta\bar{\Omega} & 1-\bar{\Omega}^2 & 0 & -2R_{bx}\mu\bar{\Omega}^2\\ -2R_{bx}\mu\bar{\Omega}^2 & 0 & k_{33}^{L} & k_{34}^{L}\\ 0 & -2R_{bx}\mu\bar{\Omega}^2 & k_{43}^{L} & k_{44}^{L}\end{bmatrix}$$

$$k_{33}^{L} = R_{rL}{}^{2} + (J_p - J_t - 4R_{bL}{}^{2}\mu + 4R_{bL}R_{bx}\mu - 2R_{bx}{}^{2}\mu)\bar{\Omega}^2 + \mu\sum_{i=1}^{4}(\bar{\Omega}^2\cos^2(\phi_{bi}))$$

$$k_{43}^{L} = 2\bar{\Omega}R_{rL}{}^{2}\varsigma + \frac{1}{2}(\mu\sum_{i=1}^{4}(\sin(2\phi_{bi})\bar{\Omega}^2)\ k_{34}^{L} = -2\bar{\Omega}R_{rL}{}^{2}\varsigma + \frac{1}{2}(\mu\sum_{i=1}^{4}(\sin(2\phi_{bi})\bar{\Omega}^2)$$

$$k_{44}^{L} = R_{rL}{}^{2} + (J_p - J_t + 4\mu - 4R_{bL}{}^{2}\mu + 4R_{bL}R_{bx}\mu - 2R_{bx}{}^{2}\mu)\bar{\Omega}^2 - \mu\sum_{i=1}^{4}(\bar{\Omega}^2\cos^2(\phi_{bi}))$$

$$\mathbf{K}_{21}^{L} = \begin{bmatrix} \mu\bar{\Omega}^2\sin(\phi_{b1}) & -\mu\bar{\Omega}^2\cos(\phi_{b1}) & \mu R_{bL}\bar{\Omega}^2\sin(\phi_{b1}) & -\mu R_{bL}\bar{\Omega}^2\cos(\phi_{b1}) \\ \mu\bar{\Omega}^2\sin(\phi_{b2}) & -\mu\bar{\Omega}^2\cos(\phi_{b2}) & \mu R_{bL}\bar{\Omega}^2\sin(\phi_{b2}) & -\mu R_{bL}\bar{\Omega}^2\cos(\phi_{b2}) \\ \mu\bar{\Omega}^2\sin(\phi_{b3}) & -\mu\bar{\Omega}^2\cos(\phi_{b3}) & -\mu(R_{bL}-R_{bx})\bar{\Omega}^2\sin(\phi_{b3}) & \mu(R_{bL}-R_{bx})\bar{\Omega}^2\cos(\phi_{b3}) \\ \mu\bar{\Omega}^2\sin(\phi_{b4}) & -\mu\bar{\Omega}^2\cos(\phi_{b4}) & -\mu(R_{bL}-R_{bx})\bar{\Omega}^2\sin(\phi_{b4}) & \mu(R_{bL}-R_{bx})\bar{\Omega}^2\cos(\phi_{b4}) \end{bmatrix}$$

$$\mathbf{K}_{22}^{L} = \begin{bmatrix} k_{11} & 0 & 0 & 0 \\ 0 & k_{22} & 0 & 0 \\ 0 & 0 & k_{33} & 0 \\ 0 & 0 & 0 & k_{44} \end{bmatrix}$$

$$k_{ii} = \mu\bar{\Omega}^2((x + R_{bL}x_p)\cos(\phi_{bi}) + (y + R_{bL}y_p)\sin(\phi_{bi})),\ i=1,2;$$

$$k_{ii} = \mu\bar{\Omega}^2((x - (R_{bL}-R_{bx})x_p)\cos(\phi_{bi}) + (y - (R_{bL}-R_{bx})y_p)\sin(\phi_{bi})),\ i=3,4;$$

$$\mathbf{K}_{12}^{L} = \begin{bmatrix} \mu\bar{\Omega}^2\sin(\phi_{b1}) & \mu\bar{\Omega}^2\sin(\phi_{b2}) & \mu\bar{\Omega}^2\sin(\phi_{b3}) & \mu\bar{\Omega}^2\sin(\phi_{b4}) \\ -\mu\bar{\Omega}^2\cos(\phi_{b1}) & -\mu\bar{\Omega}^2\cos(\phi_{b2}) & -\mu\bar{\Omega}^2\cos(\phi_{b3}) & -\mu\bar{\Omega}^2\cos(\phi_{b4}) \\ k_{31} & k_{32} & k_{33} & k_{34} \\ k_{41} & k_{42} & k_{43} & k_{44} \end{bmatrix}$$

$$k_{3j} = -\mu\bar{\Omega}^2(y_p\cos(2\phi_{bj}) + (R_{bL} - 2x_p\cos(\phi_{bj}))\sin(\phi_{bj})),\ j = 1,2$$

$$k_{3j} = -\mu\bar{\Omega}^2(y_p\cos(2\phi_{bj}) + (-R_{bL} + R_{bx} - 2x_p\cos(\phi_{bj}))\sin(\phi_{bj})),\ j = 3,4$$

$$k_{4j} = -\mu\bar{\Omega}^2(y_p\sin(2\phi_{bj}) + (R_{bL} - 2x_p\sin(\phi_{bj}))\cos(\phi_{bj})),\ j = 1,2$$

$$k_{4j} = -\mu\bar{\Omega}^2(y_p\sin(2\phi_{bj}) + (-R_{bL} + R_{bx} - 2x_p\sin(\phi_{bj}))\cos(\phi_{bj})),\ j = 3,4$$

$$\mathbf{F}_L = \begin{bmatrix} R_{ir}\mu_i\bar{\Omega}^2\cos(\phi_e) + \mu\sum_{i=1}^{4}(\bar{\Omega}^2\cos(\phi_{bi})) \\ R_{ir}\mu_i\bar{\Omega}^2\sin(\phi_e) + \mu\sum_{i=1}^{4}(\bar{\Omega}^2\sin(\phi_{bi})) \\ R_{ir}\mu_i R_{ix}\bar{\Omega}^2\cos(\phi_e) + \mu R_{bL}\sum_{i=1}^{2}(\bar{\Omega}^2\cos(\phi_{bi})) - \mu(R_{bL}-R_{bx})\sum_{i=3}^{4}(\bar{\Omega}^2\cos(\phi_{bi})) \\ R_{ir}\mu_i R_{ix}\bar{\Omega}^2\sin(\phi_e) + \mu R_{bL}\sum_{i=1}^{2}(\bar{\Omega}^2\sin(\phi_{bi})) - \mu(R_{bL}-R_{bx})\sum_{i=3}^{4}(\bar{\Omega}^2\sin(\phi_{bi})) \\ 0 \\ 0 \\ 0 \\ 0 \\ 0 \\ 0 \\ 0 \end{bmatrix}$$

A7.1

$\mathbf{C_o}$, $\mathbf{C}$ and $\mathbf{K_L}$ are given below for Eq. (2-24), Eq. (2-25) and Eq. (2-44), respectively.

$$\mathbf{C_o} = \begin{bmatrix} c & -2(m_R+2m_b)\Omega & -2m_bR_b\Omega\cos(\phi_{b1}) & -2m_bR_b\Omega\cos(\phi_{b2}) & 0 & 0 & 0 & 0 \\ 2(m_R+2m_b)\Omega & c & -2m_bR_b\Omega\sin(\phi_{b1}) & -2m_bR_b\Omega\sin(\phi_{b1}) & 0 & 0 & 0 & 0 \\ 2m_bR_b\Omega\cos(\phi_{b1}) & 2m_bR_b\Omega\sin(\phi_{b1}) & c_bR_b{}^2 & 0 & \theta_eR_b & \theta_eR_b & 0 & 0 \\ 2m_bR_b\Omega\cos(\phi_{b2}) & 2m_bR_b\Omega\sin(\phi_{b1}) & 0 & c_bR_b{}^2 & 0 & 0 & \theta_eR_b & \theta_eR_b \\ 0 & 0 & -\theta_eR_b & 0 & R_{C1}+R_{L1} & R_{C1}+R_{L1} & 0 & 0 \\ 0 & 0 & -\theta_eR_b & 0 & R_{C1}+R_{L1} & R_{C1}+R_{L1} & 0 & 0 \\ 0 & 0 & 0 & -\theta_eR_b & 0 & 0 & R_{C2}+R_{L2} & R_{C2}+R_{L2} \\ 0 & 0 & 0 & -\theta_eR_b & 0 & 0 & R_{C2}+R_{L2} & R_{C2}+R_{L2} \end{bmatrix}$$

$$\mathbf{C} = \begin{bmatrix} c & -2(m_R+2m_b)\Omega & -2m_bR_b\Omega\cos(\phi_{b1}) & -2m_bR_b\Omega\cos(\phi_{b2}) & 0 & 0 \\ 2(m_R+2m_b)\Omega & c & -2m_bR_b\Omega\sin(\phi_{b1}) & -2m_bR_b\Omega\sin(\phi_{b2}) & 0 & 0 \\ 2m_bR_b\Omega\cos(\phi_{b1}) & 2m_bR_b\Omega\sin(\phi_{b1}) & \dfrac{R_b{}^2(c_b(R_{C1}+R_{L1})+\theta_e{}^2)}{R_{C1}+R_{L1}} & 0 & 0 & 0 \\ 2m_bR_b\Omega\cos(\phi_{b2}) & 2m_bR_b\Omega\sin(\phi_{b2}) & 0 & \dfrac{R_b{}^2(c_b(R_{C2}+R_{L2})+\theta_e{}^2)}{R_{C2}+R_{L2}} & 0 & 0 \\ 0 & 0 & 0 & 0 & -\dfrac{L_1}{C_1(R_{C1}+R_{L1})} & 0 \\ 0 & 0 & 0 & 0 & 0 & -\dfrac{L_2}{C_2(R_{C2}+R_{L2})} \end{bmatrix}$$

$$\mathbf{K}_L = \begin{bmatrix} 1-\bar{\Omega}^2 & -\varsigma\bar{\Omega} & \mu\bar{\Omega}^2\sin(b_1) & \mu\bar{\Omega}^2\sin(b_2) & 0 & 0 \\ \varsigma\bar{\Omega} & 1-\bar{\Omega}^2 & -\mu\bar{\Omega}^2\cos(b_1) & -\mu\bar{\Omega}^2\cos(b_2) & 0 & 0 \\ \mu\bar{\Omega}^2\sin(b_1) & -\mu\bar{\Omega}^2\cos(b_1) & \mu\bar{\Omega}^2(x_s\cos(b_1)+y_s\sin(b_1)) & 0 & -R_n & 0 \\ \mu\bar{\Omega}^2\sin(b_2) & -\mu\bar{\Omega}^2\cos(b_2) & 0 & \mu\bar{\Omega}^2(x_s\cos(b_2)+y_s\sin(b_2)) & 0 & -R_n \\ 0 & 0 & 0 & 0 & -C_n & 0 \\ 0 & 0 & 0 & 0 & 0 & -C_n \end{bmatrix}$$

A7.2

$\mathbf{C}_{\text{wlc}}$, $\mathbf{K}_{\text{wlc}}$ are given here for Eq. (3-11).

$$\mathbf{C}_{\text{wlc}} = \begin{bmatrix} \varsigma & -2\bar{\Omega} & -2\mu(\bar{\Omega}+b'_{\text{wlc},1})\cos(b_{\text{wlc},1}) & -2\mu(\bar{\Omega}+b'_{\text{wlc},2})\cos(b_{\text{wlc},2}) & 0 & 0 \\ 2\bar{\Omega} & \varsigma & -2\mu(\bar{\Omega}+b'_{\text{wlc},1})\sin(b_{\text{wlc},1}) & -2\mu(\bar{\Omega}+b'_{\text{wlc},2})\sin(b_{\text{wlc},2}) & 0 & 0 \\ 2\mu\bar{\Omega}\cos(b_{\text{wlc},1}) & 2\mu\bar{\Omega}\sin(b_{\text{wlc},1}) & \varsigma_b+\varsigma_e & 0 & 0 & 0 \\ 2\mu\bar{\Omega}\cos(b_{\text{wlc},2}) & 2\mu\bar{\Omega}\sin(b_{\text{wlc},2}) & 0 & \varsigma_b+\varsigma_e & 0 & 0 \\ 0 & 0 & 0 & 0 & -R_n & 0 \\ 0 & 0 & 0 & 0 & 0 & -R_n \end{bmatrix}$$

$$\mathbf{K}_{\text{wlc}} = \begin{bmatrix} 1-\bar{\Omega}^2 & -\varsigma\bar{\Omega} & \mu(-b''_{\text{wlc},1}\cos(b_{\text{wlc},1}) + (b'_{\text{wlc},1}+\bar{\Omega})^2\sin(b_{\text{wlc},1})) \\ \varsigma\bar{\Omega} & 1-\bar{\Omega}^2 & -\mu(b''_{\text{wlc},1}\sin(b_{\text{wlc},1}) + (b'_{\text{wlc},1}+\bar{\Omega})^2\cos(b_{\text{wlc},1})) \\ \mu\bar{\Omega}^2\sin(b_{\text{wlc},1}) & -\mu\bar{\Omega}^2\cos(b_{\text{wlc},1}) & \mu((x_{\text{wlc}}\bar{\Omega}^2 + 2\bar{\Omega}y_{\text{wlc}} - x''_{\text{wlc}})\cos(b_{\text{wlc},1}) + (y_{\text{wlc}}\bar{\Omega}^2 - 2\bar{\Omega}x_{\text{wlc}} - y''_{\text{wlc}})\sin(b_{\text{wlc},1})) \\ \mu\bar{\Omega}^2\sin(b_{\text{wlc},2}) & -\mu\bar{\Omega}^2\cos(b_{\text{wlc},2}) & 0 \\ 0 & 0 & 0 \\ 0 & 0 & 0 \end{bmatrix}$$

$$\begin{bmatrix} \mu(-b''_{\text{wlc},2}\cos(b_{\text{wlc},2}) + (b'_{\text{wlc},2}+\bar{\Omega})^2\sin(b_{\text{wlc},2}) & 0 & 0 \\ -\mu(b''_{\text{wlc},2}\sin(b_{\text{wlc},2}) + (b'_{\text{wlc},2}+\bar{\Omega})^2\cos(b_{\text{wlc},2})) & 0 & 0 \\ 0 & -R_n & 0 \\ \mu((x_{\text{wlc}}\bar{\Omega}^2 + 2\bar{\Omega}y_{\text{wlc}} - x''_{\text{wlc}})\cos(b_{\text{wlc},2}) + (y_{\text{wlc}}\bar{\Omega}^2 - 2\bar{\Omega}x_{\text{wlc}} - y''_{\text{wlc}})\sin(b_{\text{wlc},2})) & 0 & -R_n \\ 0 & -C_n & 0 \\ 0 & 0 & -C_n \end{bmatrix}$$

A7.3

$\mathbf{M}_o$, $\mathbf{C}_o$ are given here for Eq. (4-9) and $\mathbf{M}$ is shown here for Eq. (4-10)

$$\mathbf{M_o} = \begin{bmatrix} m_R + 2m_b & 0 & -m_b R_b \sin(\phi_{b1} + \phi(t)) & -m_b R_b \sin(\phi_{b2} + \phi(t)) & 0 & 0 & 0 & 0 \\ 0 & m_R + 2m_b & m_b R_b \cos(\phi_{b1} + \phi(t)) & m_b R_b \cos(\phi_{b2} + \phi(t)) & 0 & 0 & 0 & 0 \\ -m_b R_b \sin(\phi_{b1} + \phi(t)) & m_b R_b \cos(\phi_{b1} + \phi(t)) & m_b {R_b}^2 & 0 & 0 & 0 & 0 & 0 \\ -m_b R_b \sin(\phi_{b2} + \phi(t)) & m_b R_b \cos(\phi_{b2} + \phi(t)) & 0 & m_b {R_b}^2 & 0 & 0 & 0 & 0 \\ 0 & 0 & 0 & 0 & 0 & 0 & 0 & 0 \\ 0 & 0 & 0 & 0 & 0 & L_1 & 0 & 0 \\ 0 & 0 & 0 & 0 & 0 & 0 & 0 & 0 \\ 0 & 0 & 0 & 0 & 0 & 0 & 0 & L_2 \end{bmatrix}$$

$$\mathbf{C_o} = \begin{bmatrix} c_1 & 0 & -2m_b R_b \Omega \cos(\phi_{b1} + \phi(t)) & -2m_b R_b \Omega \cos(\phi_{b2} + \phi(t)) & 0 & 0 & 0 & 0 \\ 0 & c_2 & -2m_b R_b \Omega \sin(\phi_{b1} + \phi(t)) & -2m_b R_b \Omega \sin(\phi_{b1} + \phi(t)) & 0 & 0 & 0 & 0 \\ 0 & 0 & c_b {R_b}^2 & 0 & \theta_e R_b & \theta_e R_b & 0 & 0 \\ 0 & 0 & 0 & c_b {R_b}^2 & 0 & 0 & \theta_e R_b & \theta_e R_b \\ 0 & 0 & -\theta_e R_b & 0 & R_{C1} + R_{L1} & R_{C1} + R_{L1} & 0 & 0 \\ 0 & 0 & -\theta_e R_b & 0 & R_{C1} + R_{L1} & R_{C1} + R_{L1} & 0 & 0 \\ 0 & 0 & 0 & -\theta_e R_b & 0 & 0 & R_{C2} + R_{L2} & R_{C2} + R_{L2} \\ 0 & 0 & 0 & -\theta_e R_b & 0 & 0 & R_{C2} + R_{L2} & R_{C2} + R_{L2} \end{bmatrix}$$

$$\mathbf{M} = \begin{bmatrix} m_R + 2m_b & 0 & -m_b R_b \sin(\phi_{b1} + \phi(t)) & -m_b R_b \sin(\phi_{b2} + \phi(t)) & 0 & 0 \\ 0 & m_R + 2m_b & m_b R_b \cos(\phi_{b1} + \phi(t)) & m_b R_b \cos(\phi_{b2} + \phi(t)) & 0 & 0 \\ -m_b R_b \sin(\phi_{b1} + \phi(t)) & m_b R_b \cos(\phi_{b1} + \phi(t)) & m_b {R_b}^2 & 0 & 0 & 0 \\ -m_b R_b \sin(\phi_{b2} + \phi(t)) & m_b R_b \cos(\phi_{b2} + \phi(t)) & 0 & m_b {R_b}^2 & 0 & 0 \\ 0 & 0 & \dfrac{L_1 \theta_e R_b}{R_{C1} + R_{L1}} & 0 & -L_1 & 0 \\ 0 & 0 & 0 & \dfrac{L_2 \theta_e R_b}{R_{C2} + R_{L2}} & 0 & -L_1 \end{bmatrix}$$

A7.4

$\mathbf{M}_{\text{wlc}}$, $\mathbf{F}_{\text{wlc}}$ are given here for Eq. (5-24).

$$\mathbf{M}_{\text{wlc}} = \begin{bmatrix} 1 & 0 & -\mu\sin(b_{\text{wlc},1}+\bar{\Omega}\tau) & -\mu\sin(b_{\text{wlc},2}+\bar{\Omega}\tau) & 0 & 0 \\ 0 & 1 & \mu\cos(b_{\text{wlc},1}+\bar{\Omega}\tau) & \mu\cos(b_{\text{wlc},2}+\bar{\Omega}\tau) & 0 & 0 \\ -\mu\sin(b_{\text{wlc},1}+\bar{\Omega}\tau) & \mu\cos(b_{\text{wlc},1}+\bar{\Omega}\tau) & \mu & 0 & 0 & 0 \\ -\mu\sin(b_{\text{wlc},2}+\bar{\Omega}\tau) & \mu\cos(b_{\text{wlc},2}+\bar{\Omega}\tau) & 0 & \mu & 0 & 0 \\ 0 & 0 & \varsigma_e & 0 & -1 & 0 \\ 0 & 0 & 0 & \varsigma_e & 0 & -1 \end{bmatrix}$$

$$\mathbf{F}_{\text{wlc}} = \begin{bmatrix} -x''_{\text{wlc}} - x_{\text{wlc}} - \varsigma_v x'_{\text{wlc}} + \bar{\Omega}^2\eta\cos(\varphi_e+\bar{\Omega}\tau) + \sum_{i=1}^{2}\mu b''_{\text{wlc},i}\sin(b_{\text{wlc},i}+\bar{\Omega}\tau) + \sum_{i=1}^{2}\mu(b'_{\text{wlc},i}+\bar{\Omega})^2\cos(b_{\text{wlc},i}+\bar{\Omega}\tau) \\ -y''_{\text{wlc}} - R_r{}^2 y_{\text{wlc}} - \varsigma_w y'_{\text{wlc}} + \bar{\Omega}^2\eta\cos(\varphi_e+\bar{\Omega}\tau) - \sum_{i=1}^{2}\mu b''_{\text{wlc},i}\cos(b_{\text{wlc},i}+\bar{\Omega}\tau) + \sum_{i=1}^{2}\mu(b'_{\text{wlc},i}+\bar{\Omega})^2\sin(b_{\text{wlc},i}+\bar{\Omega}\tau) \\ q_{\text{wlc},1}R_n - \mu b''_{\text{wlc},1} - \mu y''_{\text{wlc}}\cos(b_{\text{wlc},1}+\bar{\Omega}\tau) + \mu x''_{\text{wlc}}\sin(b_{\text{wlc},1}) - b'_{\text{wlc},1}(\varsigma_b+\varsigma_e) \\ q_{\text{wlc},2}R_n - \mu b''_{\text{wlc},2} - \mu y''_{\text{wlc}}\cos(b_{\text{wlc},2}+\bar{\Omega}\tau) + \mu x''_{\text{wlc}}\sin(b_{\text{wlc},2}) - b'_{\text{wlc},2}(\varsigma_b+\varsigma_e) \\ q''_{\text{wlc},1} + C_n q_{\text{wlc},1} + R_n q'_{\text{wlc},1} - \varsigma_e b''_{\text{wlc},1} \\ q''_{\text{wlc},2} + C_n q_{\text{wlc},2} + R_n q'_{\text{wlc},2} - \varsigma_e b''_{\text{wlc},2} \end{bmatrix}$$

A7.5

M, **K** are given here for Eq. (6-3).

$$\mathbf{C}=\begin{bmatrix} c & 0 & -2m_bR_b\Omega\cos(\varphi_{b1}+\Omega t) & -2m_bR_b\Omega\cos(\varphi_{b2}+\Omega t) & 0 & 0 \\ 0 & c & -2m_bR_b\Omega\sin(\varphi_{b1}+\Omega t) & -2m_bR_b\Omega\sin(\varphi_{b2}+\Omega t) & 0 & 0 \\ 0 & 0 & \dfrac{R_b{}^2(c_b(R_{C1}+R_{L1})+\theta_e{}^2)}{R_{C1}+R_{L1}} & 0 & 0 & 0 \\ 0 & 0 & 0 & \dfrac{R_b{}^2(c_b(R_{C2}+R_{L2})+\theta_e{}^2)}{R_{C2}+R_{L2}} & 0 & 0 \\ 0 & 0 & 0 & 0 & -\dfrac{L_1}{C_1(R_{C1}+R_{L1})} & 0 \\ 0 & 0 & 0 & 0 & 0 & -\dfrac{L_2}{C_2(R_{C2}+R_{L2})} \end{bmatrix}$$

$$\mathbf{F}=\begin{bmatrix} \Omega^2m_eR_e\cos(\varphi_e+\Omega t)+\sum_{i=1}^{2}\Omega^2m_bR_b\cos(\varphi_{bi}+\Omega t)+m_bR_b\cos(\varphi_{bi}+\Omega t)\dot{\varphi}_{bi}{}^2 \\ \Omega^2m_eR_e\sin(\varphi_e+\Omega t)+\sum_{i=1}^{2}\Omega^2m_bR_b\sin(\varphi_{bi}+\Omega t)+m_bR_b\sin(\varphi_{bi}+\Omega t)\dot{\varphi}_{bi}{}^2-(gm_R+gm_e+2gm_b) \\ -gm_b\cos(\Omega t+\varphi_{b1}) \\ -gm_b\cos(\Omega t+\varphi_{b2}) \\ 0 \\ 0 \end{bmatrix}$$

VITA

Xiaowen Su received both B.S. and M.S. degrees in Mechanical Engineering from Donghua University, China, in 2011 and 2014, respectively. She is currently pursuing the Ph.D. degree at the Department of Mechanical, Aerospace and Biomedical Engineering, University of Tennessee, Knoxville. Her research interests include helicopter propulsion, nonlinear dynamics, rotordynamics, mechanical vibrations and control, energy harvesting, mechanical design and analysis.